

FROM DIATOMS TO MALARIA: SYNTHESIS AND APPLICATION OF
FUNCTIONAL MATERIALS

By

Joshua David Swartz

Dissertation

Submitted to the Faculty of the
Graduate School of Vanderbilt University
in partial fulfillment of the requirements
for the degree of

DOCTOR OF PHILOSOPHY

in

Chemistry

December, 2011

Nashville, Tennessee

Approved:

Professor David W. Wright

Professor Brian O. Bachmann

Professor David E. Cliffl

Professor Frederick R. Haselton

TABLE OF CONTENTS

	Page
LIST OF SCHEMES.....	v
LIST OF TABLES	vi
LIST OF FIGURES	vii
ABSTRACT.....	xii
Chapter	
I. BIOMIMETIC SYNTHESIS OF SILICA NANOMATERIALS	1
Introduction.....	1
Metal Oxides in Nature.....	3
Diatoms	4
Biological Synthesis of Silica Nanoparticles.....	5
Biomimetic Synthesis of Silica Nanoparticles.....	8
Peptide and Peptide Derivatives	10
R5 Peptide.....	10
Poly-L-Lysine	14
Block Co-Polypeptides	15
Lanreotide	18
Polyamines.....	19
Poly(ethyleneimine).....	20
Other Unbranched Polyamines	22
Dendrimers.....	24
Other Biomimetic Templates.....	27
Conclusion	28
Dissertation Aims Using Biomimetic Syntheses	29
II. BIOMIMETIC SYNTHESIS OF ENZYME-CONTAINING SILICA NANOPARTICLES.....	30
Introduction.....	30
Nitrilase.....	31
Experimental	33
Results.....	36
β -glucosidase	45
Experimental	47
Results.....	50

	Conclusions.....	55
III.	BOTTOM-UP SYNTHESIS OF BIOLOGICALLY ACTIVE MULTILAYER FILMS USING INKJET PRINTED TEMPLATES	57
	Introduction.....	57
	Experimental.....	59
	Results	62
	Conclusions.....	71
IV.	CURRENT STRATEGIES IN MALARIA DIAGNOSTICS	72
	Introduction.....	72
	Healthcare in the Developing World	77
	Current Malaria Diagnostic Strategies.....	79
	The Future of Malarial Low-Resource Diagnostics.....	84
	Dissertation Aims for the Development of Malaria Diagnostics.....	85
V.	DEVELOPMENT OF A LOW RESOURCE PURIFICATION PLATFORM FOR PLASMODIUM FALCIPARUM HISTIDINE-RICH PROTEIN-II USING SURFACE TENSION VALVES	86
	Introduction.....	86
	Experimental.....	89
	Results	93
	Extraction Device and Physical Properties	94
	Optimization of Sample Processing Parameters	100
	Evaluation of the Current Extraction Design.....	106
	Extraction Efficiencies below the WHO's Limit of Detection	111
	Conclusions.....	112
	Future Directions	113
VI.	DEVELOPMENT OF A COFFEE RING-BASED DIAGNOSTIC PLATFORM FOR THE DETECTION OF HISTIDINE-RICH PROTEINS	115
	Introduction.....	115
	Physical Properties of Coffee Ring Formation	116
	Functional Gold Nanoparticles as Aggregation Reagents	119
	Experimental.....	122
	Results	131
	Synthesis and Characterization of Ni(II)NTA Nanoparticles	133
	Synthesis and Characterization of Functional Glass Slides.....	138
	Reaction Properties of Ni(II)NTA AuNPs.....	140
	Aggregation Properties of the Mixed-Monolayer Ni(II)NTA AuNPs with Recombinant HRP-II	152

Development of the Coffee Ring Assay	154
Discussion/Future Directions.....	161
Conclusions.....	164

Appendix

A. CRYSTAL ENGINEERING: SOLVENT EFFECTS ON β -HEMATIN FORMATION.....	165
B. SYNTHESIS OF PEPTIDES FOR RANDOM STUDIES.....	176
REFERENCES	180
CURRICULUM VITAE.....	191

LIST OF SCHEMES

Scheme	Page
1. Hydrolysis of 3-cyanopyridine with nitrilase	41
2. Reaction scheme for the synthesis of the NTA-PEG-Thiol and HO-PEG-Thiol ligand.....	134
3. Modular design of the M(II)NTA functionalized AuNPs.....	135
4. Synthesis scheme for Ni(II)NTA functionalized glass slides	138

LIST OF TABLES

Table	Page
1. Silica morphology for each copolypeptide at different synthesis conditions	16
2. Physical properties of nitrilase-containing silica nanoparticles.....	40
3. Kinetic parameters and specific activity of nitrilase-containing silica nanoparticles	42
4. Activity of GO_x as a function of starting enzyme concentration	68
5. Limits of detection for current malarial diagnostic strategies	81
6. Peptides synthesized using standard solid phase Fmoc peptide synthesis	177

LIST OF FIGURES

Figure	Page
1. Scanning electron microscopy images of the cell walls of a variety of diatom species	5
2. Chemical structure of silaffin-1 A ₁ from <i>C. fusiformis</i>	7
3. Schematic representation of the fusion protein and its use in controlled silica nanomaterial formation.....	11
4. Sphere diameter distribution for silica particles precipitated using R5 peptide and R5-EAK ₁ and the sphere size distribution for silica particles formed with R5-EAK ₁ at different temperatures.....	13
5. Proposed model of PLL induced condensation of silica platelets.	14
6. Schematic of silica tube formation	15
7. Field-emission scanning electron microscopy (FE-SEM) images of silica nanoparticles synthesized using Lys ₃₄₀ - <i>b</i> -Gly ₈₅ and Lys ₃₂₀ - <i>b</i> -Gly ₁₆₀ using Methods I, II, and III.....	17
8. Synthesis of lanreotide-templated silica nanotubes	18
9. Diameter and dispersity of silica particles formed in aqueous PEI solutions at 0.05M primary-amine concentration and 1M silicic acid in a 4:1 volume ratio at pH 9, 10, and 11	20
10. Structures of unbranched polyamines	22
11. Schematic representation of the microemulsion formation leading to hollow silica structures.....	23
12. Chemical structure of the G-3 PPI dendrimer and G-1 PAMAM dendrimer	24
13. Schematic silica encapsulation of Au ⁰ nanoparticles and CdSe/ZnS core shell AMP quantum dots	25
14. Effect of increasing the phosphate buffer concentration on GOx encapsulation...26	
15. Structure of DPTA cellulose tosylate	27

16. Silica nanotubes	28
17. Enzymatic conversion of nitriles to carboxylic acids	32
18. SEM images of nitrilase-containing silica nanoparticles.....	39
19. Size distribution graphs of the nitrilase-containing silica nanoparticles	40
20. HPLC spectra following the conversion of a 50 mM solution of 3- cyanopyridine to nicotinic acid with nitrilase-containing nanoparticles	43
21. Consecutive experiments performed on a single triplicate batch of nitrilase- containing silica	44
22. Catalytic mechanism found in the hydrolysis of oligosaccharides to glucose by <i>Aspergillus niger</i> β -glucosidase.....	49
23. Loading efficiency (left) and specific activity (right) of β -glucosidase- containing silica nanoparticles	51
24. SEM images and particle size distributions of β -glucosidase containing silica nanoparticles	52
25. Kinetic parameters of free and silica encapsulated β -glucosidase.....	53
26. Thermal and pH stability of β -glucosidase encapsulated within silica nanoparticles	55
27. The change in morphology of a printed spot as a function of reaction time with monosilicic acid using Method I.....	62
28. Height profiles of the two methods used in multicomposite formation.....	64
29. The change in morphology of a printed spot as a function of reaction time with monosilicic acid using Method II	65
30. Images of the patterned inks on gold and a 96-well plate.....	67
31. The calculated reusability of the enzyme encapsulated patterns as a function of time	70
32. Storage stability of active printed patterns.....	71
33. Estimated incidence of malaria per 1000 population, 2006.....	72
34. Life cycle of the malarial parasite.....	74

35. Typical laboratory conditions at mid-level healthcare facilities in the developing world	78
36. General light microscopy for <i>Plasmodium</i> detection.....	80
37. Dipstick malarial RDT mechanism of action.....	82
38. Malarial RDT detection rates as reported in the WHO's Malaria Rapid Diagnostic Test Performance study of 2008-2009.....	83
39. Coordination of histidine-rich targets to Ni(II)NTA ligands	88
40. General extraction device design using surface tension valves	95
41. Bead transport through water/oil interface	98
42. Extraction efficiencies of TAMRA-HRP-II using the extraction device.....	101
43. Early device design and extraction efficiencies of <i>pf</i> HRP-II from culture.....	102
44. Extraction efficiencies in complex biological media at variable times	103
45. Effect of elution chambers volume on recovery	105
46. Self-contained sample processing design	106
47. Imidazole binding study to determine the optimal blocking conditions.....	107
48. Comparison of extraction efficiencies of physiologically relevant concentrations of <i>pf</i> HRP-II in buffer, plasma and human whole blood	108
49. Quantification of HRG bound to Ni(II)NTA magnetic agarose beads in the presence of blocking conditions of imidazole.	109
50. HRG purification efficiencies in the extraction device.....	110
51. Quantification of contaminating proteins in the wash and elution chambers	111
52. Recoveries of <i>pf</i> HRP-II at and below the current WHO required limits of detection	112
53. Schematic of coffee ring formation	116
54. Surface Plasmon resonance of AuNPs.....	120

55. General coffee ring assay procedure using Ni(II)NTA AuNPs	133
56. UV-Visible spectra and table of particle diameters and Zeta potentials for NTA and mixed-monolayer AuNPs.....	136
57. Characterization of Ni(II)NTA and mixed-monolayer AuNPs.	137
58. Surface characterization of functionalized slides using contact angle measurements.....	139
59. Aggregation behavior of Ni(II)NTA AuNPs in the presence of PLH at neutral pH	142
60. Effect of imidazole on the aggregation of Ni(II)NTA AuNPs in the presence of PLH at neutral pH.....	143
61. pH dependence of PLH-induced aggregation of Ni(II)NTA AuNPs.....	144
62. Aggregation behavior of Ni(II)NTA AuNPs in the presence of acidic and basic poly amino acids at variable pH	145
63. Aggregation of Ni(II)NTA AuNPs in the presence of the malarial mimics pHRP-II and BNT-II.....	147
64. Aggregation properties in the presence of interfering proteins	150
65. Thermal stability of Ni(II)NTA AuNPs.....	152
66. Aggregation properties of mixed monolayer Ni(II)NTA AuNPs in the presence of recombinant HRP-II	153
67. Limits of detection of recombinant HRP-II in the presence of variable concentrations of 50% Ni(II)NTA AuNPs	154
68. Coffee ring formation induced by HRP-II induced pinning of Ni(II)NTA AuNPs during drop drying.....	155
69. Coffee ring formation induced by interfering proteins	156
70. Effects of glycerol on ring formation.....	158
71. Signal intensity calculated using the custom protocol on Image Pro Plus software.....	159
72. Selective coffee ring formation induced by recombinant HRP-II induced pinning of Ni(II)NTA AuNPs during drop drying.....	160

73. Demonstration of M(II)NTA polystyrene as an alternative capture bead in the coffee ring assay	162
74. Three-particle coffee ring assay format	163
75. SEM Characterization of β -hematin synthesized with acetonitrile	169
76. SEM Characterization of β -hematin synthesized with chloroform	170
77. SEM Characterization of β -hematin synthesized with DCM	171
78. SEM Characterization of β -hematin synthesized with DMF.....	172
79. SEM Characterization of β -hematin synthesized with DMSO.....	173
80. SEM Characterization of β -hematin synthesized with toluene.....	174
81. Characterization of HRP-II peptide mimics	178
82. Selected MALDI spectrum for synthesized peptides.....	179

ABSTRACT

FROM DIATOMS TO MALARIA: SYNTHESIS AND APPLICATION OF FUNCTIONAL MATERIALS

JOSHUA DAVID SWARTZ

Dissertation under the direction of David Wilson Wright

This dissertation focuses on two unique projects that attempt to solve two unique challenges. Biomimetic syntheses provide scientists the opportunity to develop functional materials that aren't available with traditional synthetic processes. Diatoms, for example, are capable of designing intricate silica structures under mild reaction conditions using amine-terminated polymeric organic compounds and post-translationally modified peptides. The goal of this half of the thesis was to capitalize on the simplicity and ease of morphological control to encapsulate functional enzymes such as nitrilase and β -glucosidase within the growing silica matrix. This matrix serves to protect the enzymes from degradation and enhances their shelf-lives. Also, piezoelectric inkjet printing techniques were utilized to pattern these enzyme-encapsulated substrates onto reactive surfaces toward the design of functional materials. The second half of this thesis focuses on developing alternative strategies for malarial diagnostics. Malaria is a tropical disease caused by the *Plasmodium* parasite. Its prevalence in most developing countries creates a financial burden on both the residents of these regions, as well as the health organizations trying to eradicate the disease. With the development of antimalarial drugs such as

chloroquine, malaria was nearly eliminated in the middle half of the 20th century. With the development of parasitic resistance, malaria has reemerged as one of the most dangerous diseases in the developing world. Paramount to effective treatment is accurate and efficient diagnosis of patients in low resource settings. Although significant progress has been made toward diagnostic strategies in these settings, the current “gold standards” still are not capable of being effective in the most remote regions, due to their reliance on electricity or sensitive reagents. The second half of this thesis is focused on circumventing the challenges of low resource diagnostics through alternative diagnostic strategies and novel sample processing technologies. Using surface tension valving to separate aqueous processing chambers, complex biological samples can be processed to collect, purify, and concentrate biomarkers for malaria diagnosis. Capitalizing on the high affinity of the malarial protein Histidine-Rich Protein II (*pf*HRP-II) towards Ni(II)NTA chelation, this sample processing technology has been demonstrated to collect and isolate this protein from human whole blood and plasma with modest yields. To circumvent the challenges associated with current diagnostic strategies, a novel coffee ring diagnostic has been developed that captures the biomarker of interest and processes it within the drying drop. Utilizing radial flow, this assay is capable of concentrating a signal into a small ring visible by the naked eye. This is the first time that this phenomenon has been used as a diagnostic platform. Whether it is for improving enzyme longevity or diagnosing malaria in the field, these functional materials serve to improve the overall wellbeing of mankind.

CHAPTER I

BIOMIMETIC SYNTHESIS OF SILICA NANOMATERIALS

Introduction

Traditionally, synthetic approaches for the production of functional metal oxide materials such as silicon dioxide (silica; SiO₂) have involved high-temperature reaction environments with energy intensive techniques such as laser ablation, ion implantation, chemical vapor deposition (CVD), photolithography, or thermal decomposition.⁴ The incorporation of these techniques provided a rapid prototyping technique, essential for the commercial development of current minimum-feature sized semiconducting integrated circuits. However, the production of these devices has come at a major price. Some of the primary challenges currently faced by high-throughput fabrication laboratories include the high cost of laborers and instruments, high temperature reaction conditions, and a surplus in generated waste.⁴ In fact, the cost of fabrication facilities are estimated to reach an outstanding \$100 billion dollars per facility by the year 2020, as the demand for smaller, lighter, and faster materials continues to grow.⁴ Additionally, manufacturers are progressing in this manner at the expense of the environment, as they accumulate hazardous chemical wastes.²² For decades, researchers have been searching for alternative methods to passivate the rate of waste production and the cost of spending in the semiconductor industry.

The most accessible resource for the synthesis of functional materials under ambient conditions is found in biology. From highly ordered nanostructures to genetically

controlled reactive surfaces, systems in biology perpetually demonstrate their ability to find effective solutions to multifaceted, real world problems using a rigorous process of natural selection.²³⁻²⁷ The versatility of biology's incredible portfolio encourages researchers to develop modified syntheses derived from nature. Their findings have been successfully organized into the field of *biomimetics*, or bio-inspired research, which encompasses alternative approaches towards developing nonmaterial's with technological applications.²⁸ Based primarily on the designs, mechanisms, and processes found in nature, biomimetics encompasses the field of structural biology while interfacing engineering, materials science, physics, and chemistry.^{24,28}

Biomimetics infers manipulating and mimicking the natural architectures and processes of biologically produced minerals, or *biominerals*, to direct the synthesis of non-natural materials. For instance, the architecture of one of the most abundant biological species on the planet, the virus, has recently been manipulated to serve as containers for the synthesis of a variety of functional molecular cargoes.^{29,30} In particular, the positively charged interior of the cowpea chlorotic mottle virus (CCMV) has been used as a container for the nucleation of spatially confined metal oxide nanomaterials.³⁰ On a larger and more complex scale, versatile strategies for substrate modification have been developed directly, through inspiration from surface mediated mineralization of biological organisms.²³ The eggshell matrix proteins from the Chinese soft-shelled turtle (composed primarily of aragonite, CaCO_3) were isolated and revealed properties that are necessary for embryonic survival.²³ It was suggested that the matrix proteins contained pelovaterin peptides as their major unit that self-assembled into micelles, altering the interfacial energy of the eggshell.³¹ Applications of such controlled mineralization could

be applied to the successful construction of functional two-dimensional (2D) reactive surfaces, with reduced nonspecific adsorption.³²⁻³⁵

As mentioned above, bio-inspired research is based on identifying and emulating the principles of biomineralization in natural systems instead of copying them directly. In fact, most strategies incorporated by natural systems are not directly applicable to engineered materials, so the need for alternative synthetic routes are required for the incorporation of non-natural elements, such as barium, nickel, copper, or aluminum, with functional nanoscale properties.^{4,28} From a materials perspective, highly intact biological structures such as diatoms, bacteria, proteins, or butterfly wings provide an excellent source of inspiration for their synthesis.

Metal Oxides in Nature

There have been as many as 60 identified biominerals that are necessary for the proper function of organisms, and more than 60% of them are reported to be coordinated to either hydroxyl moieties or water molecules, enabling the rapid release of ions in solution.²⁷ Metal oxides, in particular, provide a fundamental stepping-stone for the development of functional nanomaterials. In the oxidative environment of the atmosphere of the Earth, oxides are the lowest free energy states for most metals in the periodic table and have applications ranging from semiconductors to insulators.³⁶ As insulators, SiO_2 and Al_2O_3 are the two most commonly used supports for catalysis, as they are non-reducible oxides.³⁶ Semiconductors, such as ZnO and SnO_2 , have high electrical resistivities that provide alternative templates for gas sensors.³⁶ Currently, microelectronics rely on bulk silica as an important dielectric material that is often used

as an insulating template for further reactivity. On the nanoscale, silica can be synthesized by polymerizing silicic acid in an aqueous system or through hydrolysis and condensation of silicon alkoxides in the Stöber synthesis.³⁷ The mechanism of these two methods is unique. The first method is dominated by monomers and tetra-functionalized species. The resultant silicate sols are uniform, meaning that they are fully hydrolyzed and grow by monomer addition. On the other hand, di- and tri-functionalized species are dominant for alkoxides. Regardless of the synthesis used, these particles induce a fractal interior with minimal morphological control due to their common template, ammonium hydroxide.³⁷

Surprisingly, the properties associated with metal oxides in technology are not so far removed from what is observed in natural systems. Through precisely tuned processes, Nature is able to synthesize a variety of metal oxide nanomaterials under ambient conditions. The magnetic navigation device found in magnetotactic bacteria (MTB) is one such example.³⁸ Magnetite (Fe_3O_4) nanocrystals are aligned with the Earth's geomagnetic field and are contained within specific organelles known as magnetosomes.³⁸ Fresh water salmon, for example, utilize these magnetic nanoparticles in the nasal cavities of their forehead as a biomagnetic compass during migration.³⁹

Diatoms

Diatoms are one of the largest groups and perhaps one of the most studied single-celled eukaryotic micro algae found in almost every sea- and freshwater habitat. These microorganisms have silica-based cell walls, which range in size from ~50 to 500nm (**Figure 1**).⁴⁰ Although diatom silica is X-ray amorphous, they still exhibit highly regular

and rather exquisite patterns of pores, ridges, or tubular structures that are formed under genetically controlled processes. Studies using electron microscopy have revealed that the valves and girdle bands associated with silica formation are formed inside the cell within highly specialized membrane-bound compartments called silica deposition vesicles (SDVs).³² After morphogenesis is completed, these silica species are deposited on the cell surface using SDV exocytosis.

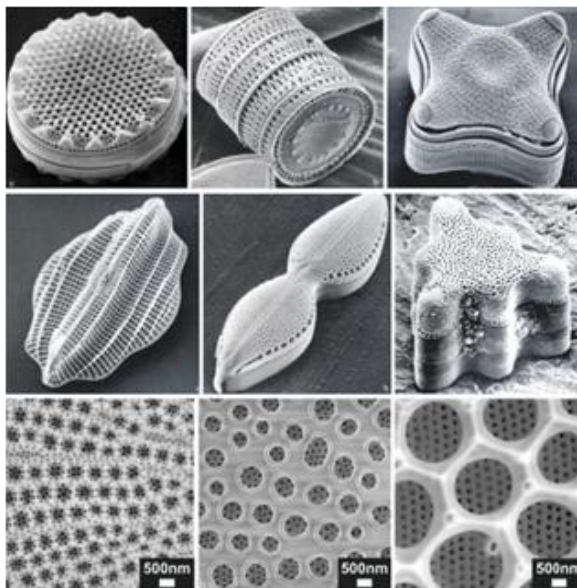


Figure 1. Scanning electron microscopy images of the cell walls of a variety of diatom species.⁵

Biological Synthesis of Silica Nanoparticles

Specific silicon transport proteins (SITs) produced by diatoms are responsible for the uptake and delivery of orthosilicic acid ($\text{Si}(\text{OH})_4$, $pK_a = 9.8$) to the diatom. Within the cell, orthosilicic acid is then concentrated up to 1000-fold, resulting in the condensation of amorphous, hydrated silica.⁵ Strikingly, poly-condensation of silica occurs in neutral to slightly acidic pH conditions under ambient temperatures and pressures. Although these conditions are considered mild, diatoms still have control over the product morphology. It

is understood that the patterns created by diatoms are species specific, so their directed growth process must be regulated by transcription.³⁷

Significant effort has been devoted to determining the specific templates used by different species of diatoms in silica formation. Although diatom cell walls consist primarily of silica doped (~97%) with trace amounts of aluminum and iron, they also contain a wide variety of incorporated organic molecules and proteins.⁴¹ In fact, solid-state nuclear magnetic resonance (NMR) spectroscopy revealed that some of these molecules and coat proteins are encapsulated within the silica matrix.^{42,43} Two main templates for silica growth were identified after dissolution of the silica cell wall with hydrogen fluoride (HF) or ammonium fluoride.

Extracted and purified from up to three species of diatoms (*C. fusiformis*, *T. pseudonana*, and *E. zoodiacus*), silaffins are polypeptides (4-17kDa) with a variety of posttranslational modifications, including propylamino-functionalized lysine side chains (**Figure 2**).⁴⁰ Currently, there have been four silaffin genes identified (one from *C. fusiformis* (sil1) and three from *T. pseudonana* (tpSil1, tpSil2, and tpSil3)), which encode for eight known polypeptides. Of these four genes, only tpSil1 and tpSil2 have shown sequence similarities, likely from gene duplication; however, the overall lack of sequence similarity strongly suggests that the posttranslational modifications of silaffins are critical to their function. These posttranslational modifications include mono-hydroxylation of lysine and proline, di-hydroxylation of proline, *o*-phosphorylation of serine, threonine, hydroxyproline and hydroxylysine, glycosylation, sulfation of carbohydrate moieties, and alkylation of ϵ -amino groups of lysine.^{41,44} These modifications are charged and stabilized through electrostatic interactions between the phosphate groups on one silaffin

to the charged amines of another, inducing a self-assembled template available for further reactivity.

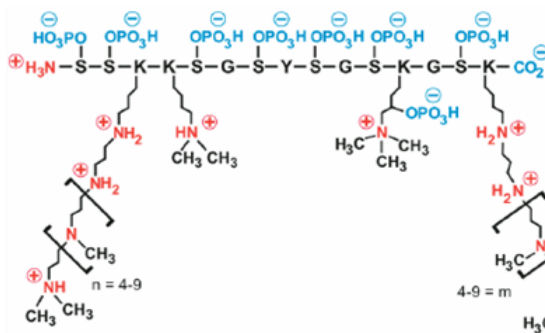


Figure 2. Chemical structure of silaffin-1 A_1 from *C. fusiformis*.²⁰

The different structures associated with different species of diatoms are directly related to the silaffin being studied. For instance, spheres (silaffin-1/2L mixture from *T. pseudonana*⁴⁵), dense plates (silaffin-3 from *T. pseudonana*⁴⁵), or porous sheets (silaffin-1/2H mixture from *T. pseudonana*⁴⁵ or natSil-2 from *C. fusiformis*⁴⁶) are all a function of a precursor template. While silaffins are responsible for controlling which shapes formed in the SDV, positively charged long-chain polyamines (LCPAs) are an integral part of silica condensation.⁵ The silaffins that are negatively charged must be stabilized by the LCPAs, or the recently discovered silacidins⁴⁷ (in *T. pseudonana*), to complete silica condensation.

LCPAs are non-protein components (>3.5kDa) that were found encapsulated in the silica matrix of the diatom and were isolated through a series of HF extractions.⁴⁸ Unlike silaffins, which utilize a peptide backbone, these polyamines consist of linear chains of C-N linked propyleneimine units that are bonded to a putrescine or putrescine derivative

backbone. The chemical composition of these long-chain polyamines is unique for each diatom species, with variable repetitions and degrees of methylation.

Similar to reactivity of silaffins, silica production in the presence of LCPA and silicic acid requires an addition of counter anion in the form of phosphate, sulfate, or citrate ions. This electrostatic matrix is projected to induce the formation of silica by microscopic aggregation of LCPAs and subsequent phase separation into a LCPA-anion-rich microdroplet.³² In his 2002 theory of cell wall morphogenesis, Manfred Sumper suggested that the formation of secondary patterns, as seen on the diatom cell wall, is related to the wall-to-wall distance of the areolae, hexagonally packed polyamine monolayers and the polyanion concentration, on the surface of the SDV.³² For example, a size-control experiment using LCPAs from *S. turris* has shown that the size of nanoparticles was dependant not only on the phosphate concentration, but also whether orthophosphate or a more highly charged pyrophosphate was used.⁴⁹

Biomimetic Synthesis of Silica Nanoparticles

The biological mechanism of diatom silica formation has been demonstrated as a valuable source for bioinspired templates for non-natural metal oxide synthesis at ambient temperatures and near-neutral pH. Moreover, silica nanostructures can be tuned according to a specific template, providing functional properties that can be directly applied in designing nanomaterials. These syntheses have integrated moieties that are tuned for a specific function, such as encapsulation of functional enzymes^{9,50} and controlled construction of nanomaterials through nanoscale building blocks.^{15,17,51}

Mimicking the nanopatterns of the diatom cell wall still remains a great challenge for materials scientists because the natural reaction mechanism still unknown, as many essential components to silica precipitation have yet to be discovered. However, it is well known that the terminal amine templates interact with monosilicic acid to induce the specific morphology of the resultant silica. A variety of different silica pre-cursors have been used with a number of templates, including tetramethyl orthosilicate (TMOS),^{6,7,9,14,52-56} tetraethyl orthosilicate (TEOS),^{10,17,57} tetrakis(2-hydroxyethyl) orthosilicate (THEOS),¹⁰ sodium silicate,⁵¹ a silicon-catecholate complex,^{15,58} and dipotassium Tris(1,2-benzenediolato-O,O') silicate.¹¹ In addition, a variety of bio-inspired templates have been used, including synthetic and natural polypeptides,^{17,52,57} polyamines,^{6,56,58} and even modified organic materials, including cellulose⁵⁹ and chitosan.⁶⁰

Recently, synthetic or natural polypeptides have been created or modified to serve as silica condensation templates. Many examples of these polypeptides include the poly(amino acids),⁶¹ the diatom-derived R5-peptide,⁵² chimeric polypeptides,^{14,15} block co-polypeptides,^{54,55,57,62} lanreotide,¹⁷ and even the naturally occurring protamine.⁵¹ These polypeptides have been used to produce a variety of silica shapes and sizes, which can be tuned to perform a variety of applications, including transport and separation of encapsulated materials⁹, or potentially for drug delivery.⁵⁶

Peptide and Peptide Derivatives

R5 Peptide

The R5 peptide ($\text{H}_2\text{N-SSKKSGSYSGSKGSKRRIL-CO}_2\text{H}$) is an unmodified biomimetic analog of the silaffin precursor peptide (sil1p) in *C. fusiformis* that exhibits silica condensation activity at neutral pH in a buffered phosphate-citrate solution.³⁴ These peptides self-assemble into an ordered matrix through electrostatic interactions facilitated by the cationic lysine and arginine residues and the anionic citrate and phosphate ions, providing an ordered template for silica condensation. Capitalizing on the high charge associated with this peptide-salt complex, several enzymes have been encapsulated within the silica matrix with the R5-peptide as the silica template, including catalyase, horseradish peroxidase, and butyrylcholinesterase.^{50,52} The silica matrix provides an inert cage around the enzyme which not only protects it from the surrounding environment and increases its shelf life but it could also provide the basis for biosensors and catalysts. In addition, CoPt, CdSe and ZnS nanoparticles were also successfully encapsulated into the silica matrix.⁵⁰ These magnetic nanoparticles could serve a wide variety of applications, including catalysis, biological labeling and detection, and electronics.⁷ In addition, these encapsulated magnetic particles have potential use in enzyme encapsulation because they could provide a physical means to separate the enzyme from the reaction mixture.

Chimeric (fusion) proteins that incorporate the R5 peptide have also been synthesized to control and precipitate silica nanoparticles. Po Foo and coworkers have utilized a two component chimeric protein consisting of the R5 polypeptide (from *C. fusiformis*) and the self-assembling domain based on the consensus repeat in the major ampullate spidroin protein 1 (MaSp1) of *N. clavipes* spider dragline silk.¹⁵ MaSp1 forms highly stable β -

sheet secondary structures that can be spun into intricate fibers, which when fused with the silica-templating R5-peptide, allow for the formation of film-like and fibrous silica structures (**Figure 3**).

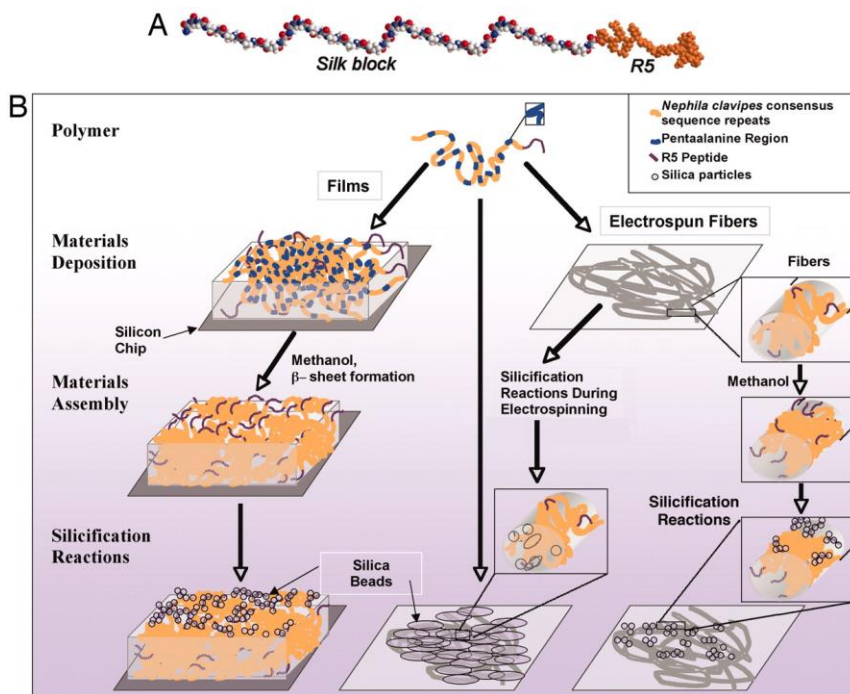


Figure 3. Schematic representation of the fusion protein and its use in controlled silica nanomaterial formation. A.) Schematic of the chimeric polypeptide consisting of the R5 and silk polypeptides. B.) Model of R5-silk polypeptide processing into films and fibers and subsequent silicification reactions.¹⁵

Two different silk motifs were investigated, one with and one without a CRGD cell-binding motif. When silica precipitation was conducted under ambient temperatures and near-neutral pH with ratios of Si:N = 22:1 in solution, silica nanospheres with $>1\mu\text{m}$ diameter were synthesized for both fusion proteins. Thermal analysis determined that $\sim 90\%$ of the material was the templating protein and the remaining 10% was silica. Nitrogen absorption analysis indicated a pore radii <10 angstroms and a low surface area ($\sim 10\text{m}^2/\text{g}$), which are smaller than the R5-peptide templated silica nanospheres (pore radii = 35 angstroms and surface area = $600\text{m}^2/\text{g}$). Although silica precipitation was

successfully conducted with the free R5-silk peptide in solution, the silk moiety provides a means for size and shape control for the growing silica nanocomposite. When these chimeric proteins were spun into fibers via electrospinning, silica nanospheres were formed with much smaller diameters (200-400 nm). In addition, when the chimera CRGD15mer + R5 was electrospun concurrently with the silica condensation reaction, silica was deposited in and on the fibers, resulting in elliptically shaped silica particles that were fused to the fibers. As a result, processing modifications can be tailored to structural templates, inducing silica nanoparticles of specific sizes and morphologies. Most importantly, since this reaction is conducted under mild conditions, these fibers have a variety of potential applications in specialty materials, including those used in the biomedical field.¹⁵

Another chimeric polypeptide consisting of the R5-peptide and a self-assembling hydrophobic-phobic (HP) protein monomer capable of self-assembly was also used to direct silica precipitation *in vitro* at neutral pH and ambient temperatures.¹⁴ The HP monomer consists of an n-AEAEAKAKAEAEAKAK-c sequence, called EAK₁. These monomers self-assemble into stable β -sheet supramolecular structures due to their binary patterns. This leads to hydrophobic and hydrophilic faces, where favorable side-chain interactions result in aggregation through hydrophobic and electrostatic interactions, respectively. Thus, an EAK₁-R5 chimeric polypeptide assembles into fibrous aggregated hydrogels and precipitates silica nanospheres with sizes dependant on the reaction temperature (**Figure 4**).

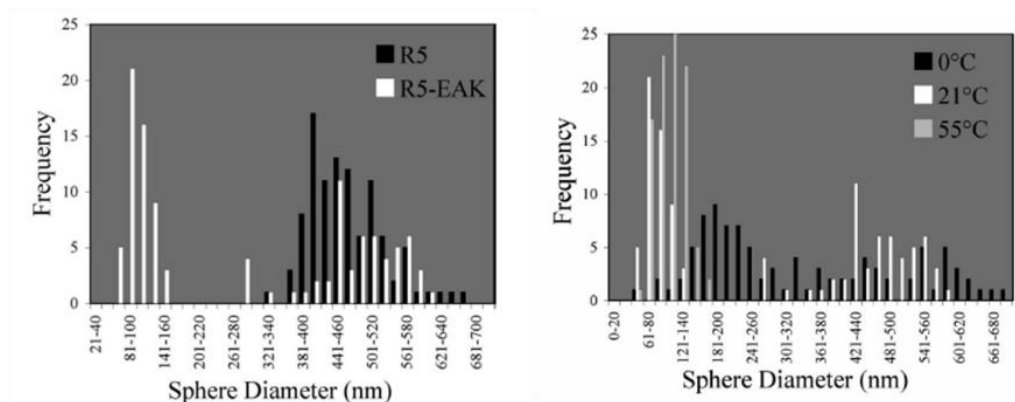


Figure 4. Sphere diameter distribution for silica particles precipitated using R5 peptide (black, left) and R5-EAK₁ (white, left) and the sphere size distribution for silica particles formed with R5-EAK₁ at different temperatures (right).¹⁴

The size distribution of the control R5 template for silica formation produced a distribution of nanoparticles in the diameter range of 402-530 nm, as opposed to the R5-EAK templates, which showed a bimodal range of diameters from 63-103 nm and 385-541 nm respectively. However, at higher temperatures, the R5-EAK₁ peptide promotes rapid nucleation, resulting in a loss of bimodal character and subsequently the production of smaller silica nanoparticles (64-116 nm in diameter). Not only does the change in diameter size with different temperatures allow for the production of size-specific tailored silica nanocomposites, but also the loss of bimodal character at higher temperature allows for an even tighter control of silica structure under these conditions. By adjusting this morphology under mild reaction conditions, biologically active matrices can be synthesized, and could be used in solid-state enzymatic catalysis, physiologically active biomatrix implants, and potentially biosensors.¹⁴

Poly-L-Lysine

Poly-L-lysine (PLL) has been implicated in silica formation because of its ability to adopt a α -helix, β -sheet, or random coil conformation under controlled conditions. For example, PLL is a random coil at neutral pH, but at high pH (~ 11) the polymer assumes a α -helical shape. Hawkins and coworkers have shown that silica pore sizes could be modified by changing the secondary structure of the polyamine.⁶³ For example, silica composites that are formed by α -helix PLL under basic conditions (pH 11.2) produced 1.5 nm pore sizes; on the other hand, silica formed using PLL β -sheets (heated to $\sim 52^\circ\text{C}$) resulted in larger pore sizes (~ 1.5 -8 nm). In both cases, silica formation was dependant on the PLL concentration and reaction conditions.

More recently, Tomczak and coworkers have shown that hexagonal silica platelets can be synthesized using PLL as a precursor.¹⁸ The morphology of silica species is highly specific to the size of the PLL polymer used. Larger molecular weight PLLs (>100 lysines) produced hexagonal silica platelets, while lower molecular weight PLLs afforded silica nanospheres. Although PLL is a random coil at near-neutral pH (7.5), electrostatic interactions between the larger PLL templates and the silica promotes a α -helical structure formation during condensation, resulting in hexagonal plates (**Figure 5**).

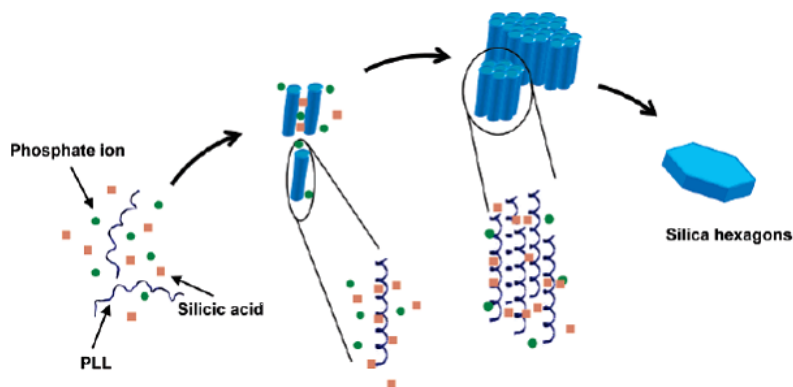


Figure 5. Proposed model of PLL induced condensation of silica platelets.¹⁸

Gautier and coworkers have also utilized PLL by incorporating the template into the pores of polycarbonate membranes to further control the silica size and morphology.¹³ Silica formation within confined spaces is important for a variety of materials applications. For example, silica encapsulated enzymes integrated into a micro or nano filter could be used in catalysis, where the substrate would pass through the membrane, interact with the enzyme, and pass through the filter as the product.

Rod-like silica tubes were synthesized once PLL was integrated into polycarbonate membrane pores (sizes ranging from 1200 nm, 400 nm, and 200 nm) (**Figure 6**). Multiple successive impregnations (5 times) of the pores with sodium silicate resulted in the formation of a silica-filled pore. The thickness of the silica wall decreased as its pore size decreased. In addition, TEM analysis determined that the primary particle diameter was independent of the pore size (~9 nm). However, this primary pore diameter was smaller than for silica formed on the surface (~11 nm), which is likely the result of PLL localization in the pore rather than silicate-PLL interactions.

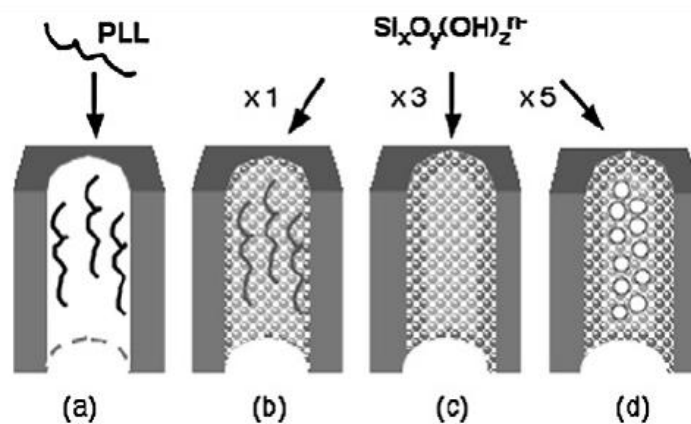


Figure 6. Schematic of silica tube formation. (a) PLL is first integrated onto the surface of the pore. (b) Addition of silicates initially results in the formation of a silica shell. (c) Multiple additions of silicates thicken the silica shell. (d) Further addition of silicates results in core particle growth.¹³

Block Co-Polypeptides

Block co-polypeptides have also been used as templates for controlled silica formation.^{54,55,57,62} These polypeptides consist of covalently linked domains (domains) of hydrophilic and hydrophobic polypeptides. Due to their unique polarities, these block segments induce an amphiphilic character, resulting in self-assembled vesicles in aqueous solution.⁵⁷ For example, a co-polypeptide consisting of polymers of linked lysine and glycine residues (*Lys-b-Gly*), was used as a silica template in the presence of orthosilicic acid and phosphate buffer at pH 7.2.⁵⁵ Different methods of silica precipitation were tested by changing the amount of silica pre-cursor or the amount of phosphate present during precipitation. Method I used 6 mmol of silica pre-cursor, while Methods II & III used 30 mmol. In addition, Method III had 7.5 mmol more phosphate buffer than the other two methods (0.1 M). An increase in phosphate buffer (Method III) resulted in a spherical morphology (40-120 nm in diameter) while the other two methods either produced mostly platelets for the *Lys-b-Gly* block copolypeptides (**Table 1**).

Table 1. Silica morphology for each copolypeptide at different synthesis conditions.⁸

Copolypeptide	Morphology (Methods I, II)	Morphology (Method III)
Lys ₂₀₀ -b-Gly ₅₀	Platelets	Spheres
Lys ₃₄₀ -b-Gly ₈₅	Platelets	Spheres
Lys ₁₁₀ -b-Gly ₅₅	Spheres and Platelets	Spheres
Lys ₃₂₀ -b-Gly ₁₆₀	Platelets	Spheres
Lys ₄₀₀ -b-Ala ₁₀₀	Spheres	Spheres
Lys ₃₉₀ -b-Ala ₆₅	Spheres	Spheres
Lys ₄₅₀	Platelets	Platelets

The formation of platelets or spheres with the *Lys-b-Gly* copolypeptide suggested that there was a morphological dependence on the phosphate concentration and the solubility of the hydrophobic block. As a result, by optimizing the hydrophobicity of the

template and the phosphate concentration, specific morphologies can be obtained. As the relative hydrophobicity was increased through the addition of glycine residues, substitution of the glycine block with the more hydrophobic alanine block, or the loss of lysine residues, the solubility of the copolyptide was decreased, making it more susceptible to phase separation. The hydrophobic block was more energetically stable when it was associated rather than by being free in solution. Aggregation of this region was induced and spherical silica condensation was promoted instead of platelets. In addition, an increase in phosphate ions (Method III) had a similar effect by electrostatically interacting with the hydrophilic lysine block and promoted silica spheres. Platelets from Method II are smaller than those from Method I, caused by the higher concentration of silica pre-cursor and subsequent increase in the rate of nucleation (Figure 7).

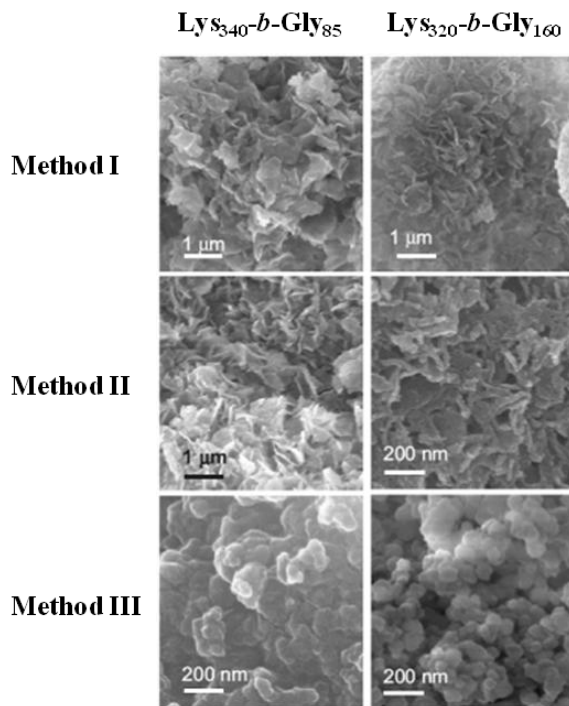


Figure 7. Field-emission scanning electron microscopy (FE-SEM) images of silica nanoparticles synthesized using (left) $\text{Lys}_{340}\text{-}b\text{-Gly}_{85}$ and (right) $\text{Lys}_{320}\text{-}b\text{-Gly}_{160}$ using (top to bottom) Methods I, II, and III respectively.⁸

Lanreotide

Cyclic lanreotide is a dicationic octapeptide that self-assembles into nanotubes in water with a monodispersed diameter of 24.4 nm and a wall thickness of 1.8 nm.¹⁷ This polypeptide has two exposed protonable amine groups that can be used as catalytic sites for silica condensation (**Figure 8**). By exposing the nanotubes to a TEOS-derived $\text{Si}(\text{OR})_3\text{O}^-$ precursor, silica was deposited and bundles of silica nanofibers were formed with a total length as long as 7 μm . Each nanotube extended as long as 3 μm .

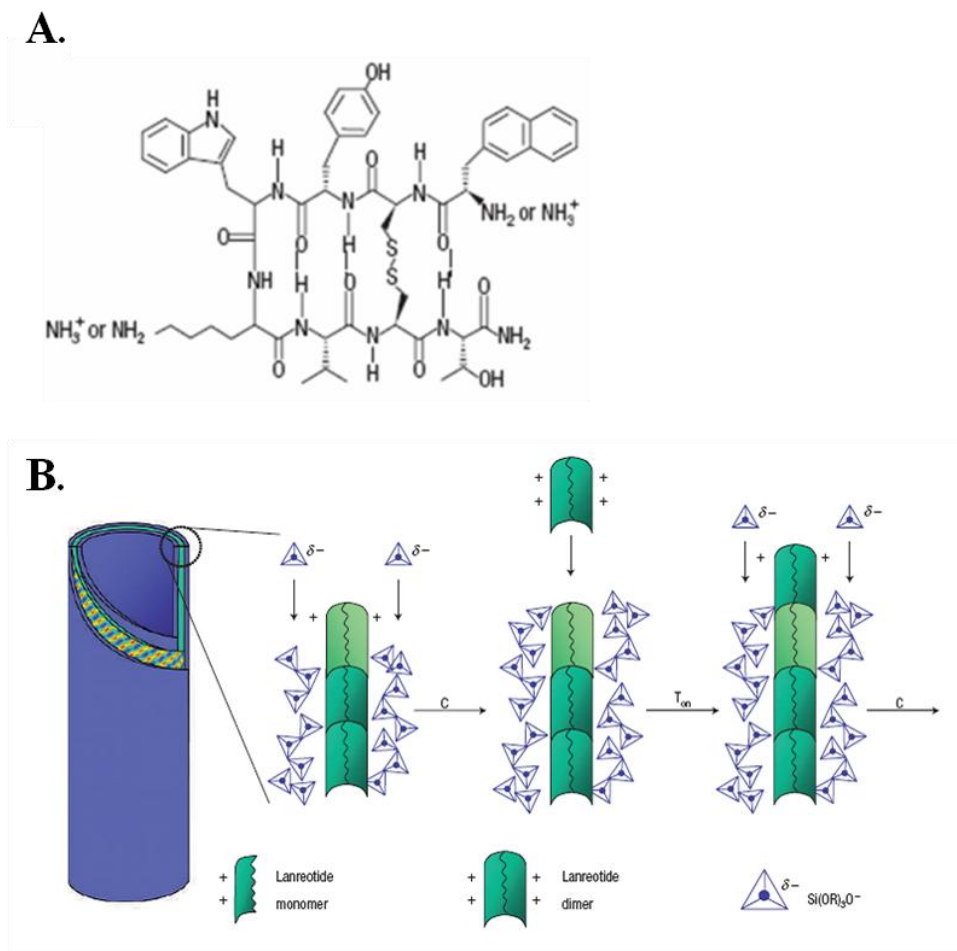


Figure 8. Synthesis of lanreotide-templated silica nanotubes. A.) Structure of lanreotide showing the two charged amine sites responsible for silica condensation. B.) Dynamic templating model for the mechanism of silica condensation into nanofibers. The cationic lanreotide nanotube surface utilizes electrostatic attraction to catalyze silica condensation (step C) and the anionic silica deposit promotes additional lanreotide assembly (step T_{on}) through neutralization of the system.¹⁷

TEM analysis determined that the dried fibers consisted of bundles of aligned nanotubes with homogeneous inner and outer diameters of 14-16 nm and 28-30 nm respectively. In addition, the two concentric tubes were both 1.4 nm thick, and were separated by 2 nm, which is the approximate width of the lanreotide molecule. The proposed dynamic templating mechanism suggested that the cationic lanreotide nanotube surface catalyzed the silica condensation by electrostatic forces, and the consequent anionic silica deposits promoted additional lanreotide assembly through synergetic neutralization of the entire system. Not only does this templating mechanism provide insight into the potential fundamental mechanisms used in biological systems, it also allows for the production of superstructures that greatly exceed the size of the original template.⁶⁴ Consequently, a variety of new silica structures could be synthesized that maintain nanoscale properties even in the microscale or larger.

Polyamines

Non-peptide biomimetic analogs to silica precipitating peptides are inspired from the isolated LCPAs found on the cell walls of diatoms. Some of these polyamines include poly(allylamine) (PAA),⁶¹ poly(ethyleneimine) (PEI),⁵⁶ *N*-methylpropylamine (PA),⁵⁸ and amine-terminated dendrimers.^{6,7,9,53} Each of these classes of compounds represents a different structural aspect to silica templating, including the number of amines, the number of spacer atoms between the amines, its relative degree of methylation, and the presence and number of branching elements. All of these factors alter the resultant physical properties and subsequent reactivity of the silica nanoparticle produced.

Poly(ethyleneimine)

Poly(ethyleneimine) (PEI) is a branched polyamine ($M_w = 1800$) consisting of a 1:2:1 ratio of primary, secondary, and tertiary amines that makes it structurally similar to polyamines isolated from *S. turnis* and *C. fusiformis*.⁶⁵ These PEIs were integrated as spherical reverse micelles (RMs) made from bis(2-ethylhexyl) sulfosuccinate sodium salt (AOT) in isooctane, providing a constrained environment for silica precipitation. These RMs exchanged their contents quickly through fusion and redispersion processes ($106\text{--}108\text{ m}^{-1}\text{s}^{-1}$). Consequently, PEIs reacted with silicic acid from a tetramethylorthosilicate (TMOS) precursor produced silica nanoparticles with size and structure control dependant on the size of the RM.⁵⁶ Before testing silica precipitation in the RM, condensation of silica was investigated at a variety of pH values (6.3-11.2) in water. Instantaneous precipitation occurred at basic pH (9-11), slow deposition of amorphous silica matrix occurred at near-neutral pH, and no precipitation occurred for acidic pH (**Figure 9**). This lack of activity is likely caused by the absence of anionic constituents (ions or polymers) in neutral or acidic solutions, which are critical for the self-assembly of the amine-functionalized template.

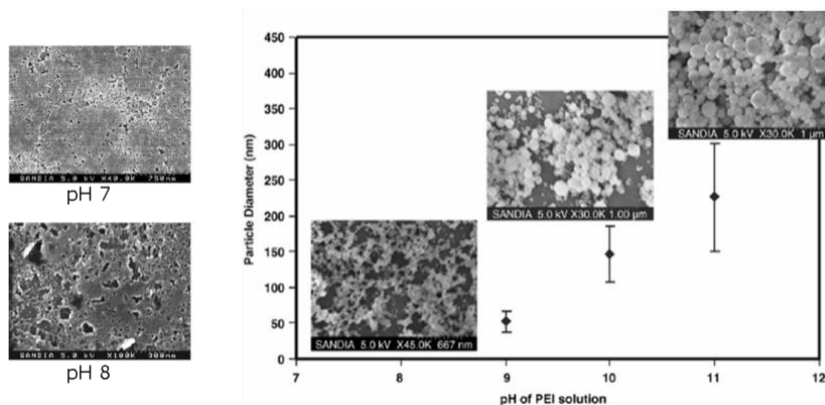


Figure 9. Diameter and dispersity of silica particles formed in aqueous PEI solutions at 0.05M primary-amine concentration and 1M silicic acid in a 4:1 volume ratio at pH 9, 10, and 11. SEM images of the nanoparticles are provided as inserts, and the silica formed in pH 7 and pH 8 is provided on the left.¹²

Consequently, it was expected that PEI would provoke similar pH dependence once reacted with the RM. However, when PEI and silicic acid were incorporated into the RMs prepared in isooctane, the initial pH of the amine solution was negligible in terms of controlled silica growth. This was confirmed by testing the AOT pH w/ 8-hydroxypyrene-1,3,6-trisulfonic acid (HPTS). It was determined that the local pH stays consistent (≥ 9), independent of the pH of the inserted PEI. In addition, alterations of the size of the water pool $w_o = 5-40$ ($w_o = [\text{H}_2\text{O}]/[\text{AOT}]$), produced a variety of particle sizes. The smallest RMs ($w_o = 5$) fashioned very small amounts of silica due to the tight interactions between the water molecules, the anionic sulfonate groups of the AOT, and cationic sodium ions. Larger RMs ($w_o = 10$) resulted hollow silica shells, with diameters on the order of $1\mu\text{m}$. In this case, the RM remained stable during the reaction, and the silica units only interacted by micellular exchange. For the largest reverse-micelle sizes $w_o \geq 20$, destabilization of the RM occurred because of the addition of additional water molecules in the RM from the condensation of silanol groups, thus increasing the w_o during the reaction.

Initial $w_o = 20$ RMs became unstable as soon as the reaction was initiated, resulting in tri-modal nanosphere diameter distributions (56 ± 6 nm, 172 ± 31 nm, and >200 nm respectively). This suggested multiple destabilization pathways of the RMs during the condensation, resulting in different silica sizes. Moreover, the morphology of the silica was determined by the size of the RM, as well as its stability during the condensation reaction. By understanding the mechanism of this reaction, the sizes and shapes of silica were tuned to serve a variety of functions, including an inert matrix for catalysis, drug delivery, and transport.⁶⁶

Other Unbranched Polyamines

To assess the role of polyamine structure in controlling the morphology of silica nanoparticles, Belton and coworkers utilized several polyamines with different degrees of polymerization, different levels of amine methylation, and different lengths of amine chain spacers (**Figure 10**).¹¹ The degree of polymerization was evaluated by comparing two naturally occurring polyamines, spermidine and spermine, to the other synthetic polyamines. Amine methylation was investigated through a set of N,N'-(bis-3-aminopropyl)-1-3-diaminopropanes with levels of methylation from 0 to 4. For each experiment, dipotassium Tris(1,2-benzenediolato-O,O')silicate served as the silica precursor.

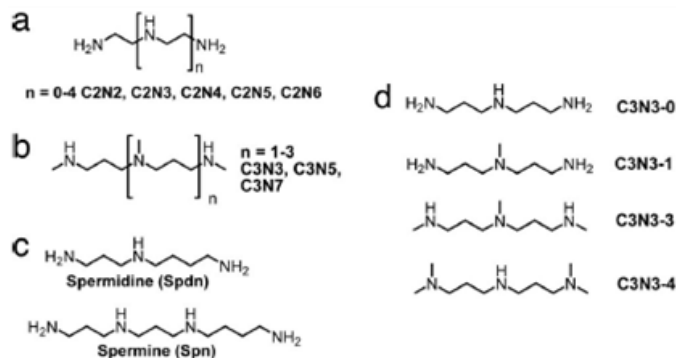


Figure 10. Structures of unbranched polyamines. a.) Ethyleneamines. b.) Propylamines. c.) Natural amines spermine and spermidine. d.) C3N3 with varying degrees of methylation.¹¹

For all of investigated samples, there were mixtures of solid and hollow particles associated with the number of amines per molecule, the amine-amine separation, and the size of the polyamine. The larger propylamines, which are the most hydrophobic and most readily form microemulsions, were the most efficient in generating hollow silica nanoparticles. Hollow silica nanoparticles are of particular interest due to their potential

applications in adsorptive filters, ultrasound imaging, photonic band gap materials, and catalysis.⁶⁷

Two critical factors were identified for controlling the nature of the resultant silica composite in this reaction. First, the template's ability to produce microemulsions determined whether solid or hollow silica was formed (**Figure 11**).¹¹ Second, the reaction kinetics of the composite was shown to increase according to the degree of charge associated with the microemulsions. A positively charged microemulsion introduced a water-free microenvironment, where water removal promoted the condensation of controllable silica.

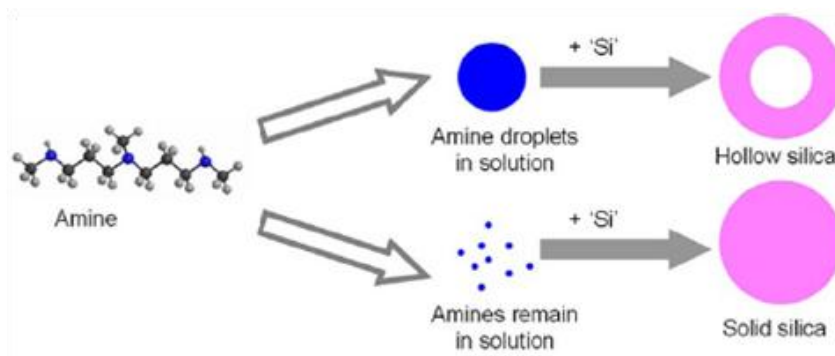


Figure 11. Schematic representation of the microemulsion formation leading to hollow silica structures.¹¹

The kinetics of each silica condensation reaction was quantified using the molybdenum blue method, which is sensitive to mono- and dimeric- silicic acid. Within the initial condensation time, there is a third-order linear relationship between $[\text{Si}(\text{OH})_4]^{2-}$ and time. As a result, it was concluded that polyamines with a three-fold increase in their third-order rate constant were kinetically active. All of the propylamines and longer chain ethyleneamines significantly influenced condensation rates, with C3N7 having a 14-fold increase in catalytic activity. C2N2-4 and the naturally occurring polyamines spermidine

and spermine observed no rate enhancement. These results suggest that there is a direct correlation between template size and its ability to catalyze silica formation. In addition, increasing the methylation levels in the C3N3 species also increased the third-order rate constant. For all of the kinetically active species, the silica nanoparticles produced were nonporous, which is likely due to rapid nucleation. Thus, by modifying the composition of the polyamine, the ability to produce microemulsions which lead to hollow silica and the porosity of the silica can be tailored, leading to the production of a variety of potential nanomaterials.¹¹

Dendrimers

Amine terminated dendrimers are unique, uni-molecular polymer templates with defined reactivity as a function generation size (the number of branching elements). Dendrimers have been utilized as a template capable of localizing a high concentration of biomimetic moieties, including silica.⁶ Not only have dendrimers been used as stabilizing templates for sol-gel composites⁶, but amine terminated polypropylenimine (PPI) and polyamidoamine (PAMAM) dendrimers have also been used as non-peptide mimics to the silaffin peptides for the controlled formation of silica nanospheres (**Figure 12**).^{6,7,9,53}

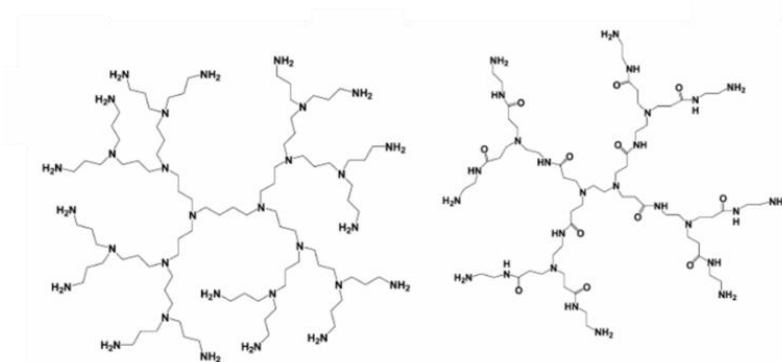


Figure 12. Chemical structure of the G-3 PPI dendrimer (left) and G-1 PAMAM dendrimer (right).⁶

Positively charged dendrimers only produce silica nanospheres in the presence of an anion, such as phosphate, sulfate, or acetate at neutral pH. The size of silica produced is dependent on the generation size of the dendrimer, where larger generations produce larger silica nanospheres. Comparisons between the PPI and PAMAM dendrimers have revealed that the PPI dendrimer has reduced specific activity because it precipitates silica much faster than the PAMAM dendrimer of similar generation size.⁶

Incorporating known concentrations of dendrimers into the silica matrix has enabled specific morphological control over the nanoparticles under mild conditions. This control could be modified and applied directly to the encapsulation of functional components that are necessary for catalysis, biological labeling and detection, and electronic devices.^{7,9} Generation 4 (G4) PAMAM dendrimers have been used to catalyze the encapsulation of gold nanoparticles and CdSe and ZnS core shell AMP Quantum Dots.⁷ In this reaction, cationic gold (Au^{3+}) is coordinated to the amine groups of the G4 PAMAM dendrimer, where it is reduced to Au^0 by NaBH_4 . After lyophilization, energy dispersive X-ray spectrometry (EDS) analysis determined that the gold was either surface passivated or incorporated with within the dendrimer matrix (**Figure 13**).

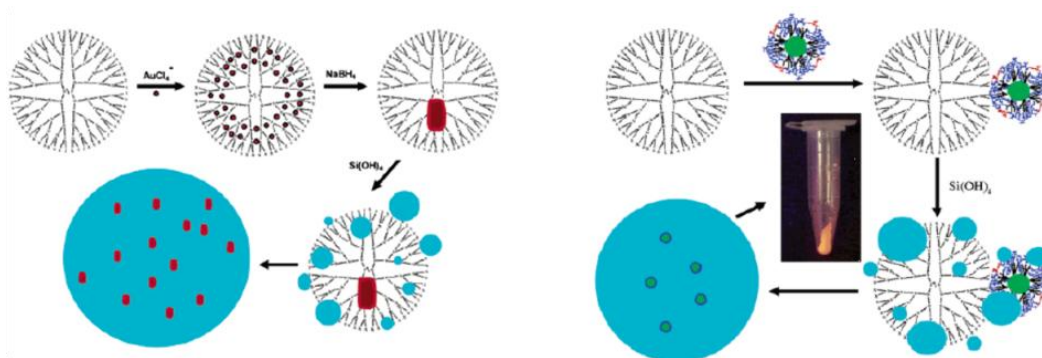


Figure 13. Schematic silica encapsulation of Au^0 nanoparticles (left) and CdSe/ZnS core shell AMP quantum dots (right).⁷

Although many of the surface dendrimer amines are occluded by the gold or quantum dot nanoparticles, silica condensation still occurs. In fact, the CdSe/ZnS core shell Quantum Dots with negatively charged surface carboxylates were encapsulated with 99% efficiency, which suggests that the electrostatic attraction between the quantum dots and the templates was sufficient for encapsulation of these materials.⁷

Enzymes have also been incorporated into the PAMAM dendrimer to produce silica nanoparticles. At physiological pH, the interaction between an enzyme and the cationic surface of the PAMAM dendrimer plays an important role in forming supramolecular complexes. As a result, the cationic dendrimer (pKa ~9.5) interacts with low pI enzymes. For example, glucose oxidase (GOx, pI ~4.2) was encapsulated in water with a quantitative yield. Since phosphate ions compete with the enzyme, GOx was poorly encapsulated as phosphate buffer concentrations increased because the phosphate ions significantly reduce the electrostatic interactions between the enzyme and dendrimer (**Figure 14**).

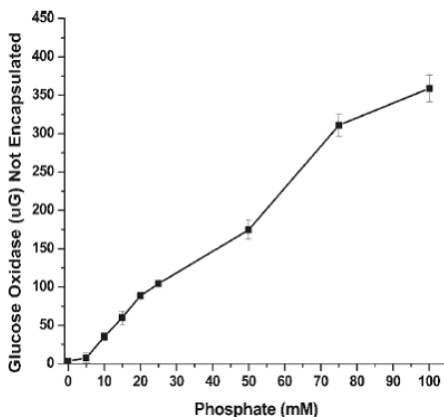


Figure 14. Effect of increasing the phosphate buffer concentration on GOx encapsulation. Note: initial reactions contained 400 μ g of GOx.⁹

A loss of half of the enzymatic activity under optimal conditions was likely due to unfavorable orientations in the silica framework or alterations in steady-state conditions due to a local increase of enzyme concentration in the silica. Long term storage effects were examined and enzymatic activity was consistent after 30 days of storage at room temperature in buffered solutions. The silica framework provides a structural matrix around the enzyme, which physically block much of the natural degradation of the enzyme, as well as provides a physical barrier from invading species, such as bacteria.⁹

Other Biomimetic Templates

Other natural biomimetic templates that utilize amines as the catalytic sites for silica precipitation have also been reported.^{59,60} Cellulose was recently used as a rigid backbone for silica nanotube formation by introducing oligopropylamido side chains derived from dipropylenetriamine (DPTA) to the C6 position of almost all of the anhydroglucose units (AGUs) (**Figure 15**).⁵⁹

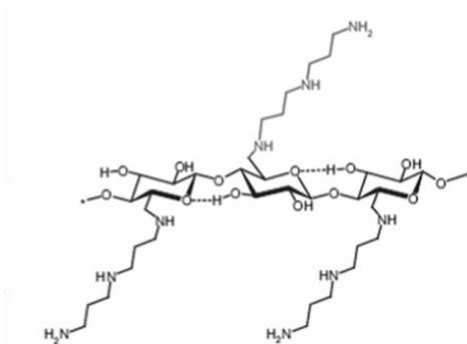


Figure 15. Structure of DPTA cellulose tosylate. Note that some tosylate residues are present at the C2 and C6 positions during the synthesis, as indicated by ¹³NMR spectroscopy.¹⁰

These silica nanotubes are of technologically significant because they could be used as a non-conductive substitute for carbon nanotubes and as templates for further

reactivity. The rigidity of the cellulose backbone exposes its surface amines in water, inducing a hydrogen bonded amine-silica network (**Figure 16**).

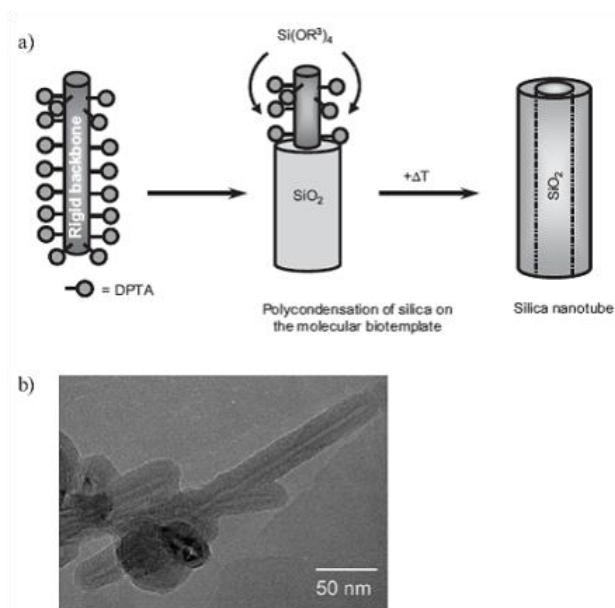


Figure 16. Silica nanotubes. a.) Schematic representation of the formation of silica nanotubes from a functionalized biopolymer. b.) TEM images of silica nanotubes formed using the DPTA cellulose

The resultant nanotubes exhibited diameters of 10-30 nm, inner core diameters of ~3 nm, and lengths of up to 500 nm. The proposed mechanism of condensation shows that the silica monomers are interacting with two amino groups on the DPTA through hydrogen bonding. This localization of silica precursor along the catalytic amine sites of cellulose induces a lateral growth of nanotubes. After the initial silica growth, condensation repeats but in a disordered fashion, resulting in a tubular coating of amorphous silica.⁵⁹

Conclusion

As scientists discover more and more about the biological mechanisms that drives silica formation of diatoms, they produce more evolved biomimics that continually

expose applications beyond catalysis, biosensing, and drug delivery. Through all of the templates examined in this section, one thing is clear: templates strongly influence the size and morphology of the silica nanoparticle. For example, the recent discovery of silacidins, which are polyanions required for silica formation *in vivo*, suggest that the anion may have an effect on the size and morphology of silica nanoparticles produced. As a result, understanding the effect of all of the factors, including the structure of the template and the conditions of the reaction (i.e. pH, temperature, and anion concentration) will influence the sizes and shapes of silica nanoparticles that material scientists will develop.

Dissertation Aims Using Biomimetic Syntheses

In the next two chapters, the topics presented will be focused on using biomimetic processes to develop silica materials containing functional enzymes. These materials are designed to capitalize on the stability of the silica matrix, which prevents enzymatic degradation and provides a facile method for biocatalyst recyclability. The focus of **Chapter II** is the in-solution silica encapsulation of two enzymes (nitrilase and β -glucosidase), which are responsible for the conversion of synthetic intermediates to industrially relevant products. **Chapter III** focuses on capitalizing on piezoelectric inkjet printing technologies to deposit functional inks used to synthesize enzyme containing silica patterns.

CHAPTER II

BIOMIMETIC SYNTHESIS OF ENZYME-CONTAINING SILICA NANOPARTICLES

Introduction

Enzyme catalysis of industrially relevant chemicals provides a green alternative to traditional synthetic processes. They are biodegradable biomaterials that perform their chemistry in environmentally friendly solvents (i.e. water) at or near physiological pH and mild temperatures.⁶⁸ In addition, enzymatic processes provide unique reaction chemistries that cannot be efficiently mimicked by traditional synthetic strategies. Enzymes however, are more expensive than many reagents, are not easily recycled after use, and may have poor shelf lives if they are not stored frozen or as lyophilized powders. To circumvent these challenges, several immobilization strategies have been developed to improve the stability of the enzyme and allow for simple separation from reaction mixtures. Three general methods have been developed: covalent enzyme attachment to a substrate, enzymatic crosslinking into reactive aggregates, and encapsulation of enzymes into an organic or inorganic polymeric matrix.⁶⁹ Previous work has shown that enzymes immobilized within silica sol-gel matrices have improved stability over time and are more easily separated from complex reaction solutions.⁷⁰ However, these processes are hindered by their inefficient loading yields and are prone to denaturation.⁷¹⁻⁷⁴ Biomimetic silica formation however, has been successfully used as an alternative encapsulation method that has shown modest enzyme yield and comparable activity.⁷⁵⁻⁷⁷ As noted in **Chapter I**, our lab has successfully encapsulated glucose oxidase (GOx) and horseradish

peroxidase (HRP) within silica nanoparticles templated by the generation 4 PAMAM dendrimer. The following chapter highlights two additional enzymes encapsulated into silica matrices (nitrilase and β -glucosidase) using a generation 4 PAMAM dendrimer as a silica template.

Nitrilase

Nitrile compounds are simple aliphatic and aromatic metabolites, cyanoglucosides, and cyanolipids serving as key compounds and intermediates in a myriad of biochemical pathways.⁷⁸ The common biochemical transformation of organonitrile hydrolysis to higher value amide and carboxylic acid groups is often inaccessible to organic synthetic strategies due to the harsh conditions required for hydrolysis.⁷⁹⁻⁸² Synthetically, organonitriles are easily produced via the addition of cyanide to alkyl halides, the Strecker reaction,⁸³⁻⁸⁶ reaction of aryl halides with copper cyanide,⁸⁷ and the dehydration of amides.⁸⁸ However, the strong acids and bases, often in conjunction with reflux conditions required to achieve nitrile hydrolysis prove impractical during the synthesis of sensitive and complex molecules.

Microbial organonitrile transformations are achieved biochemically in ambient, aqueous environments by either a combination of nitrile hydratase and nitrile amidase enzymes or by members of the nitrilase superfamily.⁸⁹ There are at least nine identified families within the nitrilase superfamily. One well studied gene-cluster from the nitrilase superfamily is the NIT1-3 cluster from *Arabidopsis thaliana*.⁹⁰ These enzymes utilize an active site cysteine residue to catalyze the direct conversion of aliphatic and aromatic

nitriles into carboxylic acids coupled with ammonia liberation and accept a wide array of substrates (**Figure 17**).

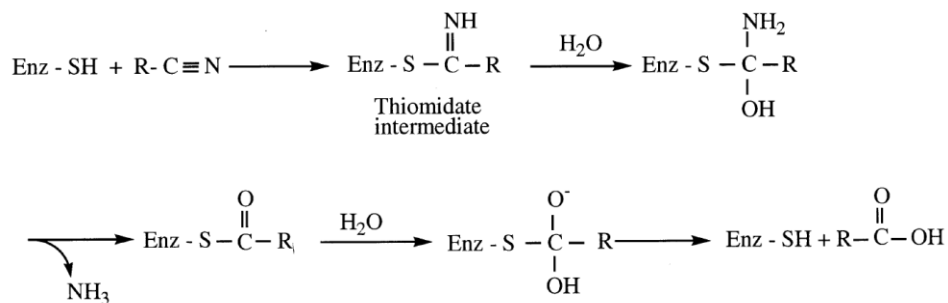


Figure 17. Enzymatic conversion of nitriles to carboxylic acids.

While nitrilase containing cell farms have found a foothold in the commercial production of some high-value fine chemicals,⁹¹ they are not commonly employed in synthetic strategies due to traditional barriers of enzymatic catalysis. In general, enzymes are more expensive than many reagents, are not easily recycled after use, and may have poor shelf lives if they are not capable of activity following lyophilization or freezing. These limitations have limited the large scale industrial use of nitrilase to maintaining various microbes expressing high levels of nitrilase, such as with acrylamide production (~ 6000 tons per year).^{92,93} Herein we report the encapsulation of a cysteine active, recombinant nitrilase inside silica nanoparticles. The reaction is performed in an aqueous buffer and mediated by a water soluble PAMAM dendrimer to yield a nitrilase-containing silica nanocomposite capable of enzymatic conversion of nitriles, easy separation from product, and reusability.

Experimental

Enzymes and Reagents: Nitrilase-102 (recombinant from *Arabidopsis Thaliana*) was purchased from Codexis. All other reagents were purchased from Sigma-Aldrich (U.S.A) and used as delivered.

Nitrilase Encapsulation: Nitrilase was suspended at 2 mg/mL in water or phosphate buffer (8, 17, and 25 mM respectively) at pH 7.8. An aliquot of 200 μ L was charged with enough generation 4 PAMAM dendrimer (Sigma; 10 wt.-% in MeOH) to afford a primary amine concentration of 20 mM. Tetramethylorthosilicate (Aldrich; 1 M; TMOS) hydrolyzed by 1 mM HCl (aq.) was then added (20 μ L) to achieve rapid precipitation of white silica nanoparticles. The nanoparticles were collected by centrifugation at 10,000 RPM and washed threefold with 25 mM phosphate buffer. General protein content was quantitated with the Bradford assay from a standard curve of nitrilase.

PPN Activity Assay: Encapsulated nitrilase specific activity was compared to free nitrilase by a fluorometric assay previously described.⁹⁴ Briefly, nitrilase was reacted with a 10 mM solution of PPN (Sigma) at 30°C for 10 minutes. The reaction was stopped upon addition of an equal volume of 0.1 M HCl. Next, the amount of ammonia produced was assayed by adding a 10 μ L aliquot of the reaction solution to a 290 μ L solution containing alcoholic o-phthaldialdehyde (Fluka) (3.75 mM) and 2-mercaptoethanol (Sigma; 3.6 mM) in 0.2 M phosphate buffer pH 7.4. This solution stood for 35 minutes, followed by excitation at 407 nm and monitored emission at 460 nm (Bio-Tek Synergy HT multi-detection microplate reader). A standard curve of NH₃ was produced for the range of 10 μ M and 1000 μ M. One unit of nitrilase activity was defined as the amount able to release 1 μ mol of NH₃/min per mg of nitrilase under the assay conditions.

Kinetic parameters were obtained by varying the PPN concentrations and collecting several time points to acquire reaction rates.

3-Cyanopyridine Activity Assay: Specific activity of encapsulated and free nitrilase toward the conversion of 3-cyanopyridine (Sigma) to nicotinic acid was determined by reacting the enzyme with a 10 mM solution of 3-cyanopyridine at 30°C for 1 hour. The reaction was quenched upon addition of an equal volume of 0.1 M HCl (aq.). The amount of ammonia released during the reaction was assayed using the same fluorometric assay used for the conversion of PPN. For kinetic experiments, 3-cyanopyridine concentrations were varied and several time points were obtained to acquire rates.

Nitrilase Reusability: Reusability of the nanoparticles was assessed by resuspension in 200 μ L of phosphate buffer and transferred to centrifuge filters (Millipore Ultrafree-MC centrifugal filter devices with a Durapore 0.1 μ m pore size PVDF filter). Before the substrate was added, the extra solvent was removed by centrifugation (Beckman Coulter Allegra X-22R) at 2500 RPM for 1 min. The reaction was initiated by the addition of 200 μ L of a 5 mM 3-cyanopyridine solution in 25 mM phosphate buffer at pH 7.8 and incubated for 1 hr at room temperature. The reaction was terminated by centrifugation of the supernatant at 2500 RPM for 1 min. The nitrilase-containing nanoparticles were then washed with 5 portions of 300 μ L of phosphate buffer to ensure that all substrate was removed before the next experiment. This reaction was repeated a total of ten successive times and the reactant and product concentrations were determined by the HPLC and the fluorometric assays.

Batch Preparation of Nicotinic Acid: Multiple batches of nitrilase-silica nanoparticles were prepared in water as described above. Two reaction vessels were prepared by

combining reaction batches (10 per reaction vessel) and a 500 μL solution of 200 mM 3-cyanopyridine in 25 mM phosphate buffer pH 7.8 was added and allowed to convert for 12 hours at 30°C. Additional aliquots of 3-cyanopyridine were added after the prior reaction solution was removed by centrifugation (10 mL total). The amount of synthesized nicotinic acid was quantified by HPLC.

HPLC Quantification: HPLC analysis was performed on the supernatant with a Waters 600E Multisolute Delivery System equipped with a Nova Pak C18 column (reversed-phase column, 3.9 x 150 mm) at a flow rate of 0.5 mL/min. A 90:10 mixture of water:acetonitrile with 0.1% trifluoroacetic acid was used as the mobile phase. The A_{218} and A_{261} were measured for 3-cyanopyridine and nicotinic acid respectively. A standard curve for 3-cyanopyridine and nicotinic acid was produced from 5 μM to 400 μM and 25 μM to 500 μM respectively.

Bradford Assay: Protein mass quantification was performed by adding 160 μL of test solution to 40 μL of Bio-Rad Protein Assay solution concentrate and mixing for 5 min. The change in color was monitored via UV-Vis (Bio-Tek Synergy HT multi-detection microplate reader) at 595 nm. A calibration curve was produced for nitrilase between the range 0.8 $\mu\text{g/mL}$ and 80 $\mu\text{g/mL}$.

NMR Analysis: NMR analysis was performed on a Bruker DPX-300 at room temperature. Samples were prepared by performing encapsulation and enzymatic activity assay in deuterated 25 mM phosphate buffer. Samples tested were collected by aspirating the supernatant following centrifugation of the reaction mixture.

Silica Quantification: Silica nanoparticles were quantified following the β -Silicomolybdate method described by Iler.⁹⁵ Samples were dissolved in 0.5 M NaOH

and incubated at 95°C for at least 30 minutes. Following incubation, the liberated dendrimers were separated from solution by Centricon filtration (American Centricon filtration devices, Millipore Inc.). Molybdate reagent was added (1:4 silicic acid/molybdate) to the filtered solutions to initiate the formation of the bright yellow product monitored by UV-Vis spectrophotometry at 410 nm and quantitated from a standard curve of silicate standards.

Scanning Electron Microscopy: Silica samples were resuspended in ethanol and placed on an aluminum surface SEM sample stage (Ted Pella Inc.) to dry. Samples were sputter-coated with a thin layer of gold via a Pelco Model 3 Sputter Coater (Ted Pella Inc.). Thereafter, samples were imaged on a Hitachi S4200 scanning electron microscope operated at variable voltage.

Results

In order to improve upon the implementation and recycling of nitrilase for large scale production and small scale research and development, we encased a commercially available nitrilase within silica nanospheres using a biomimetic template. Previous studies of oceanic diatoms have isolated a class of proteins, called silaffins, that catalyze the condensation of silicic acid into intricate exoskeletons.⁹⁶ This process is amplified by polycationic lysine modifications containing many secondary and primary amines along the Sil-1A peptide.⁹⁷ Subsequent reports indicated that similar condensation chemistry could be achieved using a variety of amine sources.^{76,98-101} Previously, we reported a rapid and efficient benchtop method for the immobilization of the model enzymes glucose oxidase and horseradish peroxidase.⁷⁷ Briefly, the enzyme is exposed to a water

miscible PAMAM dendrimer which functions as a biomimetic template providing sufficient primary amine concentrations (> 20 mM) to condense silicic acid.⁹⁸ The resulting silica flocculates and precipitates within seconds trapping both the dendrimer¹⁰² and enzyme within the particles.⁹⁹ The efficiency of enzyme entrapment can be enhanced via manipulation of electrostatic attraction between the desired enzyme and cationic dendrimer surface.⁷⁷ Compared to other enzyme immobilization strategies such as sodium silicates,¹⁰³ the dendrimer based methodology offers a significant advantage in both time and processing required to produce the immobilized biocatalysts.^{70,71} The recombinant nitrilase (Codexis) for this study has a theoretical pI between 5 and 7 and utilizes an active site cysteine similar to the NIT1-3 cluster of *Arabidopsis thaliana*.

Nitrilase-containing silica nanoparticles were initially synthesized in water by adding 20 μ L of 1 M hydrolyzed tetramethyl orthosilicate (TMOS) to a 200 μ L solution containing nitrilase (0.400 mg) and generation 4 PAMAM dendrimer (20 mM primary amine concentration) at pH 7.8. Silica quantification of the rapidly precipitated nanocomposite (191 nm \pm 44 average particle diameters (**Figures 18 & 19, Table 2**)) using the β -silicomolybdate assay method⁹⁵ showed 0.43 mg \pm 0.1 (7.16 μ moles) of silica produced for each reaction, consistent with previously published yields.^{77,98} The efficiency of enzyme encapsulation quantified by the Bradford assay was rated 92.3 % \pm 0.5 (0.3692 mg) of the starting enzyme. The remaining unencapsulated enzyme (0.0308 mg) was found in subsequent supernatant washes. The enzyme to silica mass ratio for these reaction conditions is 0.37:0.43, or 0.86:1. The specific activity of the encapsulated nitrilase was determined using a previously described fluorometric assay.⁹⁴ Activity of the nanocomposite toward 3-phenylpropionitrile (PPN) in 25 mM phosphate buffer (pH

7.8, 30°C) revealed a specific activity $59.2 \% \pm 5.8$ that of an equal amount of enzyme free in solution (**Table 3**).

Previously, we reported that the electrostatic attraction between the cationic dendrimer and surface charge of the enzyme could be tuned as a function of the ionic strength of the buffer.⁷⁷ When nitrilase was encapsulated over a range of phosphate buffer concentrations, the amount of total enzyme within the silica matrix increased as the buffer concentration decreased. In addition, the particle diameter size decreased as a function of decreasing ionic strength, consistent with previously published results.⁷⁷ Since nitrilase has a slightly acidic *pI* (~5-7), it will be slightly anionic at neutral pH. It is electrostatically attracted to the cationic dendrimer and would be in close proximity to the silica condensation event, resulting in its subsequent entrapment within the growing nanoparticle. As the ionic strength of the buffered solution is increased, the interaction between the dendrimer and enzyme is diminished, resulting in reduced encapsulation efficiency. Concurrently, the ions serve to maintain the solubility of the growing nanoparticle. As the buffer concentration is increased, the critical size for particle precipitation is increased, resulting in larger nanoparticles. It should also be noted that the absolute amount of silica produced for all of the conditions is the same regardless of the reaction conditions, suggesting that silica condensation occurs until the entire precursor is completely consumed.

Although an unbuffered solution yields optimal enzyme loading and the smallest particle diameters, it is not clear whether these conditions affect nitrilase's specific activity. Nanoparticles synthesized under each buffer condition (8, 17, and 25 mM phosphate buffer; pH 7.8) were compared to the samples prepared in water. All particles

showed a similar specific activity toward PPN, suggesting that the buffer concentration during encapsulation doesn't have a significant effect on the activity of nitrilase. Consequently, the increase in particle size seen in the buffered samples doesn't have a noticeable effect on activity, suggesting that the silica shell doesn't create a diffusion barrier between the enzyme and substrate. Therefore, the samples prepared in water, which had the highest enzyme yield, contain more total active enzyme per reaction batch.

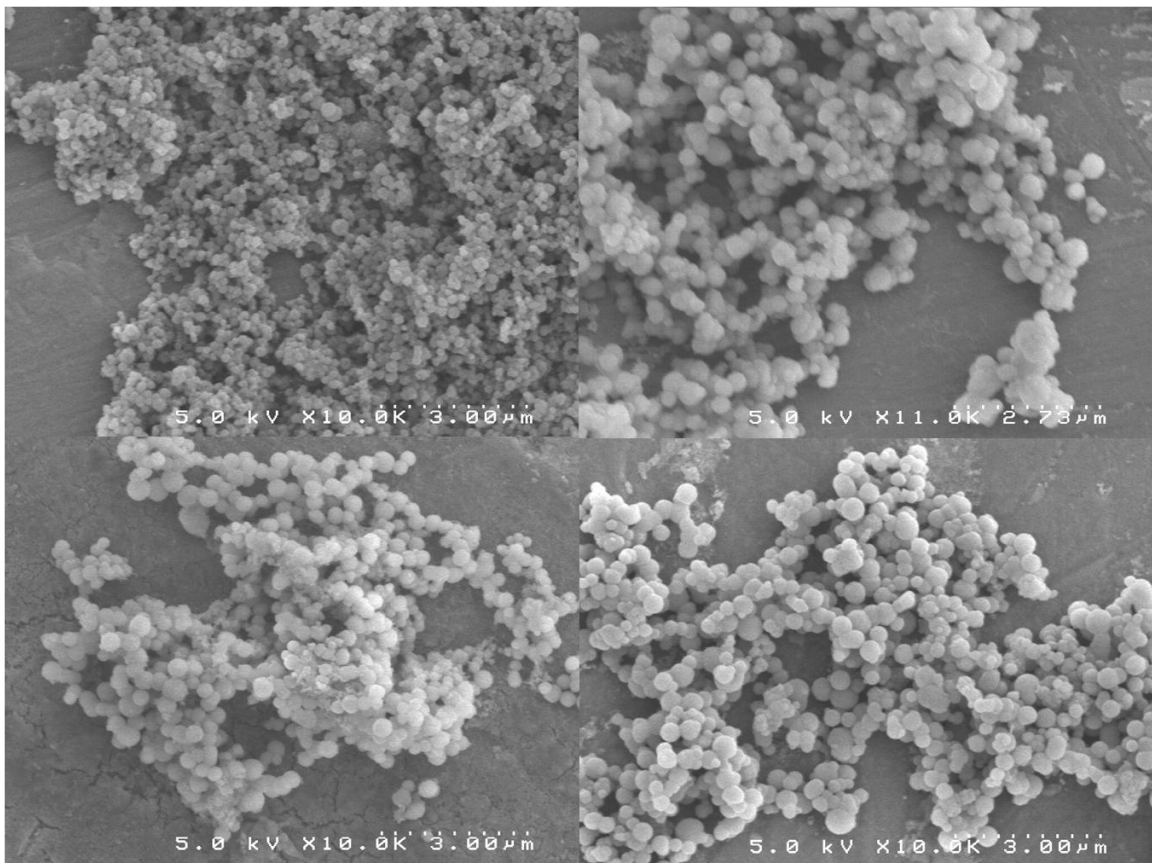


Figure 18. SEM images of nitrilase-containing silica nanoparticles formed in water (top left), 8 mM (top right), 17 mM (bottom left) and 25 mM phosphate buffer (bottom right).

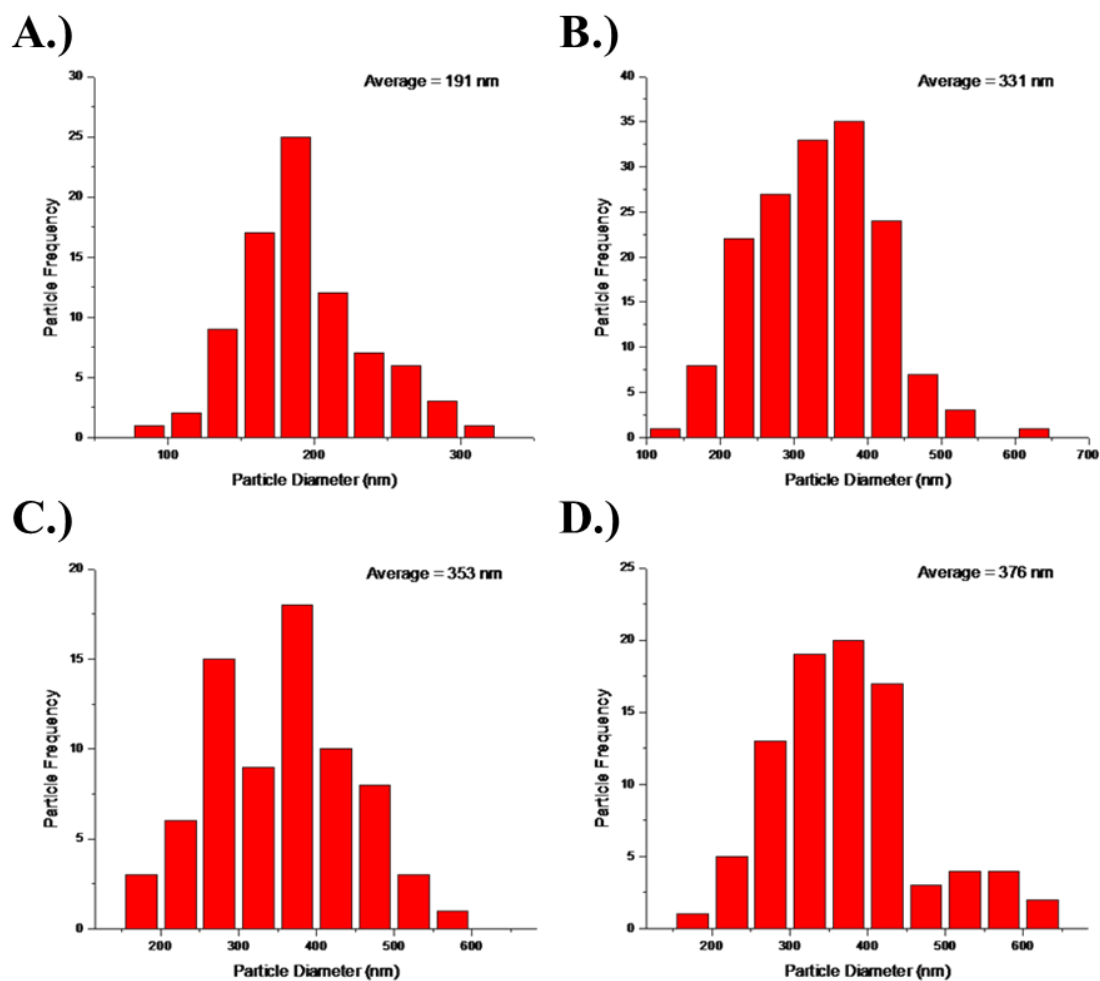
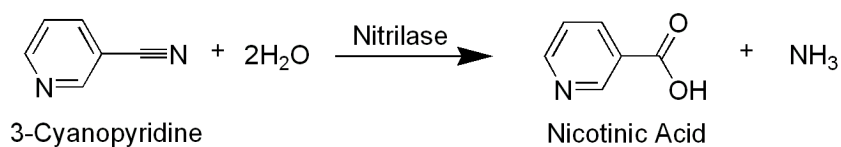


Figure 19. Size distribution graphs of the nitrilase-containing silica nanoparticles reacted in A.) water, B.) 8 mM, C.) 17 mM, and D.) 25 mM phosphate buffer.

Table 2. Physical properties of nitrilase-containing silica nanoparticles.

Encapsulation Conditions	Particle Diameters (nm)	Silica Yield Per Batch (mg)	Enzyme Yield Per Batch (mg)	Enzyme to Silica Ratio	Enzyme Yield (%)
Water	191 ± 44	0.430 ± 0.100	0.369 ± 0.002	0.858	92.3 ± 0.5
8 mM	331 ± 83	0.442 ± 0.041	0.331 ± 0.020	0.749	82.8 ± 5.0
17 mM	353 ± 88	0.419 ± 0.026	0.290 ± 0.001	0.692	72.5 ± 0.3
25 mM	376 ± 94	0.433 ± 0.030	0.275 ± 0.017	0.635	67.8 ± 4.3

To further investigate the utility of the nitrilase nanocomposite, we chose to examine nitrilase's ability to convert 3-cyanopyridine to biologically active 3-carboxypyridine (nicotinic acid; niacin) (**Scheme 1**). Previous reports have indicated that this niacin precursor is significantly less labile to nitrilase conversion as compared to PPN due to polarity and steric concerns, making it a more rigorous test for this system.^{90,104} Specific activity testing of the nanocomposite with a 10 mM solution of 3-cyanopyridine revealed that the nanoparticles have nearly identical specific activity relative to the free enzyme, regardless of particle size, again suggesting that the silica matrix doesn't create a diffusion barrier between the substrate and enzyme.



Scheme 1. Hydrolysis of 3-cyanopyridine with nitrilase.

Kinetic parameters of encapsulated nitrilase for both substrates were compared to that of free enzyme (**Table 3**). The apparent K_m value increased by ~60% for both substrates when compared to nitrilase free in solution, regardless of the encapsulation conditions. A difference in K_m within one-fold suggests that the enzyme is behaving kinetically similar to the free enzyme. Previous studies have reported changes of K_m values for biomimetically synthesized silica-enzyme nanoparticles anywhere from a one-fold decrease to a three-fold increase.^{77,105} Changes in the K_m in these systems have been attributed to a variety of factors, including limited substrate access into the silica matrix and occlusion of the enzyme active site. Since there is little control over the orientation of the enzyme within the silica, and there is no apparent kinetic variation with different

sized particles, it is likely that the active site of some of the enzyme is occluded by the silica at any given time.

Table 3. Kinetic parameters and specific activity of nitrilase-containing silica nanoparticles.

Encapsulation Conditions	K_m PPN (mM)	Specific Activity PPN (U / mg)	K_m 3-Cyanopyridine (mM)	Specific Activity 3-Cyanopyridine (U / mg)
Free Enzyme	2.02 ± 0.27	2.47 ± 0.15	0.57 ± 0.07	0.0514 ± 0.0036
Water	3.38 ± 0.63	1.47 ± 0.19	0.90 ± 0.11	0.0489 ± 0.0045
8 mM	3.18 ± 0.69	1.81 ± 0.25	0.71 ± 0.10	0.0549 ± 0.0028
17 mM	3.37 ± 0.72	1.35 ± 0.20	0.80 ± 0.13	0.0566 ± 0.0038
25 mM	3.14 ± 0.88	1.67 ± 0.24	1.12 ± 0.16	0.0352 ± 0.0017

To evaluate the applicability of these nanocomposites for the industrial synthesis of niacin, a single reaction batch of encapsulated nitrilase was used to drive the conversion of 3-cyanopyridine. The overall conversion rate was compared between the free and encapsulated conditions (**Figure 20**). The conversion was verified by HPLC and characterized by NMR (NMR data not shown). It should be noted that no enzymatic activity was observed in the supernatant, confirming that the enzyme wasn't simply absorbed onto the silica surface or isn't leeching out of the silica framework. This combined with the ease of product separation from the biocatalyst makes the silica-enzyme nanocomposites attractive for large scale use.

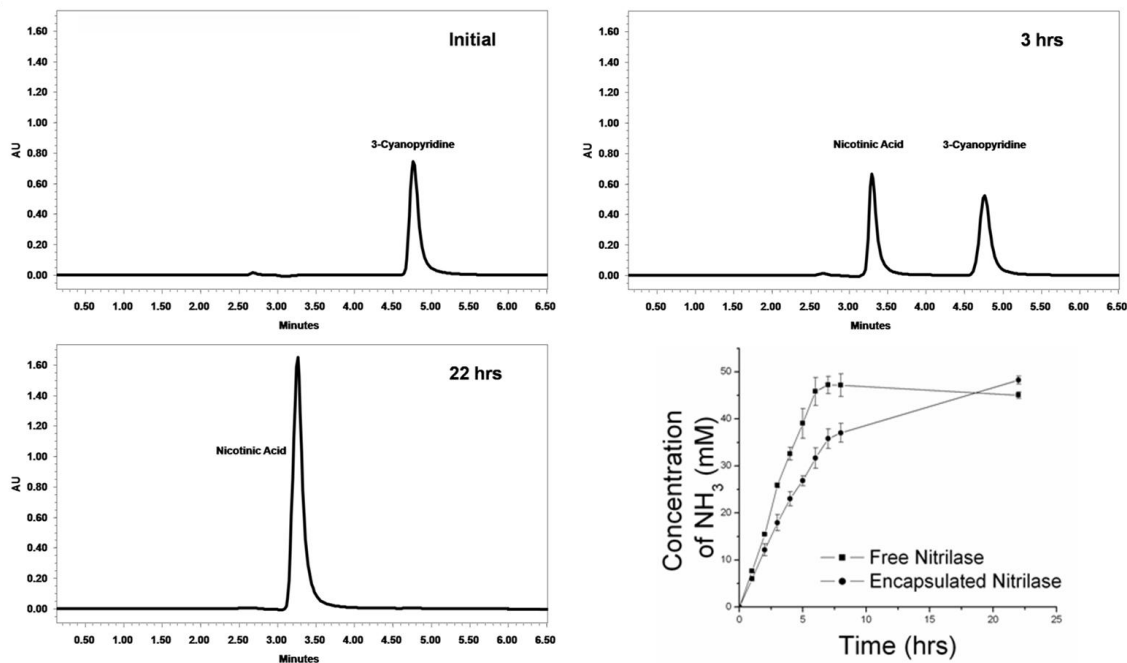


Figure 20. HPLC spectra following the conversion of a 50 mM solution of 3-cyanopyridine to nicotinic acid with nitrilase-containing nanoparticles. Time points are initial (top left), 3 hours (top right), and 22 hours (bottom left). (bottom right) Fluorometric comparison of the conversion of 50 mM 3-cyanopyridine with free and silica encapsulated nitrilase.

Since the nanocomposite can be separated from the reaction media by centrifugation, it is of interest whether the material can be used multiple times. Thus, we examined the biocomposites ability to convert multiple doses of 3-cyanopyridine. A single preparation of encapsulated nitrilase (same as above) was used to convert a 5 mM solution 3-cyanopyridine ten successive times. However, loss of silica to the multiple handling procedures reduced the amount of biocatalyst present, which has a significant impact for repeated usage. Recently, a histidine-tagged R5 peptide linked to cobalt-coated agarose beads in a flow reactor was used to immobilize silica encapsulated equine butyrylcholinesterase.⁷⁵ Although this process is an effective method for screening cholinesterase inhibitors, synthesizing a histidine-modified peptide can be expensive and time-consuming, especially at the large scale. Alternatively, inspired by a bed flow

reactor design of PEI-templated nitrobenzene nitroreductase silica nanoparticles,¹⁰⁵ the effective, repeated separation of water-soluble nicotinic acid from the nitrilase-containing nanospheres was achieved by performing the reaction in centrifuge filters (Millipore Ultrafree-MC centrifugal filter devices with a Durapore 0.1 μm pore size PVDF filter). Even after 10 consecutive experiments, only a 10% loss of activity was observed (**Figure 21**). Also, no detectable activity was observed in the supernatant after filtration. Much like the frit filters used in the nitrobenzene nitroreductase study, the centrifuge filters served as a physical barrier between the nitrilase-containing silica nanoparticles and the desired product after conversion and centrifugation, which allows for their more efficient recyclability.

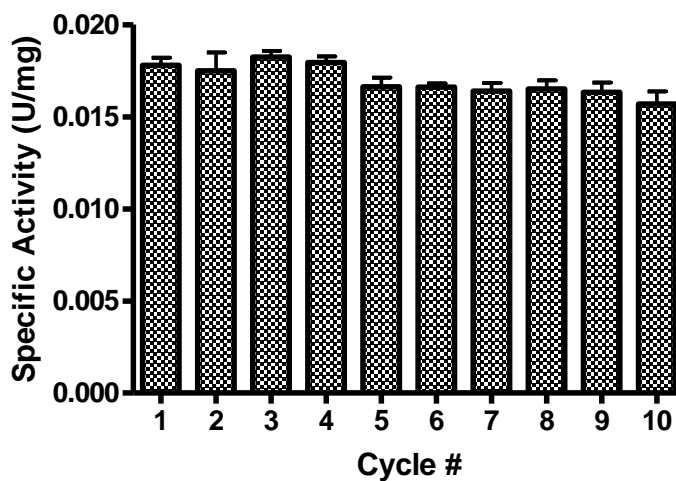


Figure 21. Consecutive experiments performed on a single triplicate batch of nitrilase-containing silica. A 5 mM 3-cyanopyridine solution was added and incubated at RT for one hour before being removed by centrifugation. Activity of the enzyme was only diminished by 10% at reaction # 10.

A scaled preparation of niacin was produced by combining 20 batches of nitrilase-containing nanoparticles (7.4 mg of total enzyme; 8.6 mg of silica) synthesized in water. A 200 mM solution of 3-cyanopyridine was then added and allowed to convert for 12

hours at 30°C. Upon centrifugation, the supernatant was readily collected and 9 additional aliquots of 3-cyanopyridine were added. After HPLC quantification of the product (10 mL total), it was determined that this system was capable of synthesizing 1.75 mg of nicotinic acid/hr throughout 10 reaction cycles.

Nitrilase containing silica particles can be utilized as a viable immobilized biocatalyst that is both rapidly produced and quickly reclaimed for use in the synthesis of nicotinic acid without loss of significant activity or need for cumbersome separation steps. Additionally, the reported long term storage of enzymes within nanoparticles with little loss in activity adds another cost effective benefit likely to be attractive for scale-up chemoenzymatic processes.^{76,77} Although there may be many challenges involved with commercializing this technology, these characteristics will greatly reduce time and costs that traditionally hinder widespread use of enzymes in pharmaceutical and fine chemical production.

β-Glucosidase

Cellulose is a polysaccharide that comprises ~40% of plant tissue that can be hydrolyzed into D-glucose, which is widely used as a feedstock for production of ethanol.¹⁰⁶ As a renewable resource, ethanol is widely considered as a viable alternative to fossil fuels that could potentially reduce the amount of imported oil, reduce air pollution, and facilitate economic development in rural areas. Traditionally, ethanol production from cellulose was achieved through the breakdown of pure cellulose powder or ball-milled cellulose.¹⁰⁷ However, in 1993, it was shown that paper mill waste fiber

and spent liquor from an ammonium-sulfite pulp process can be used as a cheaper alternative source.¹⁰⁸ Using a *P. decumbens* JU-A10 culture broth as a source of crude cellulase and *Aspergillus niger* L22 culture broth as a source of β -glucosidase, fine fibers from paper mills can be hydrolyzed to glucose. The supplementation of β -glucosidase increased the overall ethanol yield by 42.1% when compared to the activity of the *P. decumbens* JU-A10 culture broth alone.¹⁰⁸

In general, β -glucosidases are enzymes responsible for the hydrolysis of glycosidic bonds, releasing non-reducing terminal glucosyl residues from glycosides and oligosaccharides (**Figure 22**).¹ They are found most organisms are commonly used in the breakdown of glycolipids and exogenous glucosides in animals, biomass conversion in microorganisms, and catabolism of cell wall oligosaccharides.¹ Mechanistically, conversion occurs for the 240 kDa dimer of *Aspergillus niger* β -glucosidase first by the donation of a proton from the one of the two carboxylic acids to the leaving group while the other deprotonated carboxylate nucleophile attacks from the opposite side to form an α -linked intermediate. Next, the conjugate base of the catalytic acid extracts a proton from an adjacent water molecule, improving its ability to nucleophilically attack the anomeric carbon and release the products from the enzyme.

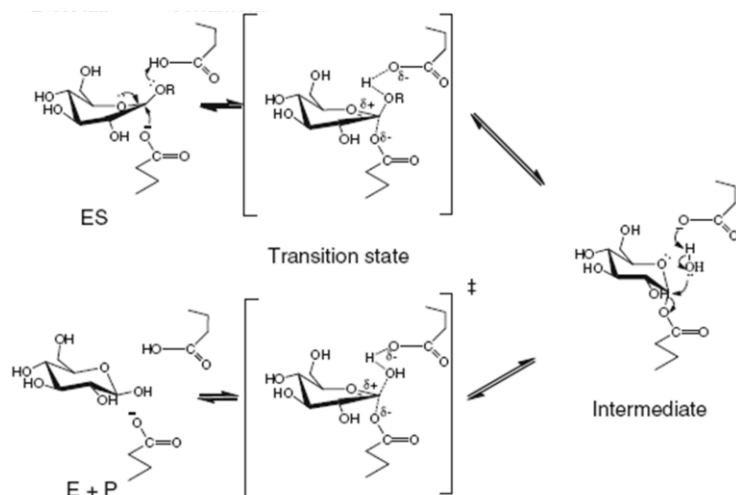


Figure 22. Catalytic mechanism found in the hydrolysis of oligosaccharides to glucose by *Aspergillus niger* β -glucosidase.¹

Although utilized in large scale industrial applications, the cost of maintaining a constant source of enzyme can be expensive and time-consuming. In addition, enzymes free in solution are susceptible to proteolytic degradation and can be thermally unstable. To circumvent these challenges, encapsulation methods to shield these enzymes from proteases have been developed. The purpose of this section is to investigate the effect of encapsulating β -glucosidase from *Aspergillus niger* into generation 4 PAMAM dendrimer-templated silica nanoparticles.

Experimental

Reagents: All reagents were purchased from Sigma-Aldrich (U.S.A) and used as delivered.

β -Glucosidase Encapsulation: All silica precipitation experiments were performed by first creating a stock solution consisting of 160 μ L of β -glucosidase at variable concentrations in 0.25 mM phosphate buffer pH 7.0 and 40 μ L of a 100 mM primary

amine solution of generation 4 PAMAM dendrimer. Tetramethylorthosilicate hydrolyzed by 1 mM HCl (aq.) was then added (20 μ L) and incubated for 5 minutes. After precipitation of silica was achieved, the particles were isolated by centrifugation (5 min, 7.2 x g). The supernatant was collected and this process was repeated three times with a 200 μ L aliquot of a 200 mM acetate buffer (pH 5.0) wash solution. Next, the particles were washed three times with 200 μ L of water and resuspended in water. General protein content in the supernatant and washes was quantitated with the Bradford assay against a standard curve of β -glucosidase.

Specific Activity Assay: Specific activity of the encapsulated enzyme was determined through the hydrolysis of pNpp-b-glucopyranoside (pNPG). Briefly, a 25 μ L aliquot of silica encapsulated β -glucosidase (0.1 mg/mL protein) was heated to 50°C for 10 minutes and subsequently added to a 125 μ L solution containing 6.0 mM pNPG in 50 mM acetate buffer pH 5.0 and incubated for 5 minutes. The reaction was then quenched with 150 μ L of 1M sodium carbonate. The resulting yellow product was then measured spectrophotometrically at 405 nm. One unit of β -glucosidase activity was defined as the amount able to release 1 μ mol of pNPG/min per mg of β -glucosidase under the assay conditions.

Activity Studies: The activity of the encapsulated enzyme was evaluated by varying the reaction pH and temperature. For the pH study, the particles were dissolved in water as noted above and incubated with 6 mM pNPG in 0.1 M KCl/HCl buffer pH 1-2, 0.1 M acetate/phosphate buffer pH 3-3.4, 0.1 M acetate buffer pH 4-5.5, and 0.1 M phosphate buffer pH 6-8, respectively. The temperature study was performed the same as the standard activity assay except that the reaction temperature was varied from 30-80°C. For

the pH stability studies, the particles were incubated for 24 hrs at 4°C under different pH conditions. After incubation, the particles were washed with water prior to addition to the activity assay. The free enzyme was incubated at variable at high concentration and diluted down into the assay conditions with water. The thermal stability assay was conducted by incubating the particles at variable temperatures for 1 hr, cooled to room temperature, and then tested for activity using the standard activity assay.

Bradford Assay: Protein mass quantification was performed by adding 160 μL of test solution to 40 μL of Bio-Rad Protein Assay solution concentrate and mixing for 5 min. The change in color was monitored via UV-Vis (Bio-Tek Synergy HT multi-detection microplate reader) at 595 nm. A calibration curve was produced for β -glucosidase between the range 0.8 $\mu\text{g}/\text{mL}$ and 80 $\mu\text{g}/\text{mL}$.

Silica Quantification: Silica nanoparticles were quantified following the β -Silicomolybdate method described by Iler.⁹⁵ Samples were dissolved in 0.5 M NaOH and incubated at 95°C for at least 30 minutes. Following incubation, the liberated dendrimers were separated from solution by Centricon filtration (American Centricon filtration devices, Millipore Inc.). Molybdate reagent was added (1:4 silicic acid/molybdate) to the filtered solutions to initiate the formation of the bright yellow product monitored by UV-Vis spectrophotometry at 410 nm and quantitated from a standard curve of silicate standards.

Scanning Electron Microscopy: Silica samples were resuspended in ethanol and placed on an aluminum surface SEM sample stage (Ted Pella Inc.) to dry. Samples were sputter-coated with a thin layer of gold via a Pelco Model 3 Sputter Coater (Ted Pella Inc.).

Thereafter, samples were imaged on a Hitachi S4200 scanning electron microscope operated at variable voltage.

Results

β -glucosidase from *Aspergillus niger* was chosen for silica encapsulation due to its low isoelectric point (~ 4.0).¹⁰⁹ The difference in overall charge between the PAMAM dendrimer and β -glucosidase at neutral pH allows for an electrostatic interaction between the two molecules. This creates a protein-polymer conjugate that is isolated within the growing silica matrix during amine-catalyzed precipitation. β -glucosidase-containing silica nanoparticles were synthesized in 0.25 mM phosphate buffer pH 7.0 by adding 20 μ L of 1 M hydrolyzed tetramethyl orthosilicate (TMOS) to a 200 μ L solution containing varying amounts of β -glucosidase and generation 4 PAMAM dendrimer (20 mM primary amine concentration). The efficiency of enzyme encapsulation quantified by the Bradford assay determined an enzyme encapsulation yield of $\sim 80\%$ irregardless of starting protein concentration (**Figure 23**). This suggests that the loading capacity of the silica nanoparticles has not yet been reached under the reaction conditions tested.

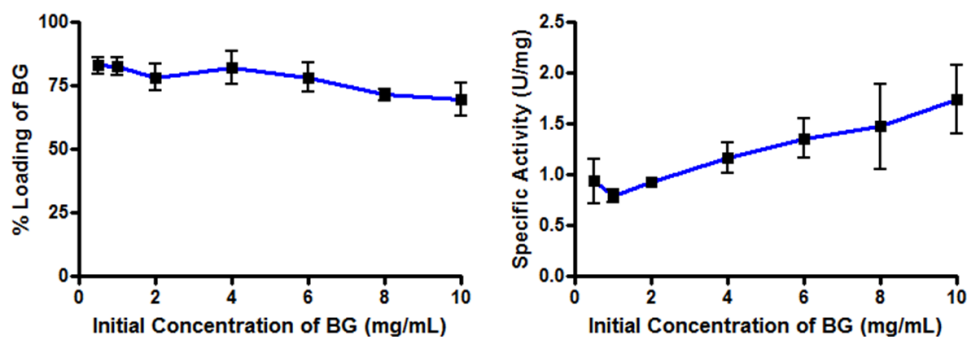


Figure 23. Loading efficiency (left) and specific activity (right) of β -glucosidase-containing silica nanoparticles.

The specific activity of the encapsulated protein was determined by monitoring the conversion of 6.0 mM pNPG in 50 mM acetate buffer at pH 5.0 for 5 minutes. A trend towards higher specific activity at the higher protein loading concentrations was observed. For example, the specific activity for the highest protein loading condition (10 mg/mL) was experimentally determined to be 1.74 ± 0.28 U/mg, which is $48.9 \pm 10.1\%$ of the activity found with the enzyme free in solution. SEM characterization of selected samples revealed a change in particle size as a function of starting enzyme concentration (**Figure 24**). In fact, particles synthesized with 10 mg/mL protein were 5x smaller than those with 1 mg/mL β -glucosidase. In general, smaller particles imply a shorter distance between the substrate in solution and the protein inside the silica matrix which may explain why the higher loading conditions had ~ 1.75 x higher specific activity.

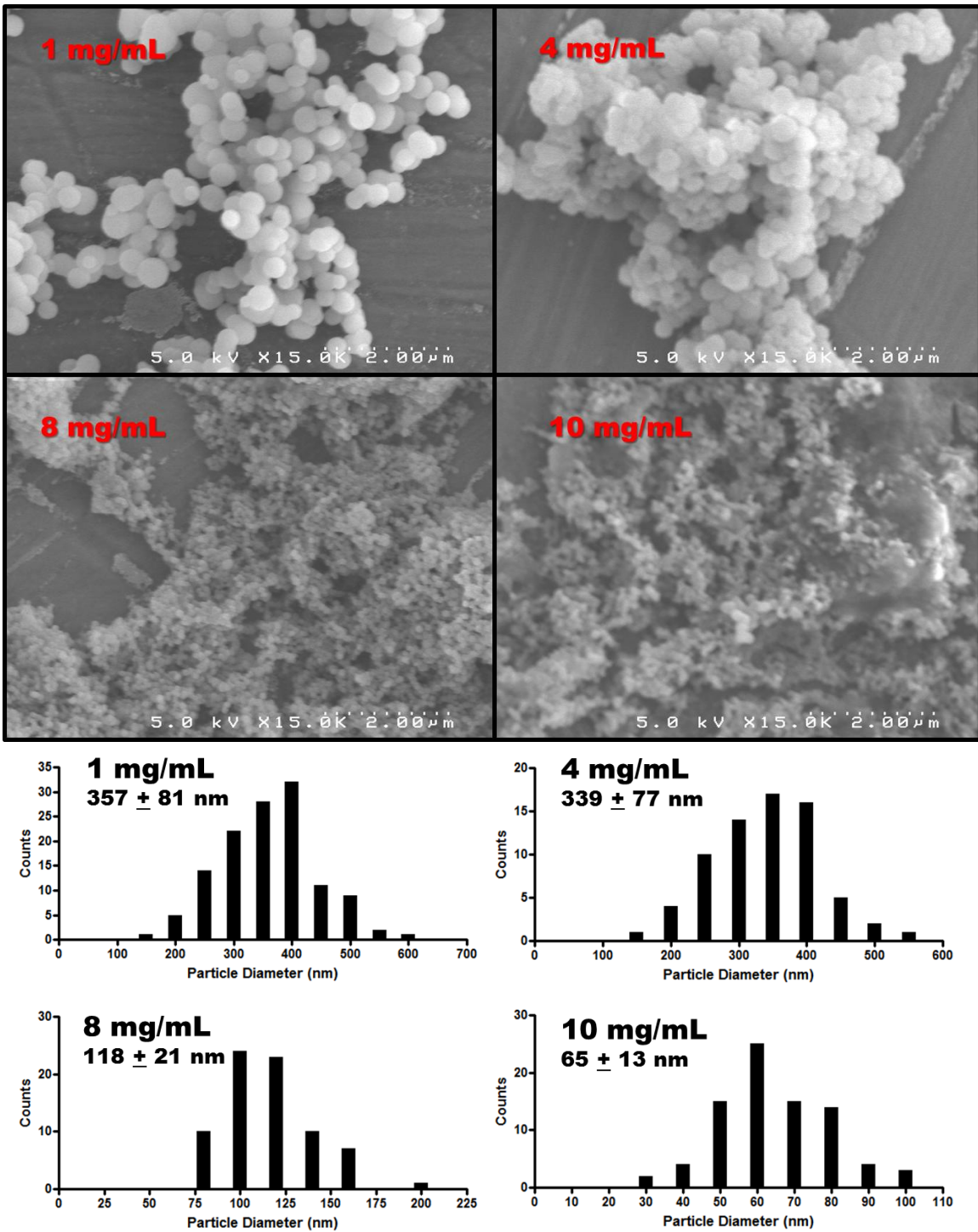
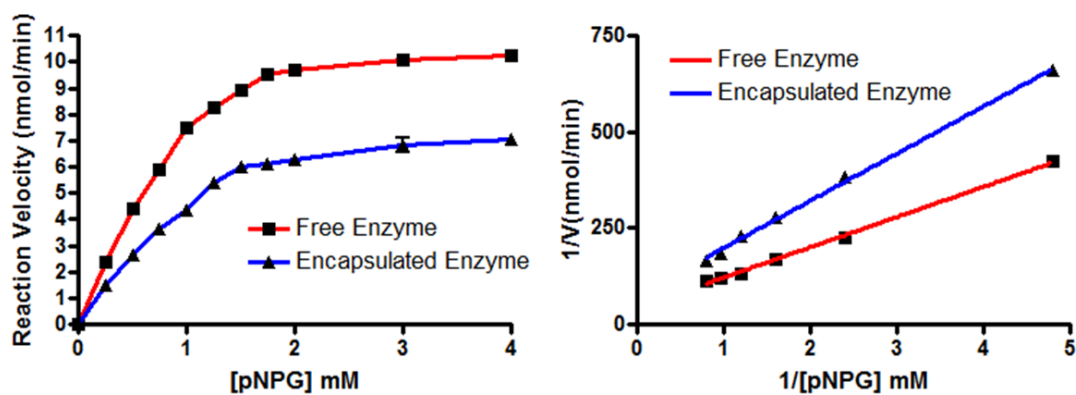


Figure 24. SEM images and particle size distributions of β -glucosidase containing silica nanoparticles.

Using the highest loading condition particles, kinetic parameters of encapsulated β -glucosidase for pNPG were compared to that of the free enzyme (**Figure 25**). The apparent K_m for the encapsulated enzyme was within 20% of the free enzyme in solution. In addition, the calculated V_{max} indicated that the encapsulated enzyme can turnover ~70% of what the free enzyme can in solution. A difference in K_m within one-fold suggests that the enzyme is behaving kinetically similar to the free enzyme. As noted above, changes of K_m in biomimetically synthesized silica-enzyme nanoparticles have ranged anywhere from a one-fold decrease to a three-fold increase.^{77,105} Given the fact that the K_m for β -glucosidase is nearly identical under both conditions, it is likely that the loss of specific activity in the silica nanoparticles is caused by the occlusion of the active site of some of the enzyme by the silica at any given time.



Encapsulation Conditions	K_m pNPG (mM)	V_{max} (nmol/min)
Free Enzyme	0.86 ± 0.09	13.32 ± 0.48
Encapsulated Enzyme	1.09 ± 0.12	9.46 ± 0.41

Figure 25. Kinetic parameters of free and silica encapsulated β -glucosidase. Michaelis-Menten (top) and Lineweaver-Burke (center) graphs.

One advantage of silica encapsulation is that the inorganic matrix serves as a cage around the enzyme which can serve to stabilize the enzyme at elevated temperatures and variable pH. For example, the specific activity of the nanoparticles was highest at pH 4, whereas the free enzyme was the most robust at pH 5 (**Figure 26**, top left). Interestingly, the encapsulated enzyme maintains >50% of the overall activity as low as pH 2.5 and as high as pH 6. Conversely, the free enzyme shows an activity window between pH 3.5-7, with maximum activity at pH 5. Silica is negatively charged, so the local pH found within the silica nanoparticles may actually be higher than the solution pH, which could account for the relative shift in activity. This phenomenon is not present when the particles are stored overnight at variable pH (**Figure 26**, bottom left). In fact, the trend in activity when the particles were is similar for both the free and encapsulated conditions.

When the reaction temperature was assayed, the free enzyme demonstrated optimal specific activity at 50°C and drastically decreased at elevated temperatures, likely caused by the denaturation of the protein (**Figure 26**, top right). Strikingly, the encapsulated protein was not only highly active at 50°C, but it also exhibited a three-fold increase in specific activity at 70°C. In addition, when the protein was heated for an hour at variable temperatures and tested for activity, the encapsulated enzyme maintained its activity even at 60°C (**Figure 26**, bottom right). The free enzyme begins to lose activity at 50°C, and has less than half of its activity at 60°C. It is likely that the silica matrix serves to stabilize the protein by reducing the number of potential inactive conformations and thereby constraining the protein into an active state.

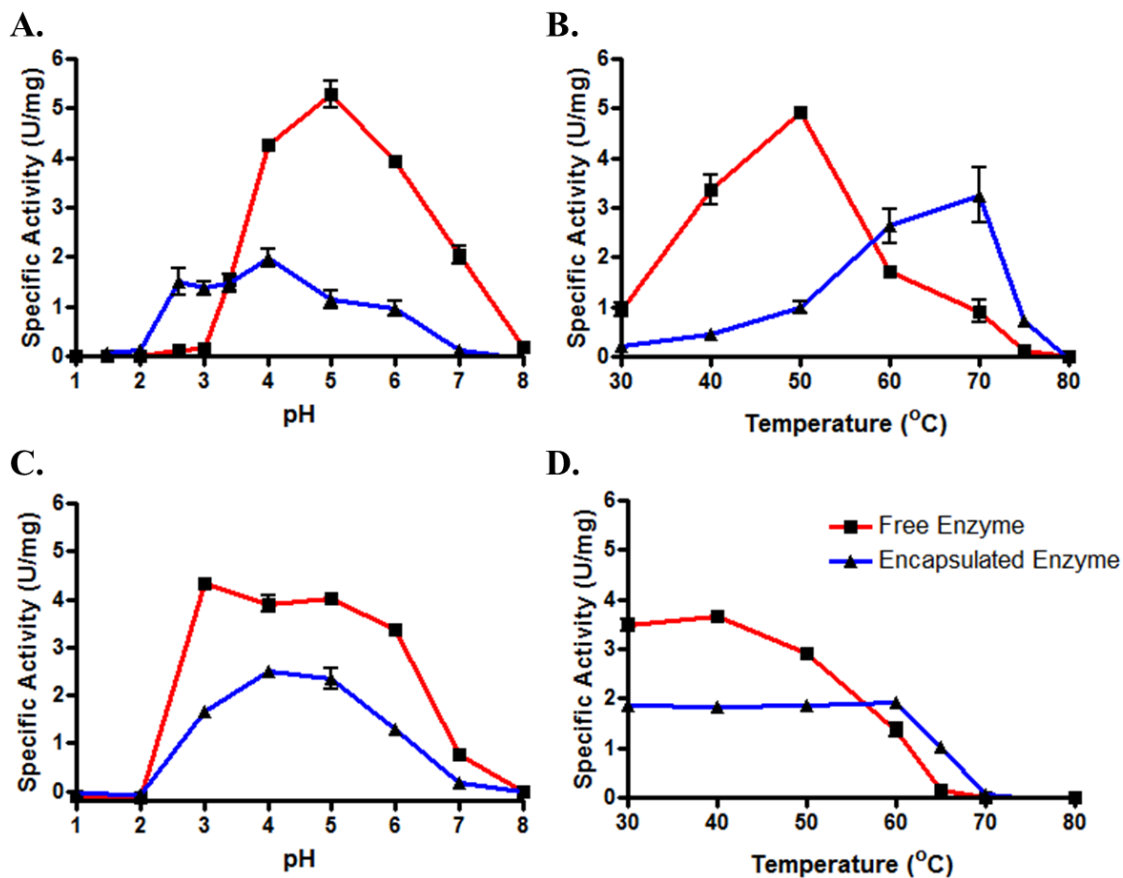


Figure 26. Thermal and pH stability of β -glucosidase encapsulated within silica nanoparticles. A.) Specific activity as a function of pH. B.) Specific activity as a function of reaction temperature. C.) Stability of encapsulated β -glucosidase after being stored at different pH's overnight. D.) Thermal stability of β -glucosidase upon incubation at variable temperatures for 1 hr.

Conclusions

Dendrimer-mediated enzyme encapsulation into silica matrices has many advantages in the context of industrial biotransformations. The silica matrix serves as a protective cage that prevents enzymatic proteolysis while still allowing free diffusion of substrates and products to and from the active site. These biocatalysts are easily recovered and purified from reaction mixtures by filtration or decantation with minimal loss of enzymatic activity. Also, the silica matrix has been shown in the case of β -glucosidase to improve the specific activity of the enzyme by stabilizing the enzyme at elevated

temperatures. One potential application of this technology is a combinatorial approach to ligand synthesis by encapsulating several enzymes from the same pathway, thereby creating a synthesis cascade that could overcome limitations that unstable enzymes provide. Another potential application is to incorporate this technology with other immobilization strategies (i.e. cross-linked enzyme aggregates) to encapsulate enzymes that are inactivated during the crosslinking process.

CHAPTER III

BOTTOM-UP SYNTHESIS OF BIOLOGICALLY ACTIVE MULTILAYER FILMS USING INKJET PRINTED TEMPLATES

Introduction

One essential characteristic of 2D bioanalytical systems is their ability to rapidly detect a panel of drugs, pathogens, or biomolecules from selectively functionalized surfaces. From point of care (POC) diagnostics to electrochemical sensing, localized areas of biologically active films serve to support and to protect a functional material, while offering higher sensitivity and increased resolution during product analysis.¹¹⁰⁻¹¹³ With the advent of recent, low temperature, micron-scale deposition techniques such as direct ink writing (DIW), screen-printing, or ink-jet printing (IJP), there has been considerable interest in modifying solid surfaces with biologically active functional materials.¹¹⁴⁻¹¹⁸ In fact, enzymes have been printed using various biomaterial deposition methods;¹¹⁹⁻¹²¹ however, real-time analysis of reaction products detected along a patterned 2D interface still remains an obstacle for functional adaptation because of the unpredictable nature of such chemically responsive surfaces.¹²²

While the structure and property relationships of 2D-active surfaces are not well understood, solution phase bio-compatible systems have been studied extensively.^{52,122,123} Previously, enzyme-containing silica particles have been synthesized via sol-gel or biomimetic encapsulation strategies, producing localized nano-environments for the soluble enzyme.^{113,124-129} When compared to the reactivity of the enzyme in solution, free diffusion of small molecules within these constrained, three-dimensional (3D) porous

silica matrices offer cheaper product separation and purification strategies and enhanced biological life-spans. Unlike traditional sol-gel methods that often incorporate multiple steps under high-temperature reaction conditions, biomimetic approaches for enzyme encapsulation have been reported to be faster and more efficient under mild reaction conditions (>30 min at room temperature compared to 32 h at variable temperatures for sol-gel formation).^{125,128,129}

As demonstrated in **Chapter II**, amine-terminated PAMAM dendrimers have been shown to direct the encapsulation of enzymes within silica nanospheres with high loading efficiency and excellent long term stability.^{123,130} This strategy utilizes the electrostatic attraction between the cationic dendrimer and anionic enzyme, creating a supramolecular complex that simultaneously polymerizes silica while immobilizing the active enzyme. More importantly, this confinement strategy does not significantly inhibit the active conformation of the enzyme, as same-fold enzymatic activity is reported when compared to the soluble enzyme in solution.^{52,118,122,123} Although these strategies are used to create highly efficient bed reactors and reaction columns in solution phase reactions,¹³⁰ the application of this approach as a 2D film has not been investigated.

In this chapter, inkjet printing, using the Dimatix Materials Printer (DMP), is used to template the 2D encapsulation of enzymes, where encapsulation efficiency and activity is studied as a function of the degree of enzyme loading. Unlike other commercially available biomaterial deposition techniques, the DMP offers non-invasive rapid prototyping ($8 \text{ m} \cdot \text{s}^{-1}$), where an applied voltage, controlled through the DMP software, induces a fluctuation in pressure within the printhead nozzles (16 nozzles, spaced $256 \mu\text{m}$); once the pressure reaches a critical point, a droplet ($< 12 \text{ pL}$) is released.^{114,131} The

very nature of the DMP provides a tunable printing environment, where any ink that is synthesized within a jettable range (viscosity of 8-15 cPs and surface tensions of 25 dynes cm^{-1}) can be optimized for uniform printing. Combining the versatility of the DMP with a previously established biomimetic dendrimer ink,¹³² a platform is developed for the efficient, bottom-up synthesis of a biologically active enzyme film.

Experimental

Materials: All reagents/compounds were purchased from Sigma-Aldrich and used with no modifications.

Pre-Preparation of the Gold Substrate: All gold substrates used for printing were cleaned in piranha solution (3:1 $\text{H}_2\text{SO}_4:\text{H}_2\text{O}_2$) for at least 30 min, washed with copious amounts of water and dried with nitrogen before use. Warning: Piranha solution should be handled with extreme caution.

Printing of Dendrimer Ink: An ink consisting of 8.6 wt% PAMAM generation 4 dendrimer and 25% w/v polyethylene glycol (PEG, Aldrich Chemical Co.) in 100 mM phosphate buffer pH 7.5 was printed using a Dimatix Materials Printer (DMP). The ink was printed with 2x coverage on either gold substrates or into the wells of a 96-well Immulon 2-HB plate. During printing, the maximum voltage pulse was 24 V, and the pulse frequency was maintained at 1.0 kHz.

Glucose Oxidase (GO_x) Silica Encapsulation on Gold:

Method 1: A gold substrate containing the printed dendrimer ink was inverted and lowered into a solution containing 500 μL of 0.1 mg/mL GO_x (in 0.25 mM phosphate buffer pH 7.0) and incubated for 10 minutes. Next, 50 μL of 1 M silicic acid was added

and the reaction was allowed to react for varied times (1-20 min). The reaction was terminated by removing the substrate from the reaction solution and washing it copiously with water. The substrates were then dried under a gentle stream of N₂. Controls were also prepared with the same method, except the reaction solution didn't contain any GO_x.

Method 2: Instead of allowing for interaction between the printed spot and GO_x, the printed substrate was inverted and lowered into a solution containing 500 μL of 0.1 mg/mL GO_x (in 0.25 mM phosphate buffer pH 7.0) and 50 μL of 1 M silicic acid. Upon addition, the reaction was allowed to proceed for 20 min. The reaction was similarly terminated by removing the substrate, washed with water, and dried with N₂. Controls without GO_x were also prepared using the same method.

Glucose Oxidase (GO_x) Encapsulation in 96-well Plates:

Method 1: A 200 μL solution of GO_x in 0.25 mM phosphate buffer pH 7.0 was added to each printed well and allowed to incubate for 10 minutes. Next, 20 μL of 1 M silicic acid was added and the reaction was allowed to proceed for 20 minutes. The reaction was terminated upon centrifugation at 3000k for five minutes and the supernatant was removed. The wells were then washed three-fold with 200 μL of 0.1 M phosphate buffer pH 6.0 to remove any unused reactants.

Method 2: A solution containing 200 μL of GO_x in 0.25 mM phosphate buffer pH 7.0 and 20 μL of 1 M silicic acid was added to each printed well and allowed to react for 20 minutes. The reaction was terminated upon centrifugation at 3000k for five minutes and the supernatant was removed. The wells were then washed three-fold with 200 μL of 0.1 M phosphate buffer pH 6.0 to remove any unused reactants.

Glucose Oxidase Activity: Activity of the encapsulated enzyme was determined by the glucose oxidase activity assay (Worthington Biochemical Corporation) with slight modifications. First, an *O*-dianisidine dye reagent was prepared by adding 100 μL of 1% *O*-dianisidine solution to 12 mL of 0.1M potassium phosphate buffer at pH 6. After purging this solution with oxygen for at least 10 minutes, an aliquot of 192 μL was added to a solution containing 25 μL of β -D-glucose (concentrations of glucose reflect consideration of mutarotation in solution) and 8.35 μL of a 0.2 mg/mL solution of horseradish peroxidase (HRP). Next, this solution was added to a 25 μL solution of appropriately diluted GO_x in H_2O or added to the printed wells containing 25 μL of water, and the change in color was observed for 5 min at 460 nm. Reusability of the wells was assayed by reacting for 5 min and then washing 3 times with buffer before reuse. The reaction was repeated a total of 10 times. Storage stability of the printed wells was assayed after storage at 4°C in 0.1 M phosphate buffer for multiple days.

Profilometry: Height profiles of the printed composite for each reaction condition were analyzed using a VEECO profilometer with a 12.5 μm stylus. The scan rate was 10 $\mu\text{m}/\text{sec}$ and the stylus was maintained at 3.00 mg.

Scanning Electron Microscopy: Scanning electron microscopy (SEM) was conducted using a Hitachi S4200 microscope operating at variable voltages. Samples were prepared by sputter-coating them with a thin layer of gold using a Pelco Model 3 Sputter Instrument (Ted Pella Inc.) to prevent substrate charging during analysis.

Results

Given its capability to be encapsulated using previously established biomimetic strategies,¹²³ its low cost, and its commercial availability.^{123,133} the enzyme, glucose oxidase (GO_x), is used as a robust model enzyme in these 2D encapsulation studies. Initially, the microstructure of a dendrimer patterns interfaced with GO_x is investigated using two methods of synthesis. In each method, a 48 mm² array, containing approximately 20 pL of dendrimer ink per spot (spots spaced at 96 μm, printed 2x), is patterned onto gold coated silicon nitride chips. The first method (Method I) applied in this study represents a layer-by-layer approach to encapsulate GO_x within an individual spot. The patterned substrates are first submerged in a solution of GO_x. Then, without directly disturbing the chip in solution, the silica precursor, monosilicic acid, is directly added. The resulting film is then studied as a function of reaction time. Once the reaction is completed, the patterns are washed extensively in DI-water, dried under Nitrogen, and analyzed using SEM and height profilometry (**Figure 27**).

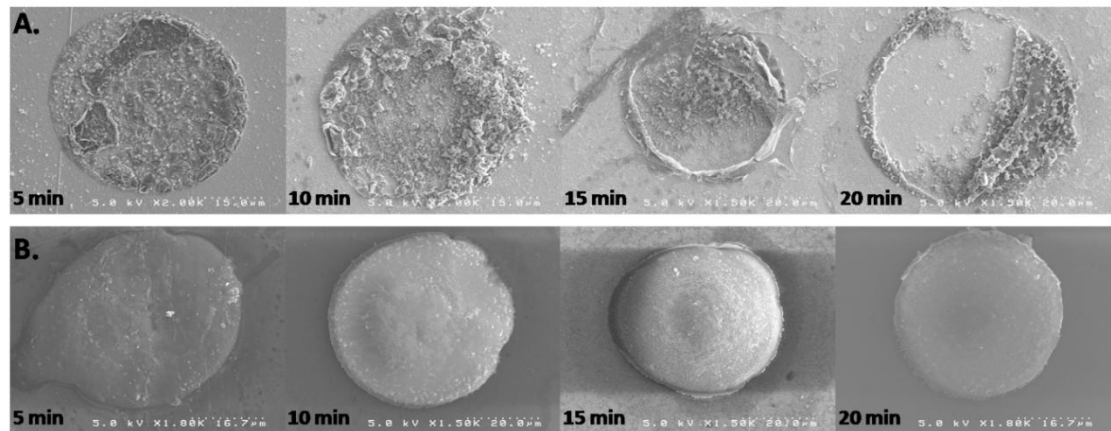


Figure 27. The change in morphology of a printed spot as a function of reaction time with monosilicic acid using Method I. **A.** Printed spot reacted first with GO_x (10 min), followed by silica encapsulation. **B.** Printed spot in the absence of GO_x as a function of silica formation.

Given the previously observed interactions between the dendrimer and enzyme in bulk solution,¹²³ it is initially anticipated that the enzyme would electrostatically adhere to the surface of the printed spot during the first incubation, essentially creating a printed anion exchange surface. Because the patterns are exposed to a locally high concentration of enzyme, silica is expected to form during the second incubation period, resulting in the effective encapsulation of the enzyme film. Analysis of the resulting composite films, however, revealed that the morphology of a spot is severely disrupted after 5 minutes of development when compared to the control conditions without enzyme. In fact, the control patterns indicate that spot morphology is sustained over the reaction period. The initial incubation period of the patterns with GO_x is observed to cause a significant morphological disruption. When the final reaction solution is assayed for enzyme activity after the chip is removed, nearly 100% of the enzyme is detected, inferring that GO_x has aggressively reacted with the printed dendrimer, solubilizing the film as a dendrimer-enzyme aggregate.

This reaction is documented over time using profilometry. When the spot is reacted with monosilicic during the second incubation period, silica is formed only along the remaining fragments of the spots but is not retained over time. Morphology is initially preserved at 5 min of reaction time ($2.6 \pm 0.9 \mu\text{m}$, **Figure 28**). After 10 min of reaction time, however, over 50 % of the physical spot dimensions are lost when compared to the control pattern, suggesting a differential disruption of the dendrimer layer at the spot interface.

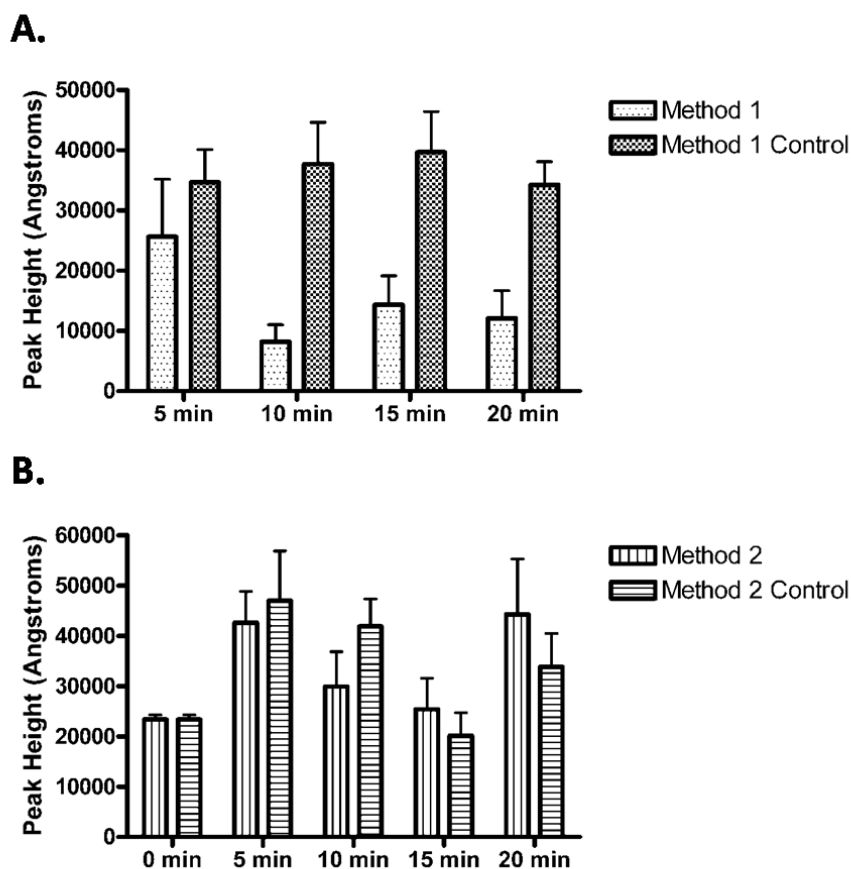


Figure 28. Height profiles of the two methods used in multicomposite formation. A. Profiles of spot height using Method I with and without GO_x . B. Profiles of spot height using Method II with and without GO_x . Time points are determined upon addition of monosilicic acid.

To eradicate impending pattern destruction witnessed in the Method I synthesis, a necessary alternative, Method II, was developed. Method II is premised on the simultaneously reaction of both GO_x and monosilicic acid with the printed chip. Since monosilicic acid is available to the patterns as the enzyme is introduced, the differential disruption observed in Method I should be eliminated. In fact, SEM and profilometry analysis confirms that uniform silica films are formed, during the simultaneous encapsulation of the enzyme (**Figure 29**).

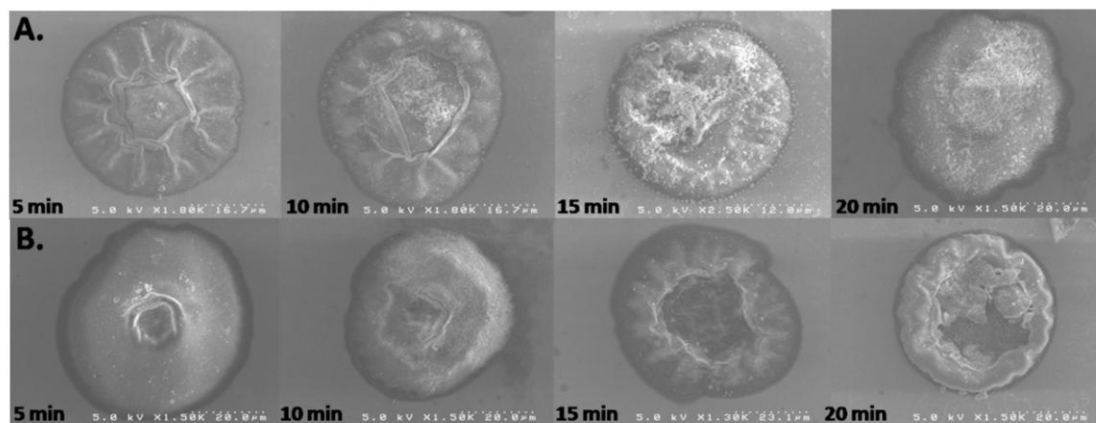


Figure 29. The change in morphology of a printed spot as a function of reaction time with monosilicic acid using Method II. **A.** Printed spot reacted with GO_x as a function of silica formation. **B.** Printed spot in the absence of GO_x as a function of silica formation.

When compared against the control patterns, examination of the enzyme-reacted spots using SEM revealed only a slight disruption in the surface morphology using the Method II synthesis; however, the overall quality and uniformity of the film is significantly improved, undoubtedly due to the immediate order of reactants. Profilometry measurements verified the integrity of the enzyme encapsulated patterns. Spot height initially increases ($4.3 \pm 0.6 \mu\text{m}$) after 5 min of reaction time and stabilizes at 20 min ($4.4 \pm 1.1 \mu\text{m}$). The decrease in spot height observed between 5-15 minutes of reaction time is likely due to the nature of the dendrimer-silica interaction.¹³² Because of the nature of this 2D reaction,¹³⁴ the original spot is understood to open up in the presence of multiple reactants, producing a metastable environment necessary for complete encapsulation. Control patterns in the absence of enzyme behaved similarly as documented in its analogous back-filling behavior, where the reacted spots varied in height again from 5 min ($4.7 \pm 1.0 \mu\text{m}$), 15 min ($2.0 \pm 0.5 \mu\text{m}$), and 20 min ($3.4 \pm 0.7 \mu\text{m}$).

In order to explain the morphological differences witnessed between the two methods of synthesis, both the composition of the ink and the reaction solution must be considered. The ink, itself, consisted of three main components: 113 mM phosphate buffer, 8.6 wt % dendrimer, and 25 wt % poly-(ethylene) glycol (PEG). Once printed onto the substrate, each pattern was submitted to control reaction conditions without enzyme. During this reaction time, it is predicted that the smaller components of the ink, such as the buffer ions and water, are exchanged with the reaction solution until equilibrium is achieved. Since the ink localized within the spot is much more concentrated than the surrounding solution (0.25 mM), water is diffused into the spot, causing it to swell and expand as silica is precipitated at the interface, which is comparable to what has previously been observed under similar reaction conditions.¹³²

When the enzyme is incorporated within the reaction mixture, the variation in spot morphology is dependent on the method of synthesis, likely due to a competing mechanism of spot disruption. As water from the far more dilute reaction solution diffuses into the patterns, the concentrated buffer within each spot begins to diffuse outward. The significant disruption of the formed spot observed during the first synthesis is likely due to the decrease in the local ionic strength of the spot during this interfacial diffusion. The high concentrations of buffer (with both anions and cations) are not reaching the spot during the Method I synthesis because of the initial GO_x (0.1 mg mL^{-1}) incubation period. The enzyme is acting as the complementary charge for the supramolecular aggregation of the dendrimer template, depleting the region of reactive products before monosilicic acid is added. This is not observed in the Method II synthesis

because the two reaction components are added simultaneously, eliminating the initial incubation, or reaction, time.

With the physical properties of the enzyme encapsulated film optimized, the activity of the constrained enzyme was examined. To test the enzyme activity, arrays (24 mm² area, cycled 2x) are printed directly into each well of a polymer coated 96-well plate to template enzyme encapsulation, and the wells are reacted using Method II synthesis (**Figure 30**). Note that the patterning in the 96-well plate are much more scattered. This is caused by the fact that printer cartridge is much farther away from the surface due to the depth (~1 cm) of the plate. Patterning within the plates however, provided a direct method for the rapid detection of enzymatic activity using a modified version of a GO_x activity assay.¹²³ In this assay, the encapsulated GO_x patterns were reacted with substrate, β-D-glucose, and molecular oxygen to produce δ-gluconolactone and hydrogen peroxide products, with the latter being easily detected through a coupled horseradish peroxidase colorimetric assay.

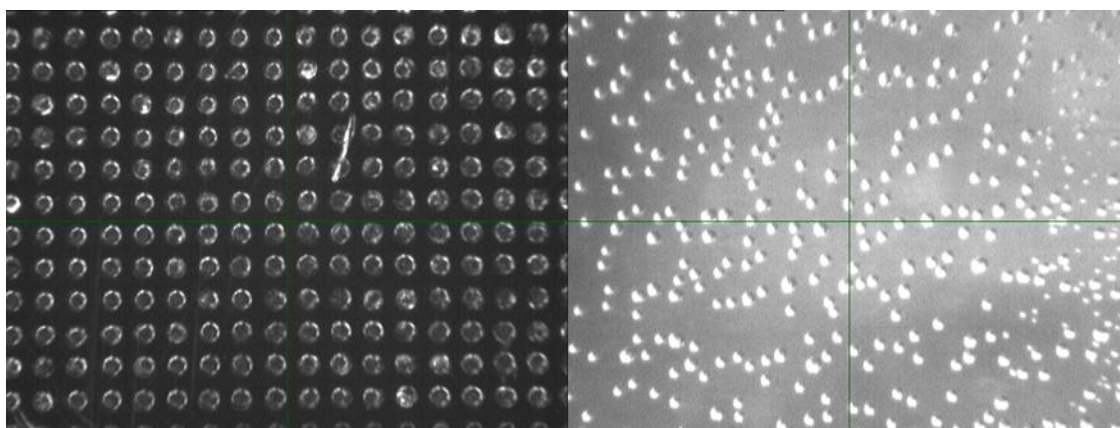


Figure 30. Images of the patterned inks on gold (left) and a 96-well plate (right)

With the ink patterned into the wells, each well are reacted for 20 min, according to the Method II synthesis, and the resulting patterns were purified through a series of

centrifugation and wash cycles. At the end of the third wash, the supernatant was extracted, and the encapsulated patterns were assayed for enzyme activity. The starting enzyme concentration within each reaction mixture was varied to determine the maximum loading capacity and encapsulation efficiency of the patterns (**Table 4**).

Table 4. Activity of the enzyme as a function of starting enzyme concentration.

Starting Enzyme Concentration [$\mu\text{g}/\text{mL}$]	Amount of Active Enzyme per Well [ng]	Reaction Velocity [nmol/min]	Relative Activity to soluble GO_x [%]
0.6	31.1 ± 0.1	1.6 ± 0.3	25.9 ± 4.5
3	80.4 ± 15.1	4.2 ± 0.8	13.4 ± 2.5
6	106.8 ± 16.8	5.6 ± 0.9	8.9 ± 1.4
12	117.6 ± 26.4	6.2 ± 1.4	4.9 ± 1.1

The most robust encapsulation parameters ($0.6 \mu\text{g mL}^{-1}$, $200 \mu\text{L}$) offered the highest % activity when compared to free GO_x in solution (25.9 ± 4.5 % of the starting enzyme activity). Enzyme saturation is observed at concentrations higher than $3 \mu\text{g mL}^{-1}$, corresponding to a maximum loading of ~ 120 ng of enzyme per reaction well. In fact, incorporating the higher starting enzyme concentrations (3 , 6 , and $12 \mu\text{g mL}^{-1}$) is reported to decrease the % of enzymatic activity within the patterns at a rate of ~ 6 nmol/min. Even the minimal fraction of activity ($\sim 5\%$) observed for the $0.6 \mu\text{g mL}^{-1}$ conditions infers that there is a trade-off between maximizing the enzymatic activity of the encapsulated patterns and optimizing the loading efficiency of the samples.

To determine whether enzyme confinement within the 2D microenvironment has affected its functionality, kinetic parameters were determined for patterned GO_x at the optimal concentration (0.6 μg mL⁻¹). When compared to GO_x free in solution, the immobilized enzyme exhibited a near two-fold decrease in K_m (24.47 ± 2.81 for soluble GO_x compared to 9.31 ± 1.37 for 2D GO_x), suggesting that restricting the enzyme to the 2D surface effectively reduces its access to the substrate. Compared to the solution-phase enzyme encapsulated nanoparticles, which exhibited 50% relative activity when compared to soluble GO_x,¹²³ the activity of the enzyme immobilized within the patterned surface demonstrated a one-fold decrease in activity. By restricting the enzyme to the 2D surface, many of the nanopores that were available during the solution phase synthesis are blocked by the substrate, and the film is restricted from diffusing through the solution. Therefore, the overall activity of the 2D phase composite is expected to be slower than the encapsulated enzyme in solution. For all of the restrictions placed on the enzyme within the pattern, however, its overall activity is still robust enough for many applications.

With the enzyme film still active on the 2D surface, their storage stability and reusability are investigated. In these studies, the encapsulated enzyme spots are initially assayed for repeated use. After 10 reaction uses over two weeks, the enzyme film demonstrated minimal degradation and remained ~98% active when compared to the initial reaction activity. (**Figure 31**).

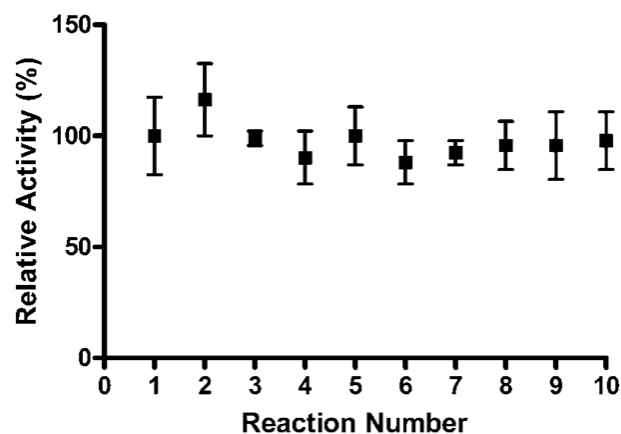


Figure 31. The calculated reusability of the enzyme encapsulated patterns as a function of time. The patterns retained near optimal activity after multiple reactions and washing steps.

Similarly, the stability of the enzyme (stored at 4°C in a phosphate buffered solution) is investigated, again over a period of two weeks (**Figure 32**). When the patterns are stored in air, nearly 75 % of the activity is lost over time; however, when the patterns are stored at 4°C, enzyme activity is essentially maintained with only slight loss of activity (25 ± 1%) at the end of the two weeks. This trend holds true for solution phase enzyme nanoparticles, as well.¹²³

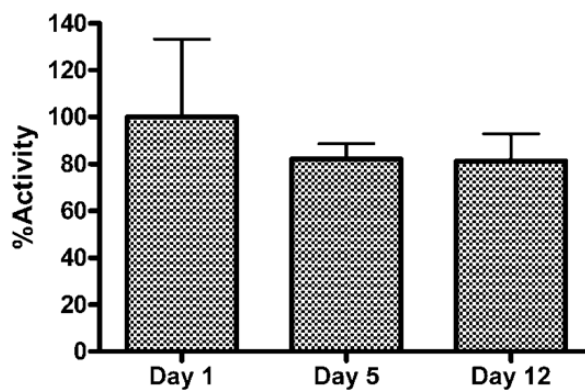


Figure 32. Storage stability of active printed patterns. The patterns were stored at 4°C in 0.1 M phosphate buffer and tested for activity after several days.

Conclusions

This chapter highlights the bottom-up synthesis of an enzyme containing film, with specific emphasis on the physical and chemical properties of the immobilized enzyme. In general, enzyme confinement within the patterns reduced the overall reactivity, reaction rate, and product yield of the enzyme when compared to solution-phase reactions. However, this loss in activity is considered negligible when compared to the overall impact of the functionally active template. Localizing the enzyme to a 2D patterned surface not only minimized the amount of reactants used during the study, but also enabled the patterns to be reused over extended periods of time without substantial loss in activity. The impact of such biologically active films can be translated into larger scale applications, serving a variety of functions, including biosensing and catalysis.

CHAPTER IV

CURRENT STRATEGIES IN MALARIA DIAGNOSTICS

Introduction

Although nearly eradicated, malaria has reemerged as one of the most prevalent diseases in the third world. Malaria is a tropical infectious disease caused by the protozoan parasites of the genus *Plasmodium*. Approximately half of the world's population is at risk for malarial infection, with 108 countries and territories reporting nearly 250 million cases (of which ~1 million were fatal) in 2008 (**Figure 33**).¹³⁵ The most susceptible population groups are young children, non-immune or semi-immune pregnant women, HIV infected individuals, and travelers/immigrants. One in five childhood deaths in Africa, occurring roughly every 45 seconds, can be attributed to malarial illness. In addition, current estimates suggest that an African child has on average between one and five episodes of malarial fever per year.¹³⁶ It also contributes to 30-50% of inpatient hospital admissions and up to 60% of outpatient health clinic visits in Africa. In countries with high infectivity rates, it is estimated that the GDP can be lessened by as much as 1.3%, placing malaria as the primary cause to the economic disparities between the infected countries and the rest of the world.¹³⁷

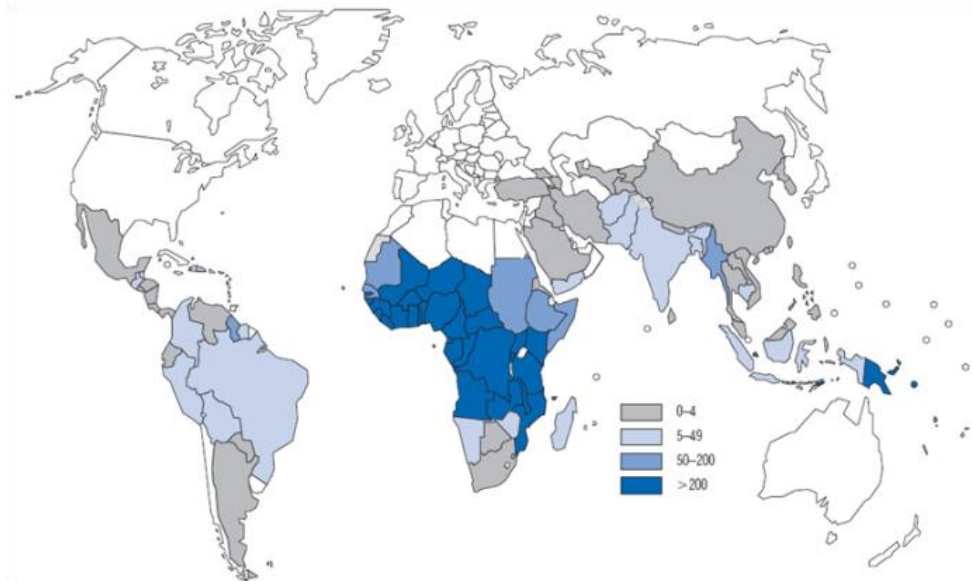


Figure 33. Estimated incidence of malaria per 1000 population, 2006.³

There are 5 types of known human malarial species: *falciparum* (by far the most common and most deadly), *vivax*, *malariae*, *ovale*, and some cases have been reported in southeast Asia with the monkey malaria parasite *P. knowlesi*.¹³⁵ Transmission of malaria into the human host is achieved exclusively through the bites of *Anopheles* mosquitoes. Typically, these mosquitoes breed in shallow collections of water which are prevalent in humid climates. In Africa, the high infection rates can be partially attributed to the African *Anopheles* mosquito, which has a relatively long lifespan that allows for the parasite to fully develop, and is highly attracted to humans.

The life cycle of the malaria parasite is shared between the human host and the *Anopheles* mosquito vector. As a sporozoite, the parasite is transmitted to humans from the *Anopheles* mosquito during a blood meal (**Figure 34**).¹⁹ Within an hour, the sporozoites are transported to the liver, where they develop into schizonts. After 1-2 weeks, the schizonts rupture, each releasing several thousand merozoites into the blood

stream. There, they invade healthy red blood cells (RBCs). Within the RBC, the merozoite matures into a schizont containing several merozoites, eventually rupturing to release these merozoites. Some merozoites differentiate into gametocytes, which are transported to the mosquito during a blood meal with an infected host. Here, they mature into sporozoites, and can be reinjected into a human host. The cycle continues as these sporozoites infect additional RBCs. Further details of the parasite's life cycle remain unclear.

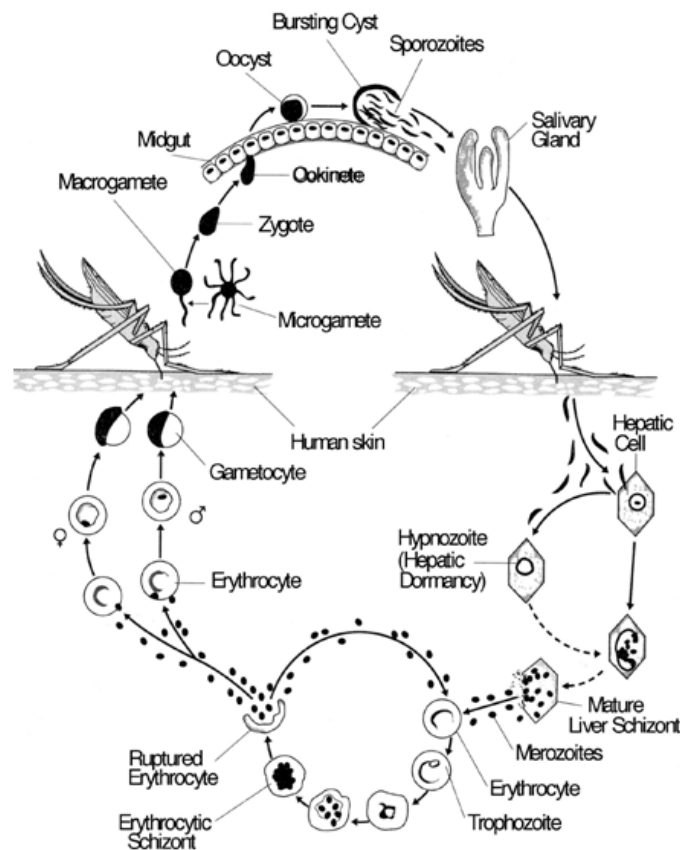


Figure 34. Life cycle of the malarial parasite.¹⁹

The rupture of RBC's marks the onset of visible symptoms of illness, including headaches, chills, and vomiting. If treatment is not administered within 24 hours of the

onset of symptoms, the infection will become severe, likely resulting in death. A major challenge in diagnosing malarial infections is that the clinical presentation of malaria is highly variable and overlaps with other common febrile illnesses, including pneumonia, sleeping sickness, and tuberculosis.^{138,139} Without effective diagnostic technologies in low resource regions, early health care workers had to rely on their ability to diagnose symptoms rather than identify biomarkers of a disease, as is the case today. In addition, of the diseases mentioned above, only malaria has traditionally been treated effectively due to the availability of cheap and effective antimalarials, including quinine from Cinchona bark and more recently synthetic chloroquine. As a result, in endemic regions, most illnesses expressing malaria-like symptoms were treated as malarial illness. For many years, the medical community essentially forwent the diagnostic process and even recommended in training manuals for health workers to treat all fevers in children with chloroquine.¹⁴⁰ In fact, it was reported that less than 20% of suspected malarial cases in 75% of African countries receive a confirmatory diagnosis before treatment.¹⁴¹

Although many lives have been saved by this “fever equals malaria unless proven otherwise” mentality, in many settings, especially where malaria is seasonal or where intensive disease controls are implemented, only a small minority of febrile patients may be parasitaemic.¹⁴² In addition, over the last few decades, overuse of chloroquine has led to parasitic resistance toward the drug, rendering it ineffective against most *P. falciparum* infections. In general, monotherapies are the cause for drug resistance because in many instances people that have been treated still have an asymptomatic parasite load capable of being transmitted back into the mosquito vector. These setbacks in malarial treatment have led to the development of a new group of highly effective, fast-acting antimalarials

known as artemisinin-based combination therapies (ACT).¹⁴³ Although highly effective, ACT incur more than 10 times the treatment costs of chloroquine, placing a severe economic burden on malaria-stricken countries.¹⁴⁴ In many Sub-Saharan African countries, as much as 40% of all health care costs being attributed to malarial treatment. In addition, a report was published in 2010 indicating that *P. falciparum* parasites in the border region of western Cambodia and eastern Thailand have shown evidence of resistance to artemisinins.¹⁴⁵ Without a current alternative treatment for malaria, accurate and efficient diagnosis and treatment of malarial infected patients is essential to suppress the spreading of resistant strains of malaria.

Malaria misdiagnosis and mismanagement also has individual and societal implications. At the individual level, misdiagnosis leads to costly drug purchases, which can also result in unwanted side effects. In addition, misdiagnosis implies that the individual is never treated for the true illness, which in many instances is potentially fatal. At a societal level, consistent mismanagement leads to a significant loss in consumer confidence in the health system. One major consequence is that the true infection rates of each disease are unknown, making it difficult for health officials to develop targeted regional strategies for each disease. To overcome these challenges, it is essential that efficient diagnostic strategies are developed and/or implemented so that both the patient and the healthcare provider have accurate information about the disease state of both the patient and of others in the region.

Healthcare in the Developing World

Of the ~7 billion people in the world, 3 billion lack basic sanitation, 2 billion do not have access to electricity, and more than 1 billion lack basic healthcare services and clean drinking water.¹⁴⁶ In addition, approximately half of the world's children live below the poverty line. More than half of the deaths in the poorest countries are the result of infectious diseases, compared to less than 5% in the richest countries.^{147,148} In developed countries, healthcare is provided through a centralized laboratory system that is capable of effective diagnosis and treatment even at the local level. In the few instances where a centralized laboratory system is available in developing countries, only the affluent upper class has access to their facilities. In general, healthcare in developing countries is divided into three classes: capital or major city level hospitals (high level); district-level healthcare providers (mid-level), and village-level healthcare workers (low-level).¹⁶ Of these three classes, diagnosis and treatment is performed primarily at the mid and local levels.

Mid-level healthcare facilities in the developing world look drastically different than those found in the U.S. Running water and electricity may or may not be available, and power is at best intermittent with wide fluctuations in voltage. Without air conditioning, the ambient temperature at such facilities can vary from 10-40°C. Dust, wind, and contaminating pathogens are very common as well. High risk human samples containing potential biosafety level 2 and 3 pathogens are typically handled with no more than gloves for protection. Maintaining and calibrating moderately advanced equipment is highly sporadic, questioning the validity of their output (**Figure 35**). Furthermore, at the

township and village level, power, running water, and refrigeration are highly intermittent or absent.¹⁴⁹



Figure 35. Typical laboratory conditions at mid-level healthcare facilities in the developing world.¹⁶

Resource limitations in the low-level and to some extent the mid-level facilities require that diagnostics performed in these settings must be self-contained. If devices have a power requirement, it must come from battery power. It needs to require little or no maintenance or calibration, be dust-proof, be easily secured at night, and operate under variable environmental conditions. In addition, healthcare workers at this level are typically capable of only performing rudimentary dipstick or test strips. Also, test results must be easy to interpret so that misdiagnosis is avoided. In general, factors typically involved in influencing adoption of a diagnostic technology in low resource settings include¹⁵⁰:

- Cost of the device
- Degree of sensitivity and specificity
- Availability and cost of related equipment and supplies
- Level of user training needed for implementation

- Total time from sample collection to diagnosis
- Sample collection and processing requirements
- Equipment maintenance needs
- Infrastructure requirements (i.e. electricity and water)
- Performance under harsh environmental conditions
- Availability of effective therapies
- Management of hazardous waste

Although these factors are not limiting, a diagnostic that sufficiently addresses these factors will most likely perform well in low-resource settings.

Current Malaria Diagnostic Strategies

Traditionally, the “gold standard” for malarial detection has been microscopic examination of thick and/or thin blood films, where an experienced microscopist manually counts the number of parasites found per unit volume of blood (**Figure 36**).¹⁵¹ When performed at a “high standard”, light microscopy is capable of accurately identifying and quantifying *Plasmodium* parasites within a timely manner in a clinical setting.¹⁵² Unfortunately, the quality of light microscopy is often limited in the clinical setting due to the difficult preparation of Romanowsky-based stains, poorly maintained equipment, and undertrained personnel.^{153,154} Ultimately, the reliance on electricity and a skilled technician limit the utility of microscopy to only high and some mid-level health care facilities in developing countries. For example, a 2006 study in Kenya showed that routine microscopy by local health workers was 69% sensitive and 62% specific when compared to expert microscopy.¹⁵⁵

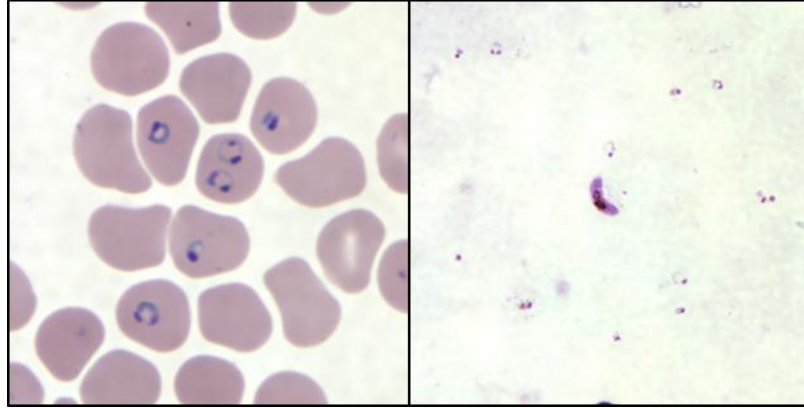


Figure 36. General light microscopy for *Plasmodium* detection. Left: A thin blood smear stained with Giemsa. Right: A thick blood smear. Images courtesy of the CDC.

Other diagnostic methods have also been developed, including fluorescence staining¹⁵⁶⁻¹⁵⁸, amperometric immunosensing¹⁵⁹, single and multiplexed PCR techniques¹⁶⁰, and enzyme-linked immunosorbent assays (ELISA) (**Table 5**).^{161,162} Each of these techniques is capable of either quantifying the parasite load or biomarker concentration with limits of detection below the WHO's recommended parasite load of < 100-200 parasites/ μ L. They are however, limited primarily to the laboratory due to their sensitivity to environmental changes, requirements for specialized reagents, slow developing time, reliance on sophisticated equipment for an interpretable readout, and the necessity of a skilled workforce to administer and interpret the diagnostic.

Table 5. Limits of detection for current malarial diagnostic strategies.

	Technique	Limit of Detection (parasites/ μ L)	References
Microscopy	Thick Film	5-20	151
	Thin Smear	50-200	151
Fluorescent Microscopy	Acridine Orange	100	156
	Quantitative Buffy Coat	100	157
Electrochemical Detection	Amperometric Immunosensor	< 100	159
PCR	18S rRNA and Circumsporozoite	< 5	160
ELISA	<i>pf</i> HRP-II	12	161
	Unified LDH and <i>pf</i> HRP-II	2	162
RDT	<i>pf</i> HRP-II	100	21

Immunochromatographic rapid diagnostic tests (RDTs) have been developed for the detection of malarial infection in low-resource setting over the last two decades.^{21,163,164} It is estimated that approximately 25 million malarial RDT's were produced globally in 2005.¹³⁷ These devices rely on detecting the *Plasmodium* antigens aldolase, lactate dehydrogenase (LDH) or *P. falciparum* specific Histidine-Rich Protein-II (*pf*HRP2) in blood obtained from a finger prick. This strategy generally works well for *P. falciparum* infection because ~97% of *pf*HRP-II is secreted as a soluble protein in the periphery of the red blood cell at picomolar to nanomolar concentrations during infection.¹⁶⁵ These devices operate by labeling the target antigen from patient blood with monoclonal antibodies conjugated with a liposome containing selenium dye or gold nanoparticles. A

nitrocellulose membrane strip coated with capture antibodies is then dipped into the sample solution. As the liquid travels up the test strip, the antibody-conjugated enzyme is captured by the antibodies on the strip, resulting in the formation of a visible band (Figure 37).²¹ The inclusion of a goat anti-mouse antibody on the test strip provides a positive band that ensures that lateral flow is achieved on the test strip.

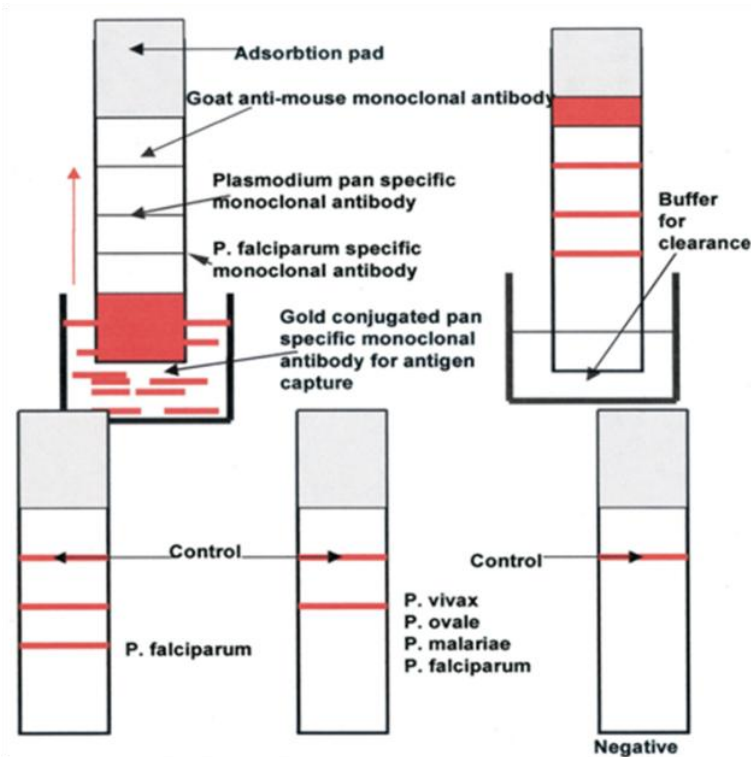


Figure 37. Dipstick malarial RDT mechanism of action.²¹ A.) The RDT is dipped into a solution containing a patient sample with gold conjugated monoclonal antibodies. The solution travels up the dipstick and passes over HRP2-specific antibodies, localizing the HRP-antibody-gold conjugate B.) A buffered solution is used to wash away any excess reaction solution. C.) The dipsticks are assessed for positive detection.

Although these techniques have performed at the same limits of detection as microscopy in laboratory testing (> 100 parasites/ μL), these techniques have not performed well when tested by the World Health Organization under high temperature (40°C) and humidity conditions (Figure 38).¹⁶⁶ In fact, of the 50 RDTs that qualified for

the study, only four had detection rates above 90% for the WHO recommended lower limit of detection of 200 parasites/ μL . This loss of sensitivity is likely due to the thermal instability of the antibodies under these conditions. In addition, many of the RDT manufactures are small companies and have traditionally had difficulty obtaining reference materials with well-characterized malarial patients and biological standards.¹⁴⁹ As a result, their ability to optimize their product and evaluate lot variability during manufacturing has been limited. One side effect of RDT variability is that health care workers at the mid and low-level health care facilities frequently ignore RDT results. This lack of confidence in the RDTs is further enhanced by ingrained treatment habits and pressure from patients and family members to treat sick patients.¹⁴² Without consistency, current RDTs will continue to be questioned by those who use them most prevalently in the field.

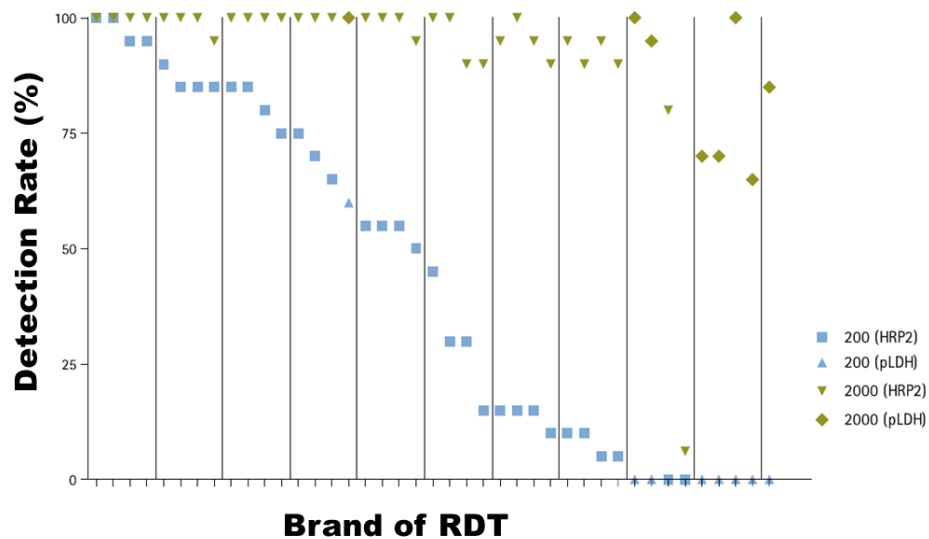


Figure 38. Malarial RDT detection rates as reported in the WHO’s Malaria Rapid Diagnostic Test Performance study of 2008-2009.² Each brand of RDT that qualified for the study was subjected to a high thermal (40°C) and high humidity (95%) incubations (2 months) prior to product testing. The RDTs were then tested against patients with low and high parasitemia (200 and 2000 parasites μL) respectively.

The Future of Malarial Low-Resource Diagnostics

Despite all of the challenges with drug and pesticide resistance¹³⁵, malaria transmission is generally declining for many of the affected regions of the world.¹⁶⁷ Because of these findings, the WHO is now recommending that all patients with symptomatic malarial infections be confirmed by parasite-based diagnosis before treatment is given. Accurate diagnosis of symptomatic patients is important to rule out those with other non-malarial febrile infections and reduce the rate of misdiagnosis. In addition, it is becoming more generally accepted by world health leaders that for malaria elimination to be achieved, identification and treatment of asymptomatic carriers of the parasite is essential.¹⁵² Current antigen-detecting RDTs are likely to miss a significant portion of asymptomatic cases in low-transmission settings.¹⁶⁸ To achieve these goals, new diagnostic strategies are needed that can detect very low levels of *Plasmodium* biomarkers in asymptomatic patients.

In addition, alternative patient sampling procedures may be needed for asymptomatic patients who won't be as willing to provide a blood sample for testing. Many societies have blood taboos that limit access to blood sampling as well.¹⁶⁹ Alternative sources of non-invasive patient sample will be required such as saliva, urine, or feces. For example, *pfHRP-II* has been detected in saliva and urine of infected patients, albeit at lower concentrations.^{169,170} One potential way to circumvent this challenge is to design a sample processing device that could purify and concentrate a large volume of patient sample (i.e. 1 mL) into a much smaller volume (i.e. 10 μ L) for diagnosis.

Considerable effort has also been put into designing portable battery operated microscopy techniques that utilize the camera capabilities of most current cellular

phones.¹⁷¹⁻¹⁷³ These devices could serve two purposes; (1) they could save diagnostic information, which could be collected and used in creating databases to determine where infections are most prevalent and (2) allow for the use of alternative diagnostic strategies that rely on complex analysis techniques (i.e. through the use of Smartphone applications) in places where it may have not been possible in the past. Despite their sophisticated hardware and software capabilities, the rapidly growing consumer use of cell phones is driving down the cost of their manufacture and implementation, making them an attractive potential component to low-resource diagnostic strategies in the next decade.

Dissertation Aims for the Development of Malaria Diagnostics

The following chapters highlight our efforts towards designing reagents to assist in improving malaria diagnosis in the field. **Chapter V** highlights a malarial sample processing technology that utilizes surface tension valuing capable of purifying and concentrating *p*fHRP-II from plasma and whole blood, which could lower the limits of detection into the asymptomatic regime necessary for malarial elimination strategies. **Chapter VI** introduces a novel coffee-ring based diagnostic platform that utilizes an antibody-free ELISA-inspired capture strategy for the detection of *p*fHRP-II.

CHAPTER V

DEVELOPMENT OF A LOW RESOURCE PURIFICATION PLATFORM FOR PLASMODIUM FALCIPARUM HISTIDINE-RICH PROTIEN-II USING SURFACE TENSION VALVES

Introduction

As global health organizations begin to focus on worldwide malarial elimination, diagnostic strategies need to be able to not only accurately diagnose symptomatic patients in low resource settings, but also be able to identify asymptomatic carriers as well. With limits of detection > 100 parasites/ μL , current lateral flow RDTs are fundamentally limited to detecting only symptomatic cases. Two possible solutions arise: (1) design a novel diagnostic platform that has lower limits of detection and/or (2) design a sample processing device capable of concentrating and purifying the biomarker of interest. Ideally, a novel platform would be capable of achieving both goals, while maintaining the simplicity of use and relative ease of interpretation seen with the current diagnostic strategies.

When considering a novel diagnostic strategy, it is important to consider the limitations faced in low resource settings. For example, complex biological media contains high concentrations of solutes (i.e. salts and proteins) that can specifically or non-specifically interfere with diagnostic reagents. For example, human whole blood consists of 45% erythrocytes and 3.5-4.5% soluble protein. If red blood cells lysis is necessary to collect more biomarker (as is the case for malarial detection using *p*fHRP-

II), then ~5 mM hemoglobin is released into the biological solution. Hemoglobin has a strong visible absorption at 414 nm from the Soret band of heme, giving blood its dark red color. If a colorimetric readout is desired for accurate detection, such as in the commercially available malaria RDTs, then elimination of biological noise is desired. These RDTs remove biological noise by continuous lateral flow, where the biomarker is captured and labeled on the nitrocellulose test strip. For alternative diagnostic strategies however, new methods of sample processing are desired.

Recently, it has been demonstrated that biomarkers such as RNA can be purified from complex mixtures using oil-liquid interfaces.¹⁷⁴⁻¹⁷⁶ The oil interface provides a barrier between the complex reaction solution and the elution chamber, preventing mixing of the chambers. Using a functionalized magnetic particle, the biomarker of interest can be specifically captured by the particles and transferred through the oil interface to an elution chamber, with minimal contamination from the biological sample solution. In general, these devices rely on the dominance of surface tension over gravity at the microscale to keep oil and aqueous phases indefinitely separated. This enables sequential loading of aqueous chambers separated by an oil interface (or valve), which is not disrupted by gravitational effects.

As noted in **Chapter IV**, one of the principle targets for *Plasmodium falciparum* malaria RDT's is *pfHRP-II*, a 67kDa protein dimer that contains histidines assembled in multiple repeats of AHH (51 total) and AHHAAD, which comprise ~85% of the total amino acids.¹⁷⁷ It is an attractive biomarker for current malarial rapid diagnostic tests (RDTs), because 97% of the protein is released into the host's blood during red blood cell rupture.¹⁷⁸ *In vitro*, *pfHRP-II* coordinates as many as 50 heme molecules per dimer

through bis-histidine axial ligation.¹⁷⁹ Ni(II) and Zn(II)NTA agarose affinity columns have been used to selectively isolate *pf*HRP-II from blood or serum samples containing human serum albumin, transferrin, α 2-macroglobulin, and histidine-rich glycoprotein.^{177,180}

Ni(II) nitrilotriacetic acid (NTA) chelation has become a widely adopted technology for the isolation and purification of hexahistidine-tagged recombinant proteins.¹⁸⁰⁻¹⁸² One advantage of Ni(II)NTA chelation is its high affinity to histidine, with an approximate dissociation constant (K_d) in the micromolar range.¹⁸³ Chelation occurs between the imidazole side chain of histidine and one of the two available coordination sites of Ni(II) (**Figure 39**). In addition, other divalent metals such as Co(II), Zn(II), and Cu(II) can also be used as chelators to histidine.^{177,184} Consequently, *pf*HRP-II represents an attractive target for Ni(II)NTA chelation within a complex biological mixture.

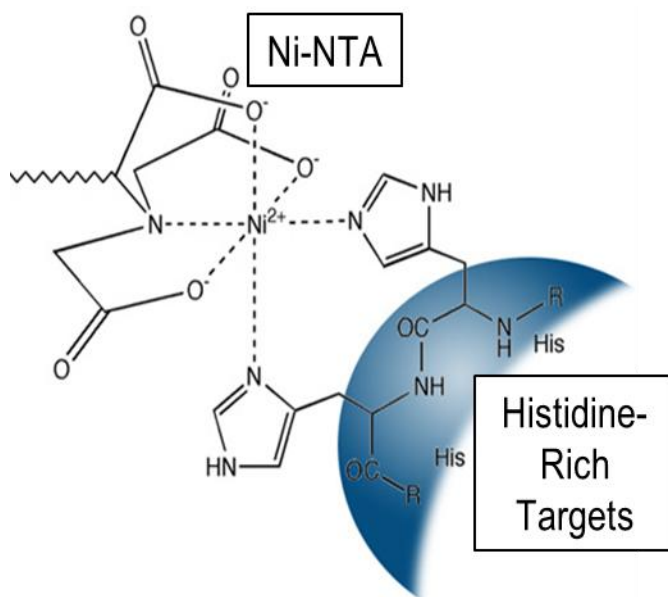


Figure 39. Coordination of histidine-rich targets to Ni(II)NTA ligands. NTA is a tetradentate ligand that coordinates with four of the six available binding sites on Ni(II) or other divalent transition metals. The remaining two binding sites are hydrated until they coordinate with the side chains of histidine.

In low resource settings, stability of reagents is a significant concern in the design of any diagnostic device component. For that reason, processing platforms are desired that do not require any biochemical or enzymatic reactions. Instead chemical and physical processes, such as Ni(II)NTA chelation, must be highlighted in an extraction cassette. This sample processing technology is designed to be a sample collection, concentration and preparation component for integration with downstream detection components to form a general diagnostic platform suitable for low resource environments. This chapter highlights the development of a low resource extraction device that isolates *p*/HRP-II from complex solutions using surface tension valves. The device utilizes the histidine-specific chelation properties of Ni(II)NTA magnetic agarose beads to selectively capture *p*/HRP-II, isolate and purify using the separation properties of surface tension valves. The protein-bead conjugate is then delivered to a small volume elution solution, which serves to release and concentrate the protein. This device aims to improve the overall limit of detection of diagnosis, irregardless of the downstream diagnostic strategy. The extraction and concentration efficiency was demonstrated in simple (buffer) and complex (serum and whole blood) solutions and quantified using ELISA. The purity of the protein from biological interferents such as histidine-rich glycoprotein and hemoglobin were also analyzed.

Experimental

Materials and Reagents: Ni-NTA Magnetic Agarose Beads (Cat # 36111) were purchased from Qiagen Inc. Human Whole Blood (A+) collected in Na Heparin (Cat # HB1050), Human Plasma (A+) collected in CPD (Cat # HP1013), and whole Human Red

Blood Cells (A+) collected in CPD (Cat # HP1002A) were all purchased from Valley Biomedical Inc. Human Histidine Rich Glycoprotein ELISA kit (Cat # SEK10836) was purchased from Sino Biological Inc. Antibodies used in the *pf*HRP-II ELISA assay (Cat # ab9206 and ab30384) were purchased from Abcam Inc. TMB One solution (Cat # G7431) was purchased from Promega Corporation. D6 strain of *P. falciparum* malarial cultures were graciously provided by WRAIR. Recombinant HRP-II (Cat # AGPF-55) was purchased from Immunology Consultants Laboratory Inc. A 2" x 1" x ¼" neodymium magnet used in this study was purchased from Emovendo LLC. All other reagents were purchased from Sigma Aldrich Inc. or Fisher Scientific Inc.

Culturing of Malarial Parasites: The D6 strain of *P. falciparum* obtained from WRAIR was cultured in A+ blood following the protocol described by Trager and Jenson.¹⁸⁵ When cultures reached a parasitemia > 5%, they were counted and frozen @ -80°C until further use. For limit of detection studies, cultures were synchronized to >95% rings using the method described by Lambros and Vanderberg.¹⁸⁶ *pf*HRP-II content of the cultures was quantified by ELISA using the recombinant HRP-II as a standard.

Design and Preparation of the Extraction Device: The extraction device was first prepared by cutting 1/16 inch inner diameter 1/32 inch thickness Tygon® tubing (Fisher Scientific, Cat # 14-169-1B) into 12 inch length pieces. Next, a PCR eppendorf tube was prepared by first puncturing a hole using a 27 ½ gage syringe needle in the top of the lid to serve as an air valve. The bottom of the tube was cut off (~1-2 mm) using a razor, leaving a hole for access to the Tygon tube. This tube was then placed into the Tygon tubing. To the opposite end of the Tygon tube, a 10 µL solution of elution buffer (0.1 M phosphate buffer, pH 8.0, 300 mM NaCl, 500 mM imidazole, 0.05% Tween 20) was

added to the tube using a gel tip. The end of the tube was then sealed with the closed end of a melting temperature tube. Next, starting at the elution buffer end of the tube, valves (50 μ L of mineral oil) and chambers (100 μ L of 0.1M phosphate buffer, pH 8.0, 300 mM NaCl, variable concentrations of imidazole, and 0.05% Tween 20) are sequentially added to the device using a 27 $\frac{1}{2}$ gauge syringe. Note: in older versions of the device, the loading chamber, wash chamber composition, and elution chamber will vary and will be noted in the text.

Extraction Protocol of Samples: The extraction of samples was performed by first incubating the sample of interest (100 μ L) with a 100 μ L solution of 2x lysis buffer containing a final concentration of 0.1 M phosphate buffer, pH 8.0, 300 mM NaCl, variable concentrations of imidazole, and 1% Triton X-100 for 1 min in the PCR tube connected to the Tygon tubing. Next, a 10 μ L solution of Ni(II)NTA magnetic agarose beads (from stock, 9×10^{-18} M beads) were added and protein binding was allowed to proceed while the sample was tumbling on a rotating rotisserie to ensure the beads remained suspended. After incubation, the agarose beads were collected using a donut magnet (250-300 mT in the center) and transferred into the first wash chamber. The beads were then diffused within the chamber for ~30 seconds and recollected before travelling into the next chamber. The overall time the samples remained in each wash chamber was ~1 min. This process was repeated until the beads reached the final chamber, where they were mixed manually for 10 minutes to ensure all protein was eluted from the beads. After elution, the magnetic beads were transported back into the adjacent oil valve and each chamber was cut out using a razor, collected in eppendorf

tubes and quantified for protein content. Note: in earlier studies, the extraction procedure will vary and will be noted in the text.

ELISA Quantification of *pf*HRP-II: A 100 μ L solution of IgM anti-HRP-II (ab9206) in 1x PBS (1 μ g/mL) was added to each well of an Immulon 2 HB 96-flat well plate and either incubated for 1 hour at room temperature or sealed with Para film and stored @ 4°C overnight. After incubation, the wells were washed three times with 1x PBS containing 0.1% Tween 20 (PBST). Next, a 300 μ L solution of PBST containing 5% BSA (by weight) was added to each of the wells and incubated at room temperature for 1 hour. After washing 3x with PBST, 100 μ L aliquots of diluted sample and controls in PBST with 0.1% BSA were added and incubated for 2 hours at room temperature. Note: the working range of the assay is 0-25 pM *pf*HRP-II. After washing the plate 5x w/ PBST, a 100 μ L solution (0.5 μ g/mL) containing IgG anti-HRP-II with HRP (ab30384) in PBST with 0.5% BSA was added and incubated at room temperature for 1 hour while protected from light. The plate was then washed 5x w/ PBST and a 100 μ L solution of TMB One solution was added and incubated for 20 minutes at room temperature under reduced light. The reaction was then quenched upon the addition of a 100 μ L solution of 2M H₂SO₄. The plate was then measured spectrophotometrically at 450 nm using a Bio-Tek Synergy HT multi-detection microplate reader.

ELISA Quantification of HRG: ELISA plates and samples were prepared according to the kit procedures provided by Sino Biological with a few modifications. After loading the detection antibody and washing, analysis was performed by adding 100 μ L of the TMB One solution and incubating at room temperature under reduced light for 20

minutes. The reaction was quenched upon the addition of 100 μL of 2M H_2SO_4 and the plate was measured spectrophotometrically at 450 nm.

Hemoglobin Quantification: Hemoglobin concentrations were quantified by collecting reaction samples, measuring their absorbance at 414 nm, and calculating their concentrations by the molar extinction coefficient of hemoglobin. Note: the molar extinction coefficient of hemoglobin is $524,280 \text{ cm}^{-1} \cdot \text{M}^{-1}$.

Whole Protein Gel Analysis: Protein content of the chambers was evaluated using SDS-PAGE gels either stained with Coomassie or silver stained. For silver staining, the gel was removed from its cassette and fixed for 1 hr in fix solution (50% MeOH, 12% acetic acid, and 0.0185% paraformaldehyde). Next, the gel was washed three times for 8 minutes with 50% MeOH. After washing, the gel was incubated for 1 min in pretreatment solution (0.02% $\text{Na}_2\text{S}_2\text{O}_3$) and washed three times for 20 seconds in water. The water was decanted, and the silver stain solution (0.2% AgNO_3) was added and incubated with the gel for 20 min. After incubation, the silver stain was removed and the gel wash washed three times for 20 seconds in water. Next, the development solution (6% Na_2CO_3 , 0.0004% $\text{Na}_2\text{S}_2\text{O}_3$, 0.0135% paraformaldehyde) was added and mixed with the gel until proper resolution was achieved. After incubation, the development solution was removed and the stop solution (50% MeOH and 12% acetic acid) was added. The gel was washed with water and analyzed for protein content.

Results

The proposed self-contained processing device captures *p*fHRP-II from complex biological matrices on the surface of a Ni(II)NTA magnetic agarose capture beads. These

beads then carry the biomarker through sequential washing solutions to reduce biological interferences and also concentrate the sample for improved diagnostic performance. The proposed device has several advantages: it (1) requires little or no power, (2) can be made suitable for an unskilled user, (3) have rapid time-to-extraction, (4) be low cost, and (5) be adaptable to multiple downstream detection designs. Currently, there is no known available low resource point-of-care extraction device that has the same level of simplicity, convenience, low cost and ease-of-use. Although the detector constraints downstream of the proposed component are undetermined, in general, detection of biomarkers of infection in patient samples is more easily achieved with a higher concentration of diagnostic biomarkers of interest and a lower concentration of interferences.

Extraction Device Design and Physical Properties

In the generic extraction device outlined in **Figure 40**, surface tension valves are created when alternating solutions of processing buffer and oil are added to Tygon tubing. The oil “valves” serve as an immiscible phase filter between buffer “chambers”, which prevent mixing of the chambers. Each chamber can be composed of an aqueous buffer solution, where purification is achieved by simply processing the sample through the chambers in the presence of a magnetic field using magnetic capture beads. The chambers can also contain unique reagents, which allow for various processing steps to be conducted sequentially with minimal contamination from previous chambers. This extraction process requires two components: (1) a magnetic capture bead capable of binding an antigen of interest and traversing through the oil valve and (2) a magnet with a

strong enough magnetic field to overcome the surface tension of the oil/water interface. The modularity of this design allows for the addition of a sample preparation chamber and an elution chamber. Depending on the application, these chambers can also be added to the extraction device to create an all-in-one sample preparation device or diagnostic.

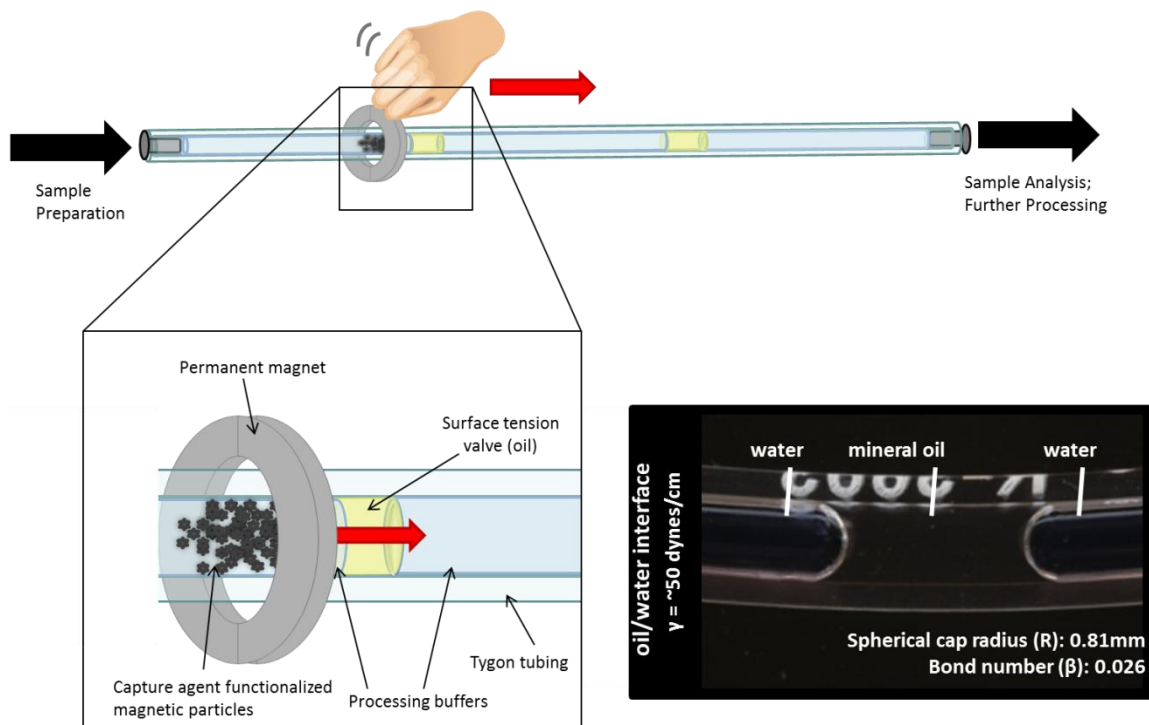


Figure 40. General extraction device design using surface tension valves. Samples are prepared either prior to processing or pre-loaded into a sample preparation chamber. Processing is achieved through magnetic capture beads that are processed through wash chambers separated by oil valves. After processing, the samples are collected either in a final chamber or outside of the device for analysis or further processing. Bottom right: Visual image of the water/oil interface and quantification of surface tension properties.

The surface tension in the small diameter tubing holds each of the solutions in place, and individual solutions remain largely undisturbed when the magnetic beads pass through the oil valves from one aqueous chamber to the next. The stability of the valve can be described by a physical property called the Bond number (β).¹⁸⁷ Bond number is a

measure of the importance of surface tension forces compared to body forces. It is described by the following formula:

$$\beta = \Delta\rho g R^2 / \gamma \quad (1)$$

where β is the bond number, ρ is density, g is the gravitational force constant, R is the spherical cap radius, and γ is the surface tension. A large Bond number indicates that the system is relatively unaffected by surface tension effects; a low number (typically less than one is the requirement) indicates that surface tension dominates. Intermediate numbers indicate a non-trivial balance between the two effects. As noted in **Figure 40**, the calculated Bond number for an oil/water interface in 1/16" inner diameter Tygon tubing has been calculated to be 0.026, which indicates that surface tension between the water and the oil dominates over gravitational forces. Contact angle $163.7 \pm 3.5^\circ$. Therefore, the valves should be stable under these conditions.

A second important measure of valve stability is defined by the capillary force on the valve. Capillary force is related to stability because solutions in the extraction cassettes must overcome the accelerative forces of handling to resist mixing. The capillary force is defined as¹⁸⁸:

$$F = 2\pi r \gamma \cos\theta \quad (2)$$

where F is the capillary force, r is the radius of the tube, γ is the surface or interfacial tension, and θ is the contact angle of the solution with the tube wall. With an experimentally determined contact angle of $163.7 \pm 3.5^\circ$, the capillary force was calculated to be -0.242 mN, indicating that the interface is stable and subsequently resistant to mixing.

Although it has been determined that the oil/water interface is stable enough to be maintained in the tubing, it is not clear whether magnetic beads can successfully travel through the valves while maintaining the integrity of the valve. The process of entering and exiting an oil valve was analyzed for Ni(II)NTA-functionalized magnetic agarose beads (**Figure 41**). Visualization was performed by placing the tubing in glycerol and taking still-shots as the beads traverse through the surface tension valves. As the beads in the aqueous chamber approach the interface by magnetic movement, they begin to disrupt the surface tension of the valve. The particles begin to protrude beyond the interface and continue to travel on the tubing surface. The surface tension of the valve is eventually overcome and the valve retracts back to its original shape, releasing the beads into the oil valve. The beads remain hydrated, carrying a small volume of water with them in the valve. Although this does introduce some non-specific carryover of contaminating solutes and proteins, it is likely necessary that the bead-protein conjugate remains solubilized to retain the structural integrity of the protein for downstream diagnosis. As the beads in the oil valve make contact with the oil/water interface, the surface tension is again disrupted, and the water chamber “absorbs” the hydrated beads. After the beads are within the original dimensions of the aqueous chamber, the interface retracts back into its original shape. Although the process of entering and exiting the valves initially disrupts the oil/water interface, as long as the oil valve is sufficiently long enough that the two water chambers don’t make contact, the interfaces remain stable and return to their original conformation.

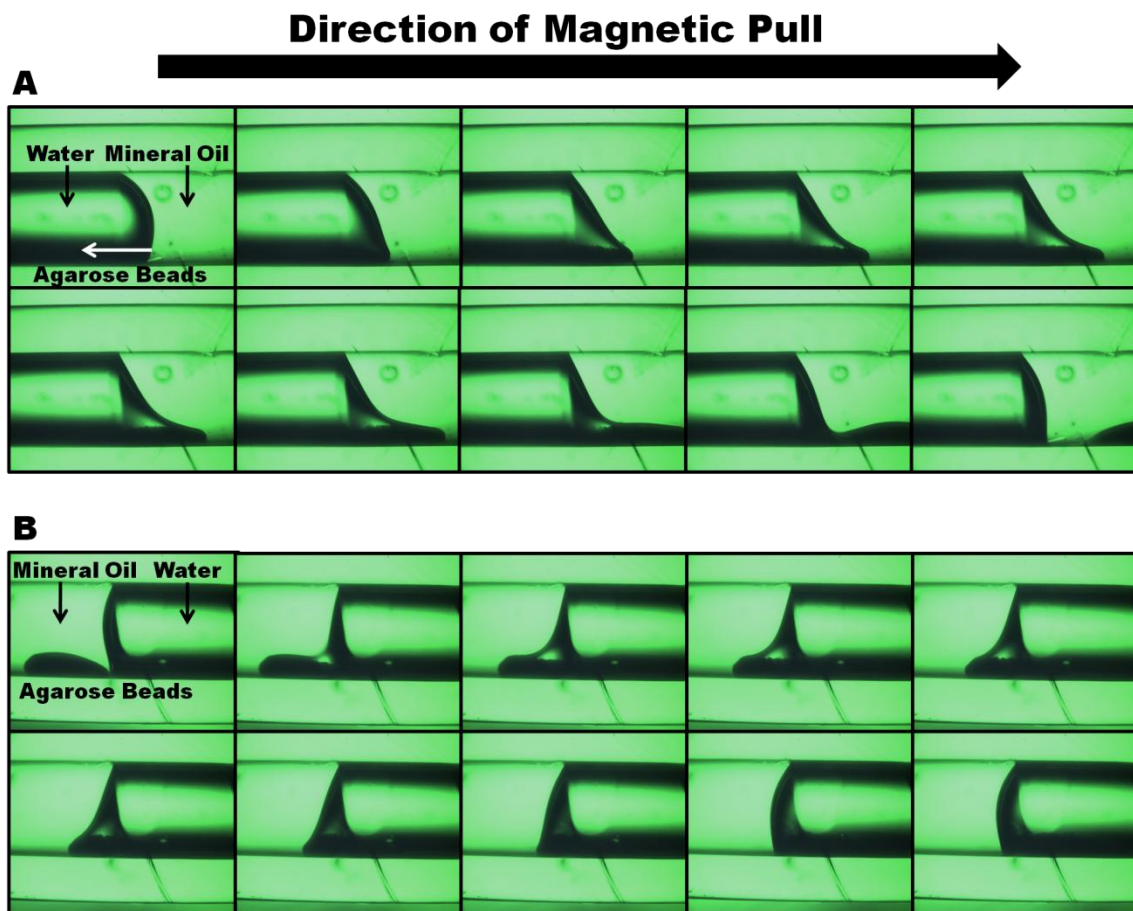


Figure 41. Bead transport through water/oil interface. A. Ni(II)NTA magnetic agarose beads are pulled through an aqueous reaction chamber into an oil valve. B. Beads as they approach and enter an adjacent water chamber after transport through an oil valve. Images provided by Catherine Majors.

We assume that the force required to transfer a functionalized bead or cloud of beads across a surface tension valve is related to the capillary force acting on the beads. This relevant force is analogous to the maximum attractive force of a sphere exiting a liquid surface through a liquid bridge. This force can be calculated by the following formula¹⁸⁹:

$$F=4\pi r\gamma\cos\theta \quad (3)$$

where γ is the surface or interfacial tension, θ is the contact angle of the solution with the particle surface, and r is the radius of the bead. Ni(II)NTA agarose beads have an average

radius of 25 μm , the surface tension at the interface is 0.05 J/m^2 , and a contact angle of at the surface of water on the magnetic agarose bead is approximately 164° if we assume that Tygon has a contact angle to the agarose surface. The capillary force acting on a single bead is $\sim 15 \text{ }\mu\text{N}$. Interestingly, these beads do not readily travel through air valves, in contrast to the silica beads used during RNA processing.¹⁷⁶ Based on the formula above, it is likely the size of the bead that inhibits them from travelling through the air interface.

The surface tension of the valve can be disrupted by the addition of surfactants such as Tween 20 and Triton X-100. Both of these surfactants are necessary with this system because Tween prevents that agarose beads from sticking the sides of the Tygon tube, and Triton is used to lyse the red blood cells. From our observations throughout this study, it appears that the addition of these surfactants does not significantly disrupt the valves, and the valves maintain their integrity throughout sample processing. This observation was also noted by Berry et al for their RNA processing strategy.¹⁷⁵

The Ni(II)NTA magnetic agarose beads used for these studies are $\sim 50 \text{ }\mu\text{m}$ in diameter (20-70 range), have a concentration of $\sim 760 \text{ beads}/\mu\text{L}$ at stock concentration, and have an estimated binding capacity of $2 \text{ }\mu\text{g}$ of His-tagged protein per μL of stock solution of beads. This corresponds to $\sim 10 \text{ pmol}$ of bound protein per μL of beads for a 24 kDa His-tagged protein. Based on estimates determined from the referenced literature^{161,162,190-192}, the upper parasite load (i.e. $2000 \text{ parasites}/\mu\text{L}$) contains $\sim 1 \text{ nmol/L}$ *pf*HRP-II, or 0.1 picomoles per $100 \text{ }\mu\text{L}$ of parasite sample. Based on these calculations, the magnetic agarose beads, if added 1:100 to the sample, will be in 100-fold excess in terms of loading capacity. It is recommended however that $10 \text{ }\mu\text{L}$ of stock agarose bead

suspension be used per assay due to their settling velocity and size. Therefore, under all physiologically relevant conditions, the agarose beads will be in binding excess relative to *pf*HRP-II. In addition, the concentration of beads in a typical reaction (210 μ L) will be ~36 beads/ μ L.

Optimization of Sample Processing Parameters

Initial studies focused on whether the oil valves would allow for the successful processing and recovery of the targets. Recovery of a peptide mimic of *pf*HRP-II was first investigated. The synthetic analog is a linear 27 amino acid containing three repeat motifs of AHHAHHAAD, and functionalized with an N-terminal TAMRA moiety. Initial experiments focused on comparing sample isolation between a standard eppendorf tube protocol and the extraction device. Extractions and controls were performed by first incubating a 90 μ L solution of TAMRA-HRP-II (10 μ M) in PBS with 0.025% Tween 20 (PBST) with 10 μ L of Ni(II)NTA agarose beads. After 10 minutes of incubation on a rotisserie, the samples were either washed 3x with PBST in the tubes (controls) or processed through the extraction device (containing 5 chambers, 3 with PBST and 2 sequential elution chambers containing PBST and 500 mM imidazole). **Figure 42** shows the isolation efficiency of both methods. In both methods, over 50% of the protein is accounted for in the elution chamber. There is also no peptide detected in the post-elution chamber, suggesting that the elution time in the primary elution chamber is sufficient to collect all of the peptide from the beads. Extraction efficiency was also tested in the presence of 100 μ g/mL of fluorescein-labeled BSA. Extraction efficiencies are essentially maintained in the presence of the biological interferent. In addition, the amount of BSA

collected in the elution chamber is < 10% even in a non-blocking solution, suggesting that TAMRA-HRP-II binds preferentially over fluorescein-BSA.

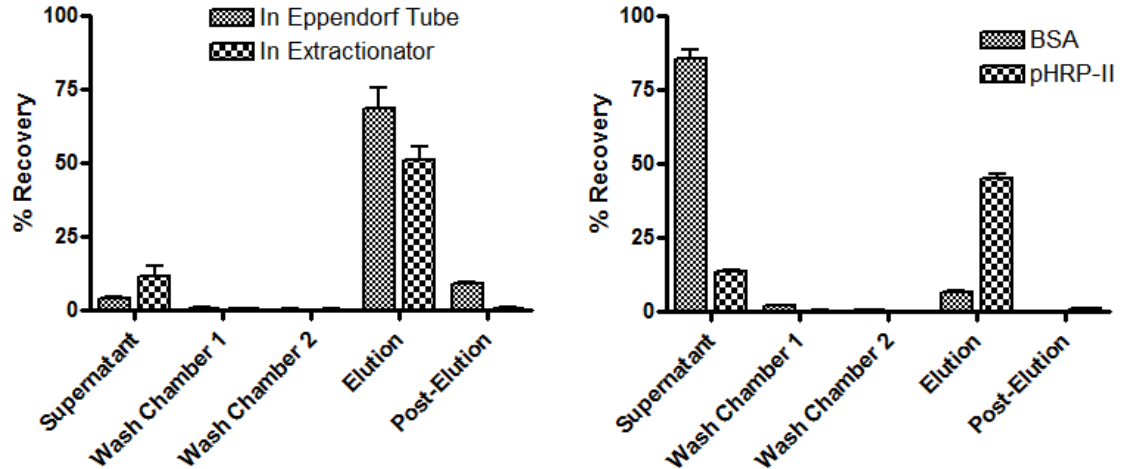


Figure 42. Extraction efficiencies of TAMRA-HRP-II using the extraction device. Left: Extraction efficiency of the peptide in eppendorf tubing and the extraction device. Right: Extraction efficiency in the presence of a biological interferent.

Inspired by these promising results, extractions were performed against unsynchronized malaria parasite culture. A stock of freeze-thawed lysed culture (0.1% parasitemia, 3.25 nM *pf*HRP-II) diluted in water was extracted using the method described in the previous paragraph, but with the wash chambers containing 200 mM imidazole (It was determined that this is the maximum concentration before competitive blocking occurs). After 30 minutes of incubation, the sample was processed through the device and the wash chambers and elution were collected. It should be noted that the elution of the protein was achieved by transferring the beads out of the tubing into an eppendorf tube containing 100 μ L of elution buffer (Prototype design highlighted in **Figure 43**). ELISA analysis of the chambers determined that ~75% of *pf*HRP-II can be found in the elution chamber (**Figure 43**, left). In addition, analysis using a commercial

RDT against *pf*HRP-II kit confirms that a majority of the protein is located in the elution chamber.

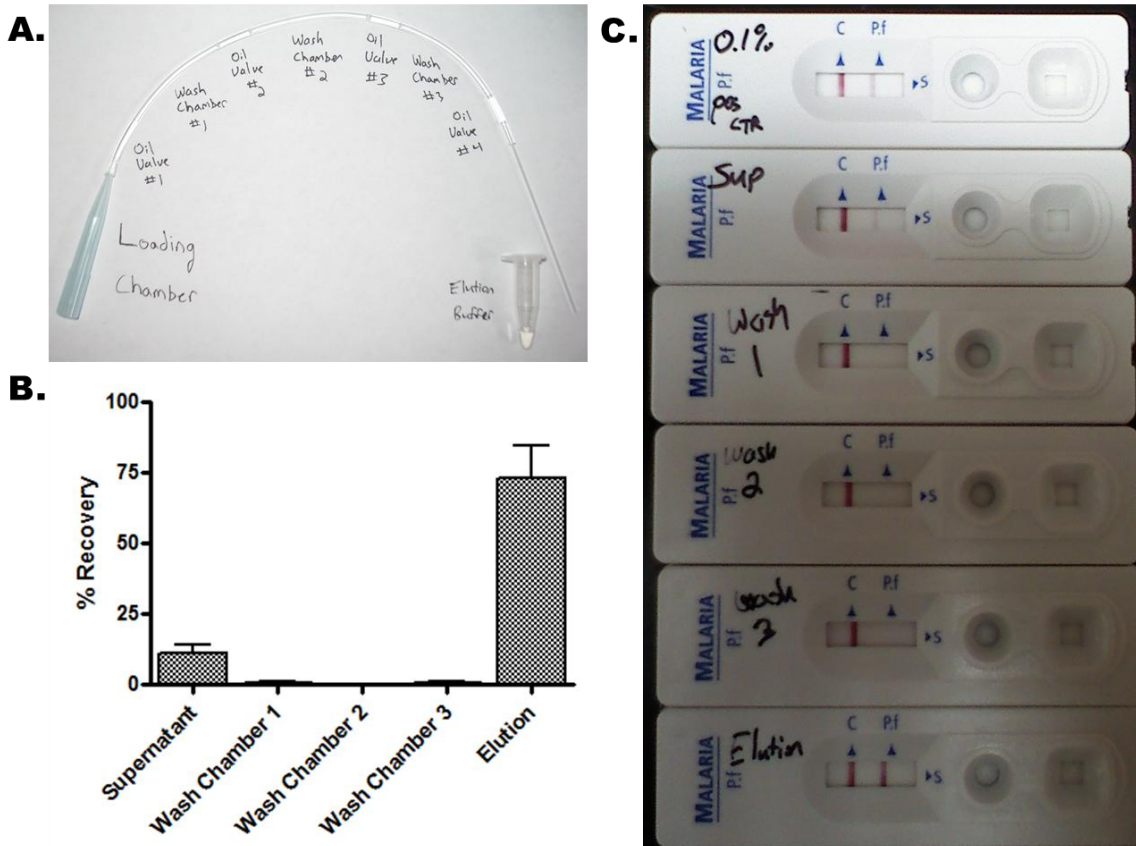


Figure 43. Early device design and extraction efficiencies of *pf*HRP-II from culture. A. Device design used in this study. The sample is reacted in an eppendorf tube prior to loading into the loading chamber. This chamber is capable of handling samples as large as 1 mL. Three wash chambers are separated by mineral oil valves. The elution buffer is independent of the device, allowing for simple handling. B. Extraction efficiency of *pf*HRP-II from culture. C. Representative RDT testing of the chambers of the device after processing.

Although promising, sample processing time must be minimized to for a rapid diagnostic device. In addition, it is still not clear whether extraction efficiencies are maintained in the presence of complex biological samples. Extractions were performed by spiking 0.04% parasitemia unsynchronized culture (1.3 nM *pf*HRP-II) into 50% plasma and 50% whole red blood cells. For these studies, a lysis buffer containing 1%

Triton X-100 was used to lyse the red blood cells prior to processing. Protein recovery in the elution solution was $89.7 \pm 5.0\%$ for plasma and $83.7 \pm 6.2\%$ for red blood cells after 30 minutes of incubation (**Figure 44**). At 10 minutes, recovery was a respectable $60.2 \pm 1.4\%$ for plasma and $47.6 \pm 1.6\%$ for red blood cells. In addition, silver staining of an SDS-PAGE gel of the blood incubated for 30 minutes indicates that there is minimal contamination of interfering proteins in the elution chambers, highlighting the purification capabilities of this extraction process.

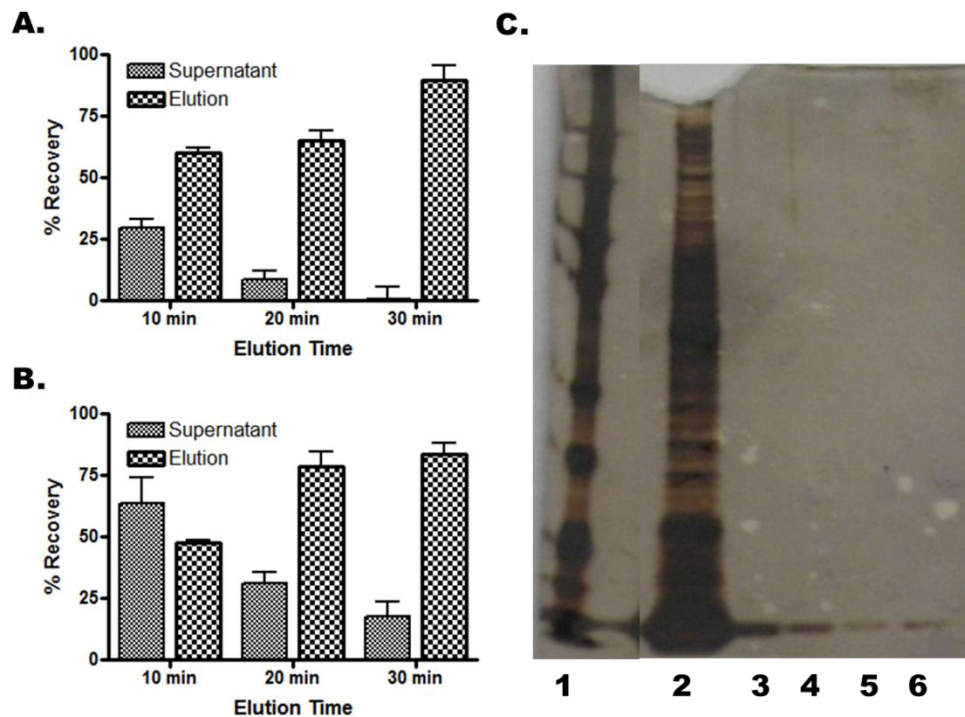


Figure 44. Extraction efficiencies in complex biological media at variable times. A. Extractions performed in 50% human plasma. B. Extractions performed in 50% lysed red blood cells. C. Silver stained gel extractions performed in 50% lysed red blood for 30 minutes. Lane 1: ladder. Lane 2: Sample loading chamber. Lanes 3-5: Sequential wash chambers. Lane 6: Elution solution.

One of the advantages of this device is the ability to modify chamber size and composition without drastically affecting the fundamental properties of the surface tension valving. Previous work utilized a loading and elution chamber that was

disconnected from the processing chambers. In a low resource setting, sample processing must be streamlined and simplified for ease of use. To address these needs, the sample and elution chambers were modified in such a way that they were contained in an all-in-one device. In addition, the device design allows for the introduction of a much smaller elution chamber capable of significantly concentrating the antigen. It is not clear however, how elution within the device in a smaller volume affects the yield. **Figure 45** highlights the recovery capabilities of the all-in-one device. Ni(II)NTA magnetic agarose beads were pre-loaded with recombinant HRP-II and processed through the chambers into variable sized elution chambers. Changing the elution chamber volume didn't affect the overall protein yield, and the smaller elution chamber (10 μ L) concentrated the sample nearly 10-fold. In addition, it was experimentally determined that elution of the protein from beads in a 10 μ L elution chamber with manual magnetic mixing yields significant protein after 2 minutes and most after 5 minutes.

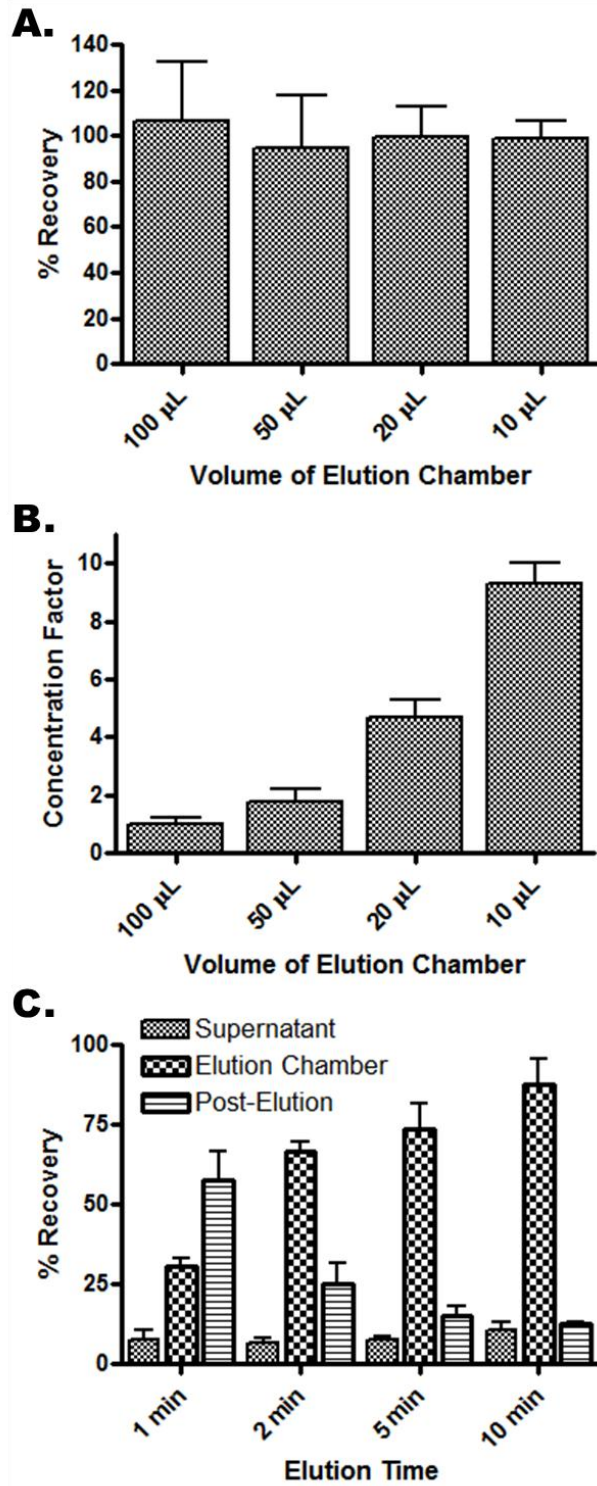


Figure 45. Effect of elution chambers volume on recovery. A. Overall relative yield of HRP-II as an $f(x)$ of elution volume. B. Effective concentration factor of the smaller elution chamber volumes. C. Time study to determine the optimal elution time with manual processing for a 10 μ L elution chamber.

Evaluation of the Current Extraction Design

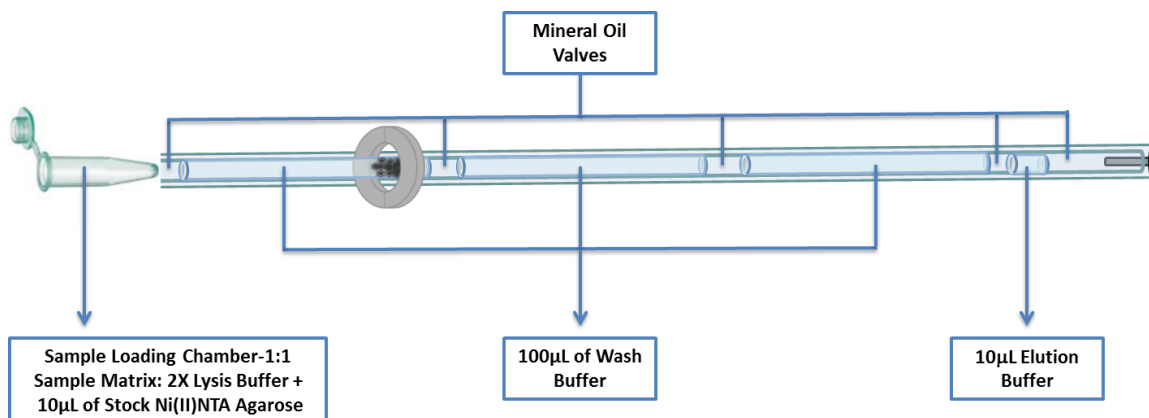


Figure 46. Self-contained sample processing design.

Using all of the information gathered with the early prototypes designed above, the current extraction design format is outlined in **Figure 46**. This design consists of 5 aqueous chambers separated by four mineral oil valves. The loading chamber contains a whole blood lysis buffer and imidazole to prevent any interfering protein interactions with the Ni(II)NTA agarose beads. The middle three chambers contain buffer with blocking concentrations of imidazole to prevent any binding of protein caught in the carryover volume of the beads. The final elution chamber has a high concentration of imidazole to ensure efficient elution of *pf*HRP-II. This chamber volume is minimized to concentrate the sample. The remaining studies all use the extraction protocol as described in the experimental section.

To determine the optimal imidazole blocking conditions, the binding efficiency of *pf*HRP-II was determined in the presence of varying concentrations of imidazole. **Figure 47** shows the loading efficiency of 1 nM *pf*HRP-II from unsynchronized parasite culture

in the presence of imidazole after 30 minutes of incubation. Binding of *pf*HRP-II to the Ni(II)NTA magnetic agarose beads is not affected significantly until ~150 mM imidazole is present in solution. Complete blocking of *pf*HRP-II is achieved at concentrations above 300 mM. Thus, optimal *pf*HRP-II binding can be achieved in conditions where the imidazole concentration is < 150 mM.

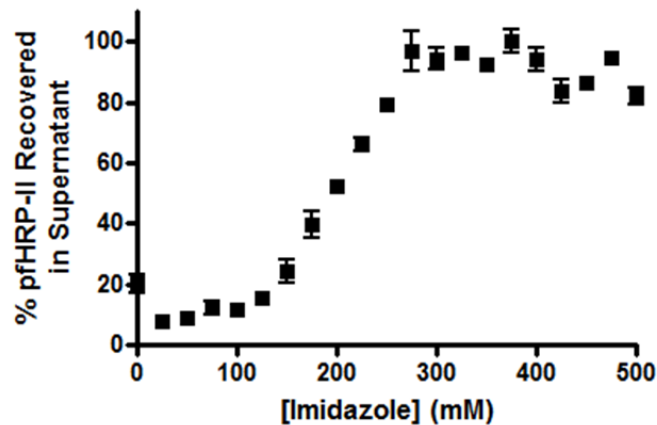


Figure 47. Imidazole binding study to determine the optimal blocking conditions

Extraction efficiency studies were performed under 125 mM imidazole blocking conditions with 10 minute incubation times at physiologically relevant concentrations in buffer, plasma, and pre-lysed whole blood. **Figure 48** highlights the *pf*HRP-II yields determined under these conditions. Under all conditions, there was a 3-4.5 fold concentration of *pf*HRP-II in the elution chamber. At 1000 pM, which corresponds to the WHO upper range of infectivity, both the buffer and plasma samples have similar recoveries, while the whole blood sample has a 3-fold concentration in signal. At 100 pM, plasma yields were similar to those at the higher concentrations, but there was a slight decrease in yield for the buffer and whole blood samples.

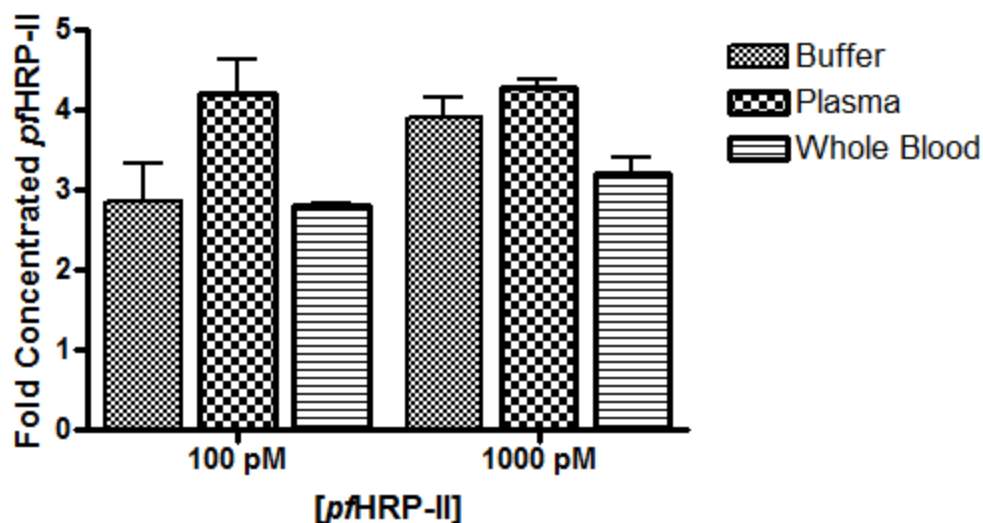


Figure 48. Comparison of extraction efficiencies of physiologically relevant concentrations of *pf*HRP-II in buffer, plasma and human whole blood.

HRG is known to have a relatively strong affinity to Ni(II)NTA, and is commonly purified from plasma using Ni(II)NTA agarose purification strategies.¹⁹³ Human plasma is reported to contain 100-200 $\mu\text{g/mL}$ of HRG, which corresponds to 1.3-2.7 μM .¹⁹⁴ Blocking studies with human plasma were performed between 125-200 mM imidazole in eppendorf tubes to determine if there was any binding overlap between HRG and *pf*HRP-II. Ni(II)NTA agarose beads were incubated with human serum for 30 minutes to allow for equilibrium to be established between free and bound HRG. After copious washing of the beads with wash buffer to remove any solubilized HRG, the remaining HRG was eluted in the presence of 500 mM imidazole and quantified using ELISA (**Figure 49**). At 125 and 150 mM imidazole, significant amounts of HRG (~25% and ~6% of the total amount found in undiluted plasma, respectively) were recovered when eluted off of the agarose beads. At 175 mM imidazole, there is still ~0.25% of total HRG found bound to

the beads. Almost complete specific blocking of HRG was achieved at 200 mM imidazole.

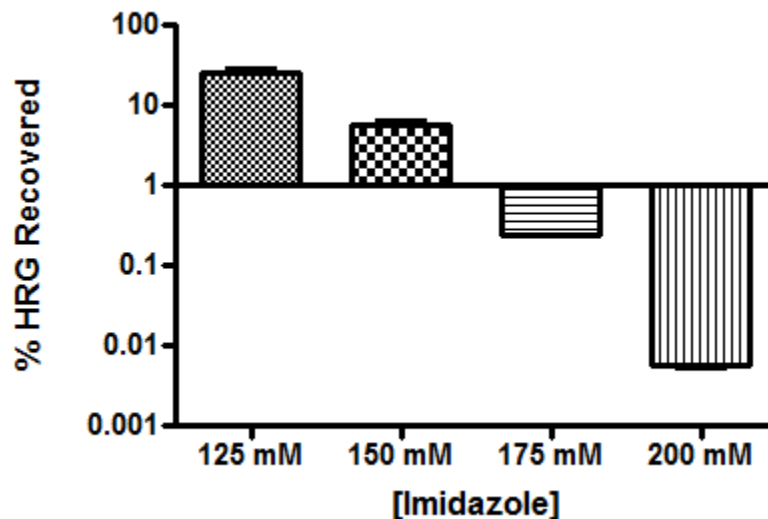


Figure 49. Quantification of HRG bound to Ni(II)NTA magnetic agarose beads in the presence of blocking conditions of imidazole.

To determine the recovery of HRG within the extraction device, control extractions were performed with plasma at 125 (“low blocking”) and 200 mM (“high blocking”) imidazole blocking conditions (**Figure 50**). Recoveries of HRG were similar to those conducted in eppendorf tubes. Under low blocking conditions, significant amounts of HRG (~17%) were recovered in the elution chamber. For the high blocking conditions, only ~0.013% of HRG can be accounted for in the elution chamber. When HRG recovery was compared between plasma and pre-lysed whole blood samples, there was no clear difference in overall recovery in the elution chamber, suggesting that the increased complexity provided by blood doesn’t lead to non-specific HRG contamination in the elution chamber.

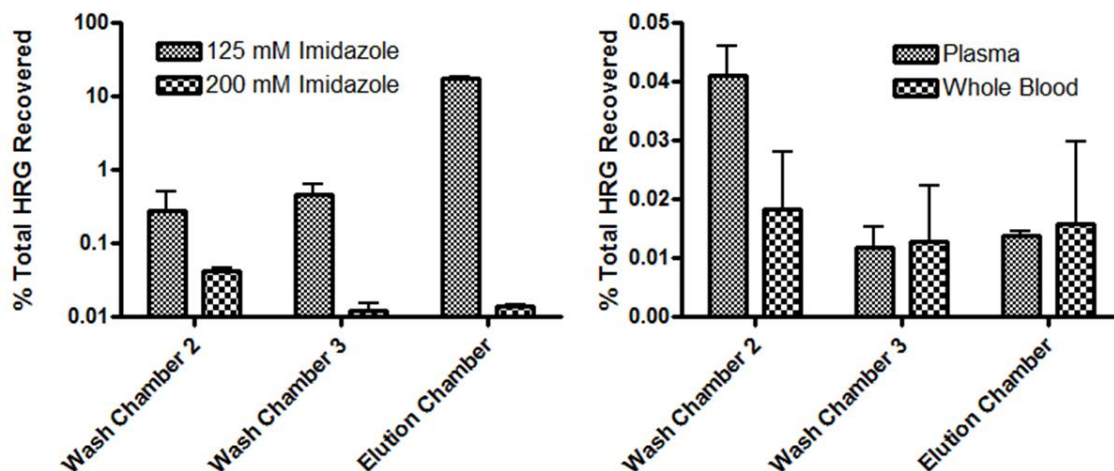


Figure 50. HRG purification efficiencies in the extraction device. Left: HRG contamination under low and high blocking conditions. Right: Effect of whole blood on HRG contamination.

In addition to HRG, hemoglobin concentrations were also quantified using its molar extinction coefficient at 414 nm. Hemoglobin quantification serves to approximate the non-specific carryover of proteins from the sample loading chamber. It was determined that there was less than 0.1% of the original hemoglobin in the elution chamber under both conditions. Also, the high blocking conditions yielded ~50x less hemoglobin than the low blocking conditions. This suggests that either hemoglobin has a slight affinity to the Ni(II)NTA agarose or in general more interferents are being carried through under the low blocking conditions. A SDS-PAGE gel was prepared from the high blocking conditions and stained using Coomassie. Although whole blood contains significant amounts of protein (lane 3), the wash chambers and especially the elution chamber indicate that contaminating proteins remain primarily in the sample loading chamber. This highlights the utility of this method because the antigen of interest is being isolated with the same order of magnitude yield, while significantly reducing the biological noise.

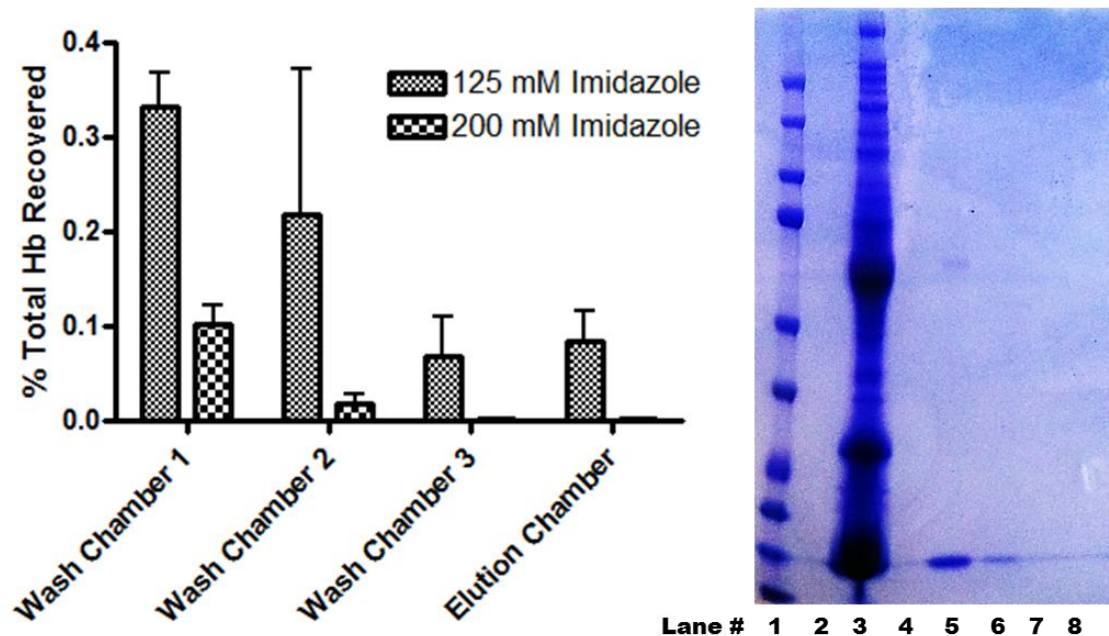


Figure 51. Quantification of contaminating proteins in the wash and elution chambers. Left: Recovery of hemoglobin at the low and high blocking conditions. Right: Coomassie stained SDS-PAGE gel of whole blood sample at high blocking condition. Lane 1: ladder. Lane 2 & 4: empty. Lane 3: sample loading chamber. Lane 5-7: sequential wash chambers. Lane 8: sample elution chamber.

Extraction Efficiencies below the WHO's Limit of Detection

One advantage of sample processing is the ability to concentrate *pf*HRP-II from a patient sample, which effectively lowers the limit of detection. Synchronized cultures were grown, counted, and lysed by freeze-thawing. Parasite loads at and below the WHO's recommended limit of detection were spiked into plasma and manually processed (**Figure 52**). At the low blocking conditions, 50% recovery of *pf*HRP-II was observed under all conditions, corresponding to an average 5-fold enhancement in signal. The high blocking conditions yielded 17-25% recovery, corresponding to a 1.7-2.5-fold enhancement in signal. Assuming that 200 parasites/ μ L is the current LOD for the best RDTs on the market, it can be hypothesized that in conjunction with this extraction device, lower limits of detection can be achieved at 40-50 parasites/ μ L. Furthermore,

when the reaction was performed at the low blocking conditions for 20 minutes, the recovery was improved to over 60% recovery (Data not shown). These results suggest that at the very least, this extraction technology could be used in conjunction with current RDT technology to improve the current LODs.

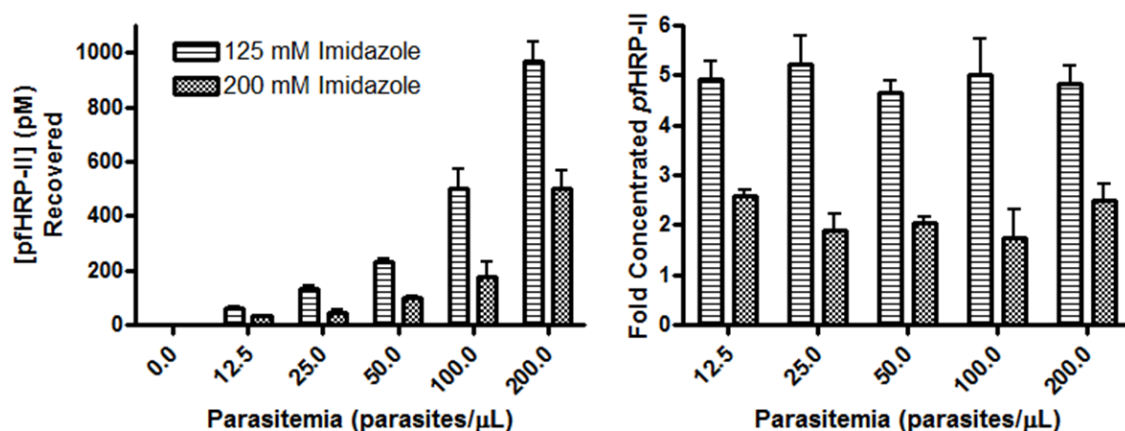


Figure 52. Recoveries of *pfHRP-II* at and below the current WHO required limits of detection. Left: Total protein recovery for the low and high blocking conditions. Right: Fold concentration of *pfHRP-II* after processing. Note: for these studies the concentration of agarose beads was doubled to ~72 beads/μL.

Conclusions

A low resource device has been developed to extract and concentrate *pfHRP-II* from biological samples utilizing the properties of surface tension valves. This device was developed from the novel observation that for a small diameter tube, solutions separated by mineral oil valves are held in place by a capillary force. In fact, the capillary forces are so high that Ni(II)NTA magnetic agarose beads moving from one solution to the next pass through the oil valve entraining large volumes of the aqueous chambers. It has been demonstrated that sample processing of *pfHRP-II* from physiologically relevant parasite loads in complex media can lower the limits of detection by 5-fold at the cost of ~25

minutes of processing. In addition, surface tension sample processing reduces biological noise by over 4 orders of magnitude. The device is fully self-contained and provides minimal sample handling, which eliminates the need for sophisticated equipment. The modularity of the device design allows for the preparation of a variety of sample volumes and compositions that can be tailored to the downstream application. Additionally, the technology is readily adaptable for the isolation of a variety of biomarkers, including other proteins, DNA, and carbohydrates.

Future Directions

Studies are currently being conducted to demonstrate the limits of detection of the device with parasite samples prepared in whole blood. This is a more realistic condition that would be seen during sample processing of an infected patient in a low resource setting. In addition, processed samples are being analyzed by a commercially available RDT to determine how much amplification in signal can be achieved with this processing device. As mentioned above, alternative patient samples, including saliva, urine, and feces should also be investigated to determine the limits of detection in these complex samples. Also, it has yet to be determined whether the device exhibits long term stability at environmentally relevant temperatures and humidity.

Many parameters may have a significant effect on design performance including bead size, bead composition, tubing diameter, tubing material, and liquid characteristics. This modularity allows for a “plug-and-play” mentality, where different components can be modified to determine the optimal device composition. For example, 1 μm Co(II)NTA magnetic beads are currently being investigated as an alternative capture bead. These

beads are advantageous because they not only traverse through oil valves they also travel through air valves. Air valves are preferred due to the reduction of overall cost of the device, and will likely be more stable than oil valves under environmentally relevant conditions. Previous work by the Haselton lab has shown that an air valve system works exceptionally well for an RNA processing device, with minimal contamination in the elution chamber.¹⁷⁶

In addition to investigating the different valve and bead formats, the size and composition of the aqueous chambers can also be modified to improve efficiency, reduce overall reagent costs, and reduce processing times. The size and composition of the tubing can also be altered as well. Larger tubing is unlikely to work, due to loss in surface tension, leading to mixing of the chambers. However, smaller diameter tubing may prove to be advantageous because sample volumes can be reduced, again reducing costs.

Furthermore, the sample processing device will eventually need to be completely self-contained and compatible with an assay for the detection of malaria to be useful in the field. As the various parameters are improved and the device is modified to become field ready, I believe that the utility of this device will become even more apparent and will catalyze the development of equivalent processing technologies for other biomarkers of interest.

CHAPTER VI

DEVELOPMENT OF A COFFEE RING-BASED DIAGNOSTIC PLATFORM FOR THE DETECTION OF HISTIDINE-RICH PROTEINS

Introduction

Alternative diagnostic strategies for malaria detection are desired to circumvent the challenges faced in the developing world. Current diagnostics are used because they operate on premises that are well understood and established. Although this is commonly the standard by which device development should be performed, sometimes an “outside-of the box” strategy provides the breakthrough needed to overcome the current limitations. In 1997, Robert Deegan published a letter in *Nature* describing the physical properties of how particles in coffee concentrate at the edge of a drying drop, leaving a visible stain.¹⁹⁵ Termed the coffee ring phenomenon, this physical process capitalizes on the radial flow of a drying drop to replace evaporative losses at the pinned line (**Figure 53**). The result is the concentration of colloidal particles into a well-defined ring, which can be easily visualized by naked eye. More recently, it has been demonstrated that this phenomenon can also be used as a nanochromatographic process where micro and nanoparticles form concentric rings that are separated based on their size.^{196,197} Unlike lateral flow assays, which utilize nanoparticles (2-5 nm) or dyes as the visible readout²¹, a radial flow assay could use particles such as nanoparticle aggregates or microparticles which would enhance the signal output. The following chapter highlights efforts toward

designing a radial flow malarial diagnostic that capitalizes on the physical properties of the coffee ring phenomenon.

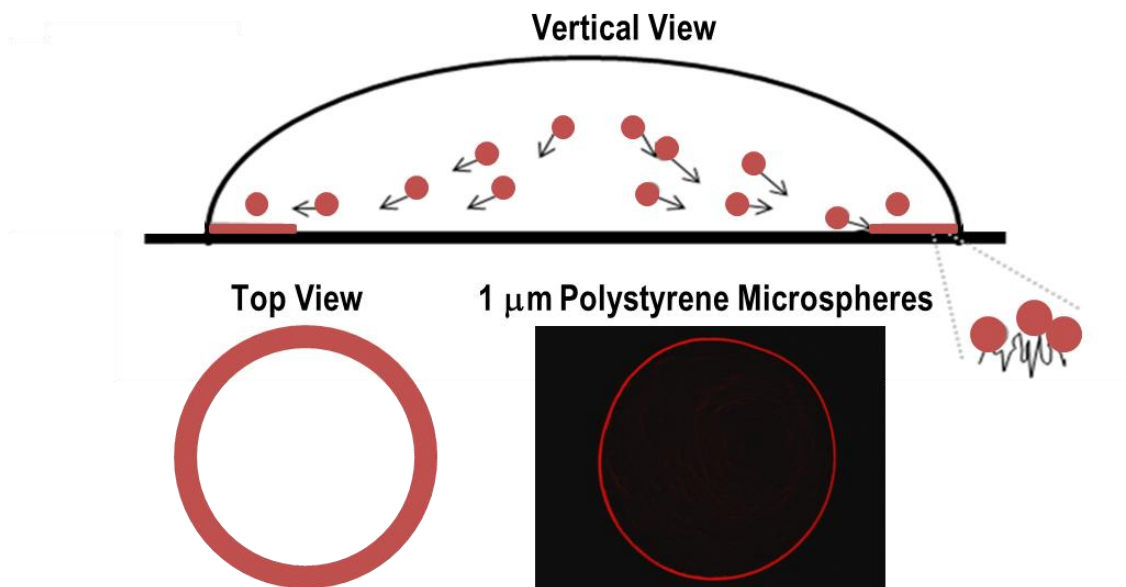


Figure 53. Schematic of coffee ring formation. Colloidal particles such as gold nanoparticles or polystyrene microspheres are deposited at the drop edge due to radial flow induced by differential evaporation of the water at the liquid-surface interface.

Physical Properties of Coffee Ring Formation

The proposed assay is based on the physics of an evaporating drop. When a drop containing a homogeneous solution of colloidal particles is deposited onto a surface and allowed to dry, the particles are concentrated into a dense ring at the periphery. Complete ring formation is dependent on three essential requirements that must be met: (1) the solvent must dry, (2) the contact angle between the droplet and the surface must be $> 0^\circ$, and (3) the contact line of the solvent must remain pinned to its initial position throughout the drying process.¹⁹⁵ Interestingly, there are several physical properties commonly associated with solute transport that are negligible in ring formation. These properties include surface-tension gradients (i.e. the Marangoni effect), solute diffusion,

electrostatic effects, and gravity effects. In fact, many of these properties are more likely to disrupt ring formation rather than to promote it. Instead, the microfluidic flow of the drop is the result of a geometric constraint imposed by the pinned contact line and differential evaporation rates between the drop edge and center.¹⁹⁸ The free surface when constrained by the pinned contact line pushes the solvent outward to compensate for evaporative losses. The evaporative flux $J(r)$ reduces the height $h(r)$ at every point r . However, since the contact line must be maintained, solvent losses at the edges must be replaced by liquid in the interior. Therefore, a radial flow is obtained, carrying any solute molecules or particles from the center of the droplet to the edge, where they are deposited during evaporation of the solvent.

The evaporation rate across the drop is heterogeneous, where the fastest rate of evaporation occurs at the drop edge.¹⁹⁸ During evaporation, solvent molecules rapidly interchange with the gas phase at the gas-liquid interface. The rate of evaporation and subsequent diffusion is dependent on the partial pressures between the solvent vapor and the ambient gas phase. At the drop surface, the solvent vapor reaches equilibrium and diffuses away from the drop into the ambient air. At the drop edge, where the substrate, liquid, and gas all meet, the solvent is bounded by relatively more ambient air than at the drop center. This gives solvent vapor more volume to diffuse into, therefore promoting a faster rate of evaporation when compared to the drop center.

Drop pinning is essential for ring formation, or the drop will recede during drying, leaving a deposition of particles on the surface with deposition densities relative to the initial height of the drop. Line pinning can be achieved by two mechanisms: (1) a rough surface due to physical or chemical heterogeneities provides enough drag force to hold

the particles in place or (2) the surface is functionalized with a capture agent, which binds the particles or particle-antigen conjugates when they come into contact with the surface.

In the initial stages of drop deposition, particles are homogeneously distributed throughout the sample. The particles nearest to the drop edge become quickly trapped at the liquid-gas-substrate interface due to surface tension interactions, or potentially captured by the surface ligands. These particles protrude from the drop, maintaining a larger contact angle than what would be observed with a drop without the particles. For pinning to occur, the overall change in the contact angle must be $\geq 0^\circ$. Evaporation decreases the contact angle, while the deposition of particles on the edge increases the contact angle governed by the following equation¹⁹⁹:

$$\Psi \equiv \varphi C_a \frac{R^4}{a^3 h_0} \geq C \equiv \frac{16}{9 \lambda n_c} \quad (4)$$

where R = drop radius, λ = drag coefficient for a particle placed in a film through which there is a mean liquid flow, n_c = # of particle chains, a = particle radius, h_0 = height of the center of the drop, C_a = capillary # representing the strength of viscous forces compared to the interfacial tension forces, and φ = volume fraction of the particles in solution.

In general, smaller initial contact angles improve ring formation because they result in a drop with a larger radius, promoting faster radial flow. Ring formation is also governed by the solute or particle concentration, where higher concentrations improve line pinning and subsequent ring formation. In addition, ring formation is inversely related to particle size, where smaller particles induce better ring formation. As the particles increase in size, the capillary force driving the receding of the pinned line overcomes the drag force and/or the binding energy of the surface ligand-biomarker

interaction keeping the particles in place. The result is that the particles are dragged inward with the receding drop.

Another important factor to consider is the settling velocity of a particle, or the amount of time it takes a particle to settle out of solution. This factor is governed by the Stoke's law:

$$V_s = \frac{2}{9} \frac{(\rho_p - \rho_f)}{\eta} gR^2 \quad (5)$$

where V_s = settling velocity; ρ_p = particle density; ρ_f = fluid density; η = fluid viscosity; R = particle radius; and g = acceleration due to gravity. Particles with high densities or large diameters may settle on the substrate before they are able to travel to the drop edge. Depending on the assay format, this physical property can be advantageous, especially if it is necessary to isolate the biomarker in the center of the drop.

Functional Gold Nanoparticles as Aggregation Reagents

Gold nanoparticles represent an ideal coffee ring capture agent due to their unique physical and chemical properties. Gold is chemically inert and does not readily oxidize below its melting temperature, making it stable under ambient conditions. Although gold has a high density (19.3 g/mL), citrate-stabilized nanoparticles below ~50 nm remain suspended in aqueous solutions. In addition, gold exhibits a visible surface Plasmon resonance induced by the collective oscillation of electrons at its surface (**Figure 54**), making it useful as a diagnostic sensor.²⁰⁰⁻²⁰⁴ These electrons form an electron gas that moves away from its equilibrium position when perturbed by light energy. Collective electron movement creates an induced surface polarization charge that serves as a restoring force on the electron gas. This results in collective oscillatory motion of the

electrons, much like what is observed for the vibrations of a water surface.²⁰⁵ Unlike other metals which have a surface Plasmon resonance in the UV, gold resonates in the visible spectrum, giving gold its representative red color in aqueous solutions.²⁰⁶ With a molar extinction coefficient of $3.64 \times 10^8 \text{ M}^{-1}\text{cm}^{-1}$, gold nanoparticles are visible into the picomolar range, which is where the lower limit of detection for *p*fHRP-II is in current diagnostic strategies.¹⁶¹

Since the nanoparticles have a high surface area to volume ratio, the Plasmon frequency is sensitive to the dielectric nature of its interface with the surrounding solution. As interparticle distances between the NPs are reduced to less than the average particle diameter (i.e. during aggregation), their surface Plasmon bands couple, resulting in visible red shifts in absorption.²⁰⁷ In addition, only small aggregates containing 2-10 particles per cluster are required to drastically shift the Plasmon resonance.^{208,209}

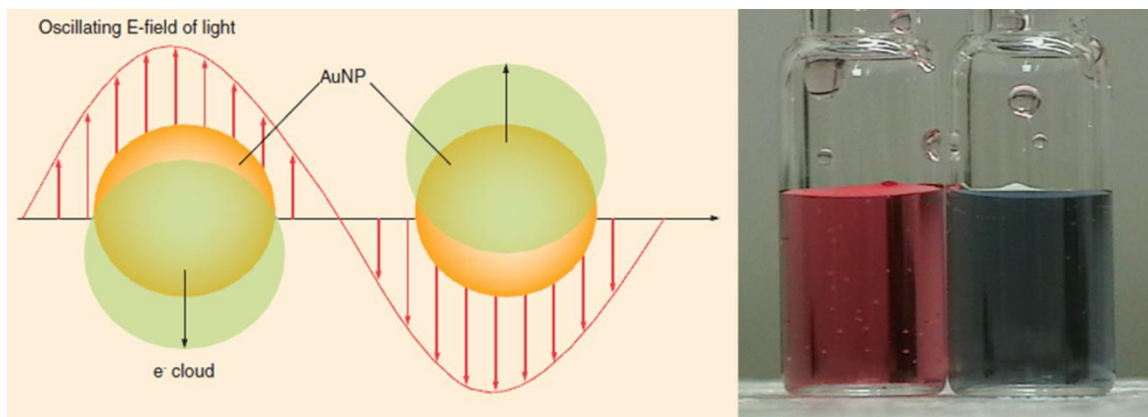


Figure 54. Surface Plasmon resonance of AuNPs. Left: The oscillating electric field of light induces a collective dipolar oscillation of the free conduction-band electrons of the AuNP. This results in absorption of light at $\sim 520 \text{ nm}$ for 15 nm AuNPs (right, first vial). As two or more nanoparticles come into close contact with one another, their surface Plasmon resonance bands couple, resulting in a red shift that makes the visible color of the particles shift to purple (right, second vial).

Another advantage of gold substrates is their reactivity towards thiolated ligands. These molecules create a monolayer on the surface, allowing for the selective

functionalization of surface substrates. These substrates can be tuned to detect specific biological or synthetic targets. Surface substrates also serve to stabilize these nanoparticles in a variety of physiologically relevant conditions.²¹⁰ Mirkin et al. have previously designed DNA recognition elements by conjugating complementary thiolated surface ligands (mercaptoalkyloligonucleotides) onto different gold nanoparticles that hybridize upon heating, inducing Plasmon coupling of the nanoparticles.²⁰⁰ Recently, this technology has been applied to the detection of single nucleotide polymorphisms.²¹¹ AuNPs functionalized with small alkanethiols, cysteine, dithiolthreitol, and glutathione have also been designed as colorimetric sensors against heavy metals such as Hg(II), Pb(II), Ag(I), Cu(II), As(III), and As(IV) with limits of detection in the nanomolar range.²¹²⁻²¹⁴ In addition, ligand-functionalized AuNPs have been used as colorimetric sensors of proteins.^{215,216}

This chapter highlights the progress towards the development of a low-cost diagnostic for the detection of malarial *pf*HRP-II based on the coffee ring phenomenon. The unique microfluidics present in an evaporating colloidal solution generates a characteristic “coffee ring” stain of gold nanoparticles visible with the naked eye. Ni(II)NTA functionalized gold nanoparticles were synthesized by assembling a monolayer of a PEGylated NTA thiol onto the surface of the metal particles. These particles serve as an in-solution capture agent that aggregates in the presence of histidine-rich targets. The functionalized particles were characterized using transmission electron microscopy (TEM), UV-visible spectroscopy, and dynamic light scattering (DLS). Aggregation behavior of Ni(II)NTA NPs in solution was evaluated in the presence of a number of poly-amino acids, *pf*HRP-II mimics, pHRP-II, BNT-II, and recombinant HRP-II in a

concentration and pH-dependent manner. The effects of long term storage at physiologically relevant temperatures on the aggregation behavior of the particles are evaluated. In addition, the particle behavior in the presence of common human serum proteins at physiological concentrations was investigated. Using a Ni(II)NTA functionalized glass surface, HRP-II-Ni(II)NTA AuNP aggregates selectively formed rings on the surface during drop drying. Optimizations of reaction parameters, including the utilization of glycerol to reduce non-specific binding, are investigated. In addition, a simple ring quantification technique that can be adapted to a Smartphone is investigated.

Experimental

Reagents: AuNPs were purchased from Ted Pella Inc. All peptide reagents were purchased from Aapptec Inc. Antibodies for HRG characterization were purchased from Abcam Inc. Pooled human serum was purchased from Cole-Parmer Inc. Human plasma was purchased from Valley Biomedical Inc. Western blotting reagents were purchased from Invitrogen Inc. Ni(II)NTA functionalized glass slides used during the ring assay were purchased from Xenopore Inc. All other reagents were purchased from Fisher Scientific Inc. or Sigma Aldrich Inc. and used without modification.

Synthesis of Ni(II)NTA AuNPs: A 2.3 nM solution of citrate-stabilized AuNPs (15 nm) was incubated with excess NTA-thiol ligand (>0.1 mM) (7) overnight at room temperature. After the initial loading period, the particles were centrifuged (45 min, 7,200 x g) to remove the unreacted thiols and washed three times with 0.1M HEPES buffer (pH 7.4) with Tween-20 (0.1-0.25%). The resuspended particles were charged with Ni(II) upon the addition of excess metal chloride solution (0.2 mM) in water and incubated

overnight. Next, the particles were centrifuged and washed three additional times with the final suspension buffer (0.1 M HEPES, 0.025% Tween 20) before storage or use. For the pH studies, the final suspension buffer for pH 5.5 was 0.1 M MES buffer, 0.025% Tween 20 and for pH 9.0 was 0.1 M CHES buffer, 0.025% Tween 20.

Synthesis of Mixed Monolayer Ni(II)NTA AuNPs: A 2.3 nM solution of citrate-stabilized AuNPs (15 nm) were initially centrifuged (10 min, 12,500 x g) and resuspended in 50:50 water:DMF with 0.1% Tween 20. Next, the thiolated ligands (7) and (8) were incubated with the particles overnight with a final thiol concentration of 0.1 mM. Next, the particles were purified by centrifugation and washing three times with 0.1 M HEPES pH 7.4 with 0.1% Tween 20. Note: the first centrifugation time was extended to 1 hr due to the inclusion of DMF in the reaction solution. After purification, the particles were charged with 0.2 mM nickel(II) chloride solution overnight and purified (same as above).

Characterization of Ni(II)NTA NPs: All particles synthesized in this study were characterized by TEM using a Phillips CM20 microscope. The hydrodynamic diameters of the particles were determined using dynamic light scattering, and Zeta potentials of the particles were determined using a Malvern Nano ZS. Spectral characterization was performed on either an Agilent 8453 UV-Visible spectrometer or a Bio-Tek Synergy HT plate reader.

Synthesis of Protein Mimics: All peptides were synthesized using standard Fmoc solid phase synthesis methods using an Apex 396 peptide synthesizer (Aapptec). BNT-II was synthesized using previously established methods using a MAP resin containing four branches.²¹⁷ All linear peptides were synthesized using a Rink amide resin. The N-

terminus of each peptide was acylated using DCM:acetic anhydride (1:1). Cleavage was performed by treating the functionalized resins with Reagent R (90:5:3:2 TFA:Thioanisole:Anisole:EDT) and precipitating the peptides in cold ether. Purification was performed using a reverse-phase HPLC (Waters Prep LC 4000) with a Waters 2487 dual wavelength detector and C18 column. The purified products were characterized using MALDI-TOF, and tested for activity against a rapid diagnostic test specific for *pf*HRP-II (Malaria Antigen *P.f.* Standard Diagnostics, Inc.).

Purification of Histidine Rich Glycoprotein (HRG): Human HRG was purified from plasma (Valley Biomedical) by Ni-NTA (Qiagen) affinity chromatography. Plasma (45 mL) was loaded onto a pre-equilibrated column of Ni-NTA resin (5 mL) and incubated at 4°C overnight with shaking. This reaction mixture contained 50 mM imidazole during incubation. After incubation, the resin was washed with 10 column volumes of 50 mM phosphate buffer, pH 8.0 with 500 mM NaCl and 50 mM imidazole. Next, the proteins were eluted using a gradient of imidazole up to 500 mM. After pooling fractions containing HRG, they were concentrated using Amicon centrifuge filtration units (30 kDa mw cutoff) and washed with 0.1 M HEPES, pH 7.4. The concentration of the protein was determined using the Bradford assay. Confirmation of the product was determined by SDS-PAGE using a 4-10% Bis-Tris gel.

Western Blot of HRG: Western blotting was also performed by running HRG on SDS-PAGE and subsequently transferring to a PVDF membrane (Invitrogen). The membrane was then blocked with 5% skimmed milk in 10 mM Tris, 0.15 M NaCl, pH 7.4, 0.1% Tween 20 (TBST) overnight at 4°C. Next, a 1:1000 dilution of HRG rabbit primary antibody (Abcam) was added and incubated for 1 hr at room temperature. After washing

5x with TBST, the membrane was incubated with 0.5 $\mu\text{g}/\text{mL}$ HRP conjugated secondary anti-rabbit IgG antibody for 1 hr. After subsequent washes with TBST, the image was developed using the ECL system (Invitrogen).

Titration Assays: Aggregation behavior of Ni(II)NTA NPs was performed by titrating various amounts of targets with the particles. Briefly, targets were dissolved in water and diluted to appropriate concentrations. To these solutions, AuNPs were added to a final concentration of 2.3 nM and incubated for 15 minutes unless otherwise noted. Aggregation was monitored either by UV-Vis or DLS. Any variations in the protocol will be mentioned in the text as appropriate.

Synthesis of Functional Glass Surfaces: Synthesis of functionalized glass slides was performed using a modified protocol from Goddard et al.²¹⁸ Glass slides purchased from Fisher Scientific were placed into a 5 slide glass chamber. A solution of piranha solution (50 mL) was added to the slides and incubated for 1 hour. Note: piranha solution is very dangerous and should be handled with extreme caution! The slides were washed five times with DI water followed by a wash with 95% ethanol. The slides were then incubated with a 50 mL solution of 2% aminopropyltriethoxysilane (APTES) in ethanol and mixed on an orbital shaker (80 rpm) for 10 minutes. After incubation, the slides were washed three times with ethanol, followed by three washes in water. The slides were then dried and cured in an oven 80°C for a minimum of 4 hours. Next, 5 amine functional slides were placed into a 5 slide glass holder and incubated for 2 hours with shaking with a 50 mL solution of 10 mM glutaraldehyde and 10 mM sodium cyanoborohydride in PBS. After activation, the slides were washed three times with DI water. The activated slides were further functionalized with amine-terminated ligands by incubating the slides

in 50 mL of 10 mM ligand and 10 mM sodium cyanoborohydride with shaking overnight. After overnight incubation, the slides were washed 5 times with DI water and dried under N₂ prior to analysis. Contact angle measurements were conducted using the sessile drop method using a goniometer located in the Jennings Lab.

Coffee Ring Assay Method 1: An 8 μ L sample of recombinant HRP-II in water was incubated with 2 μ L of 10 nM Ni(II)NTA AuNPs with 50% NTA coverage for 15 minutes. After incubation, a 0.5 μ L aliquot was collected and deposited onto a Ni(II)NTA functionalized glass slide (Xenopore Corporation) and allowed to dry overnight. After drying, the slide was visualized with microscopy under phase settings. Next, the slide was washed copiously with water, dried, and reanalyzed using microscopy.

Coffee Ring Assay Method 2: An 8 μ L sample of recombinant HRP-II in water was incubated with 2 μ L of 10 nM Ni(II)NTA AuNPs with 50% NTA coverage for 15 minutes. After incubation, a 2.5 μ L solution of glycerol in water was added to the reaction mixture. After mixing, a 1 μ L aliquot was collected and deposited onto a Ni(II)NTA functionalized glass slide (Xenopore Corporation) and allowed to dry for ~1 hour. After drying, the slide was visualized with the fluorescence microscope under phase settings. Next, the slide was washed copiously with water, dried, and reanalyzed using microscopy.

Image Processing: Images for visualization were background corrected using ImageJ. A light background was created using a rolling ball radius of 50 pixels.

Image Analysis and Quantification: Each image was processed using identical functions and settings. All processing steps were performed with custom macros in Image Pro Plus (v. 7) for consistency and reproducibility. First, the images were inverted so that

the positive signal in the assay (the presence of gold nanoparticles) can be represented by an increase in intensity. Then the images were processed through a deconvolution algorithm to flatten the background and set the lowest intensity values to zero. This algorithm is essentially a high-pass filter applied independently to each image. Using a predefined Area of Interest (AOI) at each corner, four samples of “background” intensity were captured to ensure consistency across each image. Another predefined AOI was then centered on the drop region to measure the total intensity of the drop. The size of each AOI was held constant to prevent user-bias. The final signal value was produced by subtracting the mean background intensity from the drop intensity. This value represents a difference in intensity of the region occupied by the drop compared with the rest of the image.

Synthesis of M(II)NTA Polystyrene Microspheres: A 200 μL stock solution of 0.99 μm amine-functionalized polystyrene microspheres (Spherotech; Cat # AFP-0852-2; 1.87×10^7 particles/ μL) were centrifuged and washed with 0.1M phosphate buffer pH 7.8 (1 mL). To this solution, a 100 μL aliquot of 1 mg of bis[sulfosuccinimidyl] suberate (BS^3) in 10 mM phosphate buffer pH 7.4 was added and incubated for 30 min. After incubation, the particles were washed twice with 0.1M phosphate buffer and a solution of NTA-lysine in the same buffer was added and incubated for 2 hours. The reaction was quenched upon removal of the supernatant and addition of 1 mL of Tris buffer (50 mM, pH 8.0). This solution was incubated for 15 minutes. Next, the particles were washed with phosphate buffer three times and then the particles were split into three batches for metal charging. Each aliquot was incubated with NiCl_2 , CuCl_2 , or ZnCl_2 for 2 hrs. After

incubation, the particles were washed with 10 mM phosphate buffer pH 7.4 three times before use.

Incubation of M(II)NTA Polystyrene Microspheres with TAMRA-HRP-II: A 5 μL aliquot of bead solution (1.87×10^7 particles/ μL) was incubated with 5 μL of 0.1 mg/mL TAMRA-HRP-II for 5 min. The reaction was quenched upon the addition of 150 μL of 10 mM phosphate buffer pH 7.4. The particles were centrifuged and the supernatants were collected for fluorescence (ex: 541/10 em: 595/35) and compared to a positive control of TAMRA-HRP-II.

Synthesis of NTA-thiol Ligand: Synthesis of the NTA-thiol ligand (**7**) is summarized in **Scheme 2**. It follows procedures developed by Schmitt *et al*²¹⁹ and Tinazli *et al*²²⁰. Briefly, 11-mercaptoundecanoic acid (**1**) was protected by treatment with zinc acetate to yield 11-acetyl-sulfanyl-undecanoic acid (**2**). Next, (**2**) was coupled to triethylene glycol using DCC coupling chemistry in DCM to afford (**3**). The terminal alcohol of (**3**) was then activated with carbonyldiimidazole (CDI) in DCM to generate the imidazolid intermediate (**5**). After purification, (**5**) was nucleophilically attacked with the NTA lysine moiety (**4**) synthesized using the method developed by Schmitt *et al*²²¹ to yield the protected NTA product (**6**). Final deprotection of the NTA-thiol ligand (**7**) was achieved with hydrazine acetate in DMF. Total yield under these conditions was 44.7%. The backfill ligand (**8**) was synthesized by deprotecting (**3**) using hydrazine acetate in DMF, followed by silica column purification.

S-Acetyl-MUA (**2**).

11-mercaptoundecanoic acid (MUA) (5.00 g, 21.75 mmol, Sigma, 95%) (**1**) was dissolved in DCM (60 mL) and AcOH (60 mL). Subsequently, Zn (10 g) was added to

the reaction mixture and incubated for 15 minutes. The reaction mixture was then cooled to 0°C prior to the addition of 30 mL of acetyl chloride (425 mmol). After 2 hrs of incubation, the reaction mixture was warmed to room temperature, and the reaction solution was separated from the Zn by filtration. Next, the organic solution was washed twice with chilled 0.1 M HCl and the solvent was evaporated. The crude product was purified by silica chromatography. TLC: Rf = 0.54 (ethyl acetate). Yield 5.25 g (88 %). ¹H NMR (CDCl₃): δ: 2.83(t, 2H), 2.32(t, 2H), 2.30(s, 3H), 1.5-1.62(m, 4H), 1.2-1.4(m, 12H).

S-Acetyl-MUA-PEG-OH (**3**)

To a solution of (**2**) in DCM (5.25 g, 20.2 mmol), triethylene glycol (27.5 mL, 20.6 mmol) and DMAP (0.52 g, 4.26 mmol) were added, followed by the addition of DCC (5.51 g, 26.7 mmol). The reaction mixture was stirred overnight. The reaction mixture was then filtered to remove any urea and the organic solution was washed with 0.1 M HCl. The aqueous layer was extracted once with DCM. The combined organic phases were dried over Na₂SO₄ and the solvent was evaporated. The crude product (**3**) was purified by chromatography using ethyl acetate as the eluent. TLC: Rf = 0.49 (ethyl acetate). Yield 5.7 g (72%). ¹H NMR (CDCl₃): δ: 4.22(t, 2H), 3.6-3.75(m, 10H), 2.86(t, 2H), 2.32(t, 2H), 2.31(s, 3H), 1.5-1.62(m, 4H), 1.2-1.4(m, 12H).

S-Acetyl-MUA-PEG-imidazolid (**4**)

To a 20 mL solution of (**3**) in DCM (2.85 g, 7.27 mmol), 2.35 g of carbonyldiimidazolid (CDI, 14.5 mmol) was added and incubated for 4 hours. The imidazolid product (**4**) was then purified by silica column chromatography using first a gradient of 50:50 hexane:ethyl acetate followed by ethyl acetate. Yield 3.00 g (84.7 %). TLC: Rf = 0.57

(ethyl acetate). ¹HNMR (CDCl₃) δ: 8.30 (s, 1H), 7.60(d, 1H), 7.06(d, 1H), 4.57(t, 2H), 4.17(t, 2H), 3.85(t, 2H), 3.6-3.7(m, 6H), 2.84(t, 2H), 2.30(t, 2H), 2.29(s, 3H), 1.5-1.62(m, 4H), 1.2-1.4(m, 12H). MS: 487 (ESI⁺) (MH⁺).

S-Acetyl-MUA-PEG-NTA (**6**)

N_α,N_α-Methylcarboxy-L-lysine (1.4 g, 5.34 mmol), synthesized according the method of Schmitt *et al.*²²¹ was dissolved in 15 mL of water, and the pH was adjusted to 10 with concentrated NaOH. This solution was mixed with 650 mg (1.33 mmol) of (**4**) in 15 mL of DMF and incubated overnight. The reaction was quenched with 15 mL of water and the aqueous solution was extracted three times with ethyl acetate. The aqueous phase was then acidified to pH 1.5 with 0.1M HCl and extracted four times with ethyl acetate. The combined organic fractions were washed with saturated sodium chloride and dried over anhydrous Na₂SO₄. Finally, the organic solvent was removed by vacuum. Yield 970 mg (quant.). ¹HNMR (MeOD) δ: 4.19(t, 2H), 4.15(t, 2H), 3.5-3.8(m, 13H), 3.11(t, 2H), 3.07(m, 2H), 2.85(t, 2H), 2.32(t, 2H), 2.29(s, 3H), 1.5-1.62(m, 8H), 1.2-1.4(m, 14H). MS: 681 (ESI⁺) (MH⁺Na⁺), 703 (ESI⁺) (MH⁺2Na⁺).

MUA-PEG-NTA (**7**)

Hydrazine acetate (140 mg, 1.5 mmol) was added to a 100 mg (0.15 mmol) solution of (**6**) in DMF under nitrogen. The reaction mixture was mixed overnight and the solvent was evaporated. The crude product (**7**) was resuspended in water and acidified until a precipitate formed (pH = 1.5). The precipitated product was then extracted three times using ethyl acetate. The combined organic fractions were dried using anhydrous sodium sulfate, and the solvent was evaporated. The final product was then resuspended in water and lyophilized overnight. Yield 79.6 mg (83.2%). ¹HNMR (D₂O) δ: 4.19(t, 2H), 4.13(t,

2H), 3.5-3.8(m, 13H), 3.11(t, 2H), 3.06(m, 2H), 2.67(t, 1H), 2.48(t, 2H), 2.32(t, 2H), 1.5-1.65(m, 8H), 1.2-1.4(m, 14H). MS: 637 (ESI⁻) (M⁻), 639 (ESI⁺) (MH⁺), 661 (ESI⁺) (MH⁺Na⁺).

S-MUA-PEG-OH (**8**)

Hydrazine acetate (10 g, 107 mmol) was added to a solution of (**3**) in DMF under nitrogen. The reaction mixture was mixed overnight, and extracted three times with water and DCM. Organic fractions were collected, dried with Na₂SO₄, and rotovapped. The crude oil was then purified with silica column chromatography using a 50:50 ethyl acetate:hexanes loading mixture, followed by elution with 75:25 ethyl acetate:hexanes. Samples were pooled and rotovapped, yielding a clear oil. ¹HNMR (CDCl₃) δ: 4.25 (t, 2H), 3.6-3.8 (m, 10H), 2.55 (q, 2H), 2.34 (t, 2H), 1.5-1.7 (m, 4H), 1.2-1.4 (m, 12H). MS: 351 (ESI⁺) (MH⁺), 368 (ESI⁺)(MH₂O⁺).

Results

The unique physical and chemical properties of gold nanoparticles make them powerful reagents for possible low-resource point of care diagnostics. Gold particles have a high molar extinction coefficient of their surface Plasmon resonance absorption ($3.64 \times 10^8 \text{ M}^{-1}\text{cm}^{-1}$), which allows for spectrophotometric detection of these monodisperse particles in the high picomolar range. Further, the energy gap of the Plasmon band in these particles can increase as aggregation occurs, resulting in a visible red shift in the absorption, which is spectrophotometrically and visibly detectable. This allows for the detection of targets which induce crosslinking of the particles in the nanomolar range of sensitivity.

The key to utilizing such nanoparticles is to endow them with significant selectivity through surface ligand design. The use of a Ni(II)NTA surface ligand was inspired by nickel affinity chromatography of His-tagged proteins and the realization that *p*fHRP-II is nothing if not a naturally occurring His-tagged protein. For this study, a modular synthetic NTA ligand was designed to include a module for surface functionalization in a well-ordered monolayer, a module to minimize binding of non-specific interferents, and one to specifically target histidine-rich proteins. The use of a modified alkane thiol ligand provides the functionality to coordinate to the Au surface,²²² while providing a well-ordered packing layer near the NP surface. A polyethylene glycol (PEG) spacer provides a shield between the biological target and NP surface, thus reducing non-specific interactions between the two.²¹⁰ The NTA moiety is attached adjacent to the PEG spacer. To complete the recognition element, Ni(II) is used to charge the chelate to provide the necessary affinity to histidine targets.¹⁸³

The general diagnostic strategy is outlined in **Figure 55**. Initially, Ni(II)NTA gold nanoparticles are incubated with a sample solution containing *p*fHRP-II. The particles and protein crosslink, creating AuNP aggregates, which can be detected spectrophotometrically. Next, a small volume (0.5-5 μ L) of reaction solution is deposited onto a surface coated with Ni(II)NTA and allowed to dry on the surface. The Ni(II)NTA on the surface of the slide serves to capture the protein-gold aggregate as it is deposited onto the pin line of the drop. After washing to remove any non-specific binding, the slide can be analyzed by visible inspection or microscopy to determine whether a ring was formed. A positive result occurs when the protein-nanoparticle aggregate specifically binds to the functionalized surface and the drop edge, resulting in a visible ring. If

*pf*HRP-II is not present, the particles (1) will not aggregate and (2) not specifically bind on the drop edge. Therefore, after washing, there should not be any ring formed, indicating a negative result.

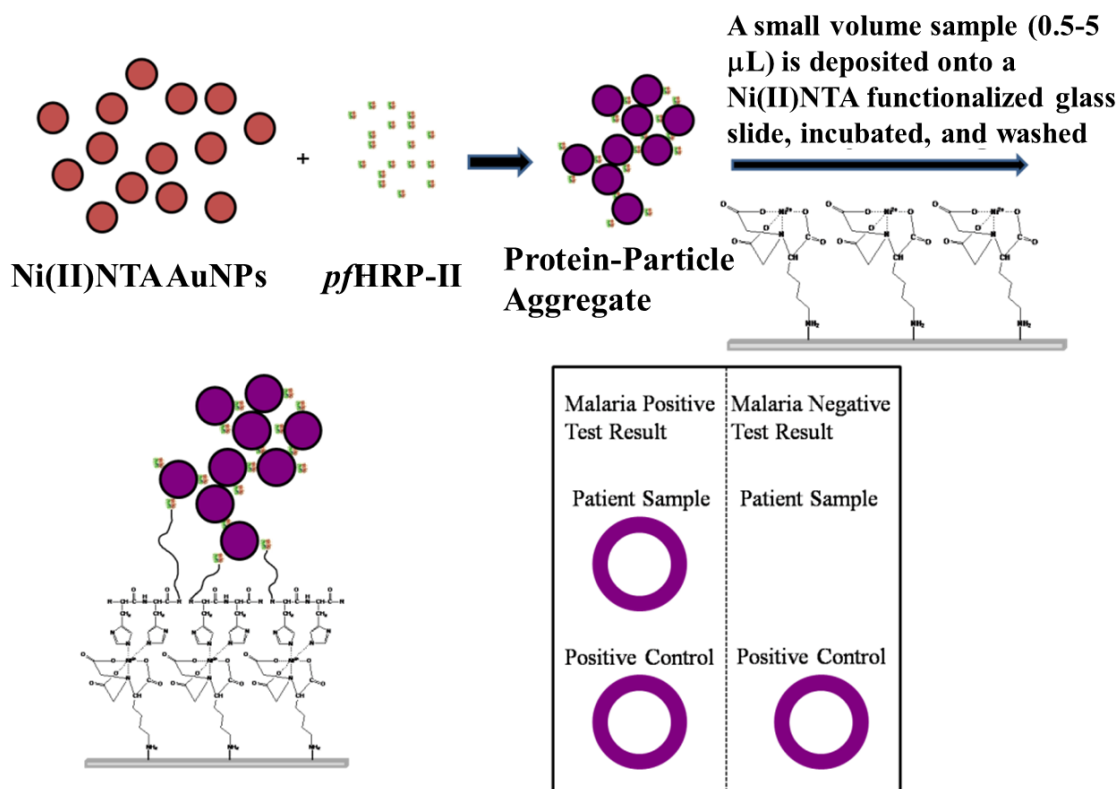
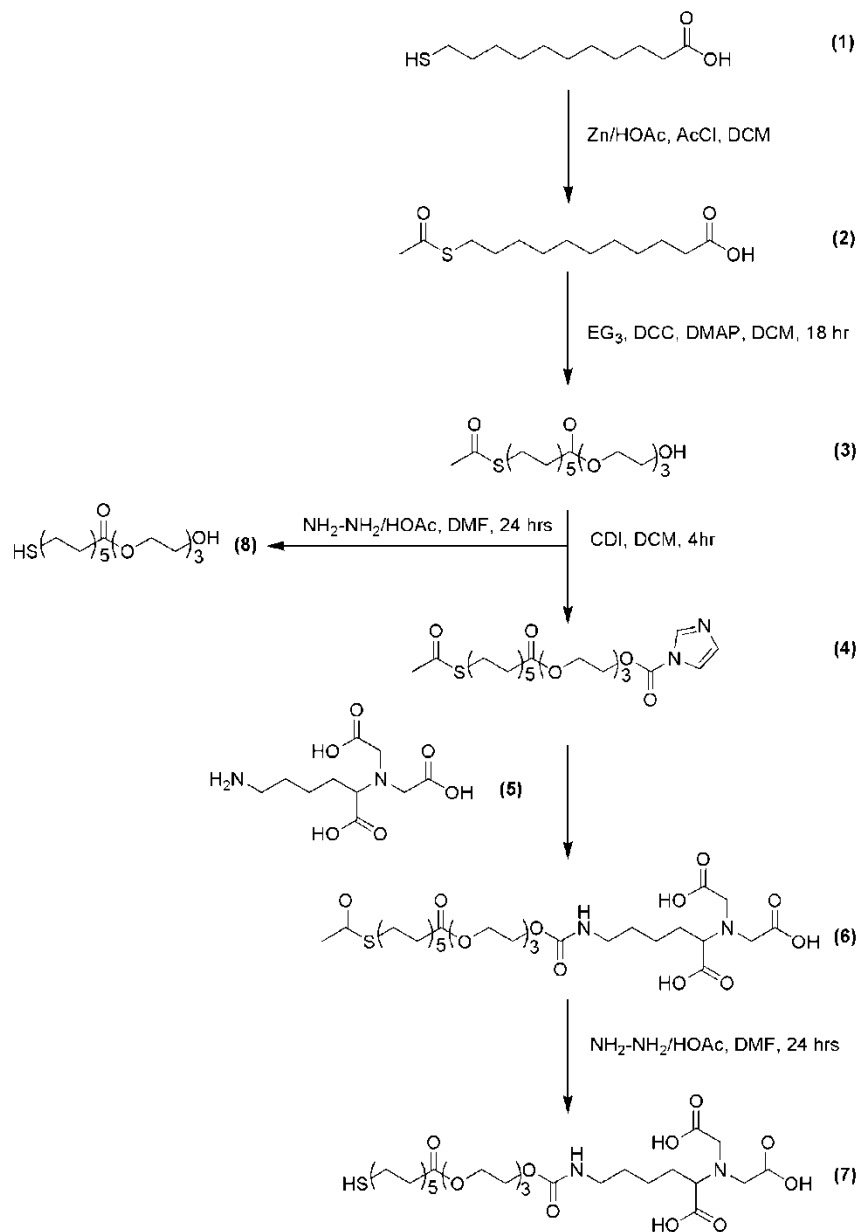


Figure 55. General coffee ring assay procedure using Ni(II)NTA AuNPs. Ni(II)NTA AuNPs are incubated in the presence of *pf*HRP-II, where they interact and crosslinked into large protein-particle aggregates. The aggregates are then deposited onto a Ni(II)NTA functionalized glass slide where they bind to the surface, pinning the contact line. Radial flow during drying concentrates the particles into the drop edge, leaving a visible ring after drying. If the biomarker isn't present, the contact line isn't pinned and the ring doesn't form.

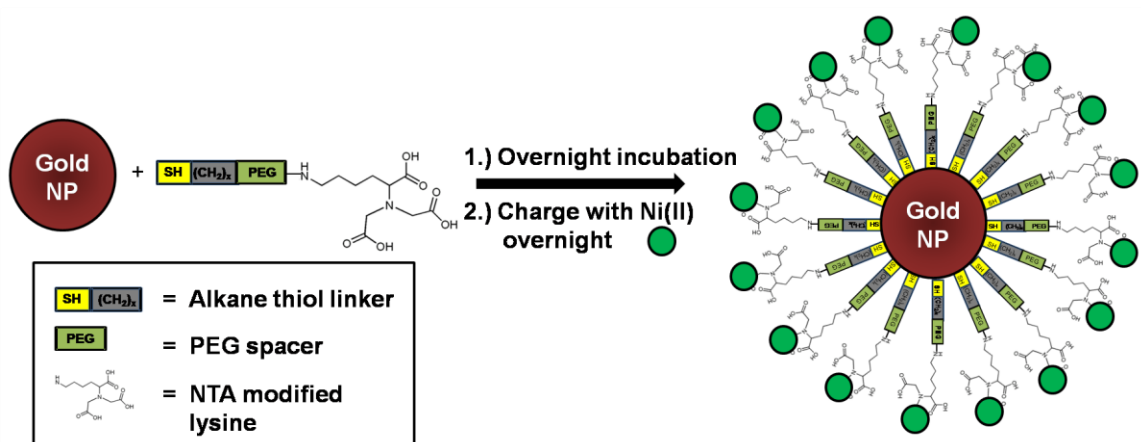
Synthesis and Characterization of Ni(II)NTA Nanoparticles

NTA functionalized Au nanoparticles were synthesized following modified procedures developed by Barton *et al.*²²³ The NTA-thiol ligand (**7**) and PEGylated backfill ligand (**8**) were synthesized (**Scheme 2**) following modifications of Schmitt *et al.*²¹⁹ and Tinazli *et al.*²²⁰. Surface functionalization of the Au nanoparticles was performed

by incubating particles overnight either with purified NTA-thiol ligand in water or the mixed thiol solution in a 50:50 solution of DMF/water, allowing for efficient packing of the ligand onto the surface of the particles (**Scheme 3**). After incubation, the NPs were centrifuged and washed three times with buffer (0.1 M HEPES buffer, pH 7.4 and 0.1% Tween 20) to remove any unreacted thiols.



Scheme 2. Reaction scheme for the synthesis of the NTA-PEG-Thiol and HO-PEG-Thiol ligand.



Scheme 3. Modular design of the M(II)NTA functionalized AuNPs.

The functionalized particles show a minimal red shift (~ 5 nm) in their surface Plasmon absorption, which is consistent with the dielectric changes induced by the monolayer of the thiolated ligands on their surfaces (**Figure 56**).^{223,224} The AuNPs have an average hydrodynamic diameter of 23-25 nm, which is 4-6 nm larger than the citrate-stabilized stock particles. This particle size increase is consistent with the addition of the thiolated ligands onto their surfaces. Although there is no measurable trend in particle size between the particles synthesized with the backfill PEG ligand and NTA, Zeta potential measurements of the particles in 0.1M CHES buffer pH 9.0 without Tween indicate a clear increase of surface potential from uncharged alcohol-terminated particles to the carboxylic acid coated NTA particles. It should be noted that the particles in the presence of Tween all have similar Zeta potentials, suggesting a close association of the surfactant with the surface of the particles. Due to the low Zeta potential of the particles with $< 10\%$ surface coverage, Tween is necessary to maintain the long-term stability of the particles. This could also explain the similar hydrodynamic diameter measured for the particles in the presence of Tween.

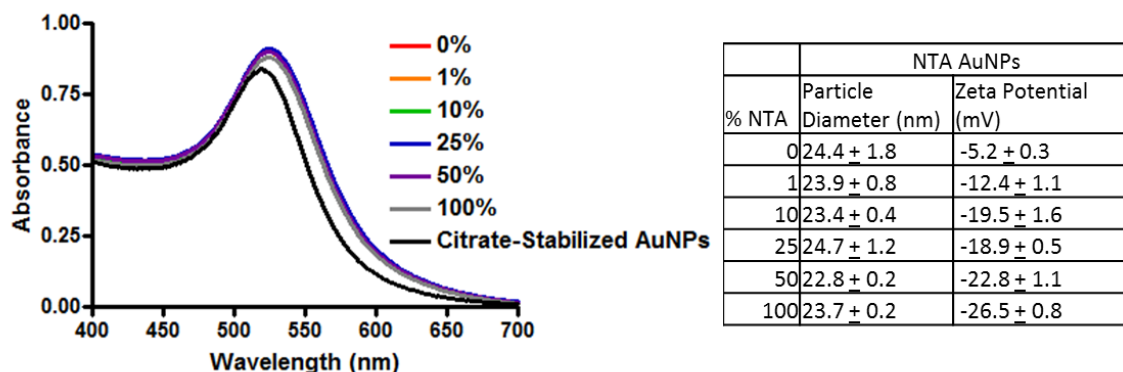


Figure 56. UV-Visible spectra and table of particle diameters and Zeta potentials for NTA and mixed-monolayer AuNPs.

Charging of the particles with Ni(II) was achieved by incubating the particles in 0.1M HEPES buffer pH 7.4 with 0.1% Tween 20 overnight with a 0.2 mM solution of NiCl₂. After purification, the particles were characterized by UV-Vis spectroscopy, DLS, and imaged with TEM (**Figure 57**). Although the total recoveries were different for each particle condition, they exhibited similar spectrophotometric behavior. In addition, their hydrodynamic diameters were between 24-27 nm, which is on average 1-2 nm larger than the NTA-functionalized AuNPs. This slight increase in particle hydrodynamic diameter is likely due to the addition of Ni(II) to the NTA moiety. The measured Zeta potential was ~9 mV under all conditions, which is likely due to the combination of charging the surface with Ni(II) and the inclusion of Tween. The Zeta potential was measured in 0.1M CHES buffer pH 9.0 with 0.1% Tween 20 because the particles are unstable without Tween when charged. During the purification process, it was noted that the particles when centrifuged created a more tightly associated pellet than what was observed when the uncharged particles. This further suggests that the metal is associated with the surface

of the particles. TEM analysis revealed that the particles are primarily monodisperse, suggesting that they do not aggregate during preparation.

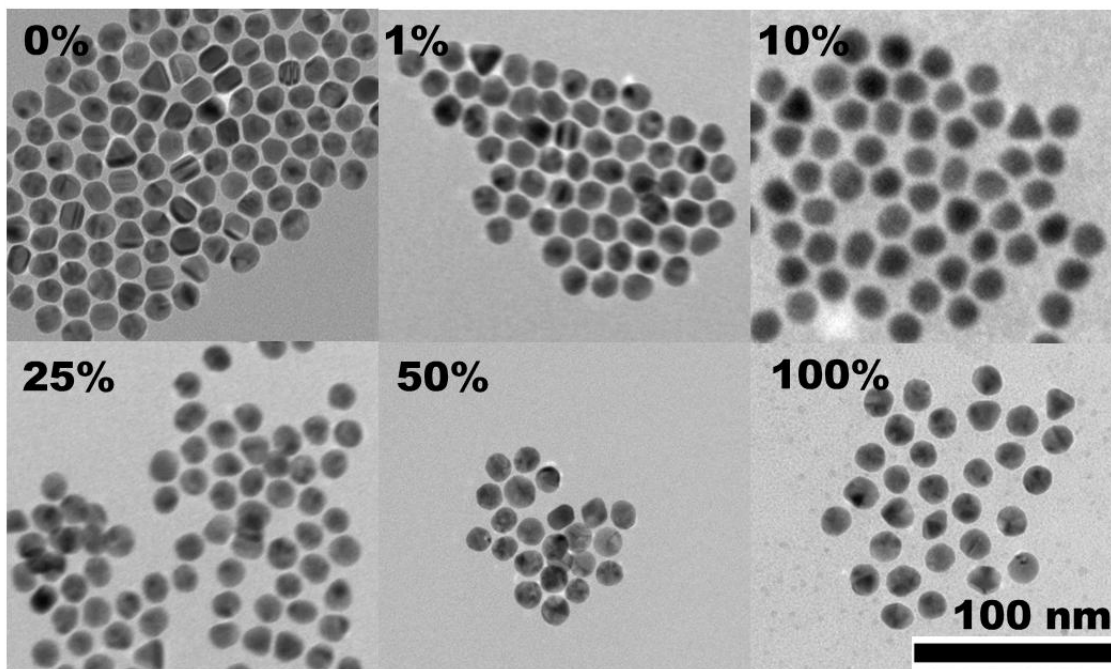
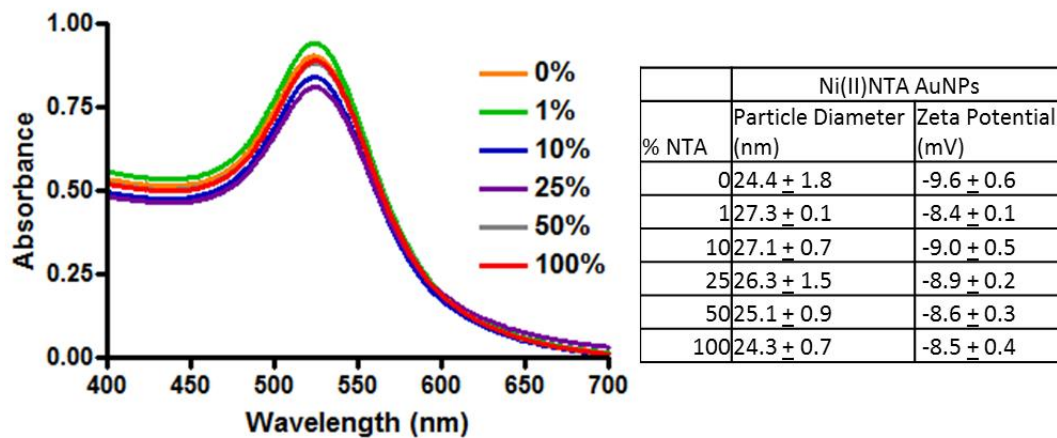
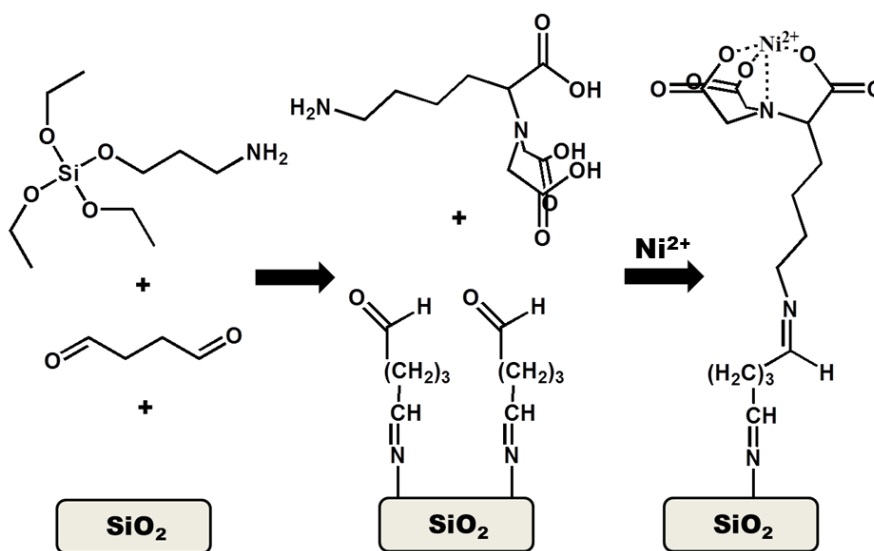


Figure 57. Characterization of Ni(II)NTA and mixed-monolayer AuNPs. Top left: UV-Visible spectra of the particles. Top right: Table containing particle size and Zeta potential information for the particles. Bottom: Representative TEM images of each of the particles.

Synthesis and Characterization of Functional Glass Slides

For the proof of concept studies described in this chapter, commercially available Ni(II)NTA glass slides were used (Xenopore Inc). However, glass slides with variable Ni(II)NTA ligand densities were also synthesized to understand the effect of capture ligand density and contact angle on the overall drop dynamics. Glass slides were initially cleaned with piranha solution to hydroxylate the glass surface (**Scheme 4**). Next, an amine functionalized silane (APTES) was added, creating an amine-functionalized surface. To add specific functionality to the surface, the crosslinker glutaraldehyde was added, forming a Schiff base, which is reduced to a stable 2° amine linkage in the presence of sodium cyanoborohydride. To complete the functional surface, a solution containing varying ratios of NTA-lysine and 3-aminopropanol were added in the presence of sodium cyanoborohydride, yielding a functional surface. For slides functionalized with NTA, charging can be achieved upon the addition of a solution of NiCl₂.



Scheme 4. Synthesis scheme for Ni(II)NTA functionalized glass slides.

Contact angle measurements were conducted for each of the slides (**Figure 58**). Piranha treated slides are completely hydroxylated, yielding a contact angle $< 5^\circ$. When the amine surface is added, the contact angle increases drastically to $56.8 \pm 5.4^\circ$. Glutaraldehyde addition increases the contact angle to $\sim 70^\circ$. The mixed monolayers of Ni(II)NTA and aminopropanol backfill ligand have variable contact angles dependent on the surface coverage of Ni(II)NTA. As the NTA ratio is increased, the contact angle increases. These results suggest that the surface properties of the glass can be tuned to accommodate the requirements of the ring assay.

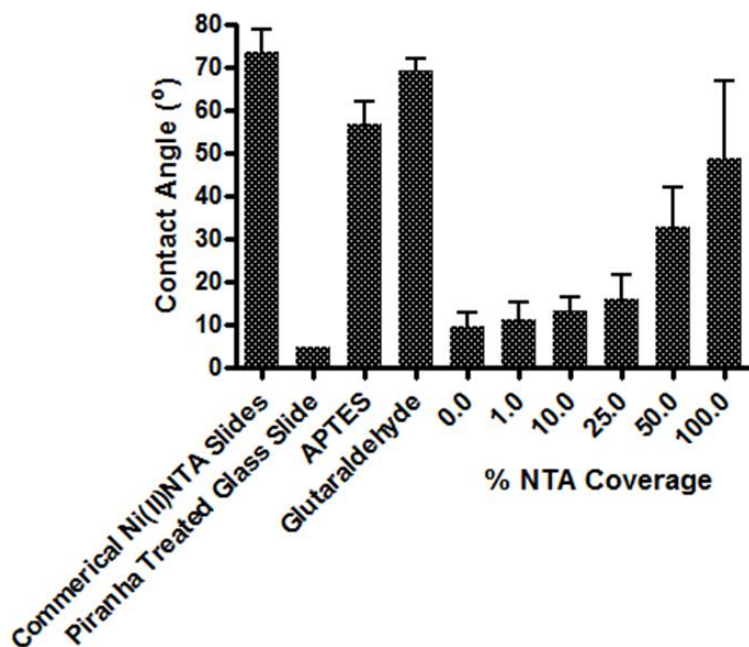


Figure 58. Surface characterization of functionalized slides using contact angle measurements.

In general, the surface functionality of the glass slides can drastically change the physical properties of ring formation. For example, slides with a high contact angle will generate smaller diameter drops that take significantly longer to dry. The tradeoff is that the resulting ring in the higher contact angle slides will be more concentrated, yielding a

more profound ring. For example, the commercial Ni(II)NTA slides have an experimentally determined contact angle of $71.3 \pm 2.0^\circ$. The drying time of a 1 μL drop on the surface is 15 minutes, as compared to 8 minutes on a glass slide. If the volume is increased to 3 μL , then the drying time spikes to 45 minutes, whereas drops that are 3-4 times larger on the glass slide yield the same drying time. It is important to understand how these parameters affect the overall ring formation, as well as the processing time needed for the assay.

Reaction Properties of Ni(II)NTA AuNPs

A number of factors influence the aggregation behavior of the nanoparticles. These include the affinity of the coordinating ligand to the Ni(II), the pKa of the potential coordinating moiety, electrostatics, hydrogen bonding, and the size of the aggregating target molecule. A systematic investigation of single amino acids, poly-amino acids and malaria biomarker epitope mimics were used to investigate the aggregation behavior of the 100% Ni(II)NTA AuNPs. A series of acidic and basic monomeric amino acids, including histidine, were incubated with the Ni(II)-charged particles at pH 5.5, 7.4 and 9.0. No aggregation behavior was observed for any of the single amino acids across the entire pH range, consistent with simple coordinative saturation of the Ni(II) binding sites. Previous work conducted by Bae *et al.* showed that 3-5 nm metal-free (uncharged) NTA-NPs did aggregate in the presence of monomeric histidine at pH 9, presumably through hydrogen bonding and electrostatic interactions.²²⁵ When Ni(II) was titrated into their reactions, the aggregation was inhibited. Thus, those single amino acids coordinating to

Ni(II) simply saturate the coordination sites on the nanoparticle resulting in no cross-linked aggregation.

The aggregation behavior of the Ni(II)NTA AuNPs was also examined in the presence of commercially available poly-L-histidine. At pH 7.4, PLH induced aggregation of AuNPs. Highlighted in **Figure 59** are UV-Vis spectra, DLS profiles, and representative TEM images for Ni(II)NTA AuNPs reacted with PLH over a concentration range of 0-440 nM. UV-Vis spectroscopy indicates a red shift caused by PLH-induced crosslinking of the nanoparticles. Significant peak broadening is observed for all concentrations and the absorption maximum shifts by ~30 nm to 555 nm for the highest concentrations for Ni(II)NTA AuNPs. DLS measurements indicated that the average hydrodynamic diameter of gold nanoparticle aggregates approached 500 nm as a function of time and target concentration. Aggregation occurs rapidly, as indicated by the minimal change in the UV-Vis after 2 minutes of incubation. TEM images further confirm that the particles form large aggregates as a result of Ni(II)NTA-PLH crosslinking.

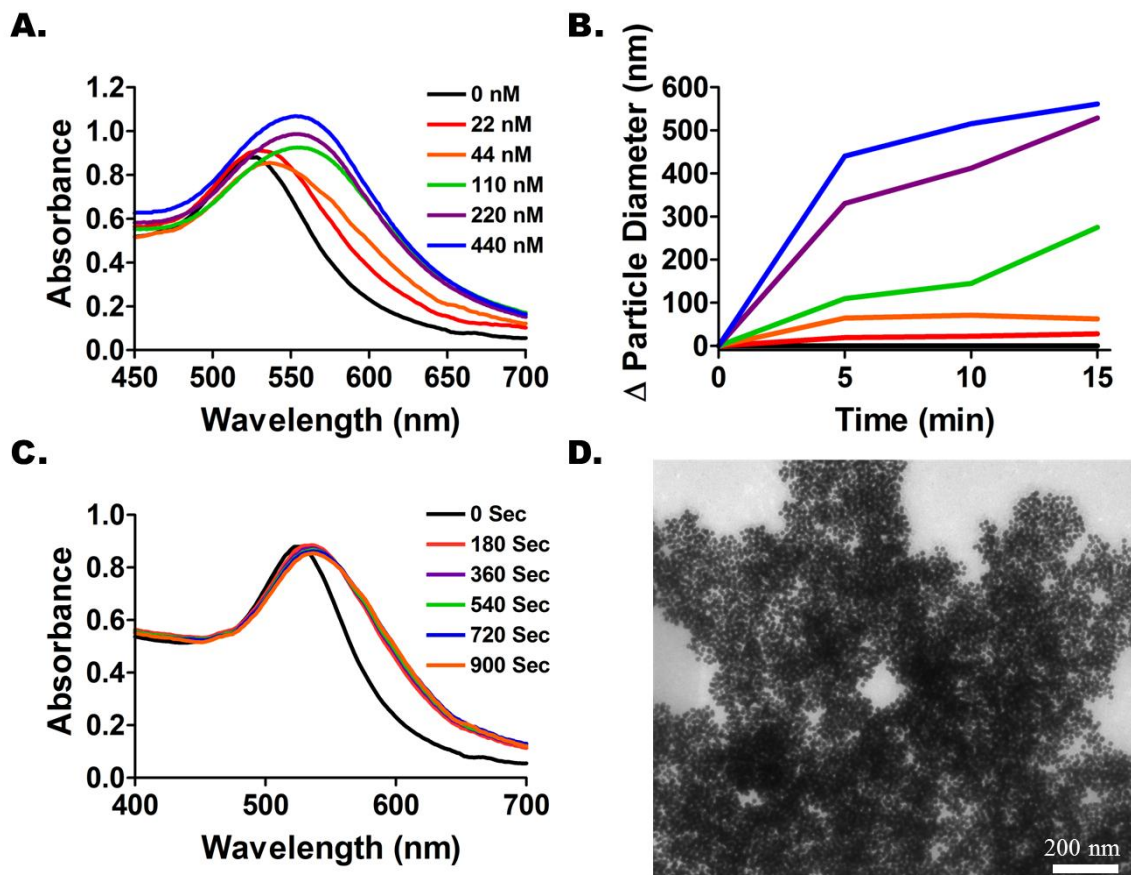


Figure 59. Aggregation behavior of Ni(II)NTA AuNPs in the presence of PLH at neutral pH. A.) UV-Visible spectra of aggregating AuNPs. B.) DLS measured hydrodynamic diameters at variable PLH concentrations. C.) Spectral profile as a function of time for particles incubated in 44 nM PLH. D.) Representative TEM image of particles aggregated in the presence of PLH.

Imidazole has been used extensively during Ni(II)NTA purification strategies due to its ability to block weakly bound proteins for binding to Ni(II)NTA, as well as its ability to elute His-tagged proteins at elevated concentrations. It was of interest to determine if imidazole could also be used to inhibit aggregation of the particles by PLH. **Figure 60** demonstrates the aggregation behavior of Ni(II)NTA and NTA-functionalized particles in the presence of 125 nM PLH and varying concentrations of imidazole. Under the non-blocking conditions, both NTA and Ni(II)NTA particles aggregate in the presence of

PLH. However, when 100 mM imidazole is included in the reaction, only Ni(II)NTA particles aggregate. In addition, peak broadening is observed even in the presence of 200 mM imidazole. For, Ni(II)NTA, it is expected that histidine can coordinate to multiple ligands on multiple particles, inducing crosslinking. As the imidazole concentration is increased, the coordination between the PLH and Ni(II)NTA is disrupted, inhibiting aggregation of the particles. In the case of the uncharged NTA particles, aggregation is likely an electrostatic event, where a small percentage of the histidines on PLH remain positively charged at neutral pH. The inclusion of imidazole serves to disrupt this electrostatic interaction, inhibiting aggregation. The fact that aggregation is inhibited at different concentrations further confirms that the Ni(II)NTA particles are in fact charged.

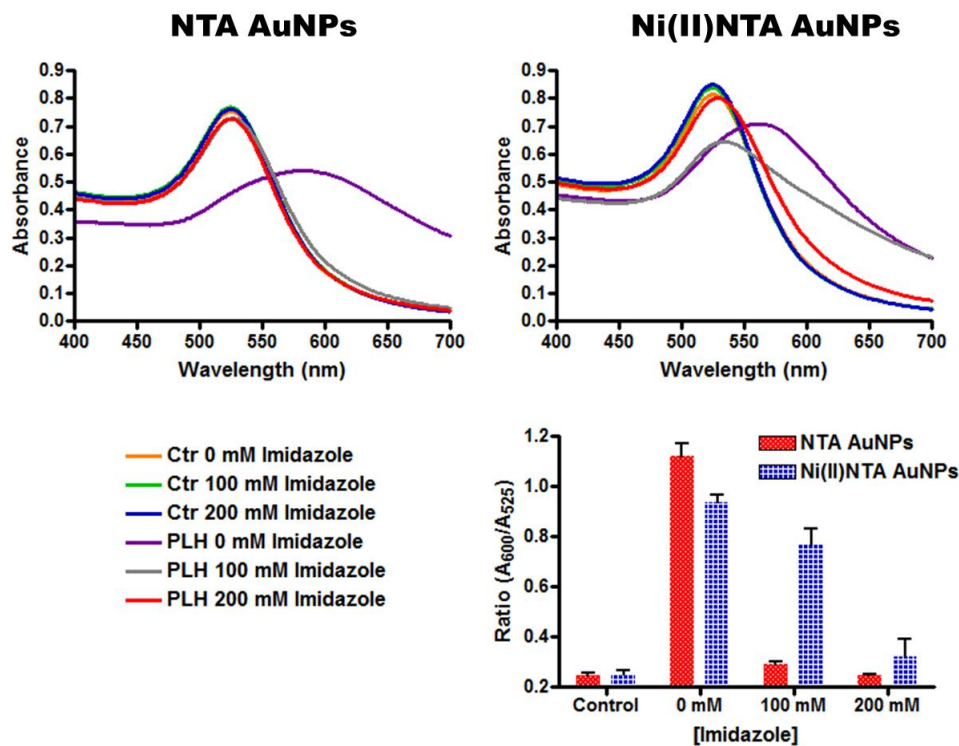


Figure 60. Effect of imidazole on the aggregation of Ni(II)NTA AuNPs in the presence of PLH at neutral pH. Top: UV-Visible spectrum of Ni(II)NTA and NTA AuNPs in the presence of 125 nM PLH and variable concentrations of imidazole (Legend is on bottom left). Bottom right: Bar graph representing aggregation of the particles. The ratio of absorbance (A_{600}/A_{525}) is used to quantify the amount of aggregation observed with the particles.

PLH induced aggregation of Ni(II)NTA AuNPs also demonstrated a pH dependence over a range of pH 4 to pH 9. It should be noted that the Ni(II)NTA particles are unstable at pH's below 4. In addition, it is known that Ni(II) leaches from NTA at low pH (Acidic solutions are commonly used to strip Ni(II) from Ni(II)NTA purification columns). Aggregation of the nanoparticles was detected spectrophotometrically for PLH below pH 9.0. **Figure 61** demonstrates the aggregation behavior of the Ni(II)NTA AuNPs in the presence of PLH (200 nM) at variable pH (4-10). Titrations with PLH were also conducted at selected pH's (5.5, 7.4, and 9.0) to determine the limit of detection of aggregation. The limit of detection for aggregation was 32.6 nM at pH 5.5 and 14.0 nM at pH 7.4. No significant aggregation was observed at pH 9.0 even at ~425 nM.

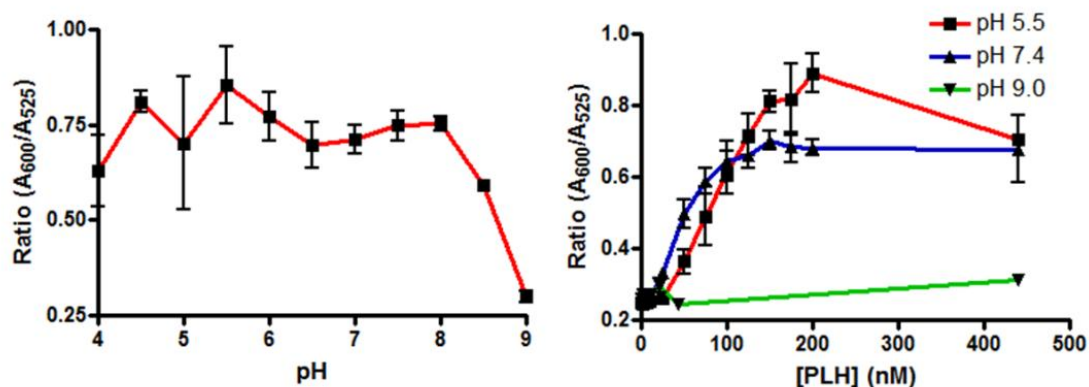


Figure 61. pH dependence of PLH-induced aggregation of Ni(II)NTA AuNPs. Left: Aggregation as a function of pH. Right: Titrations of PLH at selected pH's.

In addition to PLH, the Ni(II)NTA AuNPs aggregate in the presence of the basic polymeric amino acids PLL and PLR, consistent with the idea that multivalent targets induce the required crosslinks for aggregation (**Figure 62**). Each of the basic poly-amino acid ligands induced aggregation of the nanoparticles at each of the pH's tested, while poly-L-aspartic acid (PLD) did not. It is likely that the multivalent carboxylic acids

outcompete NTA for binding of the Ni(II) ion and subsequently leach it from the nanoparticle, much like EDTA strips Ni(II) from an Ni(II)NTA agarose column.¹⁸³ As aggregation could be inhibited above pH 7 by high concentrations of imidazole, these poly-amino acids likely serve as coordinative crosslinks between nanoparticles. In addition, aggregation of the particles appears to be dependent on the size of the polymer. Titrations performed with variable sized PLL polymers at neutral pH suggest that larger polymers induce aggregation of the particles at lower concentrations. Since larger polymers have more binding groups per polymer, it is likely that they are able to coordinate to multiple particles, inducing crosslinking at lower concentrations. This also correlates well with the higher limits of detection observed for PLH, for the polymer is only ~8,000 g/mol.

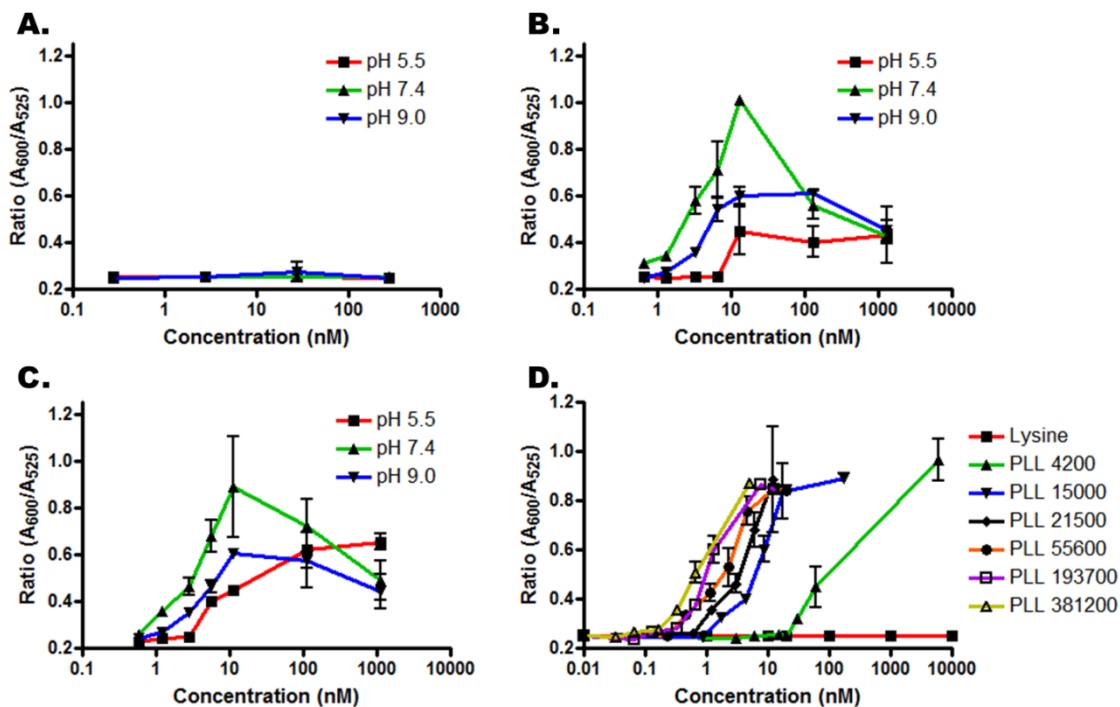


Figure 62. Aggregation behavior of Ni(II)NTA AuNPs in the presence of acidic and basic poly amino acids at variable pH. Titrations with PLD (A), PLR (B), and PLL (C). Note: polymer sizes are 12,500 g/mol for PLD, 12,500 g/mol for PLR, and 55,600 g/mol PLL, respectively. D.) Effect of polymer size on aggregation of Ni(II)NTA AuNPs.

To understand how the gold interacts with a biologically relevant sample, the particles were tested for aggregation behavior in the presence of two peptide mimics of the malarial protein *pf*HRP-II. pHRP-II is a 27 amino acid linear peptide containing the antigenic repeat (AHHAHHAAD)₃ targeted by many RDT's. BNT-II is a functional dendrimeric mimic of *pf*HRP-II previously synthesized by Zeigler and coworkers.²¹⁷ This peptide contains 4 branched repeats of (AHHAHHAAD)₂, which provides 16 heme binding motifs (its natural substrate) and a more realistic globular structure. Much like PLH, both mimics induced aggregation of the nanoparticles at pH's below 6.5, however no particle aggregation was observed at neutral pH or higher (**Figure 63**). Titrations of the mimic targets at pH 5.5 revealed that the limit of detection of pHRP-II is 616.6 nM. With the more realistic biological mimic BNT-II, the limit of detection is improved to 189.7 nM.

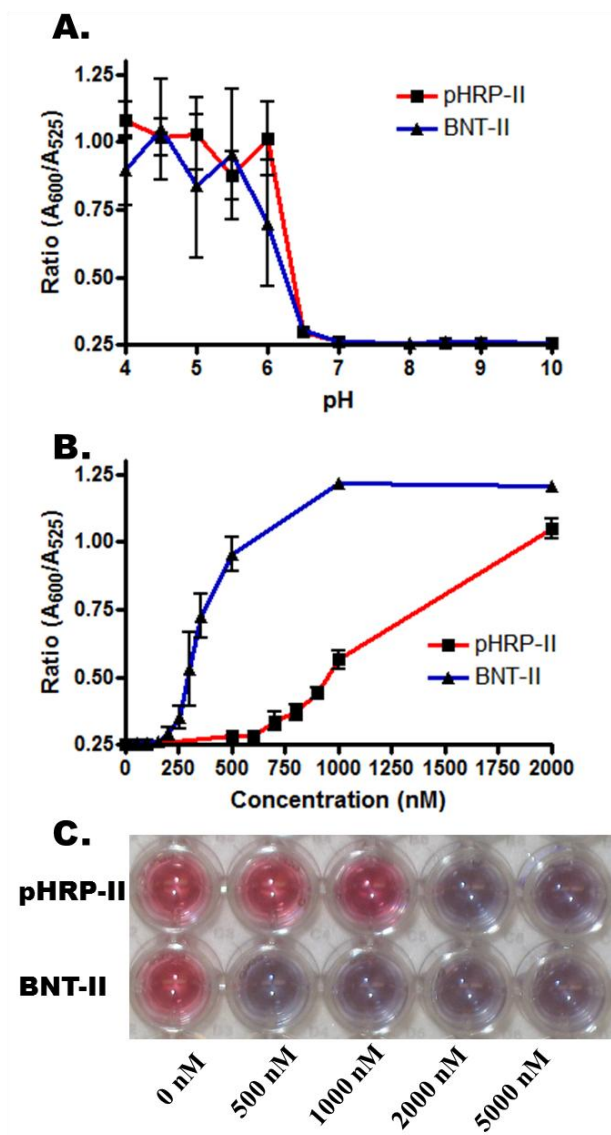


Figure 63. Aggregation of Ni(II)NTA AuNPs in the presence of the malarial mimics pHRP-II and BNT-II. A.) pH dependence of aggregation. B.) Titration of the mimics at pH 5.5. C.) Photographic image of Ni(II)NTA AuNPs in the presence of variable concentrations of malarial mimics.

When the smaller malaria mimics, pHRP-II and BNT-II were reacted with Ni(II)NTA AuNP's, the aggregation behavior of the NP's was very sensitive to the pH of the solution. Indeed, BNT-II and pHRP-II only induced aggregation at pH's below 6, showing a marked decrease in aggregation at pH's higher than the pK_a of histidine. As noted above, the ~8,000 mw amino acid PLH polymer induced aggregation of the

particles throughout the pH range tested. This difference suggests that the smaller, globular mimics are aggregating through a mechanism different than only simple coordinative crosslinking. At the pKa of histidine, 50% of the imidazole rings are deprotonated and available to coordinate the Ni(II) within the functionalized NP's. The other 50% are protonated and available for the formation of hydrogen bonds to deprotonated histidines on other mimic molecules or electrostatic crosslinks. The resulting composite is likely an aggregate of mimics coordinated to the Ni(II) of the NPs and cross-linked to other target mimic molecules through hydrogen bonding and electrostatic interactions. Similar pH dependent assembly of multi-valent histidine coated nanoparticles has been previously observed.²²⁶ At higher pH, the small peptide mimics simply saturatively coordinate the Ni(II) sites covering the nanoparticles, effectively blocking aggregation. Unlike the larger amino acid polymers, the small size of these mimics prevents particle-particle crosslinks due to repulsive particle-particle forces. Consequently, little aggregation is seen above pH 6. Consistent with this model is the fact that over the range of detectable aggregation the ratio of BNT-II to particles is ~80:1 at the LOD.

In complex biological mixtures such as human blood or saliva, proteins such as transferrin (TF), histidine rich glycoprotein (HRG), human serum albumin (HSA), and α -2 macroglobulin (α 2) are at high concentrations and could act as interferents to the aggregation assay by inducing non-specific aggregation. Physiological concentrations of these proteins were incubated with the Ni(II)NTA AuNPs at pH 5.5 and 7.4 and no aggregation was observed. UV-Visible spectral profiles of Ni(II)NTA AuNPs in the presence of the protein targets indicated a slight 2 nm shift for the Plasmon absorption

without any significant peak broadening (**Figure 64**). This is in stark contrast to particles reacted with the histidine-rich targets, which showed dramatic shifts in their Plasmon absorption to longer wavelengths. Interferents can also inhibit aggregation by absorbing to the particles and reducing the binding sites available to bind to the target. To test the aggregation properties of PLH in the presence of a complex mixture, a 9% serum solution was spiked into a solution of Ni(II)NTA AuNPs and reacted against PLH at neutral pH. Aggregation of the particles by PLH was drastically perturbed and only began to show particle instability micromolar range, as compared to ~25 nM in buffer only. In addition, the inclusion of 75 mM imidazole as a blocking agent did not recover the aggregation behavior as well. This suggests that complex mixtures may inhibit or drastically reduce the aggregation capabilities of the particles.

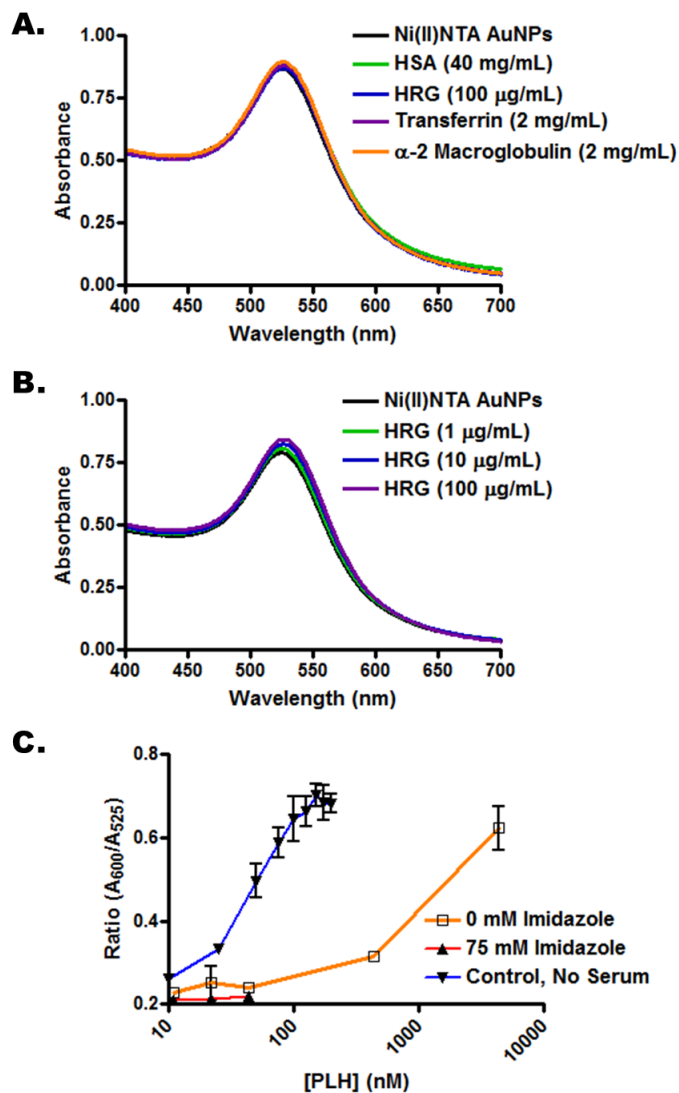


Figure 64. Aggregation properties in the presence of interfering proteins. A.) UV-Visible spectra of Ni(II)NTA AuNPs in the presence of physiological concentrations of serum proteins at pH 5.5. B.) UV-Visible spectra in the presence of variable concentrations of HRG at pH 7.4. C.) Titration profile of the particles in the presence of serum and imidazole.

A requirement for the ultimate application of these functionalized nanoparticles in diagnostic assays is that non-specific interactions between the nanoparticles and other components found in a complex biological matrix do not induce aggregation. Current RDTs for malaria target *pf*HRP-II in either whole blood or saliva from an infected

patient.²¹ Within such complex mixtures are proteins (e.g. HRG, TF, HSA, and α_2) which are known to have some affinity to M(II)NTA columns at neutral pH.¹⁷⁷ For example, HRG is a 75 kDa protein (507 amino acids) found in relatively high concentrations in human serum (100-200 $\mu\text{g/mL}$).²²⁷ Of the six domains that make up the HRG protein, only the 60 amino acid region of the histidine-rich region (HRR) contains tandem repeats of histidine.¹⁹⁴ Within this region, there are conserved repeats of GHHPH, which serve as a Zn^{2+} and heme binding domains. Much like *pf*HRP-II, HRG has been readily purified from serum using Ni(II)NTA agarose affinity chromatography.²²⁸ However, the experimental evidence suggests that neither HRG nor HSA induces aggregation of the particles at pH 5.5, where aggregation was observed for the *pf*HRP-II mimics. In the case of HRG, the localization of the histidine-rich site concentrated in a single protein domain, as opposed to the complete distribution of such sites in *pf*HRP-II, limits possible crosslinked driven particle aggregation. Furthermore, at low pH, these control proteins will be protonated, thereby reducing their ability to coordinate with Ni(II)NTA. Similarly, the negative control HSA protein did not induce aggregation of the nanoparticles. While these control serum proteins may show some slight affinity to the nanoparticles, they do not induce aggregation at normal physiological concentrations.

One of the primary advantages of using metal chelation based molecular recognition is the avoidance of thermally sensitive reagents such as antibodies. The long-term stability of the particles was evaluated by storing the particles at room temperature and 37°C for several weeks before testing their aggregation behavior with PLH. After four weeks of storage, the Ni(II)NTA AuNPs showed no indication of storage-induced aggregation and similar aggregation behavior in the presence of PLH, suggesting that

these particles are stable throughout the study (**Figure 65**). Therefore, Ni(II)NTA AuNPs demonstrate the potential thermal and storage stability required for further development in global health applications.

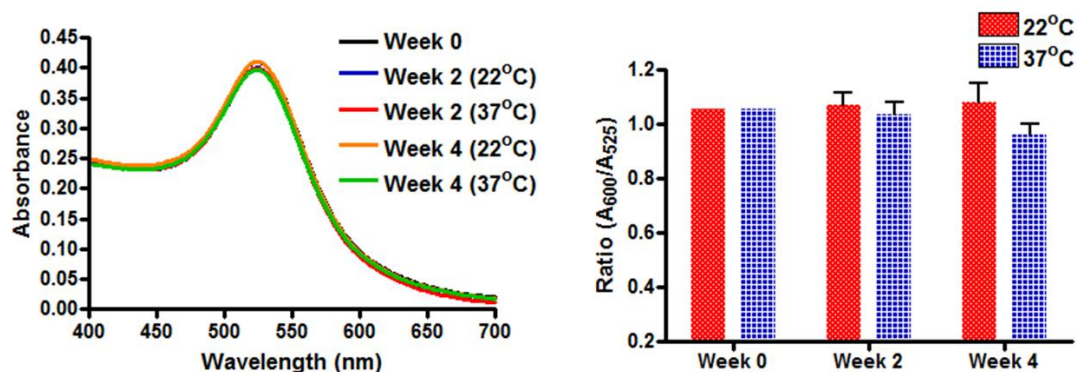


Figure 65. Thermal stability of Ni(II)NTA AuNPs. Left: UV-Visible spectra of the particles after multiple weeks of storage at room temperature and elevated temperatures. Right: Aggregation behavior of the particles in the presence of PLH after multiple weeks of storage.

Aggregation Properties of the Mixed-Monolayer Ni(II)NTA AuNPs with Recombinant HRP-II

After all of the systematic studies were conducted using 100% Ni(II)NTA AuNPs, polymeric amino acids and malarial mimics, a recombinant HRP-II was obtained. This particular protein consists of a 30 kDa monomer of *pf*HRP-II tagged with a 25 kDa glutathione-S-transferase (GST) tag, which is used for protein purification. This protein mimic, although not a complete replicate of *pf*HRP-II, should induce aggregation of the particles. A systematic study was conducted to determine the ideal pH range for aggregation as well as the optimal NTA surface coverage of the particles (**Figure 66**). Using a 1 nM particle concentration, the particles with 25 and 50% coverage are the most sensitive toward aggregation in the presence of recombinant HRP-II (135 nM). Particles

that are completely coated with Ni(II)NTA are less sensitive to aggregation, likely due to the steric crowding associated with loading such a bulky ligand to the surface of the particles. As the surface coverage is lessened to 1-10% coverage, the particles aggregate much less, suggesting that there is insufficient Ni(II)NTA coverage to induce particle crosslinking. Particles with only the HO-PEG-Thiol did not aggregate under any conditions tested, confirming that the Ni(II)NTA moiety is necessary for aggregation to occur. Using the 50% Ni(II)NTA nanoparticles, the pH dependence was investigated. Much like the peptide mimics, aggregation is most prevalent around the pKa of the protein, confirming that the mechanism proposed for the peptide mimics also holds true for recombinant HRP-II.

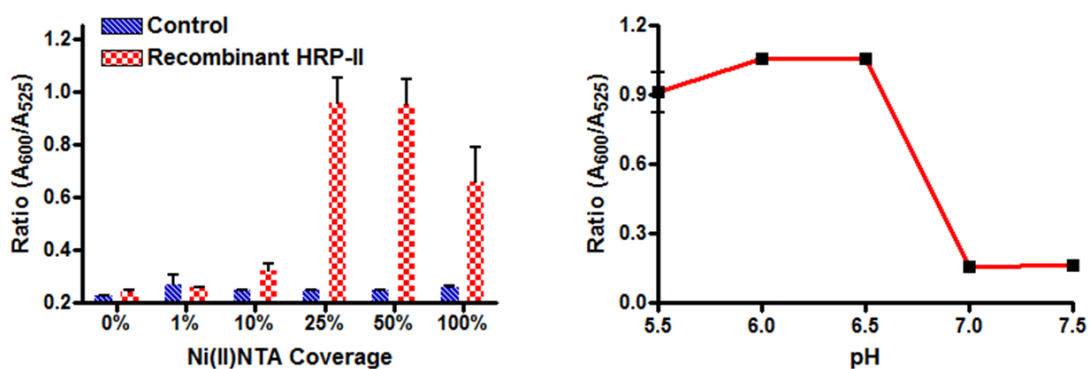


Figure 66. Aggregation properties of mixed monolayer Ni(II)NTA AuNPs in the presence of recombinant HRP-II. Left: Comparison of aggregation properties as a function of surface coverage. Right: pH dependence of aggregation using the 50% Ni(II)NTA AuNPs.

The limit of detection for recombinant HRP-II was determined at variable concentrations of AuNPs. Spectrophotometric limits of detection for AuNPs is ~100 pM, so titrations were performed for 0.1-2 nM nanoparticle concentrations (**Figure 67**). There is an aggregation dependence on particle concentration from 0.5-2 nM. At concentrations below 0.5 nM, the concentration of particles is so dilute that there is no difference in

aggregation. Using a sigmoidal curve fit for the higher concentrations, the limits of detection were determined to be 32.6 nM, 56.7 nM, and 80.7 nM for 0.5 nM, 1 nM, and 2 nM particles, respectively. As the particle concentration is increased, it takes more protein to destabilize the particles and induce aggregation.

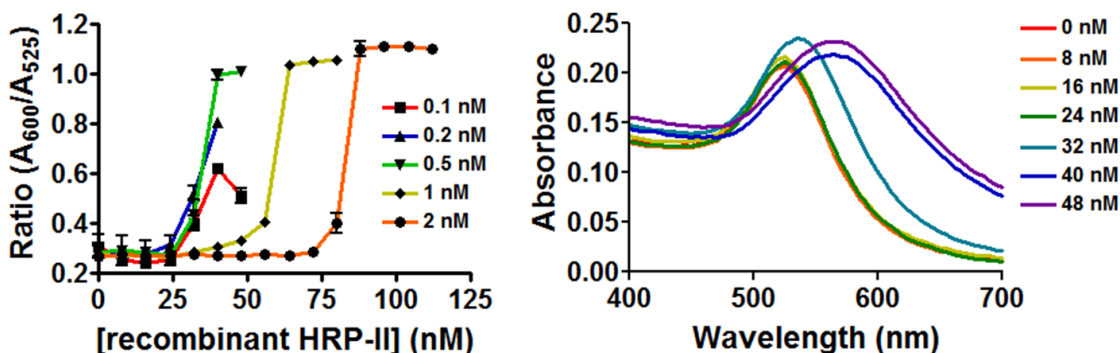


Figure 67. Limits of detection of recombinant HRP-II in the presence of variable concentrations of 50% Ni(II)NTA AuNPs. Left: Titrations at variable concentrations of particles and target. Right: UV-Visible spectral profile of the titrations with 0.5 nM Ni(II)NTA AuNPs.

Development of the Coffee Ring Assay

Ring formation was initially inspected by depositing reaction solutions containing a 2 nM solution of 50% Ni(II)NTA AuNPs in the presence of recombinant HRP-II. A 2 nM solution was chosen because it is very difficult to visible detect aggregation of AuNPs at lower concentrations. The incubation of the particles was conducted for 15 minutes, after which a 0.5 μ L drop was deposited onto a Ni(II)NTA functionalized glass slide and allowed to completely dry. After drying, the slide was washed copiously with water to remove any weakly bound particles and residual salts and inspected with microscopy (**Figure 68**). Upon visual inspection of the samples, a clear, well defined ring is present at concentrations above 80 nM. At higher concentrations (>120 nM, not shown), the particles are largely aggregated, and likely precipitate out of solution before they are able

to travel to the drying drop edge. With a density of 19.3 g/mL, large gold aggregates are likely to precipitate and readily settle out of solution. Below the limit of detection, there is residual gold remaining on the slide, but the ring diameter is significantly reduced. It is likely that during the drying process, the contact line recedes until the overall concentration of gold remaining in solution is high enough to induce contact line pinning.

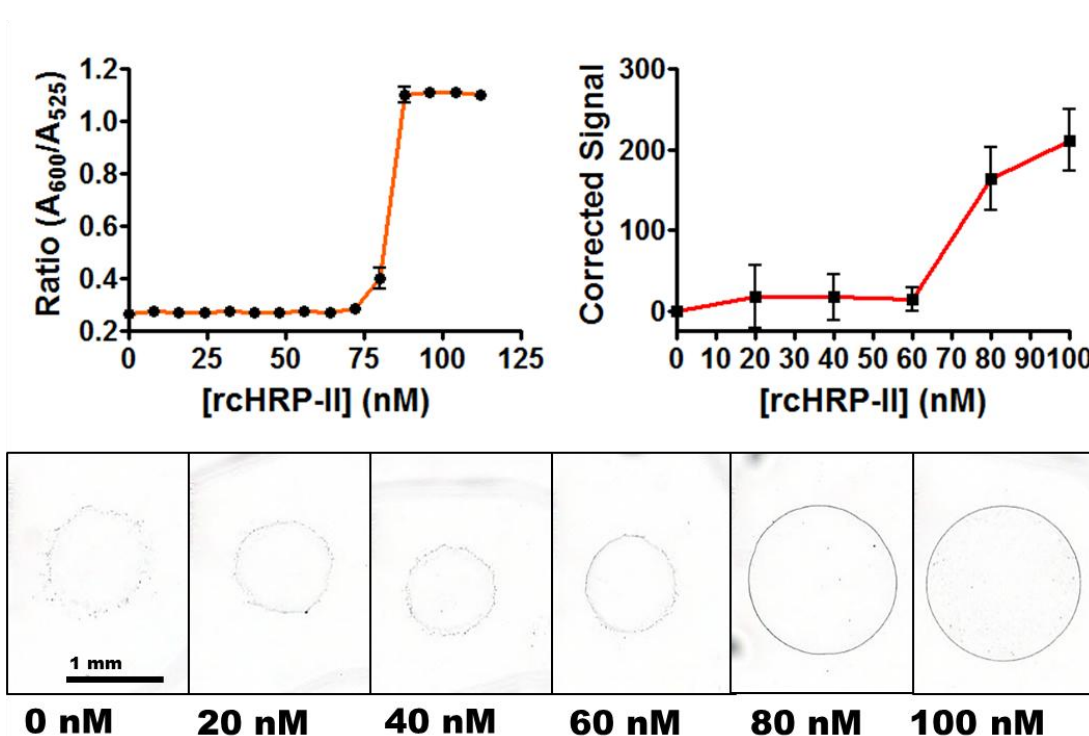


Figure 68. Coffee ring formation induced by HRP-II induced pinning of Ni(II)NTA AuNPs during drop drying. Top left: UV-Visible titration of recombinant HRP-II in the presence of 2 nM Ni(II)NTA AuNPs. Top right: Corrected total signal of the drops deposited onto a Ni(II)NTA glass slide. The corrected signal is calculated by subtracting the total signal by the control without protein. Bottom: Representative images of coffee rings formed as a function of protein concentration.

The total signal of the ring was measured using a custom protocol in Image Pro Plus. First, the images were inverted so that the gold nanoparticle ring represents a positive signal. The images were then background corrected to flatten the image and set the background to zero. Next, a predefined Area of Interest (AOI) at each corner was

measured for signal intensity to normalize any variation across the image. Another predefined AOI was then centered on the drop region to measure the total intensity of the drop. The final signal value was produced by subtracting the mean background intensity from the drop intensity. This value represents a difference in intensity of the region occupied by the drop compared with the rest of the image. For the titration above, the overall signal is visibly higher for images that contain well-defined rings.

Even though there is a clear indication that the presence of recombinant HRP-II induces contact line pinning and subsequent ring formation, it is not clear whether interfering proteins would also induce ring formation. Using a 1 μL drop, samples containing 48 nM human serum albumin (HSA) and glutathione-S-transferase (GST) were deposited on Ni(II)NTA slides, allowed to dry, and washed (**Figure 69**). Both control proteins produced partial ring structures that generated high signal values. Although the proteins do not induce the in-solution aggregation of the particles, their interaction with the particles in a confined space along the drop edge assists in pinning the particles.

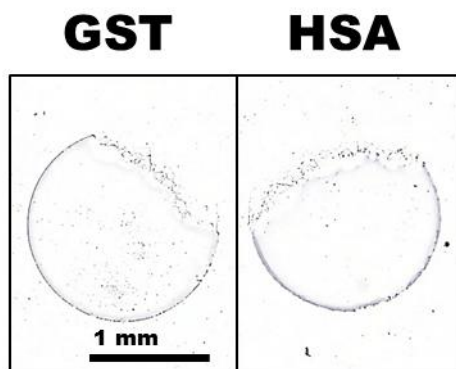


Figure 69. Coffee ring formation induced by interfering proteins. A solution of 2 nM AuNPs was incubated with 48 mM GST or HSA and spotted onto a Ni(II)NTA slide and dried. The addition of the proteins induced ring formation.

One way to reduce this interfering interaction is to include glycerol in the drop solution, which prevents complete drying of the drop. Glycerol at relatively high concentrations is commonly used to disrupt the coffee ring phenomenon by disrupting the pinning of the contact line in microarray applications.²²⁹ Since this assay relies on coordinative capture of the particles on the surface rather than surface heterogeneities, glycerol may actually be useful in disrupting non-specific interactions. Glycerol was included in the drop by first incubating the particles in the presence of the recombinant HRP-II, followed by addition of a small volume of glycerol prior to drop formation. **Figures 70** and **71** show the ring profiles as a function of glycerol for both particles only and particles incubated with recombinant HRP-II. The overall signal of the control is reduced 4-fold with the addition 1% glycerol, whereas the positive control maintains ~60% of its total signal. Ring formation is maintained up to 2.25% glycerol, with a steady decrease in signal. At 2.5% glycerol, ring formation is completely disrupted. Inspecting the control drops prior to washing revealed a trend in film behavior. Without glycerol, there is a film deposited onto the slide, likely from the salts found in the drops. As the glycerol concentration is increased, a small collection of fluid remains on the slide, consistent with increasing volumes of glycerol which will not dry. For the negative control, the contact line doesn't pin above 1% glycerol and the particles appear to recede with the residual glycerol. For the positive control, the behavior of the pre-washed slide indicates that the contact line is initially pinned and remains until the final stages of drying. The decrease in overall signal may be partially a result of increasing volumes of liquid that doesn't dry.

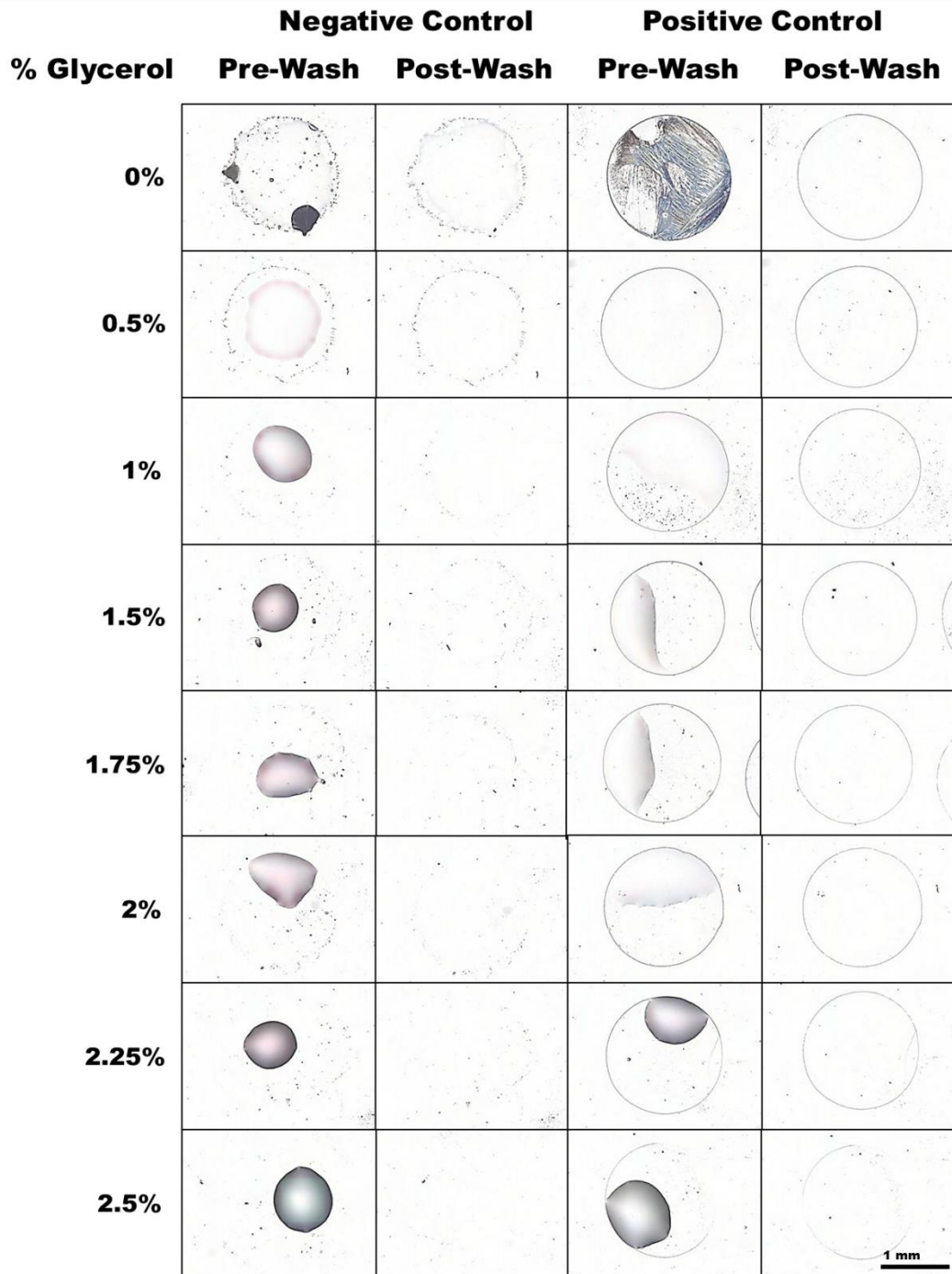


Figure 70. Effects of glycerol on ring formation. Solutions containing 2 nM particles and either 64 nM recombinant HRP-II or water were incubated for 15 minutes, followed by the addition of glycerol prior to drop deposition. Background interference is significantly reduced with 1% glycerol and rings are still visible for the positive controls in the presence of 2.25% glycerol.

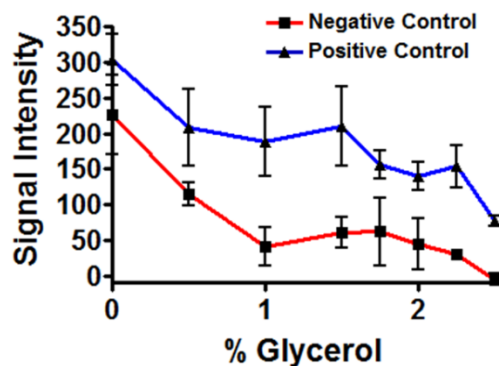


Figure 71. Signal intensity calculated using the custom protocol on Image Pro Plus software. As the concentration of glycerol is increased, the amount of background signal is significantly decreased while the ring signal remains relatively strong.

After determining that glycerol can reduce the non-specific signal generated by a negative control, titrations were performed with recombinant HRP-II and the two control proteins with 1.75% glycerol. **Figure 72** shows the functionalized surfaces after incubation with Ni(II)NTA nanoparticles in the presence of recombinant HRP-II, GST, and human serum albumin (HSA). In this case, not only are rings formed for recombinant HRP-II, there is essentially no background signal for either of the control proteins. In addition, there appears to be detectable ring formation at 64 nM, which was not observed under the glycerol-free conditions. Glycerol not only prevents the drop from drying, it also likely slows down the rate of evaporation. Since the reaction was allowed to proceed longer, it is likely this extended period of time allows the aggregates longer periods of time to bind to the functionalized surface.

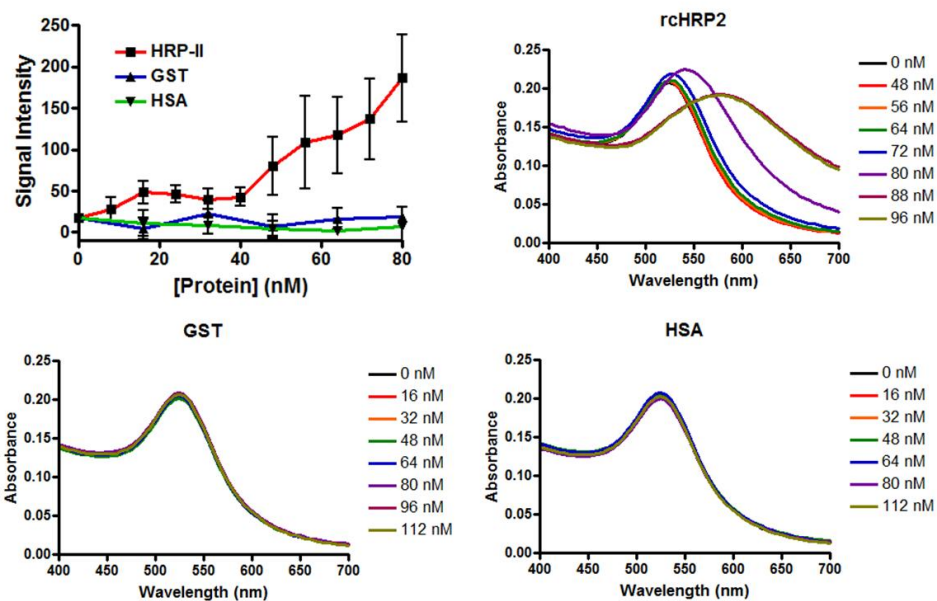
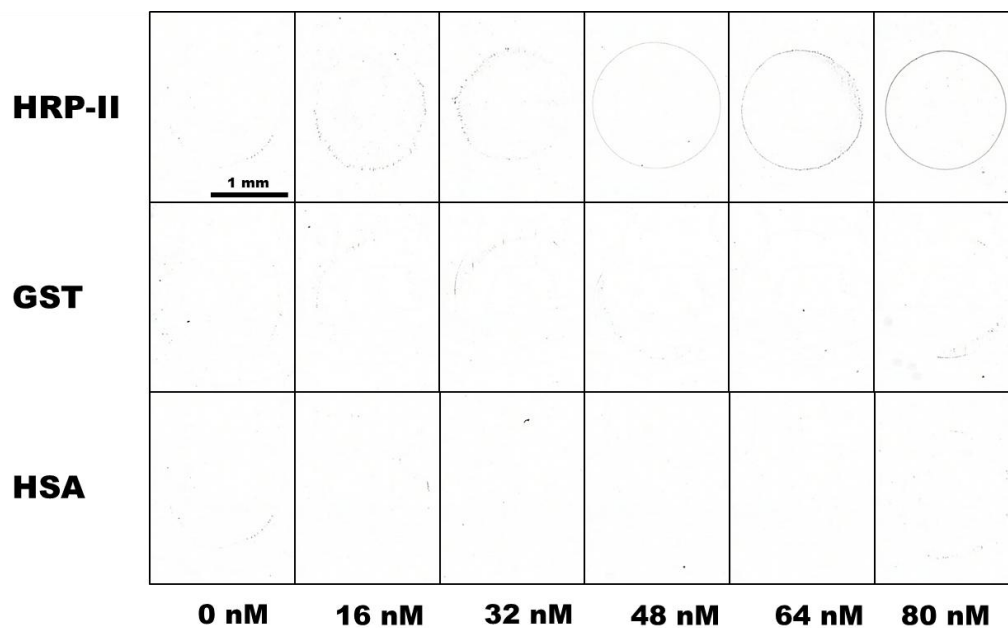


Figure 72. Selective coffee ring formation induced by recombinant HRP-II induced pinning of Ni(II)NTA AuNPs during drop drying. Using 1.75% glycerol during drop drying, the particles were incubated with varying concentrations of recombinant HRP-II and the interfering proteins. The presence of glycerol inhibits ring formation for the interfering proteins, while rings readily form in a concentration dependent for HRP-II. Middle left: Signal calculated using the custom analysis protocol. Bottom and right: UV-visible spectra of the particles in the presence of the proteins.

Discussion/Future Directions

Based on the above data, we have successfully employed Ni(II)NTA AuNPs to induce a colorimetric change upon aggregation with recombinant HRP-II. Through radial flow of an evaporating drop, the aggregated particles radially flow to the drop edge and selectively form purple rings detectable by microscopy. Although AuNPs maintain several advantages including a high coefficient of diffusion due to their size, facile and well-developed surface chemistry, and colorimetric sensitivity toward particle aggregation, there are several fundamental limitations with the current system. AuNP rings at lower limits of detection are difficult to see by eye, likely due to their small sizes. In addition, the current limits of detection with this system are in the nanomolar range, which are still 1-2 orders of magnitude above the desired limit of detection. Although this current design appears to lack the robustness to be applicable in the field, the built-in modularity of the technology allow for the modification of assay components to improve the limits of detection.

One obvious approach is to increase the size of the capture bead so that it provides more signal on a per bead basis. Larger gold nanoparticles are likely poor candidates because of their rapid settling velocities above 50 nm, as well as the complete loss of their colorimetric properties. Instead, larger particles consisting of other materials, such as silica or polystyrene can be used instead. For example, a 1 μm polystyrene particle has a density of 1.05 g/mL, which makes it essentially soluble in water during the drop drying process. Work is currently being performed involving overcoating polystyrene microspheres with a layer of gold, which allows for facile surface functionalization of thiolated ligands. Previously, it was demonstrated that polystyrene particles readily form

rings in aqueous solutions (**Figure 73**). In addition, preliminary work shows that M(II)NTA polystyrene microspheres synthesized by chemical crosslinking of NTA to amine-functionalized microspheres selectively capture TAMRA-HRP-II at neutral pH. In addition, protein can be recovered off of the beads upon the addition of an imidazole solution (Data not shown). Although there is no indication that the ring assay would in fact work with these beads, their ability to capture HRP-II mimics is a promising step toward modifying the ring assay.

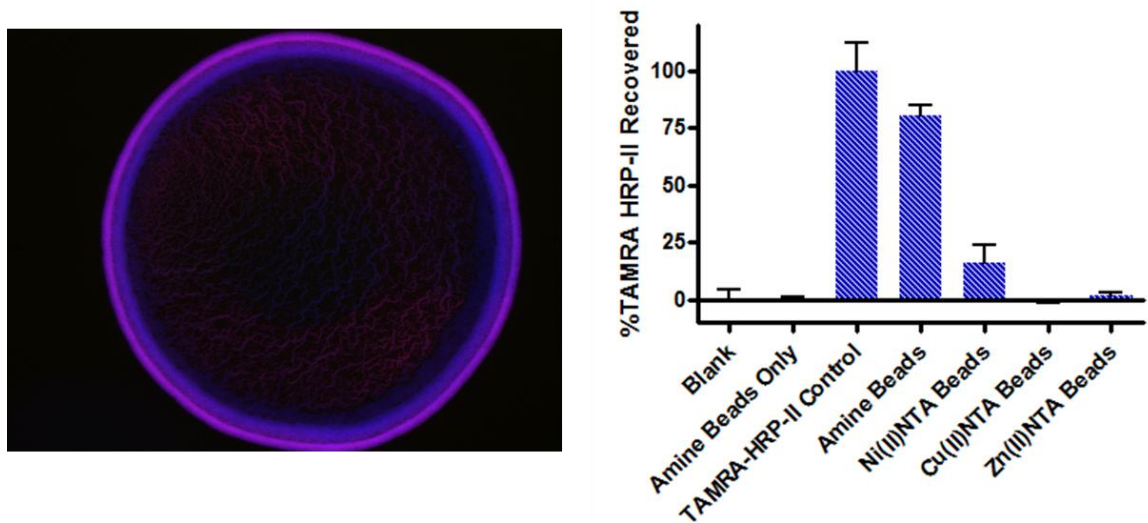


Figure 73. Demonstration of M(II)NTA polystyrene as an alternative capture bead in the coffee ring assay. Left: Polystyrene microspheres readily form coffee rings on glass substrates. Right: Demonstration of the selective binding of HRP-II mimics to M(II)NTA functionalized polystyrene microparticles.

Another modification of the current assay is to rethink how the coffee ring phenomenon is utilized. Although it is attractive to utilize radial flow to capture the beads onto the drying drop edge, most other solute materials, including interfering proteins, will also travel to the edge. Instead, an alternative design strategy has been developed in the Haselton lab that capitalizes on the radial flow to process the sample. Termed the “3-

bead” assay, this method utilizes three unique beads that serve specific functions (**Figure 74**). A control bead is introduced that always flows to the drop edge, serving to pin it in place and provide a control ring for reference. The other two beads are functionalized with capture ligands that selectively bind to the biomarker. One of these beads is magnetic, which allows for magnetic separation into the center of the drop, concentrating it. If selective capture is achieved, then both the magnetic and non-magnetic bead will be isolated in the center of the ring, yielding a colored bulls-eye.

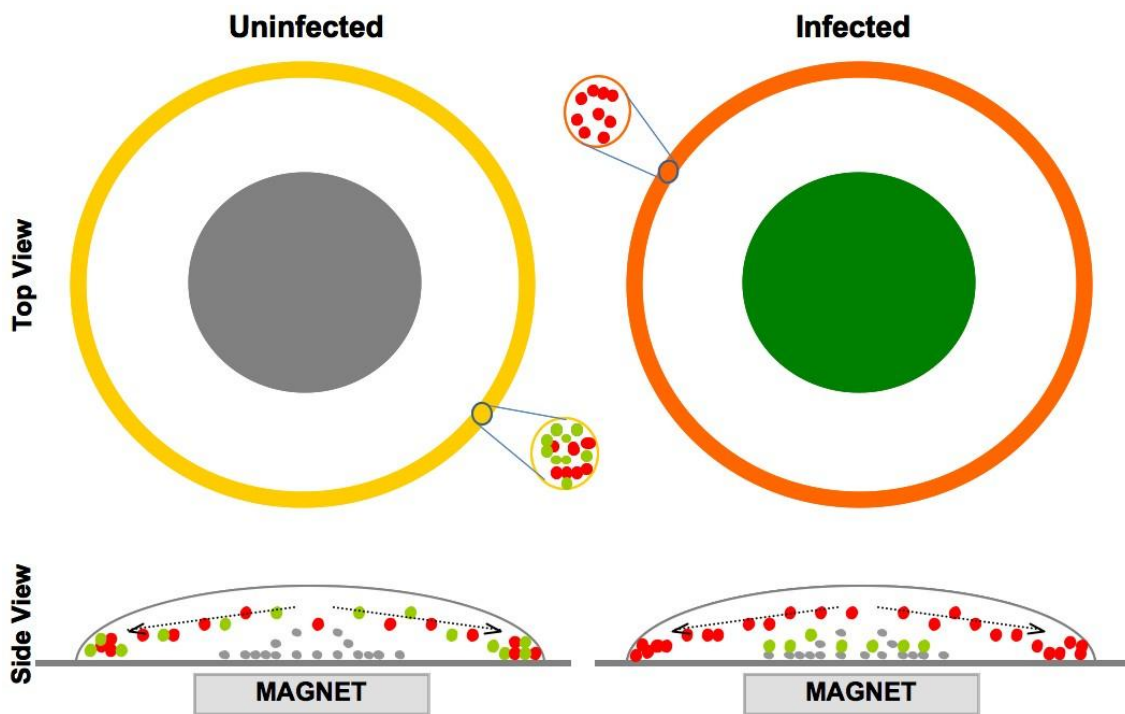


Figure 74. Three-particle coffee ring assay format. Two capture beads, one of which is magnetic are crosslinked in the presence of the biomarker. A control bead is also included to serve as a pinning agent and subsequent control ring. If the biomarker is present, the non-magnetic capture bead is entrained with the magnetic bead, generating a bulls-eye in the center of the drop. In a negative sample, the non-magnetic capture bead travels to the drop edge via radial flow and is deposited at the ring edge.

With the modified assay strategy in hand, optimization of the various parameters can be conducted. For example, the surface chemistry of the substrate can be tuned to

optimize sample resolution and drying time. In addition, the composition of the capture agent on the beads can be adjusted by the addition of backfill ligands, which could improve the overall signal of the assay. It is important to remember that every adjustable parameter is an opportunity to improve the overall efficacy of the assay and should be evaluated thoroughly.

Conclusions

In its current format, the limit of detection against recombinant HRP-II is two orders of magnitude higher than what is needed to match current diagnostic strategies. In addition, human whole blood poses a challenge because it provides colorimetric interference, as well as a potential aggregation inhibitor. As a standalone assay, this method doesn't meet the demands necessary of a low resource diagnostic. To circumvent these challenges, modifications of the assay are currently being developed that capitalize on the signal enhancement of a larger reporter bead and the concentration of the bead into a small central dot. These modifications will hopefully improve upon the limit of detection obtained in the current single AuNP capture bead strategy. In addition, it would be ideal if the coffee ring assay must be compatible with the sample processing technologies outlined in **Chapter V**. Together, this processing technology could be coupled with the coffee ring assay to detect *pf*HRP-II from whole blood in a simple and self-contained diagnostic for use in the developing world.

APPENDIX A

CRYSTAL ENGINEERING: SOLVENT EFFECTS ON β -HEMATIN FORMATION

Introduction

Blood feeding organisms implicated in malaria (*Plasmodium*), schistosomiasis (*Schistosoma mansoni*) and Chagas disease (*Rhodnius prolixus*) all digest large quantities of hemoglobin to meet their nutritional requirements.²³⁰ During the process, amino acids necessary for development and heme (Fe(III)PPIX) are released. In its free state, heme induces oxygen dependent free radical formation^{231,232}, lipid peroxidation^{233,234}, and protein²³⁵ and DNA²³⁶ oxidation. To eliminate heme toxicity, these organisms have developed a detoxification mechanism that converts the toxic free heme into a non-toxic crystalline form known as hemozoin.^{237,238} Powder X-ray diffraction analysis of this crystal revealed a triclinic unit cell with a space group of $P\bar{1}$.²³⁹ With average sizes in microns, the crystal is composed of heme dimers formed through reciprocal iron-carboxylate bonds²⁴⁰, where one of the two propionic side chains of a heme molecule coordinates with the axial Fe(III) of another. The remaining propionic acid group then hydrogen bonds with an adjacent dimer, forming an extended network of dimers.²³⁹ Hemozoin has traditionally been a key target in antimalarial drugs because disruption of crystal formation results in accumulation of free heme in the parasite, leading to death. Understanding the molecular details of hemozoin formation could lead to novel antimalarial designs.

Acquisition of hemozoin from model animals is labor intensive, and the yields are on the milligram scale at best. Research focused on hemozoin has relied heavily on a synthetic analog of hemozoin known as β -hematin. These crystals are chemically and structurally identical. Various synthetic routes have been widely used as synthetic routes for β -hematin formation, including benzoic acid²⁴¹, acetic acid²⁴², neutral lipids,²⁴³⁻²⁴⁵ detergents²⁴⁶, and alcohol²⁴⁷ systems. All the mentioned methods require that soluble heme is introduced to a crystal mediating system. Although each method appears to generate crystals, limited data is available on the comparability of β -hematin synthesized using these various systems. Hemozoin synthesized by the different parasites possesses a conserved molecular structure however; crystal morphologies differ significantly between the species. Crystals synthesized by *Plasmodium* are very regular in shape with well-defined crystal faces.²⁴⁸ *S. mansoni* derived hemozoin is roughly spherical and heterogeneous in size, ranging from 50 nm to a few micrometers in diameter.^{248,249} Hemozoin crystals extracted from *R. prolixus* exhibit irregular surface topography and are generally much larger than crystals obtained from *Plasmodium*.^{248,250} It is likely that the size and morphology differences between the species are directly related to the mediators used by the different species during *in vivo* crystallization.

This study focuses on the controllability of crystal morphologies using various solvent systems. A solvent mediated approach is a valuable method for investigating the mechanisms of chemical reactions in solutions that lead to crystal nucleation. Correlations between crystal morphologies and solvents' water miscibility and polarity properties are investigated. The controllability of crystal habits through the manipulation of solvent selection was also examined. My primary contribution to this study was to

synthesize β -hematin in the presence of a variety of solvents and analyze the products via scanning electron microscopy (SEM).

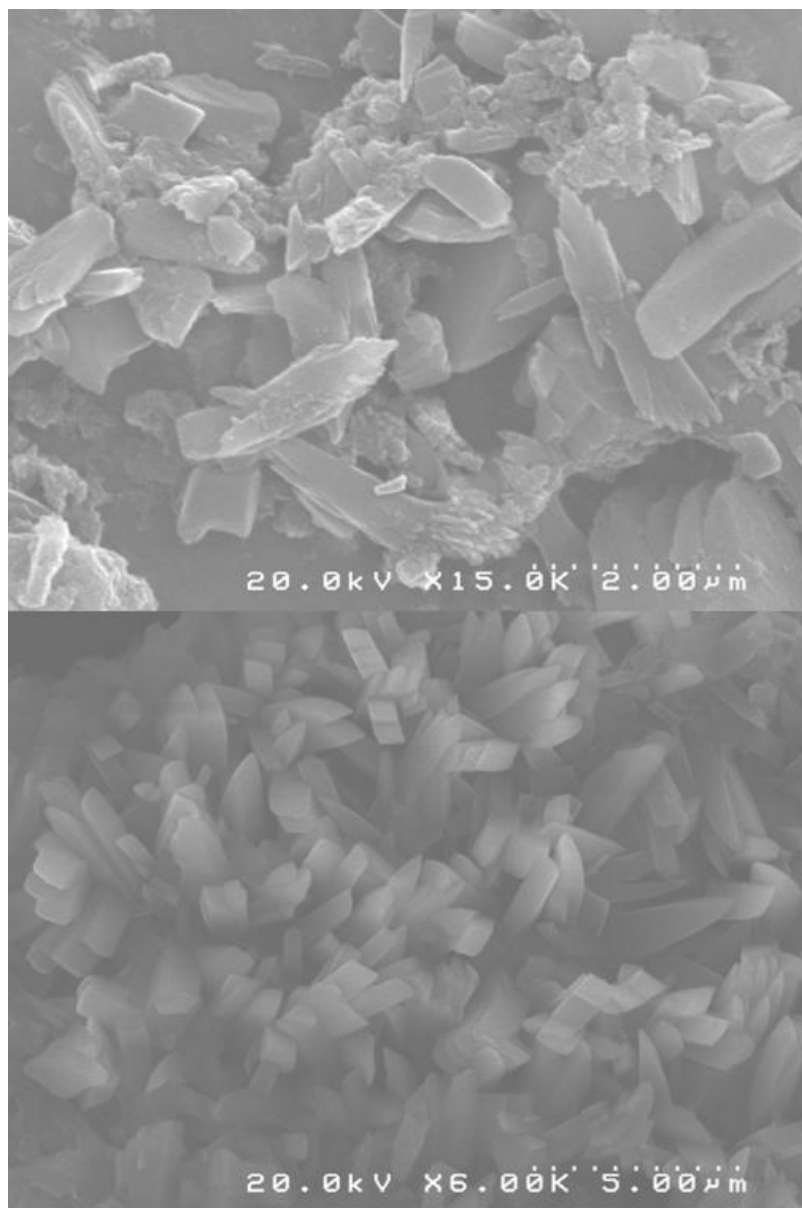
Methods

Synthesis of β -hematin with organic solvents: Hemin porcine (7 mg) was dissolved in 500 mL of solvent. The solid was dissolved by sonication. To this solution, 500 mL of 50 mM citrate buffer pH 4.8 was added and the solution was incubated at 40°C for 10 days. After incubation, the resulting crystals were centrifuged and washed with several aliquots of water and 0.1M sodium bicarbonate until the crystals were clean. The products were then dissolved in acetone and spotted onto SEM pucks and dried. The samples were then analyzed by SEM.

Results

Unlike β -hematin synthesized with other solvent systems^{251,252} which produce homogenous, bricklike crystals resembling hemozoin from *P. falciparum*^{248,253}, crystals produced in the current organic solvent/citrate buffer systems exhibited distinct morphologies that are dependent on the solvent conditions. Crystals formed by DMSO and acetonitrile exhibited morphologies that are regular in shape with the longest dimension being a few microns (**Figures 169 & 173**). These crystals are brick shaped with tapered ends that resemble hemozoin extracted from *P. falciparum* as reported by Sullivan *et al.* and Noland *et al.*^{250,253} Crystals formed in the DMF system were significantly striated, with many of the crystals being smaller than 300 nm in size.

Less size homogeneity was observed for crystals formed with chloroform and toluene. There are still tapering effects, although they are less frequent than what was observed for acetonitrile, DMF, and DMSO. Crystals formed under these solvents appear plate-like (**Figures 169, 172, and 173**). Crystals from the toluene system are very thin and extend approximately six times longer than those synthesized by the DMSO and DMF systems (**Figure 174**). β -hematin from the DCM system exhibits some level of crystal thickness with a smooth surface (**Figure 171**). Both DCM and toluene are only slightly soluble in water, so the likely location for β -hematin formation is at the aqueous-organic interface. Hexanes were also investigated, but didn't promote β -hematin formation. It is thought that the solvents must be at least slightly soluble so that some heme can reside in the aqueous phase for crystal promotion to occur.



Acetonitrile

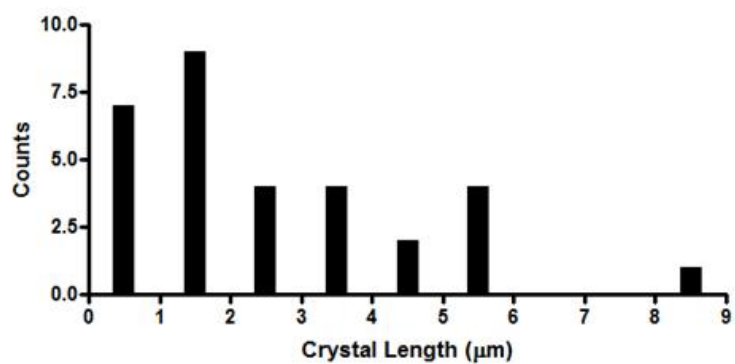
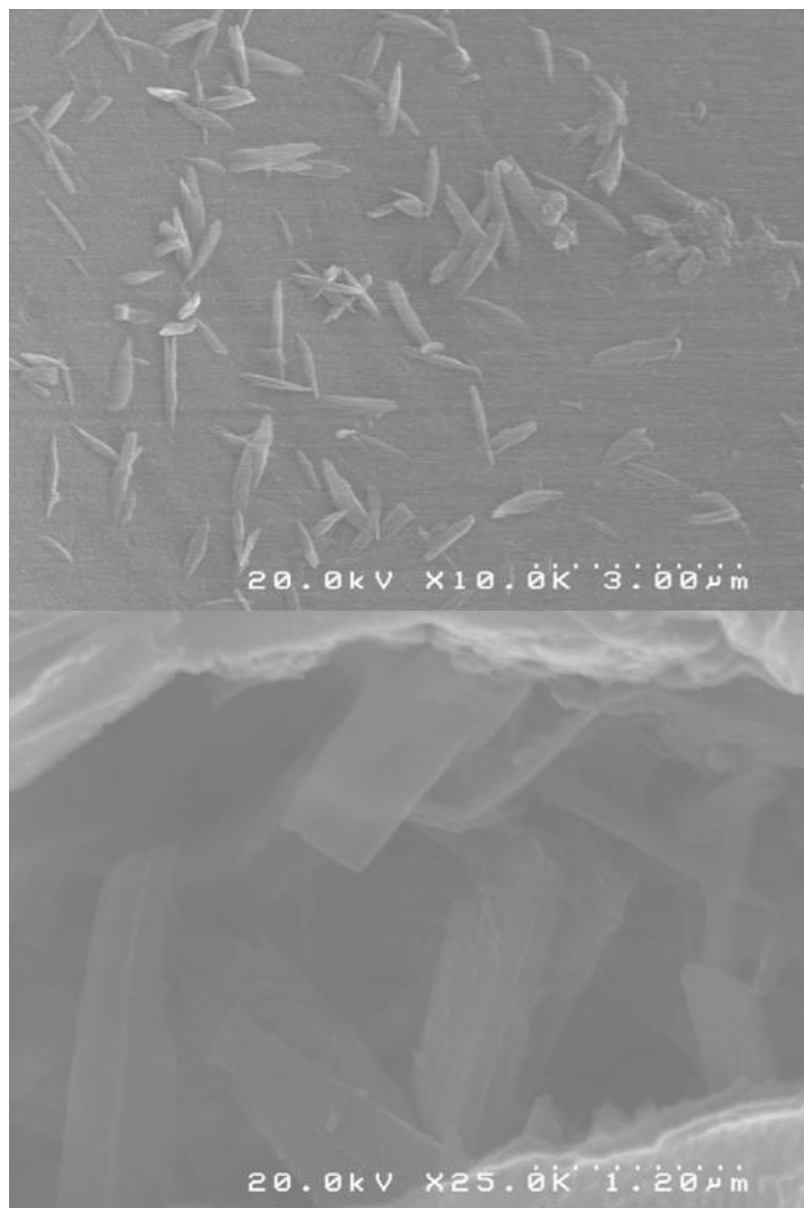


Figure 75. SEM Characterization of β -hematin synthesized with acetonitrile.



Chloroform

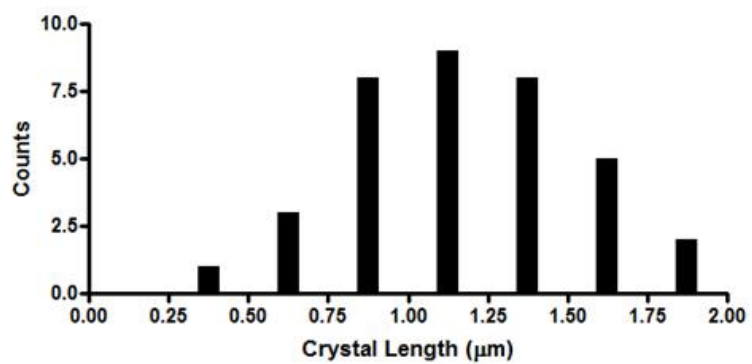
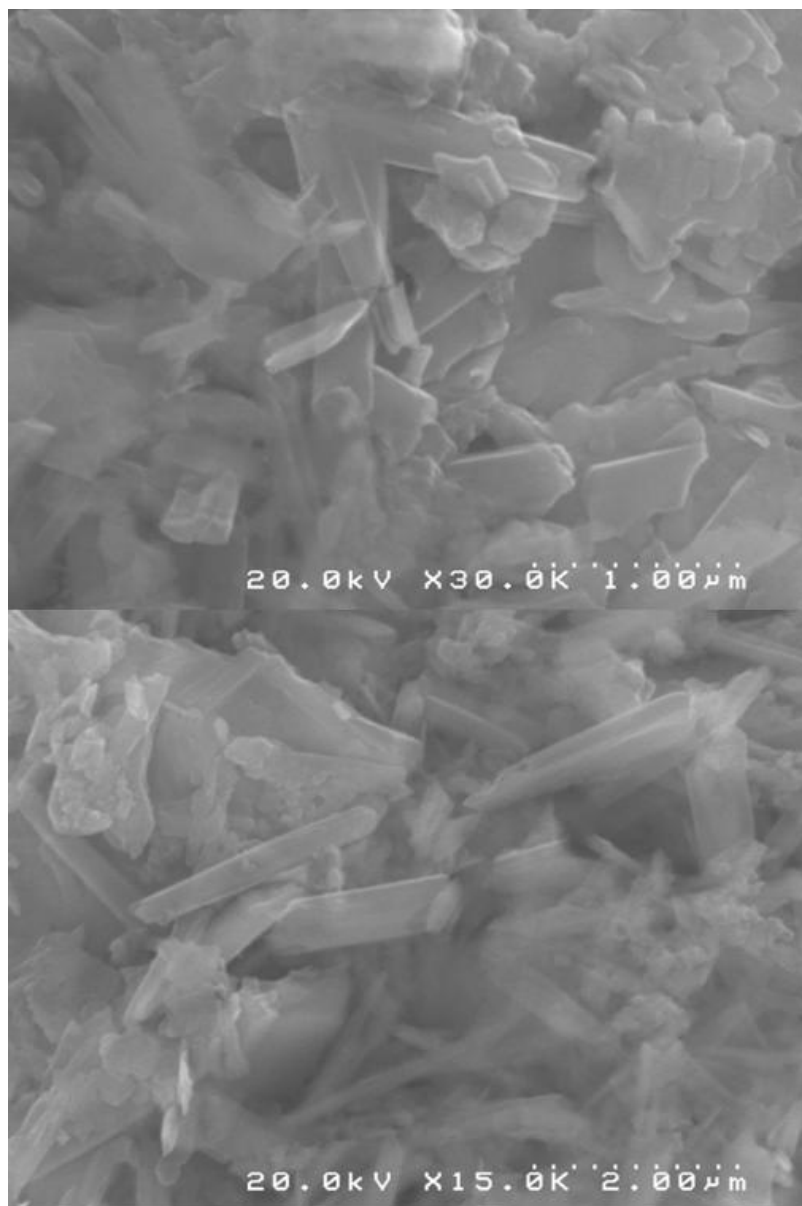


Figure 76. SEM Characterization of β -hematin synthesized with chloroform.



DCM

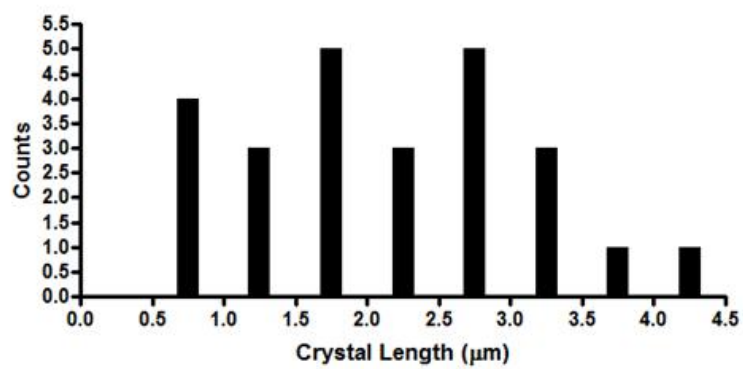
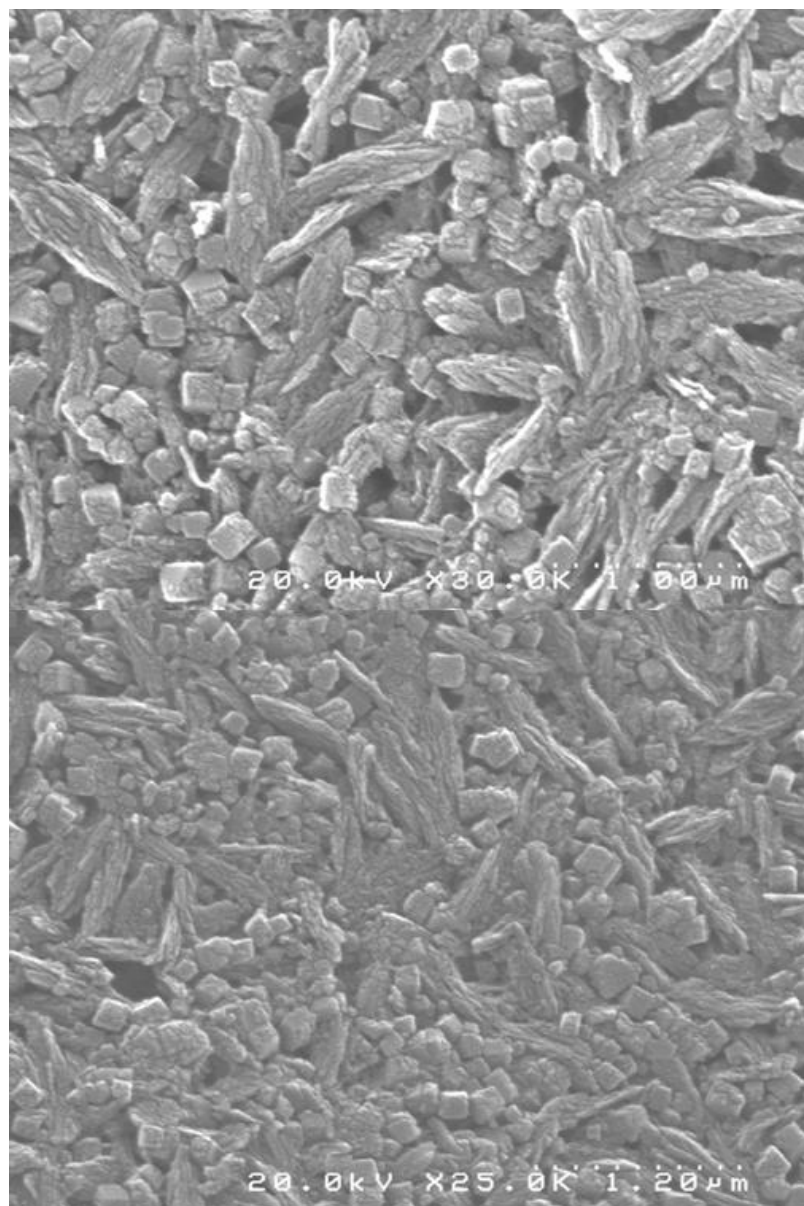


Figure 77. SEM Characterization of β -hematin synthesized with DCM.



DMF

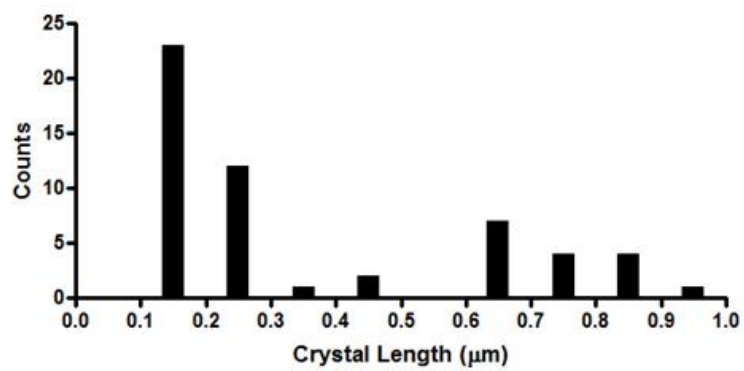
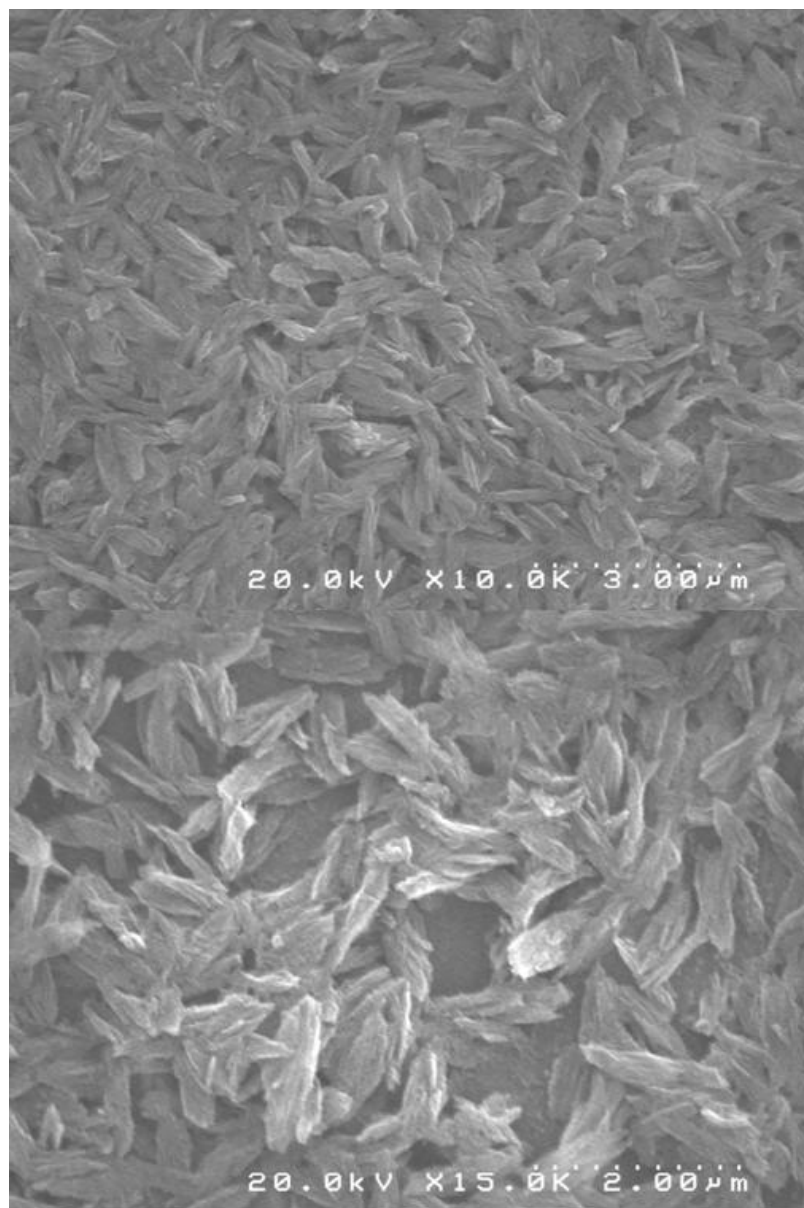


Figure 78. SEM Characterization of β -hematin synthesized with DMF.



DMSO

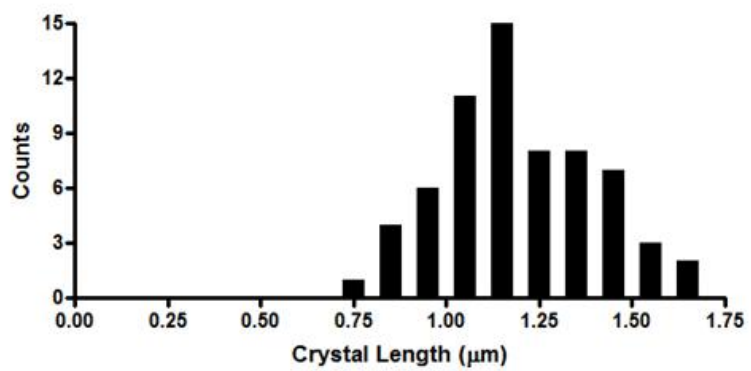


Figure 79. SEM Characterization of β -hematin synthesized with DMSO.



Toluene

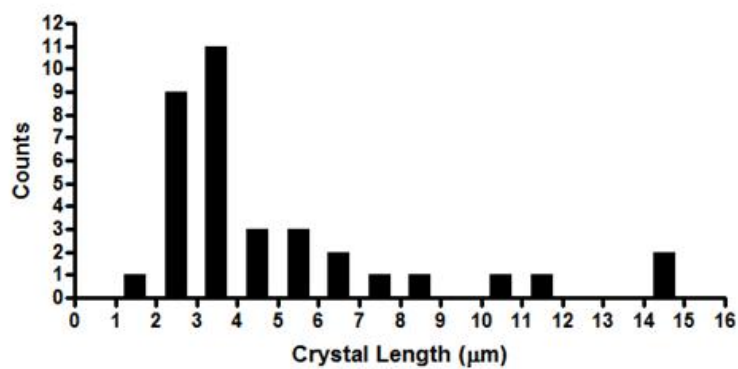


Figure 80. SEM Characterization of β -hematin synthesized with toluene.

Conclusions

This study provides a systemic approach to β -hematin crystal engineering. The introduction of heme to an acidic citrate buffered system containing water miscible solvents (DMSO, DMF, and acetonitrile) increased heme solubility and promoted spontaneous β -hematin crystallization. Morphological analysis of these crystals demonstrated brick-like structures, resembling Hz produced in *P. falciparum*. Slightly soluble solvents (DCM, chloroform, or Toluene) formed β -hematin exhibiting plate-like structures, similar to hemozoin synthesized by *P. vivax*. These results suggest that crystal size and morphology can be controlled by the mediating solvent system.

APPENDIX B

SYNTHESIS OF PEPTIDES FOR RANDOM STUDIES

This appendix highlights the peptides I synthesized that have been used for various experiments during my graduate studies. Each peptide was synthesized using standard continuous flow Fmoc solid phase peptide synthesis protocols on an Apex 396 Aaptec Automated Peptide synthesizer. Each peptide was purified by using a C18 reverse-phase column on a Waters Prep HPLC. Fractions were collected, lyophilized, and characterized using MALDI mass spectrometry. **Table 6** lists all of the peptides that were used in various experiments. The level of effort on my part varied from simply synthesizing the peptide on the resin and giving the protected product to the project leaders for deprotection and purification to personally purifying the samples. Following **Table 6** are several **Figures (81 & 82)** representing purification and characterization of the peptides I performed.

Table 6. Peptides synthesized using standard solid phase Fmoc peptide synthesis.

	Peptide Name	Peptide Sequence	Molecular Mass (g/mol)
HNE Adducts	IKK α	Ac-DVDQGSLSCTSFVGTLLQYLAPELFENK-NH ₂	2916.2
	IKK β	Ac-ELDQGSLSCTSFVGTLLQYLAPELLEQQK-NH ₂	3052.4
RSV B-cell and T-cell epitopes	B-cell epitopes	CLSLINDMPITNDQKKLMS	2164.6
		LSLINDMPITNDQKKLMSC	2164.6
		CLSLINDMPITNDQKKLMSC	2267.8
	T-cell epitopes	C-PEG8-AIAFFSRZWAIRIPNKKPG	2797.4
		WAIARIPNKKPGAIAFFSRQ-PEG8-C	2797.4
b-hematin mediating peptides		Ac-ASDQEPS-NH ₂	773.7
		Ac-EDDQNS-NH ₂	861.7
		Ac-EDKKPIR-NH ₂	926.0
		Ac-EDKNNVA-NH ₂	829.8
		Ac-KPSRPSR-NH ₂	868.0
		Ac-NNVKTFE-NH ₂	892.0
		Ac-PLGAAPG-NH ₂	622.7
		Ac-TAHLRIW-NH ₂	937.1
		Ac-TWHTRHW-NH ₂	1064.2
TNT binding epitopes		C-PEG8ISVPMLPRQWHW	2076.8
		C-PEG8-IVGWLTSPTRHW	1979.6
		C-PEG8-RQHLYKSFNPH	2066.6
		C-PEG6-WHWK	1094.5
		C-PEG6-WHW	966.4
		C-PEG6-WHWS	1053.4
		C-PEG6-WHWR	1122.5
	C-PEG6-WHWH	1103.5	
pfHRP-II Mimics	pHRP-II	Ac-AHHAHHAADAHHAHHAADAHHAHHAAD-NH ₂	2902.6
	TAMRA-HRP-II	TAMRA-AHHAHHAADAHHAHHAADAHHAHHAAD-NH ₂	3274.1
	BNT-II	Ac-AHHAHHAADAHHAHHAADA-MAP	8205.4

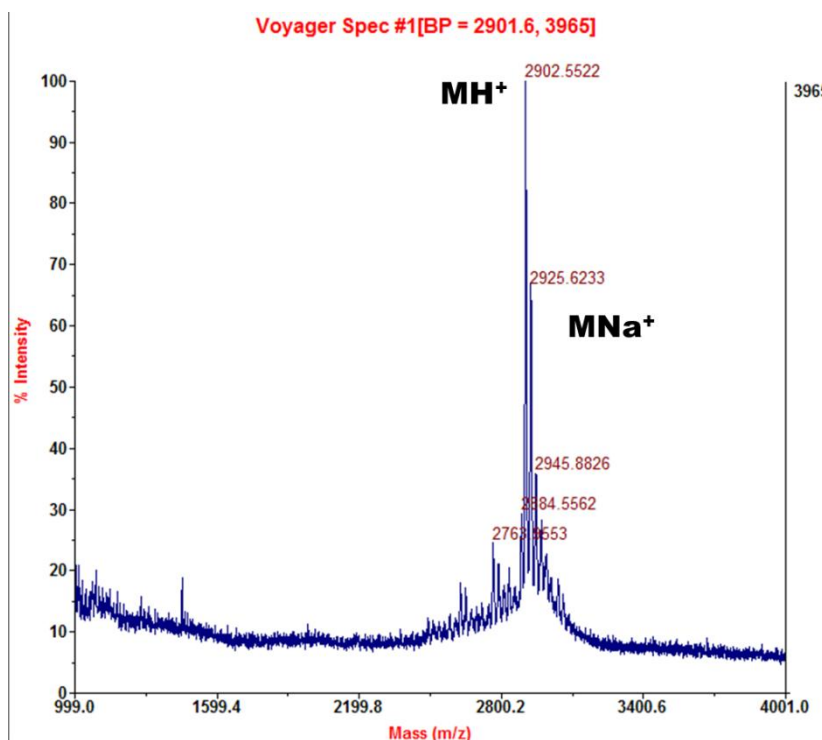
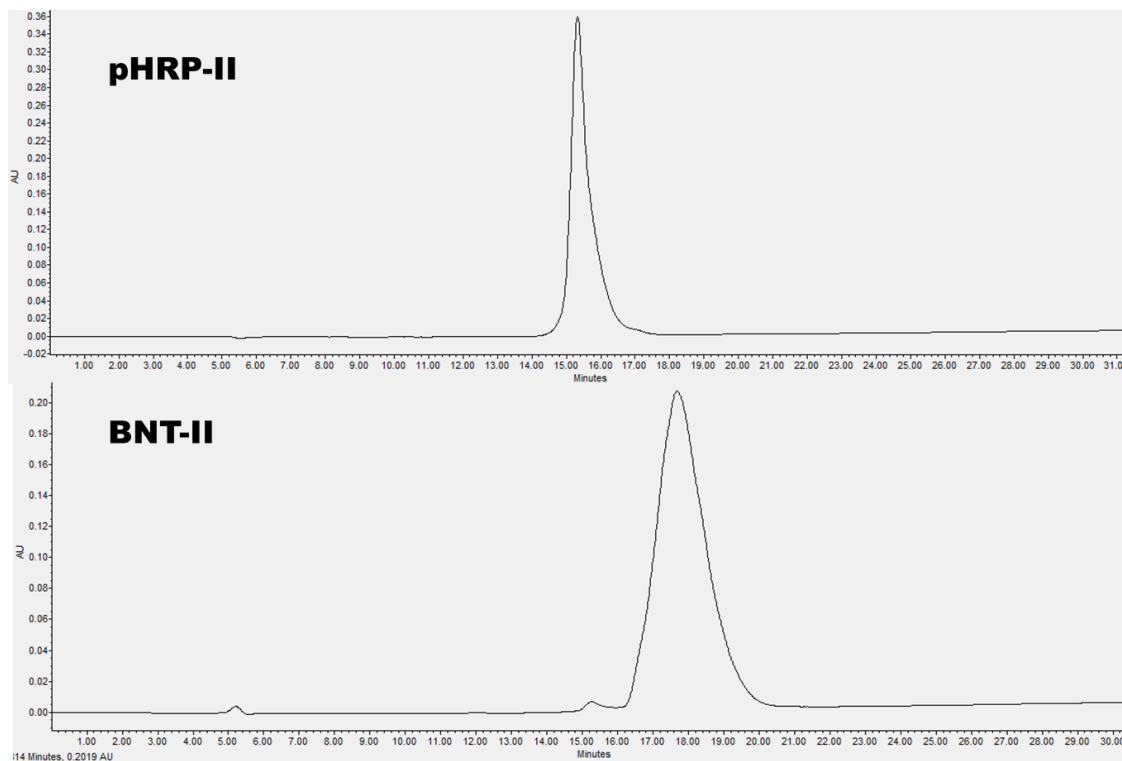


Figure 81. Characterization of HRP-II peptide mimics. HPLC purification spectrum of pHRP-II and BNT-II used in titrations with Ni(II)NTA AuNPs. MALDI characterization of pHRP-II

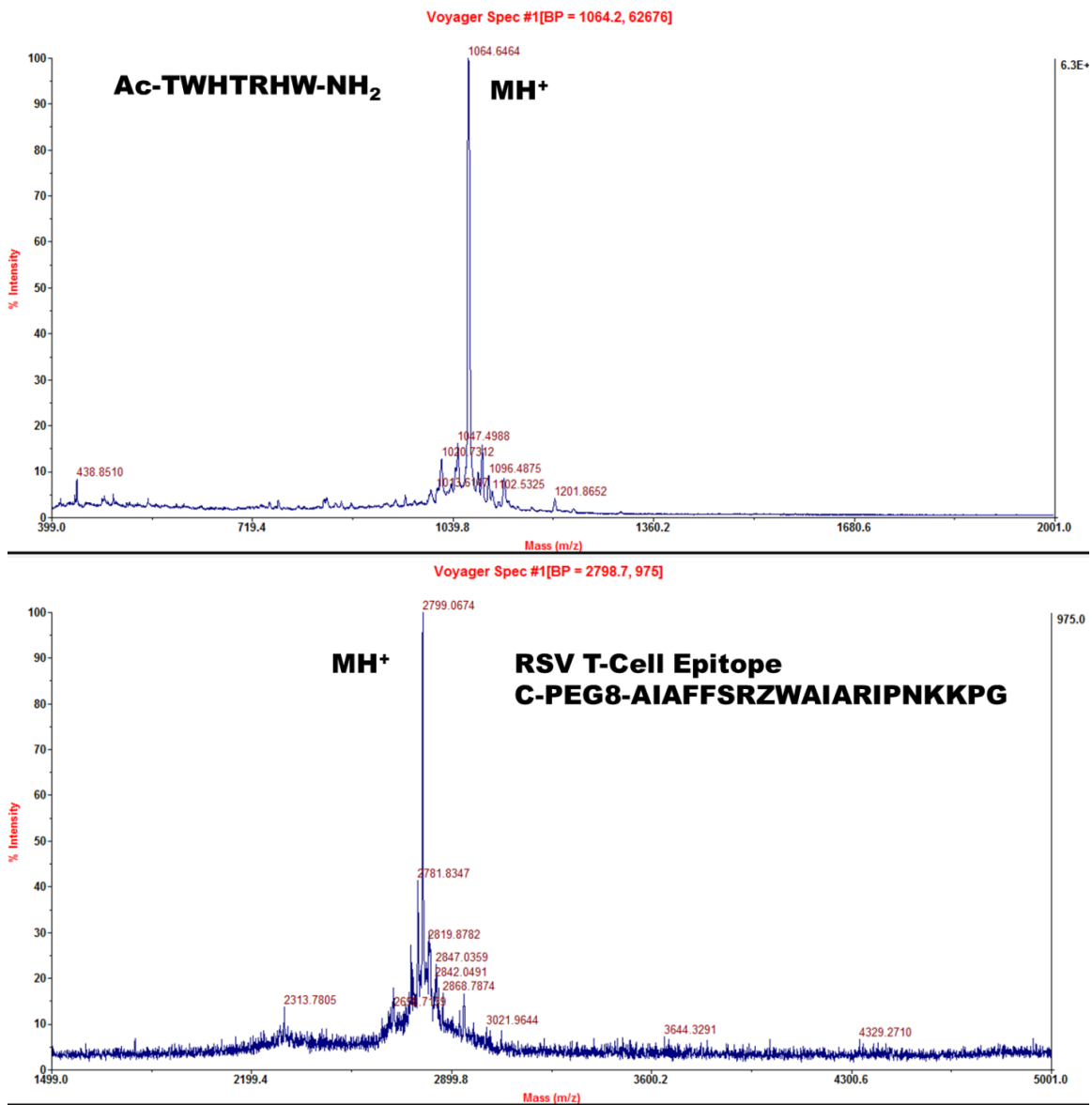


Figure 82. Selected MALDI spectrum for synthesized peptides.

REFERENCES

- (1) Cairns, J. R. K.; Esen, A. *Cellular and Molecular Life Sciences* **2010**, *67*, 3389.
- (2) *Malaria Rapid Diagnostic Test Performance*, World Health Organization, 2009.
- (3) WHO *Special Programme for Research & Training in Tropical Diseases* **2006**.
- (4) Wolf, S. *Microchip Manufacturing*; Lattice Press: Sunset Beach, 2004.
- (5) Kröger, N. *Current Opinion in Chemical Biology* **2007**, *11*, 662.
- (6) Knecht, M. R.; Wright, D. W. *Langmuir* **2004**, *20*, 4728.
- (7) Knecht, M. R.; Wright, D. W. *Chemistry of Materials*. **2004**, *16*, 4890.
- (8) Jan, J. S.; Shantz, D. F. *Advanced Materials* **2007**, *19*, 2951.
- (9) Miller, S. A.; Hong, E. D.; Wright, D. W. *Macromolecular Bioscience* **2006**, *6*, 839.
- (10) Zollfrank, C.; Scheel, H.; Greil, P. *Advanced Materials* **2007**, *19*, 984.
- (11) Belton, D. J.; Patwardhan, S. V.; Annenkov, V. V.; Danilovtseva, E. N.; Perry, C. C. *Proceedings of the National Academy of Sciences* **2008**, *105*, 5963.
- (12) Bauer, C. A.; Robinson, D. B.; Simmons, Blake A. *Small* **2007**, *3*, 58.
- (13) Gautier, C.; Lopez, P. J.; Livage, J.; Coradin, T. *Journal of Colloid and Interface Science* **2007**, *309*, 44.
- (14) Marner, W. D.; Shaikh, A. S.; Muller, S. J.; Keasling, J. D. *Biomacromolecules* **2008**, *9*, 1.
- (15) Wong Po Foo, C.; Patwardhan, S. V.; Belton, D. J.; Kitchel, B.; Anastasiades, D.; Huang, J.; Naik, R. R.; Perry, C. C.; Kaplan, D. L. *Proceedings of the National Academy of Sciences* **2006**, *103*, 9428.
- (16) Yager, P.; Edwards, T.; Fu, E.; Helton, K.; Nelson, K.; Tam, M. R.; Weigl, B. H. *Nature* **2006**, *442*, 412.
- (17) Pouget, E.; Dujardin, E.; Cavalier, A.; Moreac, A.; Valery, C.; Marchi-artzner, V.; Weiss, T.; Renault, A.; Paternostre, M.; Artzner, F. *Nature Materials* **2007**, *6*, 434.
- (18) Tomczak, M. M.; Glawe, D. D.; Drummy, L. F.; Lawrence, C. G.; Stone, M. O.; Perry, C. C.; Pochan, D. J.; Deming, T. J.; Naik, R. R. *Journal of the American Chemical Society* **2005**, *127*, 12577.
- (19) Weissbuch, I.; Leiserowitz, L. *Chemical Reviews* **2008**, *108*, 4899.
- (20) Sumper, M.; Brunner, E. *Advanced Functional Materials* **2006**, *16*, 17.
- (21) Moody, A. *Clinical Microbiological Reviews* **2002**, *15*, 66.
- (22) Kumar, U.; Shete, A.; Harle, A. S.; Kasyutich, O.; Schwarzacher, W.; Pundle, A.; Poddar, P. *Chemistry of Materials* **2008**, *20*, 1484.
- (23) Weiner, S.; Dove, P. M. *An overview of Biomineralization Processes and the Problem of the Vital Effect*; The Mineralogical Society of America: Washington D.C., 2003; Vol. 54.
- (24) Bar-Cohen, Y. *Bioinspired Biomimicry* **2006**, *1*, 1.

- (25) Carney, C. K.; Harry, S. R.; Sewell, S. L. *Topics in Current Chemistry* **2007**, *270*, 155.
- (26) Gorna, K.; Munoz-Espi, R.; Grohn, F.; Wegner, G. *Macromolecular Biosciences* **2007**, *7*, 163.
- (27) Perry, C. C. *Biomaterials*; Wiley-VCH: New York, **1998**.
- (28) Fratzl, P. *Journal of the Royal Society Interface* **2007**, *4*, 637.
- (29) Douglas, T.; Young, M. *Science* **2006**, *312*, 873.
- (30) Douglas, T.; Young, M. *Advanced Materials* **1999**, *11*, 679.
- (31) Lakshminarayanan, R.; Vivekanandan, S.; Samy, R. P.; Banerjee, Y.; Chi-Jin, E. O.; Teo, K. W.; Jois, S. D. S.; Kini, M.; Valiyaveetil, S. *Journal of American Chemical Society* **2008**, *130*, 4660.
- (32) Sumper, M. *Science* **2002**, *295*, 2430.
- (33) Lee, H.; Dellatore, S. M.; Miller, W. M.; Messersmith, P. B. *Science* **2007**, *318*, 426.
- (34) Kroger, N.; Deutzmann, R.; Sumper, M. *Science* **1999**, *286*, 1129.
- (35) Zurcher, S.; Wackerlin, D.; Bethuel, Y.; Malisova, B.; Textor, M.; Tosatti, S.; Gademann, K. *Journal of American Chemical Society* **2006**, *128*, 1064.
- (36) Henrich, V. E.; Cox, P. A. *The Surface Science of Metal Oxides*; Cambridge University Press: Boston, **1994**.
- (37) Halas, N. J. *ACS Nano* **2008**, *2*, 179.
- (38) Lang, C.; Schuler, D.; Faivre, D. *Macromolecular Biosciences* **2007**, *7*, 144.
- (39) Jun, Y.-W.; Seo, J.-W.; Cheon, J. *Accounts of Chemical Research* **2008**, *41*, 170.
- (40) Gröger, C.; Lutz, K.; Brunner, E. *Cell Biochemistry and Biophysics* **2008**, *50*, 23.
- (41) Noll, F.; Sumper, M.; Hampp, N. *Nano Letters* **2002**, *2*, 91.
- (42) *Handbook of Biomineralization: Biomimetic and Bioinspired Chemistry*; Brunner, E.; Lutz, K., Eds.; Weinheim: Wiley-VCH, **2007**; Vol. 2.
- (43) Christiansen, S. C.; Hedin, N.; Epping, J. D.; Janicke, M. T.; del Amo, Y.; Demarest, M.; Brzezinski, M.; Chmelka, B. F. *Solid State Nuclear Magnetic Resonance* **2006**, *29*, 170.
- (44) M. Sumper, E. B. *Advanced Functional Materials* **2006**, *16*, 17.
- (45) Poulsen, N.; Kroger, N. *J. Biol. Chem.* **2004**, *279*, 42993.
- (46) Poulsen, N.; Sumper, M.; Kroger, N. *Proceedings of the National Academy of Sciences* **2003**, *100*, 12075.
- (47) Wenzl, S.; Hett, R.; Richthammer, P.; Sumper, M. *Angewandte Chemie International Edition* **2008**, *47*, 1729.
- (48) Kroger, N.; Deutzmann, R.; Bergsdorf, C.; Sumper, M. *Proceedings of the National Academy of Sciences* **2000**, *97*, 14133.
- (49) Sumper, M.; Kroger, N. *Journal of Materials Chemistry* **2004**, *14*, 2059.
- (50) Naik, R. R.; Tomczak, M. M.; Luckarift, H. R.; Spain, J. C.; Stone, M. O. *Chemical Communications* **2004**, 1684.
- (51) Zhang, Y.; Wu, H.; Li, J.; Li, L.; Jiang, Y.; Jiang, Y.; Jiang, Z. *Chem. Mater.* **2008**, *20*, 1041.

- (52) Luckarift, H. R.; Spain, J. C.; Naik, R. R.; Stone, M. O. *Nature Biotechnology* **2004**, *22*, 211.
- (53) Knecht, M. R.; Sewell, S. L.; Wright, D. W. *Langmuir* **2005**, *21*, 2058.
- (54) Jan, J. S.; Lee, S.; Carr, C. S.; Shantz, D. F. *Chemistry of Materials* **2005**, *17*, 4310.
- (55) J.-S. Jan, D. F. S. *Advanced Materials* **2007**, *19*, 2951.
- (56) Christina A. Bauer, D. B. R. Blake A. S. *Small* **2007**, *3*, 58.
- (57) Cha, J. N.; Stucky, G. D.; Morse, D. E.; Deming, T. J. *Nature* **2000**, *403*, 289.
- (58) Annenkov, V. V.; Patwardhan, S. V.; Belton, D.; Danilovtseva, E. N.; Perry, C. C. *Chemical Communications* **2006**, 1521.
- (59) C. Zollfrank, H. S. P. G. *Advanced Materials* **2007**, *19*, 984.
- (60) Chang, J. S.; Kong, Z. L.; Hwang, D. F.; Chang, K. L. B. *Chemistry of Materials* **2006**, *18*, 702.
- (61) Lutz, K.; Groger, C.; Sumper, M.; Brunner, E. *Physical Chemistry Chemical Physics* **2005**, *7*, 2812.
- (62) Wong, M. S.; Cha, J. N.; Choi, K. S.; Deming, T. J.; Stucky, G. D. *Nano Letters* **2002**, *2*, 583.
- (63) Hawkins, K. M.; Wang, S. S. S.; Ford, D. M.; Shantz, D. F. *Journal of the American Chemical Society* **2004**, *126*, 9112.
- (64) Brunner, E. *Nature Materials* **2007**, *6*, 398.
- (65) Sumper, M.; Lorenz, S.; Brunner, E. *Angewandte Chemie International Edition* **2003**, *42*, 5192.
- (66) Lose, E.; Park, R. J.; Warren, J.; Meldrum, F. C. *Advanced Functional Materials* **2004**, *14*, 1211.
- (67) Nuraje, N.; Su, K.; Haboosheh, A.; Samson, J.; Manning, E. P.; Yang, N.-I.; Matsui, H. *Advanced Materials* **2006**, *18*, 807.
- (68) Sheldon, R. A.; van Rantwijk, F. *Australian Journal of Chemistry* **2004**, *57*, 281.
- (69) Sheldon, R. A. *Advanced Synthesis & Catalysis* **2007**, *349*, 1289.
- (70) Avnir, D.; Braun, S.; Lev, O.; Ottolenghi, M. *Chemistry of Materials* **1994**, *6*, 1605.
- (71) Gill, I.; Ballesteros, A. *Journal of the American Chemical Society* **1998**, *120*, 8587.
- (72) Dave, B. C.; Miller, J. M.; Dunn, B.; Valentine, J. S.; Zink, J. I. *Journal of Sol-Gel Science and Technology* **1997**, *8*, 629.
- (73) Monnier, A.; Schuth, F.; Huo, Q.; Kumar, D.; Margolese, D.; Maxwell, R. S.; Stucky, G. D.; Krishnamurty, M.; Petroff, P.; Firouzi, A.; Janicke, M.; Chmelka, B. F. *Science* **1993**, *261*, 1299.
- (74) Oliver, S.; Kuperman, A.; Coombs, N.; Lough, A.; Ozin, G. A. *Nature* **1995**, *378*, 47.
- (75) Luckarift, H. R.; Johnson, G. R.; Spain, J. C. *Journal of Chromatography B* **2006**, *843*, 310.
- (76) Luckarift, H. R.; Spain, J. C.; Naik, R. R.; Stone, M. O. *Nature Biotechnology* **2004**, *22*, 211.
- (77) Miller, S. A.; Hong, E. D.; Wright, D. *Macromolecular Bioscience* **2006**,

- 6, 839.
- (78) Legras, J. I.; Cguzel, G.; Arnaud, A.; Galzy, P. *World Journal of Microbiology and Biotechnology* **1990**, *6*, 83.
- (79) Bennett, M. A.; Yoshida, T. *Journal of the American Chemical Society* **1973**, *95*, 3030.
- (80) Chin, J.; Kim, J. H. *Angewandte Chemie* **1990**, *102*, 580.
- (81) DiBiase, S. A.; Wolak, R. P., Jr.; Dishong, D. M.; Gokel, G. W. *Journal of Organic Chemistry* **1980**, *45*, 3630.
- (82) Paraskewas, S. *Synthesis* **1974**, 574.
- (83) Surendra, K.; Krishnaveni, N. S.; Mahesh, A.; Rao, K. R. *Journal of Organic Chemistry* **2006**, *71*, 2532.
- (84) Yadav, J. S.; Reddy, B. V. S.; Eeshwaraiah, B.; Srinivas, M. *Tetrahedron* **2004**, *60*, 1767.
- (85) Strecker, A. *Liebigs Annalen der Chemie* **1850**, *75*, 27.
- (86) Surendra, K.; Krishnaveni, N. S.; Mahesh, A.; Rao, K. R. *Journal of Organic Chemistry* **2006**, *71*, 2532.
- (87) Clarke, H. T.; Read, R. R. *Journal of the American Chemical Society* **1924**, *46*, 1001.
- (88) Harrison, C. R.; Hodge, P.; Rogers, W. J. *Synthesis* **1977**, 41.
- (89) Brenner, C. *Current Opinion in Structural Biology* **2002**, *12*, 775.
- (90) Vorwek, S.; Biernacki, S.; Hillebrand, H.; Janzik, I.; Muller, A.; Weiler, E. W.; Piotrowski, M. *Planta* **2001**, *212*, 508.
- (91) Breuer, M.; Ditrach, K.; Habicher, T.; Hauer, B.; KeBeler, M.; Sturmer, R.; Zelinski, T. *Angewandte Chemie International Edition* **2004**, *43*, 788.
- (92) Nagasawa, T.; Yamada, H. *Trends in Biotechnology* **1989**, *7*, 153.
- (93) Kobayashi, M.; Nagasawa, T.; Yamada, H. *TIBTECH* **1992**, *10*, 402.
- (94) Banerjee, A.; Sharma, R.; Banerjee, U. C. *Biotechnology and Applied Biochemistry* **2003**, *37*, 289.
- (95) Iler, R. K. *The Chemistry of Silica*; Wiley: New York, 1979.
- (96) Kröger, N.; Lehmann, G.; Rachel, R.; Sumper, M. *European Journal of Biochemistry* **1997**, *250*, 99.
- (97) Kröger, N.; Deutzmann, R.; Sumper, M. *Science* **1999**, *286*, 1129.
- (98) Knecht, M. R.; Wright, D. W. *Langmuir* **2004**, *20*, 4728
- (99) Larsen, G.; Marquez, M.; Lotero, E. *Journal of Physical Chemistry B* **2000**, *104*, 4840.
- (100) Roth, K. M.; Zhou, Y.; Yang, W.; Morse, D. E. *Journal of the American Chemical Society* **2005**, *127*, 325.
- (101) Jian-Jun, Y.; Ren-Hua, J. *Advanced Materials* **2005**, *17*, 885.
- (102) Knecht, M. R.; Wright, D. W. *Chemistry of Materials* **2004**, *16*, 4890.
- (103) Bhatia, R. B., Brinker, Jeffrey C., Gupta, Alok K., and Singh, Anup K. *Chemistry of Materials* **2000**, *12*, 2434.
- (104) Mathew, C. D.; Nagasawa, T.; Kobayashi, M.; Yamada, H. *Applied and Environmental Microbiology* **1988**, *54*, 1030.
- (105) Berne, C.; Betancor, L.; Luckarift, H. R.; Spain, J. C. *Biomacromolecules* **2006**, *7*, 2631.
- (106) Hendy, N. A.; Wilke, C. R.; Blanch, H. W. *Enzyme and Microbial*

- Technology* **1984**, 6, 73.
- (107) Mais, U.; Esteghlalian, A. R.; Saddler, J. N.; Mansfield, S. D. *Applied Biochemistry and Biotechnology* **2002**, 98, 815.
- (108) Xin, Z.; Yinbo, Q.; Peiji, G. *Enzyme and Microbial Technology* **1993**, 15, 62.
- (109) Watanabe, T.; Sato, T.; Yoshioka, S.; Koshijima, T.; Kuwahara, M. *European Journal of Biochemistry* **1992**, 209, 651.
- (110) Lee, S.; Lee, B.; Kim, B. J.; Park, J.; Yoo, M.; Bae, W. K.; Char, K.; Hawker, C. J.; Bang, J.; Cho, J. *Journal of American Chemical Society* **2009**, 131, 2579.
- (111) Hasenbank, M. S.; Edwards, T.; Fu, E.; Garzon, R.; Kosar, F.; Look, M.; Mashadi-Hosseini, A.; Yager, P. *Analytica Chimica Acta* **2008**, 611, 80.
- (112) Sanders, W.; Vargas, R. *Langmuir* **2008**, 24, 6133.
- (113) Berne, C.; Betancor, L.; Luckarift, H. R.; Spain, J. C. *Biomacromolecules* **2006**, 7, 2631.
- (114) Sumerel, J.; Lewis, J.; Doraiswamy, A.; Deravi, L. F.; Sewell, S. L.; Gerdon, A. E.; Wright, D. W.; Narayan, R. J. *Biotechnology Journal* **2006**.
- (115) Bowman, C. N.; Kloxin, C. J. *AIChE Journal* **2008**, 54, 2775.
- (116) Sebra, R. P.; Reddy, S. K.; Masters, K. S.; Bowman, C. N.; Anseth, K. S. *Acta Biomaterialia* **2007**, 3, 151.
- (117) Pirone, D. M.; Qi, L.; Colecraft, H.; Chen, C. S. *Biomedical Microdevices*, 10, 561.
- (118) Hynd, M. R. F., John P.; Burnham, Mary-Rose; Martin, David L.; Dowell-Mesfin, Natalie M.; Turner, James N.; Shain, William *Journal of Biomedical Materials Research, Part A* **2007**, 81A, 347.
- (119) Arrabito, G.; Musumeci, C.; Aiello, V.; Libertino, S.; Compagnini, G.; Pignataro, B. *Langmuir* **2009**, 25, 6312.
- (120) Di Risio, S.; Yan, N. *Macromolecular Rapid Communications* **2007**, 28, 1934.
- (121) Wilhelm, T.; Wittstock, G. *Angewandte Chemie-International Edition* **2003**, 42, 2247.
- (122) Laurent, N.; Haddoub, R.; Flitsch, S. L. *Trends in Biotechnology* **2008**, 26, 328.
- (123) Miller, S. A.; Hong, E. D.; Wright, D. W. *Macromolecular Bioscience* **2006**, 6, 839.
- (124) Betancor, L.; Luckarift, H. R. *Trends in Biotechnology* **2008**, 26, 566.
- (125) Luckarift, H. R. *Journal of Liquid Chromatography & Related Technologies* **2008**, 21, 1568.
- (126) He, P.; Greenway, G.; Haswell, S. J. *Nanotechnology* **2008**, 19, 315603.
- (127) Luckarift, H. R.; Johnson, G. R.; Spain, J. C. *Journal of Chromatography B* **2006**, 843, 310.
- (128) Dunker, A. K.; Fernandez, A. *Trends in Biotechnology* **2007**, 25, 189.
- (129) Kunzelmann, U.; Bottcher, H. *Sensors and Actuators B* **1997**, 38-39, 222.
- (130) Swartz, J. D.; Miller, S. A.; Wright, D. W. *Organic Process Research & Development* **2009**, 13, 584.
- (131) Deravi, L. F.; Sumerel, J. L.; Gerdon, A. E.; Cliffel, D. E.; Wright, D. W.

- Applied Physics Letters* **2007**, *91*, 113114.
- (132) Deravi, L. F.; Sumerel, J. L.; Sewell, S. L.; Wright, D. W. *Small* **2009**, *4*, 2127.
- (133) Smoukov, S. K.; Bishop, K. J. M.; Kowalczyk, B.; Kalsin, A. M.; Grzybowski, B. A. *Journal of American Chemical Society* **2007**, *129*, 15623.
- (134) Deravi, L. F.; Sumerel, J. L.; Sewell, S. L.; Wright, D. W. *Small* **2008**, *4*, 2127.
- (135) World Health Organization *World Malaria Report* **2010**.
- (136) <http://www.gatesfoundation.org/topics/Pages/malaria.aspx>.
- (137) World Health Organization *Malaria Fact Sheet* **2007**.
- (138) Black, R. E.; Cousens, S.; Johnson, H. L.; Lawn, J. E.; Rudan, I.; Bassani, D. G.; Jha, P.; Campbell, H.; Walker, C. F.; Cibulskis, R.; Eisele, T.; Liu, L.; Mathers, C.; UNICEF, *Lancet* **2010**, *375*, 1969.
- (139) Källander, K.; Nsungwa-Sabiiti, J.; Peterson, S. *Acta Tropica* **2004**, *90*, 211.
- (140) *Management of Uncomplicated Malaria; A Practical Guide for Health Workers*, Uganda Malaria Control Programme Ministry of Health, **2005**.
- (141) World Health Organization *World Malaria Report* **2008**.
- (142) Reyburn, H.; Mbakilwa, H.; Mwangi, R.; Mwerinde, O.; Olomi, R.; Drakeley, C.; Whitty, C. J. *BMJ* **2007**, *334*, 403.
- (143) Ogbonna, A.; Uneke, C. J. *Transactions of the Royal Society of Tropical Medicine and Hygiene* **2008**, *102*, 621.
- (144) Chandler, C. I.; Mwangi, R.; Mbakilwa, H.; Olomi, R.; Whitty, C. J.; Reyburn, H. *Health Policy Plan* **2008**, *23*, 170.
- (145) Dondorp, A. M.; Nosten, F.; Yi, P.; Das, D.; Phyto, A. P.; Tarning, J.; Lwin, K. M.; Ariey, F.; Hanpithakpong, W.; Lee, S. J.; Ringwald, P.; Silamut, K.; Imwong, M.; Chotivanich, K.; Lim, P.; Herdman, T.; An, S. S.; Yeung, S.; Singhasivanon, P.; Day, N. P.; Lindegardh, N.; Socheat, D.; White, N. J. *New England Journal of Medicine* **2009**, *361*, 455.
- (146) Black, R. E.; Morris, S. S.; Bryce, J. *Lancet* **2003**, *361*, 2226.
- (147) Morens, D. M.; Folkers, G. K.; Fauci, A. S. *Nature* **2004**, *430*, 242.
- (148) Fauci, A. S. *Clinical Infectious Diseases* **2001**, *32*, 675.
- (149) Perkins, M. D.; Bell, D. R. *Malaria Journal* **2008**, *7* Supplementary Data 1, S5.
- (150) Weigl, B. H.; Boyle, D. S.; de los Santos, T.; Peck, R. B.; Steele, M. S. *Expert Review of Medical Devices* **2009**, *6*, 461.
- (151) Warhurst, D. C.; Williams, J. E. *Journal of Clinical Pathology* **1996**, *49*, 533.
- (152) malERA Consultative Group on Diagnoses and Diagnostics. *PLoS Med* **2011**, *8*, e1000396.
- (153) Coleman, R. E.; Maneechai, N.; Rachaphaew, N.; Kumpitak, C.; Miller, R. S.; Soyseng, V.; Thimasarn, K.; Sattabongkot, J. *American Journal of Tropical Medical and Hygiene* **2002**, *67*, 141.
- (154) Power, K. T. *American Journal of Medical Technology* **1982**, *48*, 519.
- (155) Kilian, A. H.; Metzger, W. G.; Mutschelknauss, E. J.; Kabagambe, G.;

- Langi, P.; Korte, R.; von Sonnenburg, F. *Tropical Medicine & International Health* **2000**, *5*, 3.
- (156) Gay, F.; Traore, B.; Zanoni, J.; Danis, M.; Fribourg-Blanc, A. *Transactions of the Royal Society of Tropical Medicine and Hygiene* **1996**, *90*, 516.
- (157) Cooke, A. H.; Moody, A. H.; Lemon, K.; Chiodini, P. L.; Horton, J. *Transactions of the Royal Society of Tropical Medicine and Hygiene* **1992**, *86*, 378.
- (158) Srinivasan, S.; Moody, A. H.; Chiodini, P. L. *Annals of Tropical Medicine and Parasitology* **2000**, *94*, 227.
- (159) Sharma, M. K.; Rao, V. K.; Agarwal, G. S.; Rai, G. P.; Gopalan, N.; Prakash, S.; Sharma, S. K.; Vijayaraghavan, R. *Journal of Clinical Microbiology* **2008**, *46*, 3759.
- (160) Snounou, G.; Viriyakosol, S.; Jarra, W.; Thaithong, S.; Brown, K. N. *Molecular and Biochemistry Parasitology* **1993**, *58*, 283.
- (161) Kifude, C. M.; Rajasekariah, H. G.; Sullivan, D. J., Jr.; Stewart, V. A.; Angov, E.; Martin, S. K.; Diggs, C. L.; Waitumbi, J. N. *Clinical and Vaccine Immunology* **2008**, *15*, 1012.
- (162) Martin, S. K.; Rajasekariah, G. H.; Awinda, G.; Waitumbi, J.; Kifude, C. *The American Journal of Tropical Medicine and Hygiene* **2009**, *80*, 516.
- (163) Quintana, M.; Piper, R.; Boling, H. L.; Makler, M.; Sherman, C.; Gill, E.; Fernandez, E.; Martin, S. *The American Journal of Tropical Medicine and Hygiene* **1998**, *59*, 868.
- (164) Singh, N.; Saxena, A.; Valecha, N. *Trop Med Int Health* **2000**, *5*, 765.
- (165) Akompong, T.; Kadekoppala, M.; Harrison, T.; Oksman, A.; Goldberg, D. E.; Fujioka, H.; Samuel, B. U.; Sullivan, D.; Halder, K. *Journal of Biological Chemistry* **2002**, *277*, 28923.
- (166) World Health Organization *World Malaria Report* **2009**.
- (167) World Health Organization *World Malaria Report* **2009**.
- (168) Collins, W. E.; Jeffery, G. M. *The American Journal of Tropical Medicine and Hygiene* **1999**, *61*, 44.
- (169) Wilson, N. O.; Adjei, A. A.; Anderson, W.; Baidoo, S.; Stiles, J. K. *The American Journal of Tropical Medicine and Hygiene* **2008**, *78*, 733.
- (170) Genton, B.; Paget, S.; Beck, H. P.; Gibson, N.; Alpers, M. P.; Hii, J. *Southeast Asian Journal of Tropical Medicine and Public Health* **1998**, *29*, 35.
- (171) Miller, A. R.; Davis, G. L.; Oden, Z. M.; Razavi, M. R.; Fateh, A.; Ghazanfari, M.; Abdolrahimi, F.; Poorazar, S.; Sakhaie, F.; Olsen, R. J.; Bahrmand, A. R.; Pierce, M. C.; Graviss, E. A.; Richards-Kortum, R. *PLoS One* **2010**, *5*, e11890.
- (172) Tseng, D.; Mudanyali, O.; Oztoprak, C.; Isikman, S. O.; Sencan, I.; Yaglidere, O.; Ozcan, A. *Lab on a Chip* **2010**, *10*, 1787.
- (173) Breslauer, D. N.; Maamari, R. N.; Switz, N. A.; Lam, W. A.; Fletcher, D. A. *PLoS One* **2009**, *4*, e6320.
- (174) Sur, K.; McFall, S. M.; Yeh, E. T.; Jangam, S. R.; Hayden, M. A.;

- Stroupe, S. D.; Kelso, D. M. *Journal of Molecular Diagnostics* **2010**, *12*, 620.
- (175) Berry, S. M.; Alarid, E. T.; Beebe, D. J. *Lab on a Chip* **2011**.
- (176) Bordelon, H.; Adams, N. M.; Klemm, A. S.; Russ, P. K.; Williams, J. V.; Talbot, H. K.; Wright, D. W.; Haselton, F. R. *ACS Applied Material Interfaces* **2011**, *3*, 2161.
- (177) Panton, L. J.; McPhie, P.; Maloy, W. L.; Wellems, T. E.; Taylor, D. W.; Howard, R. J. *Molecular and Biochemical Parasitology* **1989**, *35*, 149.
- (178) Chiodini, P. L.; Bowers, K.; Jorgensen, P.; Barnwell, J. W.; Grady, K. K.; Luchavez, J.; Moody, A. H.; Cenizal, A.; Bell, D. *Transactions of the Royal Society of Tropical Medicine and Hygiene* **2007**, *101*, 331.
- (179) Schneider, E. L.; Marletta, M. A. *Biochemistry* **2005**, *44*, 979.
- (180) Ghimire, P.; Samantaray, J. C.; Mirdha, B. R.; Patra, A. K.; Panda, A. K. *Southeast Asian Journal of Tropical Medicine and Public Health* **2003**, *34*, 739.
- (181) Terpe, K. *Applied Microbiology and Biotechnology* **2003**, *60*, 523.
- (182) Mori, S.; Takahashi, H. K.; Yamaoka, K.; Okamoto, M.; Nishibori, M. *Life Sciences* **2003**, *73*, 93.
- (183) Knecht, S.; Ricklin, D.; Eberle, A. N.; Ernst, B. *Journal of Molecular Recognition* **2009**, *22*, 270.
- (184) Helena Block, B. M., Anne Spriestersbach, Nicole Brinker, Jan Kubicek, Roland Fabis, Jorg Labahn, and Frank Schafer *Immobilized-Metal Affinity Chromatography (IMAC): A Review*; Elsevier Inc., **2009**.
- (185) Trager, W.; Jenson, J. B. *Nature* **1978**, *273*, 621.
- (186) Lambros, C.; Vanderberg, J. P. *Journal of Parasitology* **1979**, *65*, 418.
- (187) Clift, R.; Grace, J. R.; Weber, M. E. *Bubbles, Drops, and Particles*; Academic Press: New York, 1978.
- (188) Gennes, P.-G. d.; Brochard-Wyart, F.; Quéré, D. *Capillarity and Wetting Phenomena : Drops, Bubbles, Pearls, Waves*; Springer: New York, **2004**.
- (189) Israelachvili, J. N. *Intermolecular and Surface Forces*; 2nd ed.; Academic Press: London, **1992**.
- (190) Dondorp, A. M.; Desakorn, V.; Pongtavornpinyo, W.; Sahassananda, D.; Silamut, K.; Chotivanich, K.; Newton, P. N.; Pitisuttithum, P.; Smithyman, A. M.; White, N. J.; Day, N. P. *PLoS Medicine* **2005**, *2*, e204.
- (191) Minigo, G.; Woodberry, T.; Piera, K. A.; Salwati, E.; Tjitra, E.; Kenangalem, E.; Price, R. N.; Engwerda, C. R.; Anstey, N. M.; Plebanski, M. *PLoS Pathogens* **2009**, *5*, e1000402.
- (192) Piper, R.; Lebras, J.; Wentworth, L.; Hunt-Cooke, A.; Houze, S.; Chiodini, P.; Makler, M. *The American Journal of Tropical Medicine and Hygiene* **1999**, *60*, 109.
- (193) Rydengard, V.; Olsson, A. K.; Morgelin, M.; Schmidtchen, A. *FEBS Journal* **2007**, *274*, 377.
- (194) Jones, A. L.; Hulett, M. D.; Parish, C. R. *Immunology & Cell Biology* **2005**, *83*, 106.
- (195) Deegan, R. D.; Bakajin, O.; Dupont, T. F.; Huber, G.; Nagel, S. R.; Witten, T. A. *Nature* **1997**, *389*, 827.

- (196) Wong, T. S.; Chen, T. H.; Shen, X.; Ho, C. M. *Analytical Chemistry* **2011**, *83*, 1871.
- (197) Monteux, C.; Lequeux, F. *Langmuir* **2011**.
- (198) Deegan, R. D. *Physical Review E* **2000**, *61*, 475.
- (199) Sangani, A. S.; Lu, C. H.; Su, K. H.; Schwarz, J. A. *Physical Review E* **2009**, *80*.
- (200) Elghanian, R.; Storhoff, J. J.; Mucic, R. C.; Letsinger, R. L.; Mirkin, C. A. *Science* **1997**, *277*, 1078.
- (201) Gao, J.; Fu, J.; Lin, C.; Lin, J.; Han, Y.; Yu, X.; Pan, C. *Langmuir* **2004**, *20*, 9775.
- (202) Yu, J. S.; Liao, H. X.; Gerdon, A. E.; Huffman, B.; Scarce, R. M.; McAdams, M.; Alam, S. M.; Popernack, P. M.; Sullivan, N. J.; Wright, D.; Cliffler, D. E.; Nabel, G. J.; Haynes, B. F. *Journal of Virological Methods* **2006**, *137*, 219.
- (203) Hainfeld, J. F.; Liu, W. Q.; Halsey, C. M. R.; Freimuth, P.; Powell, R. D. *Journal of Structural Biology* **1999**, *127*, 185.
- (204) Storhoff, J. J.; Elghanian, R.; Mucic, R. C.; Mirkin, C. A.; Letsinger, R. L. *Journal of the American Chemical Society* **1998**, *120*, 1959.
- (205) Myroshnychenko, V.; Rodriguez-Fernandez, J.; Pastoriza-Santos, I.; Funston, A. M.; Novo, C.; Mulvaney, P.; Liz-Marzan, L. M.; de Abajo, F. J. G. *Chemical Society Reviews* **2008**, *37*, 1792.
- (206) Radwan, S. H.; Azzazy, H. M. *Expert Reviews of Molecular Diagnostics* **2009**, *9*, 511.
- (207) Kreibitz, U.; Genzel, L. *Surface Science* **1985**, *156*, 678.
- (208) Quinten, M.; Kreibitz, U. *Surface Science* **1986**, *172*, 557.
- (209) Prodan, E.; Nordlander, P. *Journal of Chemical Physics* **2004**, *120*, 5444.
- (210) Wuelfing, W. P.; Gross, S. M.; Miles, D. T.; Murray, R. W. *Journal of the American Chemical Society* **1998**, *120*, 12696.
- (211) Cho, K.; Lee, Y.; Lee, C. H.; Lee, K.; Kim, Y.; Choi, H.; Ryu, P. D.; Lee, S. Y.; Joo, S. W. *Journal of Physical Chemistry C* **2008**, *112*, 8629.
- (212) Liu, D. B.; Qu, W. S.; Chen, W. W.; Zhang, W.; Wang, Z.; Jiang, X. Y. *Analytical Chemistry* **2010**, *82*, 9606.
- (213) Hung, Y. L.; Hsiung, T. M.; Chen, Y. Y.; Huang, Y. F.; Huang, C. C. *Journal of Physical Chemistry C* **2010**, *114*, 16329.
- (214) Kalluri, J. R.; Arbneshi, T.; Khan, S. A.; Neely, A.; Candice, P.; Varisli, B.; Washington, M.; McAfee, S.; Robinson, B.; Banerjee, S.; Singh, A. K.; Senapati, D.; Ray, P. C. *Angewandte Chemie International Edition* **2009**, *48*, 9668.
- (215) Tsai, C. S.; Yu, T. B.; Chen, C. T. *Chemical Communications* **2005**, 4273.
- (216) Zhang, X.; Kong, X.; Fan, W.; Du, X. *Langmuir* **2011**, *27*, 6504.
- (217) Ziegler, J.; Chang, R. T.; Wright, D. W. *Journal of the American Chemical Society* **1999**, *121*, 2395.
- (218) Goddard, J. M.; Erickson, D. *Analytical & Bioanalytical Chemistry* **2009**, *394*, 469.
- (219) Schmitt, L.; Ludwig, M.; Gaub, H. E.; Tampe, R. *Biophysical Journal* **2000**, *78*, 3275.

- (220) Tinazli, A.; Tang, J. L.; Valiokas, R.; Picuric, S.; Lata, S.; Piehler, J.; Liedberg, B.; Tampe, R. *Chemistry-a European Journal* **2005**, *11*, 5249.
- (221) Schmitt, L.; Dietrich, C.; Tampe, R. *Journal of the American Chemical Society* **1994**, *116*, 8485.
- (222) Nuzzo, R. G.; Zegarski, B. R.; Dubois, L. H. *Journal of the American Chemical Society* **1987**, *109*, 733.
- (223) Barton, C. S.; Waniganayake, L.; Wie, G.; McMurchie, E. J.; Leifert, W. R.; Jamting, A.; Raguse, B.; Weiczorek, L. *ICONN* **2006**.
- (224) Mulvaney, P. *Langmuir* **1996**, *12*, 788.
- (225) Bae, D. R.; Han, W. S.; Lim, J. M.; Kang, S.; Lee, J. Y.; Kang, D.; Jung, J. H. *Langmuir* **2009**, *26*, 2181.
- (226) Slocik, J. M. Thesis (Ph D in Chemistry), Vanderbilt University, Dec. 2004.
- (227) Heimburger, N.; Haupt, H.; Kranz, T.; Baudner, S. *Hoppe-Seyler's Zeitschrift für physiologische Chemie* **1972**, *353*, 1133.
- (228) Manderson, G. A.; Martin, M.; Onnerfjord, P.; Saxne, T.; Schmidtchen, A.; Mollnes, T. E.; Heinegard, D.; Blom, A. M. *Molecular Immunology* **2009**, *46*, 3388.
- (229) Blättler, T. M.; Senn, P.; Textor, M.; Vörös, J.; Reimhult, E. *Colloids and Surfaces A: Physicochemical and Engineering Aspects* **2009**, *346*, 61.
- (230) Francis, S. E.; Sullivan Jr., D. J.; Goldbery, D. E. *Annual Review of Microbiology* **1997**, *51*, 97.
- (231) Davies, M. *Biochimica et Biophysica Acta*. **1988**, *964*, 28.
- (232) Van der Zee, J.; Barr, D.; Mason, R. *Free Radical Biology and Medicine* **1996**, *20*, 199.
- (233) Tappel, A. *Journal of Biological Chemistry* **1995**, *271*, 721.
- (234) Gutteridge, J.; Smith, A. *Biochemistry Journal* **1988**, *256*, 861.
- (235) Aft, R.; Mueller, G. *Journal of Biological Chemistry* **1984**, *259*, 301.
- (236) Aft, R.; Mueller, G. *Journal of Biological Chemistry* **1983**, *258*, 12069.
- (237) Goldberg, D.; Slater, A.; Beavis, R.; Chait, B.; Cerami, A.; Henderson, G. *The Journal of Experimental Medicine* **1991**, *173*, 961.
- (238) Homewood, C. A.; Jewsbury, J. M.; Chance, M. L. *Comparative Biochemistry and Physiology* **1972**, *43*, 517.
- (239) Pagola, S.; Stephens, P. W.; Bohle, D. S.; Kosar, A. D.; Madsen, S. K. *Nature* **2000**, *404*, 307.
- (240) Slater, A. F.; Swiggard, W. J.; Orton, B. R.; Flitter, W. D.; Goldberg, D. E.; Cerami, A.; Henderson, G. B. *Proceedings of the National Academy of Sciences* **1991**, *88*, 325.
- (241) Egan, T. J.; Tshivhase, M. G. *Dalton Transactions* **2006**, 5024.
- (242) Egan, T. J.; Mavuso, W. W.; Ncokazi, K. K. *Biochemistry* **2001**, *40*, 204.
- (243) Hoang, A. N.; Ncokazi, K. K.; de Villiers, K. A.; Wright, D. W.; Egan, T. J. *Dalton Transactions* **2010**, *39*, 1235.
- (244) Egan, T. J.; Chen, J. Y.-J.; de Villiers, K. A.; Mobotha, T. E.; Naidoo, K. J.; Ncokazi, K. K.; Langford, S. J.; McNaughton, D.; Pandiancherri, S.; Wood, B. R. *FEBS Letters* **2006**, *580*, 5105.
- (245) Jackson, K. E.; Klonis, N.; Ferguson, D. J. P.; Adisa, A.; Dogovski, C.;

- Tilley, L. *Molecular Microbiology* **2004**, *54*, 109.
- (246) Carter, M. D.; Phelan, V. V.; Sandlin R.D; Bachmann, B. O.; Wright, D. W. *Combinatorial Chemistry High Throughput Screening* **2010**, *13*, 285.
- (247) Huy, N. T.; Maeda, A.; Uyen, D. T.; Trang, D. T. X.; Shiono, M. T.; Oida, T.; Harada, S.; Kamei, K. *Acta Tropica* **2007**, *101*, 130.
- (248) Noland, G. S.; Briones, N. B.; Sullivan, D. J. *Molecular and Biochemical Parasitology* **2003**, *130*, 91.
- (249) Oliveira, M. F.; Kycia, S. W.; Gomez, A.; Kosar, A. D.; Bohle, D. S.; Hempelmann, E.; Menezes, D.; Vannier-Santos, M. A.; Oliveira, P. L.; Ferreira, S. T. *FEBS Letters* **2005**, *579*, 6010.
- (250) Oliveira, M. F.; Timm, B. L.; Machado, E. A.; Miranda, K.; Attias, M.; Silva, J. R.; Dansa-Petretski, M.; de Oliveira, M. A.; de Souza, W.; Sousa, N. M.; Vugman, N. V.; Oliveira, P. L. *FEBS Letters* **2002**, *512*, 139.
- (251) Stiebler, R.; Hoang, A. N.; Egan, T. J.; Wright, D. W.; Oliveira, M. F. *PLoS ONE* **2010**.
- (252) Bohle, D. S.; Kosar, A. D.; Stephens, P. W. *Acta Crystallographica* **2002**, *D58*, 1752.
- (253) Sullivan, D. J.; Gluzman, I. Y.; Russell, D. G.; Goldberg, D. E. *Proceedings of the National Academy of Sciences* **1996**, *93*, 11865.

CURRICULUM VITAE

JOSHUA DAVID SWARTZ

306 Watts Circle, Nashville, TN 37209 | 614-598-1795 | Joshua.d.swartz@vanderbilt.edu

EDUCATION

Vanderbilt University, Nashville, TN

Ph.D. in Chemistry

2011

Dissertation: "From Diatoms to Malaria; Synthesis and Applications of Functional Materials"

Anticipated Graduation Date: August 2011

Advisor: David W. Wright

Capital University, Columbus, OH

B.A. in Chemistry (ACS Certified) and Biochemistry

2007

Minor: Computational Science

Advisor: Jens Hemmingsen

RESEARCH EXPERIENCE

Vanderbilt University, Nashville, TN

Graduate Research Assistant with the Department of Chemistry

August 2007 – July 2011

Advisor: Dr. David W. Wright

Studied the synthesis and application of silica-templated enzymatic materials and the development of low resource malaria diagnostics.

Nationwide Children's Hospital and The Ohio State University, Columbus, OH

Research Aide May 2006 – Fall 2009

Advisor: Dr. Carlos Alvarez

Analyze microarrays for DNA copy number variation and develop improved methods for analyzing large data sets.

TEACHING EXPERIENCE

Vanderbilt University, Nashville, TN

Scientist in the Classroom – In collaboration with Metro Nashville Public Schools

2010-2011

Through the Center for Science Outreach (CSO); provided teaching and laboratory assistance for 8th grade science at Issac Litton Middle School and 10th grade science at Stratford High School

Student Teaching Fellow

Dr. Joel Tellinghuisen

Fall 2008 and Fall 2009

Taught general chemistry recitation. Designed study guides and quizzes for the students.

Organic Chemistry Teaching Assistant

Dr. Adam List

2007-2008

Prepared laboratory lectures and instructed organic chemistry laboratories

Capital University, Columbus, OH

Organic Chemistry Lecture/Lab Assistant

2005-2007

Dr. L. Nyenty Arrey

Assist students during laboratory and grade lab reports/exams.

Peer Lead Teen Learning Workshop Leader

Dr. Tracey Murray

2005-2007

Equivalent to student teaching fellow at Vanderbilt University

PUBLICATIONS

“Bottom-Up Synthesis of Biologically Active Multilayer Films Using Inkjet-Printed Templates” Joshua D. Swartz, Leila F. Deravi, David W. Wright *Advanced Functional Materials* **2010** 20 (9), 1488-1492

“Rapid Production of Nitrilase Containing Silica Nanoparticles Offers an Effective and Reusable Biocatalyst for Synthetic Nitrile Hydrolysis” Joshua D. Swartz, Scott A. Miller, David Wright *Organic Process Research & Development* **2009** 13 (3), 584-589

“Development of a Histidine-Targeted Spectrophotometric Sensor Using Ni(II)NTA Functionalized Au and Ag Nanoparticles” Joshua D. Swartz, Christopher P. Gulka, Frederick R. Haselton, David W. Wright *Submitted to Langmuir*

“The Biomimetic Synthesis of Metal Oxide Nanomaterials” Leila F. Deravi, Joshua D. Swartz, David W. Wright *Nanomaterials for the Life Sciences* **2008** 2, 3-54

“Piezoelectric Inkjet Printing of Biomimetic Surfaces for Enzyme Encapsulation” Leila F. Deravi, Joshua D. Swartz, Jan L. Sumerel, David W. Wright *NIP24 and Digital Fabrication Proceedings* **2008**, 504-507.

“Development of a Low Resource Purification Platform for *Plasmodium falciparum* Histidine-Rich Protein-II Using Surface Tension Valves” Joshua D. Swartz, Keersten M. Davis, Frederick R. Haselton, David W. Wright *In preparation*.

“Utilization of the Coffee-Ring Phenomenon as a Histidine Sensor” Joshua D. Swartz, Corey M. Peak, Alexander J. Denton, Frederick R. Haselton, David W. Wright *In preparation*.

“Crystal Engineering: Solvents Effect on Beta-Hematin Formation” Anh N. Hoang, Renata Stiebler, Joshua D. Swartz, Timothy J. Egan, Marcus F. Oliveira, David W. Wright *In preparation*.

“Biomimetic Synthesis and Applications of Metal Oxide Nanocomposites” Sarah L. Sewell, Joshua D. Swartz, David W. Wright *Encyclopedia of Nanoscience and Nanotechnology* **2011** 12, 73-95

“Mapping DNA Structural Variation in Dogs” Wei-Kong Chen, Joshua D. Swartz, Laura J. Rush, and Carlos E. Alvarez *Genome Research* **2009** 19(3), 500-509

ABSTRACTS AND PRESENTATIONS

“Synthesis of Silica Nanoparticles Containing Functionally Active Nitrilase Offers An Effective and Reusable Biocatalyst for Synthetic Nitrile Hydrolysis” Joshua D. Swartz, Scott A. Miller, David W. Wright

AWARDS

Hercules Fellowship, Vanderbilt University August 2007 – July 2009

Student Teaching Fellowship Fall 2008 and Fall 2009

MEMBERSHIPS

American Chemical Society: Student Affiliate 2004-2007; Full Member 2007-Current

REFERENCES

Dr. David W. Wright

Vanderbilt University, Department of Chemistry, Station B 351822, Nashville, TN, 37235

(615) 322-2636, david.wright@vanderbilt.edu

Dr. Frederick R. Haselton

Vanderbilt University, Department of Biomedical Engineering, Station B 351631, Nashville, TN, 37235

(615) 322-6622, rick.haselton@vanderbilt.edu

Dr. Carlos E. Alvarez

The Research Institute at Nationwide Children’s Hospital, 700 Childrens Drive, Columbus, OH, 43205

(614) 355-3600, Carlos.Alvarez@nationwidechildrens.org